Dynamics-guided Vibration Signal Analysis for Fixed-axis Gearbox Fault Diagnosis

by

Xingkai Yang

A thesis submitted in partial fulfillment of the requirements for the degree of

Doctor of Philosophy

Department of Mechanical Engineering
University of Alberta

Abstract

Gearboxes are key components commonly employed to transfer torque and power and adjust speed in mechatronic systems, such as wind turbines, automobiles, and mining machines. Due to the harsh working environment, various faults may occur in gearboxes. Tooth cracks account for a large proportion of gearbox faults. Detection and severity assessment of early tooth cracks is of vital significance to prevent gearbox failures since it enables efficient condition-based maintenance activities, which not only improves system reliability but also reduces operation and maintenance costs. Vibration analysis has been widely utilized for gear tooth crack detection and severity assessment. In industrial applications, gearboxes may work under either constant or time-varying operating conditions. Besides, gearboxes may suffer from either one single tooth crack or multiple tooth cracks depending on their working environment. All these factors render it challenging to get a good understanding of vibration characteristics of gearboxes with tooth cracks owing to their complexity, which undermines the effectiveness of vibration analysis for tooth crack detection and severity assessment.

This thesis aims to procure some insights into vibration characteristics of fixed-axis spur gearboxes with tooth cracks through dynamic simulation, and the obtained insights are further adopted to guide the development of effective vibration signal analysis methods for tooth crack detection and severity assessment. To this end, the overarching objective of this thesis consists of four sub-objectives, which aim to address four issues related to tooth crack detection and severity assessment for fixed-axis spur gearboxes. Firstly, inspired by the observation that the Crack Induced Impulses (CII) contain more information on tooth crack growth, two novel condition indicators are developed by a proposed method which conducts a thorough analysis on the CII and

are adopted for early tooth crack severity assessment. Secondly, to effectively track tooth crack severity progression under time-varying operating conditions, a comprehensive study on how time-varying operating conditions affect vibration signals of a fixed-axis spur gearbox with a tooth crack is conducted. A linear dependence of the Amplitude Modulation (AM) of the CII on the time-varying operating conditions is identified, through which a new condition indicator is proposed to track tooth crack severity progression under time-varying operating conditions. In addition, inspired by the finding that the AM of the CII is resulted from operating condition variations, a normalization method is proposed to remove the speed variation-induced AM of the CII and a normalized CII is obtained. The normalized CII preserve information on tooth crack growth and are free from gearbox speed fluctuations, which are used to track tooth crack severity progression under variable speed conditions. Lastly, insights into vibration characteristics of a fixed-axis spur gearbox with multiple tooth cracks are obtained using dynamic simulation and are further experimentally validated. Besides, inspired by the observation that the CII can well reflect tooth cracks, a method focusing on the CII is proposed to detect the number and locations of multiple tooth cracks in fixed-axis spur gearboxes.

The research work conducted in this thesis enables us to procure a good understanding of vibration characteristics of fixed-axis spur gearboxes with tooth cracks working under both constant and time-varying operating conditions and provides effective vibration signal analysis methods for tooth crack detection and severity assessment of fixed-axis spur gearboxes. Future work will explore the effects of tooth lubrication and bearing faults on gearbox vibration characteristics.

Preface

The material presented in this thesis is based on the original work by Xingkai Yang. As detailed in the following, material from some chapters of this thesis has been published or submitted in four refereed journal articles and two conference papers under the supervisions of Dr. Zhigang Tian and Dr. Ming J. Zuo in review and editing, project administration, and providing resources. The generated journal articles and conference papers are with Xingkai Yang as the first author since Xingkai Yang proposed all these research topics and did the primary research work, Dr. Zhigang Tian as the corresponding author, and Dr. Ming J. Zuo as a coauthor. Dr. Peng Zhou, Dr. Zhike Peng, and Mr. Dongdong Wei are coauthors for some publications.

The work presented in Chapter 2 has been published partially in a conference paper and as a whole in a journal article, which are as follows.

- X. Yang, M.J. Zuo, Z. Tian, "Tooth Crack Severity Assessment in the Early Stage of Crack Propagation Using Gearbox Dynamic Model", PHM_CONF. 11 (2019). https://doi.org/10.36001/phmconf.2019.v11i1.801.
- X. Yang, M.J. Zuo, Z. Tian, "Development of crack induced impulse-based condition indicators for early tooth crack severity assessment", Mech. Syst. Signal Process. 165 (2022) 108327. https://doi.org/10.1016/j.ymssp.2021.108327.

The work presented in Chapter 3 has been submitted as a journal paper which is under review currently. The submitted journal paper is as follows. The contributions of coauthors Dr. Peng Zhou and Dr. Zhike Peng were on software and manuscript revision.

- X. Yang, P. Zhou, M.J. Zuo, Z. Tian, Z. Peng, "The effect of time-varying operating condition on the crack induced impulses and its application to gearbox tooth crack diagnosis", Mech. Syst. Signal Process., pp. 1-40, Submitted on Oct. 18, 2021 (Under 2nd round review).

The work presented in Chapter 4 has been published partially in a conference paper and as a whole in a journal paper, which are as follows. The contributions of the coauthor Dr. Peng Zhou were on software and manuscript revision.

- X. Yang, M.J. Zuo, Z. Tian, “Normalization of gearbox vibration signal for tracking tooth crack severity progression under time-varying operating conditions”, in: 2020 Asia-Pacific International Symposium on Advanced Reliability and Maintenance Modeling (APARM), 2020: pp. 1–6. https://doi.org/10.1109/APARM49247.2020.9209396.
- X. Yang, P. Zhou, M.J. Zuo, Z. Tian, “Normalization of gearbox vibration signal for tooth crack diagnosis under variable speed conditions”, Quality and Reliability Engineering International. (2021) 1–27. https://doi.org/10.1002/qre.3029.

The work presented in Chapter 5 has been submitted as a journal paper as follows. The submitted journal paper is under review currently. The coauthor Mr. Dongdong Wei’s contribution was on manuscript revision.

- X. Yang, D. Wei, M.J. Zuo, Z. Tian, “Analysis of vibration signals and detection for multiple tooth cracks in spur gearboxes”, Mech. Syst. Signal Process., pp. 1-46, Submitted on Feb. 04, 2022 (Under 3rd round review).

Acknowledgements

First and foremost, I would like to express my sincere appreciation to my esteemed supervisors, Dr. Zhigang Tian and Dr. Ming J. Zuo, for their invaluable supervision, continuous support, kind assistance, and great encouragement during my PhD study. Their plentiful experience, immense knowledge, and passion for academic research have encouraged me a lot in my PhD journey and daily life. Under their guidance, I have procured solid knowledge of my research filed and leaned how to conduct academic research and deal with practical problems. Without their tutelage and supervision, my research achievements obtained so far would be impossible. The work experience with them and their words and deeds will be treasured in my future career.

My sincere gratitude also goes to my PhD examining committee members, Dr. Xiaodong Wang, Dr. Wilson Wang, Dr. Yong Li, and Dr. Zengtao Chen, for their valuable comments and suggestions on my thesis. Particularly, I thank Dr. Zengtao Chen for being my supervisory committee member, thank Dr. Wilson Wang for being my external examiner, thank Dr. Yong Li for being my examiner, and thank Dr. Xiaodong Wang for being my examination chair very much.

I am very grateful to all the members in the Reliability Research Lab for their help, support, and encouragement. It is really an amazing experience and time working and studying with them. In addition, I would like to express my thanks to the China Scholarship Council and the Future Energy System-Canada First Research Excellence Fund for providing me the funding to conduct my PhD study in Canada.

Finally, I cannot forget to thank my family and my girlfriend Dr. Qiao Gao for their tremendous understanding, unconditional support, careful and meticulous consideration, and endless love. They always give me the strength and courage to move forward. Without them, it would be impossible for me to complete my PhD study. This thesis is dedicated to my family and my girlfriend.

Table of Contents

List of Tables

List of Figures

List of Acronyms

AHD	Adaptive Harmonic Decomposition
AIR	Average Increase Rate
AM	Amplitude Modulation
CI	Condition Indicator
CIs	Condition Indicators
CII	Crack Induced Impulse(s)
CII-NAMVOC	Crack Induced Impulses obtained by the NAMVOC method
CII-Proposed	Crack Induced Impulses obtained by the proposed normalization method
DOF	Degree(s) Of Freedom
EDM	Electric Discharge Machine
EDS	Exponentially Damped Sinusoid
EEMD	Ensemble Empirical Mode Decomposition
EHNR	Envelope Harmonic-to-Noise Ratio
EMD	Empirical Mode Decomposition
GMF	Gear Meshing Frequency
GSA	Generalized Synchronous Average
FD	Frechet Distance
FEM	Finite Element Modeling
FM	Frequency Modulation
HHT	Hilbert-Huang Transform
HPSTC	Highest Point of Single Tooth Contact
HT	Hilbert Transform
HTLSM	Hankel Total Least Square Method
IIR	Infinite Impulse Response
IR	Impulse Response
LDA	Linear Discriminant Analysis
LDN	Load Demodulation Normalisation
LMD	Local Mean Decomposition
LPI	Load Profile I

LPII	Load Profile II
LPM	Lumped Parameter Modeling
LPSTC	Lowest Point of Single Tooth Contact
MPM	Matrix Pencil Method
NAMVOC	Normalization of the AM caused by Varying Operating Conditions
OIR	Overall Increase Rate
PM	Prony's Method
PMI	Periodic Modulation Intensity
RCOCV	Ratio of *CIIAM* to Operating Condition Variation
RecCII	Reconstructed CII
RMS	Root Mean Square
SC	Singular Component
SCs	Singular Components
SDOF IRs	Single Degree-Of-Freedom Impulse Responses
SPI	Speed Profile I
SPII	Speed Profile II
SSW	Speed-Spectral Whitening
STFT	Short-Time Fourier Transform
SVD	Singular Value Decomposition
TSA	Time Synchronous Average
WT	Wavelet Transform
WVD	Wigner–Ville Distribution

List of Symbols

$a_m(t)$	Tooth crack-related AM in the phenomenological model for gearbox vibration signals
$A_d(t)$	Upper envelope of the CII
A_i	Amplitude of the i^{th} EDS
$b_m(t)$	Tooth crack-related FM in the phenomenological model for gearbox vibration signals
cl	Value vector of the tooth crack level
c_c	Damping coefficient of the coupling
c_p, c_g	Damping coefficients of the input and output couplings
c_r	Damping coefficient of the bearings
c_t	Gear tooth mesh damping coefficient
c_{x1}, c_{x2}	Horizontal radial damping coefficients of the input and output bearings
c_{y1}, c_{y2}	Vertical radial damping coefficients of the input and output bearings
C	Damping coefficient matrix of a one-stage fixed-axis spur gearbox
C_{bc}	Matrix for the damping coefficient of bearings and couplings
C_G	Cracked gear tooth
C_P	Cracked pinion tooth
$CIIAM$	Variable load-induced or variable speed-induced AM of the CII
CII_{norm}	Normalized CII with the speed variation-induced AM removed
C_{mesh}	Matrix for the gear tooth mesh damping coefficient
$\boldsymbol{D}$	Matrix for the second-order difference operator
D_i	Damping coefficient of the i^{th} EDS
E	Modulus of elasticity
E_{CIIEnv}	Energy of the envelope of the resonant vibration
E_{ImpVC}	Energy of the impulse vibration component
E_m	Energy of the m^{th} SDOF IR
E_{RecCII}	Energy of the Reconstructed CII
E_x	Energy of a continuous-time signal $x(t)$
f_i	Carrier (resonance) frequency of the i^{th} EDS

f_s	Pinion shaft rotating frequency
f_{mesh}	Gear meshing frequency
F	Force vector of a one-stage fixed-axis spur gearbox
FB_i	i^{th} frequency band
$\mathrm{GMF}_{\mathrm{in}}$	Gear meshing frequency of the input mesh pair (experimental case)
$\mathrm{GMF}_{\mathrm{out}}$	Gear meshing frequency of the output mesh pair (experimental case)
$\boldsymbol{H}$	An $m \times n$ real matrix
H	Conjugate transpose
$H(t)$	Heaviside function
H_G	Healthy gear tooth
H_P	Healthy pinion tooth
I_1	Mass moment of inertia of the pinion
I_2	Mass moment of inertia of the gear
I_b	Mass moment of inertia of the load machine
I_m	Mass moment of inertia of the driving motor
k_a	Axial compressive stiffness
k_b	Bending stiffness
k_c	Torsional stiffness of the couplings
k_h	Hertzian stiffness
k_r	Radial stiffness of the bearings
k_s	Shear stiffness
k_p, k_g	Torsional stiffness of the input and output couplings
k_t	Gear tooth mesh stiffness
k_{x1}, k_{x2}	Horizontal radial stiffness of the input and output bearings
k_{y1}, k_{y2}	Vertical radial stiffness of the input and output bearings
K	Stiffness matrix of a one-stage fixed-axis spur gearbox
K_I	Tooth mesh stiffness for the "Scenario 1" of multiple tooth cracks
K_{II}	Tooth mesh stiffness for the "Scenario 2" of multiple tooth cracks
K_{III}	Tooth mesh stiffness for the "Scenario 3" of multiple tooth cracks
K_{bc}	Matrix for the stiffness of bearings and couplings
K_{mesh}	Matrix for the gear tooth mesh stiffness
$ln(\cdot)$	Natural logarithm

L	Pencil parameter
m_1	Mass of the pinion
m_2	Mass of the gear
M	Mass matrix of a one-stage fixed-axis spur gearbox
M_1	Torque of the driving motor
M_2	Torque exerted on the load machine
M_{CIIAM}	Mean value of $CIIAM$
n	Sampling point
N_p	Number of teeth of the pinion
N_g	Number of teeth of the gear
p_{TH}	Pre-set threshold for selecting SCs for signal reconstruction
$P_m^{AF}(t)$	FM induced by variable speed condition in the phenomenological model for gearbox vibration signals
PMI_{SC_k}	PMI value of SC_k
$PS\text{-}I$	PS-I indicator
q	Half-length of tooth chordal thickness of target pinion (experimental case)
q_0	Target pinion tooth crack depth (experimental case)
q_g	Gear tooth crack depth
q_{max}	Maximum tooth crack depth that a cracked pinion tooth can have theoretically
q_p	Pinion tooth crack depth
$Q_i^{Imp}(t)$	AM of the CII induced by variable speed condition in the phenomenological model for gearbox vibration signals
$Q_m^{AF}(t)$	AM induced by variable speed condition in the phenomenological model for gearbox vibration signals
$round(\cdot)$	A function that rounds a digital number to nearest decimal or integer
R_{b1}	Base circle radius of the pinion
R_{b2}	Base circle radius of the gear
$Res(t)$	Residual signal (used as the input of SVD)
$ResBpf(t)$	Band-pass filtered residual signal (used as the input of SVD)
$\boldsymbol{s}$	Reconstructed signal obtained using SVD
$s_k(\theta)$	Signal component for the k^{th} order in the order-cluster of the CII
SC_k	SCs with PMI values greater than the threshold p_{TH}

SE_{FB_i}	Sum of the energy of the SDOF IRs with carrier frequencies in the frequency band FB_i
$SEnv_g$	Squared envelope of TSA_g
$SEnv_p$	Squared envelope of TSA_p
Spd	Variable speed (experimental case)
SPD	Driving motor rotational speed (dynamic simulation)
t	Time variable
T	Operation of matrix transposition
T_p	Pinion shaft rotating period
Trq	Variable torque (experimental case)
T_s	Sampling period
TSA_g	TSA signal for the gear
TSA_p	TSA signal for the pinion
$u, \dot{u}, \ddot{u}$	Displacement, velocity, acceleration vectors of a one-stage fixed-axis spur gearbox
$u_k(\theta), v_k(\theta)$	Two demodulated signal components of $s_k(\theta)$
$\boldsymbol{U}$	An $m \times m$ orthonormal matrix
v	Value vector of a CI
$\boldsymbol{V}$	An $n \times n$ orthonormal matrix
V	Value of a CI for a specific tooth crack level
V_{norm}	Normalized result of V
V_{ref}	Value of a CI for the reference crack level (healthy case)
w	Whole tooth face width of the target pinion (experimental case)
w_0	Tooth crack length of the target pinion (experimental case)
x_g	X-axis displacement of the gear of a fixed-axis spur gearbox
x_p	X-axis displacement of the pinion of a fixed-axis spur gearbox
$y_{AF}(t)$	Gear mesh-related components in the phenomenological model for gearbox vibration signals
y_g	Y-axis displacement of the gear of a fixed-axis spur gearbox
y_p	Y-axis displacement of the pinion of a fixed-axis spur gearbox
$\mathbf{z}$	Comb notch filtered signal in the angle domain

$\boldsymbol{\Sigma}$	A diagonal matrix storing the singular values of the matrix $\boldsymbol{H}$ in the descending order
α_0	Pressure angle
α_1	Angle between the action force F and its vertical component F_b
α_2	Half of the base tooth angle of the pinion tooth
α_c	Tooth crack angle (experimental case)
β	CII magnification factor representing the tooth crack severity level
$\beta y_{Imp\_ad}(\varphi)$	Angle-domain resampled CII in the phenomenological model for gearbox vibration signals
$\beta y_{Imp}(t)$	CII in the phenomenological model for gearbox vibration signals
θ_b	Angular displacement of the load machine of a fixed-axis spur gearbox
θ_{end}	Pinion angular displacement at the end of the engagement of a pair of engaged teeth
θ_d	Lasting angle of one Double-tooth-pair mesh duration
θ_g	Rotational displacement of the gear of a fixed-axis spur gearbox
θ_i	Phase of the i^{th} EDS
θ_m	Rotational displacement of the driving motor of a fixed-axis spur gearbox
θ_p	Rotational displacement of the pinion of a fixed-axis spur gearbox
θ_s	Lasting angle of one Single-tooth-pair mesh duration
θ_{HPSTC}	Pinion angular displacement at the HPSTC of the engagement of a pair of engaged teeth
θ_{LPSTC}	Pinion angular displacement at the LPSTC of the engagement of a pair of engaged teeth
υ	Poisson's ratio
μ	Scale constant between c_t and k_t
ϕ	Tooth crack angle (dynamic simulation)
λ	Penalty coefficient

Chapter 1: Introduction

This chapter consists of three sections. Section 1.1 introduces the background of this thesis, which mainly includes the gearbox fundamentals, gear fault modes, gearbox operating conditions, fundamentals of gearbox dynamic simulation, vibration analysis for gear fault diagnosis. Section 1.2 presents a review of the literature on dynamic simulation and vibration-based gear tooth fault diagnosis for fixed-axis spur gearboxes. The thesis objective, research topics and their contributions, and thesis organization are described in Section 1.3.

1.1 Background

1.1.1 Fundamentals of gearboxes and gears

Gearboxes are key components of mechatronic systems used in the industry, such as wind turbines, automobiles, and mining machines. The main function of gearboxes is to transfer torque and power, adjust rotating speed, and change motion direction of transmission systems. A wind turbine gearbox and an automobile gearbox are shown in Fig. 1.1. A wind turbine gearbox is a critical component of the wind turbine drive train, which is used to increase the rotational speed from a low-speed rotor to a higher speed electrical generator [1]. A gearbox in an automobile is employed to vary the speed ratio and torque ratio between the car engine and the driving wheels [2].

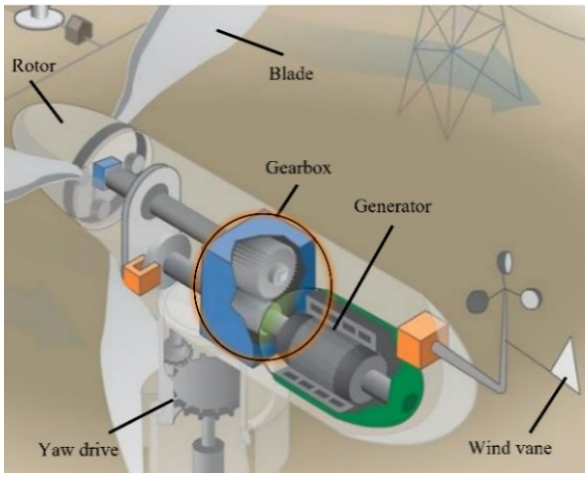

(a) A wind turbine gearbox [1]

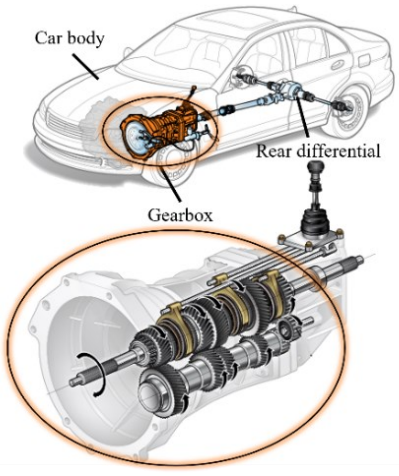

(b) An automobile gearbox [3]

Fig. 1.1: Gearboxes used in industrial applications

Gearboxes are mechanical devices mainly consisting of gears, shafts, bearings, and a housing. Gears are the core of a gearbox. There are various methods for classifying gearboxes based on the arrangement of gear axes. In this subsection, two classification methods of gearboxes are introduced, which are based on gear axis configuration and movement of gear axes, respectively. Firstly, gear axis configuration refers to the orientations of gear axes, along which the gear shafts lay and around which the gears rotate [4]. In the industry, there are three principal gear axis configurations in gearboxes: parallel, intersecting, and non-parallel and non-intersecting. On this basis, gear systems can be classified into parallel axes gears, intersecting axes gears, non-parallel and non-intersecting axes gears, which are shown in Fig. 1.2. Parallel configurations indicates that the gear shafts lay along parallel axes within the same plane, while for intersecting configurations, the gear shafts are on intersecting axes within the same plane. However, non-parallel and non-intersecting configurations mean that gear shafts exist on axes which cross (non-parallel) but not on the same plane (non-intersecting) [4].

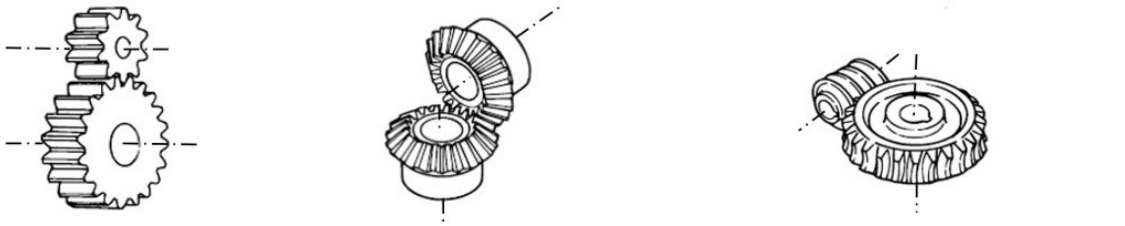

(a) Parallel (b) Intersecting (c) Non-parallel and non-intersecting

Fig. 1.2: Three gear axis configurations [5]

Secondly, according to the movement of gear axes, gearboxes can be generally classified into two categories, namely fixed-axis gearboxes, and planetary gearboxes. For a fixed-axis gearbox, it has a fixed-axis gear set, all the gear shafts of which are fixed. For a planetary gearbox, it has a planetary gear set, usually the planet gear shafts of which are not fixed and are always rotated along with the carrier. Fig. 1.3(a) shows a one-stage fixed-axis gear set, which consists of a pinion and a gear. Generally, the “pinion” refers to the smaller gear while the “gear” is the bigger one. It is noted that the terminology “gear” always refers to the bigger gear when it appears together with the “pinion”. However, in other situations, the terminology “gear” has a broader meaning [5]. Fig. 1.3(b) shows a one-stage planetary gear set, from which it is seen that a planetary gear set is consisted of a ring gear, a sun gear, several planet gears (usually three or four), and a carrier. The

sun gear is located centrally, and the planet gears mesh with the sun gear and the ring gear simultaneously when they rotate alongside the carrier.

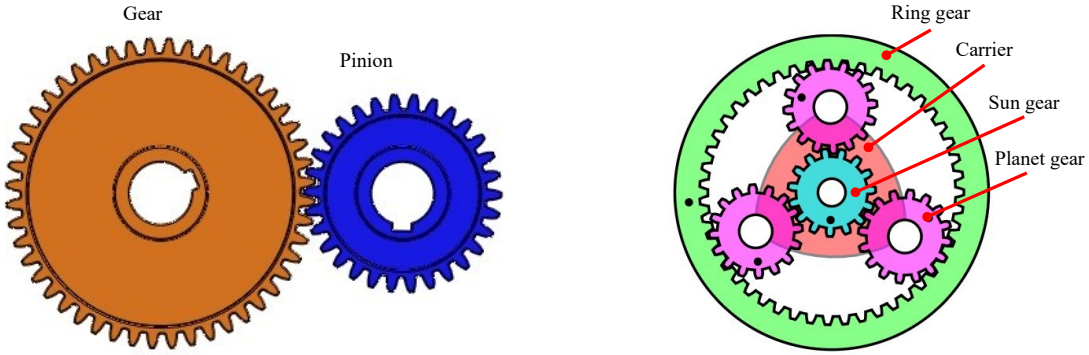

(a) A one-stage fixed-axis gear set [6] (b) A one-stage planetary gear set [7]

Fig. 1.3: Structures of two kinds of gear sets

Gears can be classified into different categories according to gear body shapes, gear teeth placement, and gear tooth profile, respectively. According to gear body shapes, gears can be classified into circular gears and non-circular (elliptical or triangular) gears [8]. Most types of gears belong to circular gears, the gear body of which is a cylinder and has a circular face, and the gear teeth are arranged around the cylindrical gear body [8]. According to gear teeth placement, gears can be categorized as external gears and internal gears. In an external gear, all the gear teeth are placed on the outer surface of the gear body and point outward from the gear center. On the contrary, all the gear teeth of an internal gear are placed on the inter surface of the gear body and point inward towards to the gear center [8]. For example, in Fig. 1.3(b), the sun gear and the planet gears are external gears while the ring gear is an internal gear. According to gear tooth profile, gears can be categorized as involute gears, trochoid gears, and cycloid gears [8]. The teeth of an involute gear have the involute tooth profiles, which means that they follow a shape designated using the involute curve of a circle. In industrial applications, most gears are involute gears since they are easier to manufacture and to operate. In contrast, trochoid gears and cycloid gears are only used in limited and specialized applications.

Besides, based on the gear axis configurations and gear design characteristics described above, gear sets can be divided into several types, such as spur gears, helical gears, and bevel gears, and so on. Fig. 1.4 shows spur gears, helical gears, and bevel gears. Spur gears usually have cylindrical gear bodies and transmit power through parallel shafts and teeth of spur gears are parallel to gear

shaft axes [4]. Helical gears also have cylindrical gear bodies and the parallel configuration, but their teeth are oriented at an angle to gear shaft axes [4]. The angle is termed “helical angle”. Unlike spur gears and helical gears, bevel gears are cone-shaped gears, which means that their teeth are placed along the conical surface [8]. Bevel gears have the intersecting configuration, so they are always adopted to transmit power between shafts that intersect at a 90-degree angle.

(a) Spur gears (b) Helical gears (c) Bevel gears

Fig. 1.4: Three different types of gears [9]

To sum up, based on above descriptions, it is seen that different combinations of gear axis configurations, gear axis movements, and gears could result in various gearbox systems. In this thesis, only the parallel fixed-axis gearboxes with circular (cylindrical gear body) external involute spur gears are involved and studied, which are termed “fixed-axis spur gearboxes” for short in the rest of this thesis.

1.1.2 Gear fault modes

Due to their harsh working environment, gearboxes may suffer from severe failures resulting from their component faults. For example, wind turbine gearboxes can fail in drastically different ways due to gear faults, bearing faults, and lubricant contamination [10]. Gear faults account for a large proportion of gearbox damages [11]. Typical gear fault modes include tooth bending fatigue, tooth contact fatigue, and tooth wear [12].

Tooth bending fatigues are always caused by repeated loading exerted on gear teeth, which include three specific modes: tooth root fillet cracks, tooth profile cracks, and tooth end cracks [12]. Tooth bending fatigues usually occur in three stages. Firstly, microscopic cracks are initiated in the areas of stress concentration or discontinuities. Afterwards, a smooth crack grows perpendicular to the maximum tensile stress [12]. Lastly, when a crack becomes large enough, it will result in sudden gear tooth fracture. Most gear tooth bending fatigues occur in the tooth root fillets, which means that tooth root fillet cracks are more commonly occurred in gears. The reason is that tooth root

fillets are the areas where stress concentration easily happens when gear teeth are subject to repeated loading. Because gearboxes have different loading conditions in different situations, there may exist one single tooth root fillet crack in some scenarios, while multiple tooth root fillet cracks may occur in other scenarios. The mechanism for the occurrence of multiple tooth root fillet cracks is that when a gearbox is operating, the cyclic loading can result in the initiation of a crack at the root fillet of one gear tooth. As the crack propagates, the cracked tooth is deflected, which leads to an extra load imposing on other teeth. In this situation, the load on the first cracked tooth is relieved, but the higher load on other teeth initiates cracks on their root fillets very soon. As a result, the repeated loading induces multiple tooth root fillet cracks [13,14]. Multiple tooth root fillet cracks include two possible categories: (1) cracks on the root fillets of two or more adjacent or nonadjacent teeth of a single gear; (2) cracks on the root fillets of teeth of two or more gears, usually on two mating gears [13–15].

Tooth contact fatigue is also called Hertzian fatigue, which mainly includes macro-pitting and micro-pitting. Macro-pitting is the severer form of micro-pitting. Macro-pitting can be categorized as nonprogressive macro-pitting, progressive macro-pitting, spalling, and flake [12]. Spalling is a fault mode that the pits coalesce and form irregular craters over a large area. On the contrary, micro-pitting refers to the case that tooth contact surface is covered by very tiny pits, which are less than 20 micrometers deep [12].

Tooth wear refers to the fault that involves the removal or displacement of tooth material from tooth surfaces thanks to mechanical, chemical, or electrical actions [12]. Tooth wear mainly consists of three types, which are adhesion, abrasion, and polishing. To be specific, adhesion is the transfer of tooth material from one tooth surface to another, which is always caused by welding and tearing. Severe adhesion is usually termed scuffing [12]. Abrasion is resulted from lubricant contamination, such as the sand, dust, wear debris, and machining chips in the lubrication oil. Severe abrasion can reduce tooth thickness significantly and the tooth tip may be reduced to a sharp edge in some situations [12]. Lastly, polishing is the fine-scale abrasion, which gives a mirror-like finish to the gear teeth. Polishing is always promoted by chemically active lubricants which are contaminated with fine abrasives [12].

For illustration, some specific gear tooth fault modes, which include tooth root fillet crack, tooth pitting and spalling, and tooth wear, are shown in Fig. 1.5. In this thesis, the research scope is

within gear tooth root fillet cracks, including the case of one single tooth root fillet crack and the case of multiple tooth root fillet cracks in fixed-axis spur gearboxes. For simplicity, tooth root fillet cracks are termed “tooth cracks” for short in the rest of this thesis.

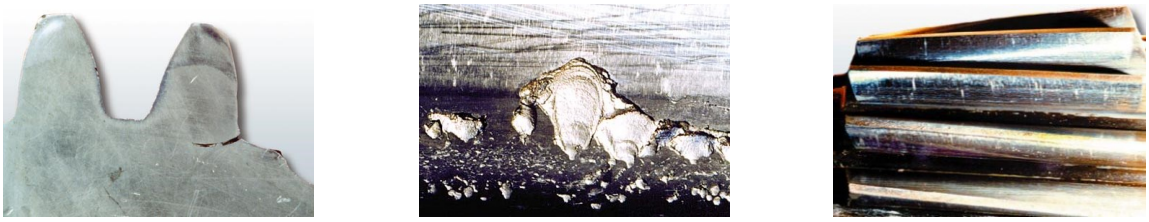

(a) Tooth root fillet crack (b) Tooth pitting and spalling (c) Tooth wear (adhesion)

Fig. 1.5: Gear tooth fault modes [12]

1.1.3 Gearbox operating conditions

In industrial applications, gearboxes may work under either constant or time-varying operating conditions. When gearboxes work under constant operating conditions, both the gearbox speed and the load are constant. It is noted that “load” is equivalent to “torque” herein and hereafter and vice versa. When gearboxes work under time-varying operating conditions, three scenarios are included, which are the constant load and variable speed condition, the variable load and constant speed condition, and the variable load and variable speed condition. Therefore, gearboxes may experience these four scenarios of operating conditions when working in the industry.

Gearboxes are usually adopted to adjust the speed and load characteristics of electric motors in mechatronic systems in the industry. When electric motors are controlled using closed-loop control strategies, either the motor speed or the load can be set to the desired values [16]. In other words, it is feasible to make either the motor speed or the load time-varying, while the other keeps constant, thus realizing the two scenarios of time-varying operating conditions under which gearboxes work, namely the constant load and variable speed condition and the variable load and constant speed condition. Gearboxes may experience the constant load and variable speed condition when used to drive conveyors and plow systems in coal mining industries, and may experience the variable load and constant speed condition when used in wind turbines [17].

When electric motors are operated in open-loop control status, the relationship between the motor speed and the motor torque is determined by the motor speed-torque characteristic curve [18,19], which means that the speed and the torque change simultaneously according to a certain law. For

example, if the external load exerted on a gearbox is variable, the driving torque of the electric motor will also vary accordingly, which makes the motor speed change according to the motor speed-torque characteristic curve, therefore changing the gearbox speed [20]. In this situation, gearboxes work under variable speed and variable load conditions. The scenarios that gearboxes experience variable speed and variable load conditions can be seen in the driving units of mining machines [19,21] and in wind turbine drive trains [22]. For a gearbox transmission system subjected to a constant external load, when the torque equilibrium status between the motor torque and the external load is obtained, the motor speed will become steady, thus render the gearbox speed constant. Therefore, in this situation, gearboxes work under constant speed and constant load conditions.

1.1.4 Fundamentals of gearbox dynamic simulation

To get a good understanding of the vibration characteristics and behaviours of gearboxes with or without gear faults under either constant or time-varying operating conditions, gearbox dynamic simulation is a good choice. The reason is that gearbox dynamic simulation techniques can not only eliminate the interferences of environmental noise but also isolate the effects of gear faults and gearbox operating condition variations on gearbox vibration signals, which helps obtain useful insights into gear fault generation mechanisms and gearbox vibration signal changes due to gear faults and operation condition variations. In addition, conducting gearbox dynamic simulation is more cost-efficient and effective to simulate various gear faults with different severity levels involving operating condition variations comparing to doing physical experiments [23,24]. Gearbox dynamic simulation generally consists of three aspects. The first aspect is to conduct gearbox dynamic modelling, the second one is to evaluate gear tooth mesh stiffness, and the last one is to conduct gear fault modelling and analyze the effects gear faults on vibration behaviours of gearbox systems.

Gearbox dynamic modeling usually utilizes physical laws, such as the Newton's Laws of Motion and the law of Conservation of Energy, to simulate the vibration responses of gearbox systems [5,23]. Generally, to ease the construction of gearbox dynamic models, real gearbox systems are always simplified into a discrete model with main features kept [23]. The Lumped Parameter Modeling (LPM) and the Finite Element Modeling (FEM) are two techniques commonly used for gearbox dynamic modeling. For a lumped parameter model of a gearbox, gearbox components are

viewed as solid bodies with their mass concentrated at a set of points [25] and vibration responses are obtained by solving motion equations of the gearbox system, and modelling accuracy can be guaranteed. For a finite element model, a gearbox system is discretized into finite elements and vibration responses are obtained by assembling the collection of all elements [25]. Because the FEM is sensitive to the types of elements, the mesh density, and the contact property, this thesis does not consider the FEM and only focuses on the LPM for gearbox dynamic modelling.

Gear tooth mesh stiffness is one of the main internal excitations of gearboxes. Correct evaluation of gear tooth mesh stiffness is important to simulate dynamic responses of gearboxes. The time-varying property of gear tooth mesh stiffness is induced by the variation of tooth contact number and contact position during gear teeth mesh process [26]. In the literature, four types of methods have been commonly adopted to evaluate gear tooth mesh stiffness, including the square waveform method, the finite element method, the experimental method, and the potential energy method [23]. For the square waveform method, a periodic square waveform is used to approximate the gear tooth mesh stiffness [19]. The period of a square waveform is used to determine the gear tooth mesh period, which is equal to the time duration of one gear revolution divided by the number of gear teeth [23]. However, the square waveform method can only reflect the change of tooth contact number, failing to represent the variation of tooth contact positions [27]. Besides, the magnitudes of square waveforms are always specified subjectively, which have no relationship to the physical parameters of gearbox systems. For the finite element method, it can implicitly evaluate the gear tooth mesh stiffness when used to simulate gearbox dynamic responses. In the finite element method, the gear tooth mesh stiffness is calculated as the ratio of the contact force carried out by a tooth to the corresponding total deformation of the gear tooth [28]. Generally, the finite element method can evaluate gear tooth mesh stiffness for gear teeth with all kinds of geometries and profiles. However, the accuracy of the gear tooth mesh stiffness obtained using the finite element method is sensitive to the types of elements, the mesh density, and the contact property. For the experimental method, some techniques have been employed to evaluate gear tooth mesh stiffness, including the photoelasticity technique [29] and the strain gauge technique [30]. However, the gear tooth mesh stiffness obtained by experimental methods are always affected by the precision of the experimental equipment and it is also very costly to conduct those experiments. For the potential energy method, gear teeth are assumed as non-uniform cantilever beams and the beam theory and

gear meshing theory are used to analytically evaluate the gear tooth mesh stiffness [23]. The gear tooth mesh stiffness obtained by the potential energy method is directly related to gear tooth geometry and material property, tooth fault types and severity levels. Besides, the gear tooth mesh stiffness can be expressed as a function of gear rotation angle using the potential energy method, which is very convenient for those who are unfamiliar with the beam theory and gear meshing theory [23]. In this thesis, the potential energy method will be used to evaluate the gear tooth mesh stiffness since it is a powerful and convenient tool.

Gear fault modelling is used to represent gear tooth faults and how their severities progress via models. The effects of gear tooth faults on gear tooth mesh stiffness also need to be studied mathematically. Because this thesis only studies gear tooth cracks, only gear tooth crack modelling is introduced herein. As introduced in Subsection 1.1.2, gear tooth cracks always occur in the tooth root fillets, tooth root fillets are chosen as the places where tooth cracks initiate. After a tooth crack initiates, it will propagate gradually as the gear rotates. Gear tooth crack propagation path is affected by many factors, including gear rim and web thickness, initial crack location, gear tooth geometry factors (number of gear teeth, diametral pitch, tooth pressure angle), and backup ratio (rim thickness divided by tooth height), which have been studied in Ref. [31] via finite element method and principles of linear elastic fracture mechanics. It was also found that gear tooth crack propagation paths were generally smooth, continuous, and rather straight lines with only a slight curvature [32]. On this basis, gear tooth cracks have been always modelled as straight lines [26,33] or slight curves [34] initiating from tooth root fillets, which is illustrated in Fig. 1.6. In addition, a tooth crack may have three different propagation scenarios according to the distribution of the load exerted on the gear tooth [35]. In the first scenario, a tooth crack was assumed to propagate in both the crack depth and the crack length directions simultaneously. The second scenario assumed that a tooth crack extended through the whole tooth width with a uniform crack depth distribution. In the third scenario, a tooth crack was assumed to extend through the whole tooth width with a parabolic crack depth distribution. This thesis will involve the first and second scenarios of tooth crack propagation since they are more commonly occurred in the industrial applications and are easily to be manufactured for experimentation.

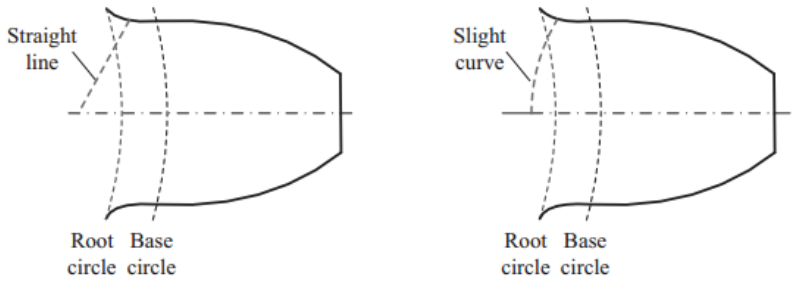

Fig. 1.6: Schematics of two simplified gear tooth cracks adopted for crack modelling [23]

1.1.5 Vibration analysis for gear fault detection and severity assessment

It is of great importance to conduct gear fault detection and severity assessment prior to gearbox failures since it can guarantee that gearbox systems are free from severe damages, thus improving system reliability and reducing downtime and maintenance costs. The fundamental idea behind gear fault detection is to analyze raw gearbox vibration signals in time domain or their transformations in other domains, such as frequency domain and time-frequency domain, to extract specific features that can characterize gear health status and compare them with thresholds, which are always obtained from reference signals (signals collected in healthy conditions) [36]. Once changes in extracted features are found, it indicates that there are faults emerged in gears, therefore the goal of gear fault detection is achieved. Afterwards, the gear faults can be assessed to see how severe they are, which is within the scope of fault severity assessment. Generally, gear fault severity progresses continuously, so severity of a gear fault can be tracked once the fault is detected. Another feasible way is to discrete gear fault severity into several levels and assess which severity level that the fault belongs to.

To conduct gear fault detection and severity assessment, many techniques have been employed to monitor and diagnose the health states of gearboxes, which mainly consist of vibration analysis, acoustic analysis, and oil debris analysis. Generally, gearboxes with faults always have larger vibration levels than they are in healthy status. Therefore, provided that vibration signals of gearboxes are collected, vibration analysis is a powerful tool to monitor and assess the health status of gearboxes and their components and also predict their failures [37]. Acoustic analysis is also called sonic analysis, which is the measurement and analysis of sound waves caused by component contacts inside equipment [38]. Acoustic analysis has been commonly utilized in the music recording industry, but its application in the condition monitoring of gearboxes is relatively new.

Unlike vibration analysis, acoustic analysis relies on the analysis of audio signals to identify how healthy the gearboxes and their components are. Oil debris analysis has been used to analyze the debris or particles in the lubrication oil inside gearboxes to check if there exists mechanical wear. To be specific, the metallic particles in the lubrication oil usually indicate a wear condition that separates different sizes and shapes of metallic dust from components such as gears or bearings [39]. This thesis focuses on vibration analysis since gearbox vibration signals contain abundant information on gear tooth health conditions and are easy to acquire.

Vibration analysis generally consists of several principles, such as time domain analysis, frequency domain analysis, time-frequency domain analysis, and modal analysis [37,40,41]. Time domain analysis mainly includes time-statistical analysis and Time Synchronous Average (TSA) [37]. Time-statistical analysis refers to the developments of health condition indicators using vibration signals and their variants, such as Root Mean Square (RMS), kurtosis, and so forth [37]. The latter is a signal processing method used to extract periodic components from noisy vibration signals, which has been demonstrated to be very suitable to process gearbox vibration signals [42]. Frequency domain analysis reveals the relationships between the amplitudes and phases of vibration signals and their frequency composition, which includes spectral analysis methods, such as amplitude spectrum, phase spectrum, power spectral density, energy spectral density, and so on. Time-frequency domain analysis has been commonly adopted to process nonstationary vibration signals in the filed of gearbox fault diagnosis, which comprises the approaches that study the nonstationary vibrations signals in both time and frequency domains simultaneously [43]. Time-frequency domain analysis methods include Short-Time Fourier Transform (STFT) [44], Wavelet Transform (WT) [45], Wigner–Ville Distribution (WVD) [46], Hilbert–Huang Transform (HHT) [47], and so on. Modal analysis is always used to study the dynamic characteristics of mechanical systems, such as the natural frequencies, damping, and mode shapes [48]. A good understanding of the modal characteristics of a structure is very useful when conducting a structural dynamic analysis [48], which could facilitate the resonance demodulation analysis. To conduct vibration analysis, vibration signals need to be collected. Generally, vibration signals include three categories: displacement signals, velocity signals, and acceleration signals, which can be collected using displacement sensors, velocity sensors, and accelerometers, respectively. Acceleration signal is the easiest one to be collected among the three kinds of signals. Therefore, this thesis only

focuses on analyzing the acceleration signals of gearboxes when conducting vibration analysis for gearbox fault diagnosis.

Although many vibration analysis methods for conducting gear tooth fault detection and severity assessment for fixed-axis spur gearboxes have been reported in the literature, the vibration characteristics of fixed-axis spur gearboxes with tooth cracks working under either constant or time-varying operating conditions have not been fully understood, which undermines the effectiveness of vibration-based gearbox diagnostics to some extent. To overcome this deficiency, this thesis aims to first get a good understanding of vibration characteristics of fixed-axis spur gearboxes with tooth cracks working under both constant and time-varying operating conditions via dynamic simulation. Afterwards, the obtained insights into gearbox vibration characteristics are employed to guide the development of new vibration analysis techniques for effective detection and severity assessment of gear tooth cracks under both constant and time-varying operating conditions.

1.2 Literature review

This section presents a detailed review of literature on dynamic simulation of fixed-axis spur gearboxes and vibration analysis methods for gear tooth crack detection and severity assessment. This section consists of two subsections: Section 1.2.1 reviews the reported studies on dynamic simulation of fixed-axis spur gearboxes; Section 1.2.2 reviews the vibration analysis methods employed for tooth crack detection and severity assessment for fixed-axis spur gearboxes.

1.2.1 Dynamic simulation of fixed-axis spur gearboxes

Dynamic simulation of fixed-axis spur gearboxes is a powerful tool to procure insights into the vibration characteristics of fixed-axis spur gearboxes with tooth cracks under either constant or time-varying operating conditions. A good understanding of gearbox vibration characteristics obtained via dynamic simulation is helpful to guide the development of effective vibration analysis methods for gear tooth crack detection and severity assessment. This subsection reviews the techniques which have been used for dynamic simulation of fixed-axis spur gearboxes, including the dynamic models of fixed-axis spur gearboxes, the evaluation of gear tooth mesh stiffness using the potential energy method, and the effect of tooth cracks on gear tooth mesh stiffness.

1.2.1.1 Dynamic models of fixed-axis spur gearboxes

Gearbox dynamic models have been widely adopted to help gearbox diagnostic inference since it can give useful insights into gearbox vibration characteristics [49]. As discussed in Subsection 1.1.4, there are two kinds of methods for gear dynamic modelling, namely the LPM and the FEM, and this thesis focuses on the former. Therefore, reported studies on dynamic modelling of fixed-axis spur gearboxes using lumped parameter models are reviewed in this subsection.

Dynamic modelling of gearboxes undergoes a process from simplicity to complexity. In the 1920s and early 1930s, studies on gear dynamics were emerged [50]. Those early studies on gear dynamics were mainly focused on the determination of dynamic loads on gear teeth, which contributed to the calculation of gear root stress. Afterwards, in 1950s and thereafter, studies on gear dynamics entered a new era because vibratory models were employed in the analysis of gear dynamics [50]. In those gear vibratory models, gear mesh interactions were modelled as spring-mass systems [51–53], which were still too simple and were mainly used to calculate dynamic loads of gear systems, failing to represent other gearbox dynamic properties. Fig. 1.7 shows two examples of early gear vibratory models consisting of mass and spring components.

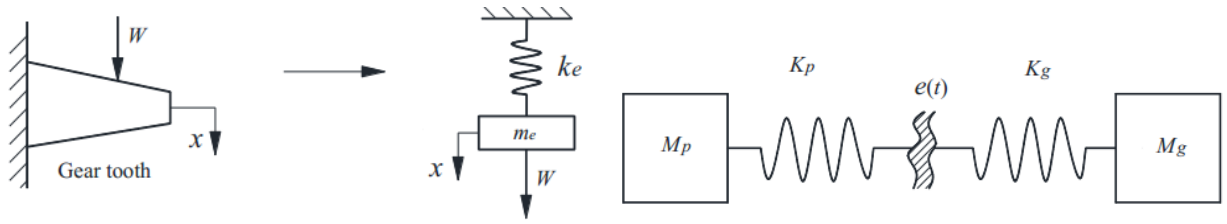

(a) A mass-spring model for gear mesh [52,54] (b) A vibratory model for mating gears [53,54]

Fig. 1.7: Two vibratory models of gears

To represent dynamic behaviours of gearbox systems, more involved dynamic models were developed in the 1970s and thereafter by taking more factors associated with gearbox systems into consideration, such as time-varying gear tooth mesh stiffness, gear tooth mesh damping, backlash, transmission error, stiffness and damping of bearings and couplings, torsional and transverse (lateral) motions of gearbox components, and so on [50,55]. In order to obtain a more accurate analysis of gearbox dynamics, there are two feasible approaches for improving the modelling accuracy: the first one is to increase the degrees of freedom of gearbox dynamic models; the second one is to keep the degrees of freedom unchanged while considering more factors related to gearbox

properties [56]. Herein, the former is adopted as the thread to present the review of the reported studies on gearbox dynamic modelling.

At the very beginning, a one Degree Of Freedom (1-DOF) dynamic model shown in Fig. 1.8 was used to represent a gear pair and analyze its torsional dynamics [56], where the gear tooth mesh stiffness and mesh damping were involved. In this 1-DOF model, the equivalent DOF is the dynamic transmission error (the difference between the displacements of the two gears along the line of action). Later, Kahraman and Singh [57] also adopted a 1-DOF dynamic model of a spur gear pair with backlash to study the effects of gearbox system parameters on the vibrations excited by the static transmission error.

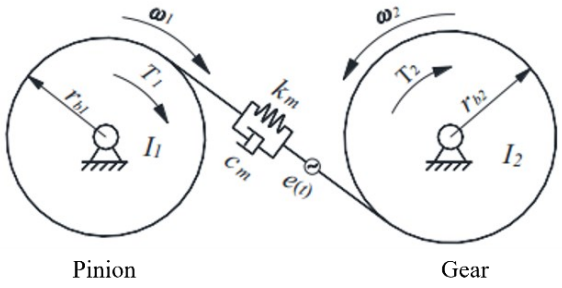

Fig. 1.8: A 1-DOF dynamic model of a pair of engaged gears [54,56]

Soon after, to include the effects of shaft and bearing compliance, the 1-DOF dynamic model presented in Ref. [57] was further extended into a 3-DOF dynamic model by Kahraman and Singh [58], which considered the radial clearance in the rolling element bearings and backlash between a spur gear pair. The 3-DOF gearbox dynamic model is shown in Fig. 1.9, and the three degrees of freedom are the vertical displacements of the two gears and the difference between the dynamic transmission error and the static transmission error [58]. Parametric studies were conducted to obtain insights into the non-linear dynamic behaviours of a spur gearbox caused by gearbox system parameters, such as bearing stiffness, gear tooth mesh stiffness, and so forth [58,59]. Besides, Iida et al. [60] adopted a 3-DOF dynamic model of a spur geared system to study the coupled torsional-flexural vibration of a shaft, which also considered the geometrical eccentricity of gears and mass unbalance. Recently, a 3-DOF dynamic model was also established to study the effect of tooth contact temperature on the tooth meshing surfaces on the gearbox dynamic behaviours, including system chaos, doubling bifurcation and Hopf bifurcation [61].

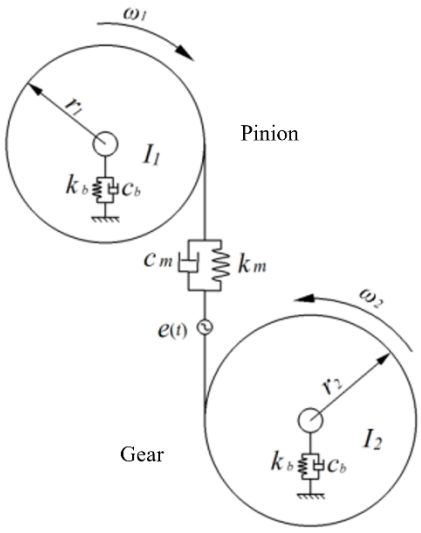

Fig. 1.9: A 3-DOF dynamic model of a spur gearbox [54,58,59]

The 3-DOF dynamic model of a spur geared system was further extended into a 6-DOF dynamic model by considering the x-axis displacements of the gear pair [62,63]. The 6-DOF dynamic model of a spur geared system is shown in Fig. 1.10, in which the six degrees of freedom were the x-axis displacements, the y-axis displacements, and the torsional displacements of the two gears, namely, x_p, x_g, y_p, y_g, θ_p, θ_g. In this model, the coupling between the torsional and transverse vibrations of the two gears were considered. Gearbox responses to gear geometric eccentricities, mass unbalances, static transmission error, and gear tooth mesh stiffness variation were studied [62].

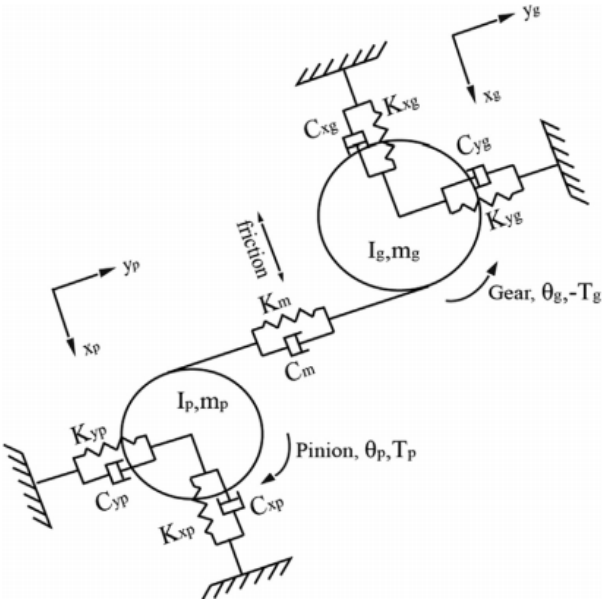

Fig. 1.10: A 6-DOF dynamic model of a spur gearbox [62,63]

The literature on gearbox dynamic modelling reviewed so far did not include the driving motor and the driven load machine, which are necessary components of a gearbox transmission system. To overcome this deficiency, Bartelmus [49] developed a spur gearbox dynamic model with 8-DOF by considering both the torsional and lateral vibrations of the two engaged gears and the torsional vibrations of the driving motor and the load machine. The 8-DOF dynamic model is shown in Fig. 11, and the eight degrees of freedom are x_p, x_g, y_p, y_g, θ_p, θ_g, θ_m, and θ_b, respectively. Besides, if the x-axis displacements of the two gears are neglected, this 8-DOF model will be reduced to a 6-DOF model [63]. This 8-DOF dynamic model is well-developed enough to study the vibration characteristics of a one-stage spur gearbox transmission system with a driving motor and a load machine involved. Besides, the effects of time-varying gear tooth mesh stiffness, mesh damping, inter-tooth friction on gearbox dynamic behaviours can also be studied using this 8-DOF dynamic model, which made this model very popular in modelling one-stage spur gearbox transmission systems [26,28,63–66].

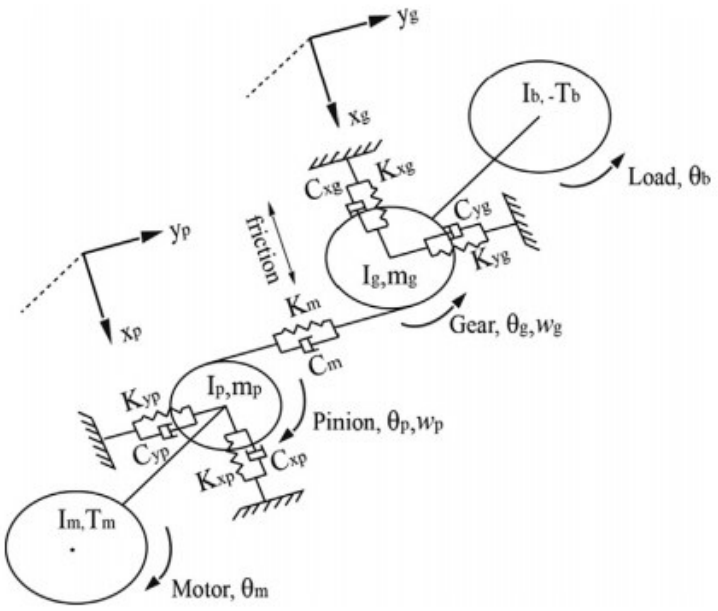

Fig. 1.11: An 8-DOF dynamic model of a spur gearbox [49,63]

During the past decade, to model a one-stage spur gearbox transmission system, more factors of gearbox components or motions have been considered, thus resulting in some dynamic models with more than 8 DOF. For example, by considering the lateral vibrations of the gearbox casing apart from the 8 DOF of the gear pair, the driving motor, and the load machines, a 10-DOF

dynamic model was built [54,67]. In order to include the gyroscopic effects of the gear pair, two more rotational degrees of freedom of each gear were added into the 8-DOF dynamic model shown in Fig. 1.11, resulting in a dynamic model with 12-DOF [63], which is shown in Fig. 1.12. The 12 DOF are x_p, x_g, y_p, y_g, θ_p, θ_g, ϕ_p, ϕ_g, ψ_p, ψ_g, θ_m and θ_b, respectively. All these models are actually the extensions and variations of the 8-DOF dynamic model reported in Ref. [49]. Besides, except for the dynamic models with various number of degrees of freedom of one-stage fixed-axis spur gearbox systems reviewed above, dynamic models of two-stage spur gearbox systems [49,68] have also been developed to study the gearbox vibration characteristics. Dynamic models of two-stage spur gearbox systems are extensions of those for one-stage fixed-axis spur gearboxes.

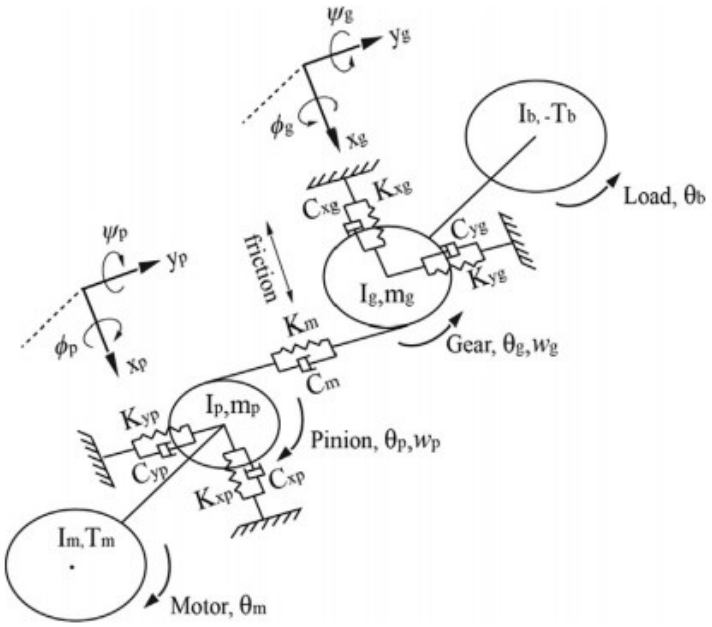

Fig. 1.12: A 12-DOF dynamic model of a spur gearbox [63]

According to the literature reviewed above, it is found that various dynamic models have been developed to model fixed-axis spur gearboxes. However, for those dynamic models, most of them only focused on the scenario that gearboxes work under constant speed and constant load (torque) conditions. Although Ref. [66] considered load variations when conducting dynamic modelling, it failed to cover other scenarios of time-varying operating conditions. To overcome this deficiency, Chapter 3 of this thesis will consider time-varying operating conditions when modelling fixed-axis spur gearboxes and study the effects of operating condition variations on gearbox vibration characteristics.

1.2.1.2 Gear tooth mesh stiffness evaluation using the potential energy method

As introduced in Subsection 1.1.4, four methods have been commonly employed to evaluate gear tooth mesh stiffness, which are the square waveform method, the finite element method, the experimental method, and the potential energy method, respectively. In this thesis, the potential energy method will be utilized due to its efficiency and effectiveness. Reported studies on the evaluation of tooth mesh stiffness of a spur gear pair using the potential energy method are reviewed in what follows.

Yang and Lin might be the researchers who first proposed the potential energy method for evaluating the gear tooth mesh stiffness [69]. They pointed out that the total potential energy stored in a meshing gear pair consisted of three parts: the Hertzian energy, the bending energy, and the axial compressive energy. The formulae of these three types of energy were derived using the beam theory since gear teeth are assumed as non-uniform cantilever beams [69]. To be specific, the Hertzian energy was referred to the energy stored in the vicinity of the tooth surface contact due to the tooth elastic deformation, which was used to calculate the Hertzian contact stiffness. The bending energy was resulting from the bending deflection of the gear teeth and was adopted to calculate the bending stiffness. The axial compressive energy was caused by the compressive strain in the axial direction of the gear teeth, which was used for the calculation of the axial compressive stiffness. The Hertzian contact stiffness was found to be a constant along the entire line of action and was independent of the position of tooth contact. On the contrary, the bending stiffness and the axial compressive stiffness were time varying since they were dependent on the variation of the number of contact pairs and tooth contact points [69].

However, Yang and Lin [69] did not consider the shear energy stored in a gear tooth when calculating the total potential energy of a meshing gear pair. To overcome this deficiency, Tian [26] analytically derived the formula for calculating the shear energy based on the beam theory as well. The shear energy was further used to calculate the shear stiffness. Based on the Hertzian stiffness, the bending stiffness, the axial compressive stiffness, the shear stiffness, and the gear meshing properties, the calculation formula of the total mesh stiffness of a gear pair for the double-tooth-pair and single-tooth-pair meshing durations were derived. Each type of stiffness was also derived as a function of the pinion angular displacement. Besides, Tian [26] found that the values of the total mesh stiffness were about two times higher than those with the shear stiffness

considered, which indicated that the shear stiffness affected the total mesh stiffness of a gear pair greatly. The relations of the bending stiffness, the shear stiffness, and the axial compressive stiffness were also studied via their mutual ratios, which showed that the magnitudes of the axial compressive stiffness were close to those of the shear stiffness but were much smaller than those of the bending stiffness. Therefore, the axial compressive stiffness and the shear stiffness can not be neglected when evaluating the total mesh stiffness of a gear pair [26].

For the studies reported in Refs. [26,69], they all assumed that the gear bodies were rigid and the root of each tooth did not experience any deflection, which ignored the effect of fillet foundation deflection on the gear tooth mesh stiffness. To overcome this drawback, Sainsot et al. [70] investigated the effect of fillet foundation deflection on the gear tooth mesh stiffness and derived the mathematical formula of this deflection. The fillet foundation deflection was adopted to calculate the stiffness due to the fillet foundation deflection [35]. Later, Zhou et al. [71] assumed that both a gear tooth and the rim of a gear suffered the deflections and derived the bending stiffness and the shear stiffness under the new assumptions. They compared their stiffness results to those obtained using the formulae presented in Ref. [26] and the finite element methods, and found that their stiffness results were closer to the latter while smaller than the former.

For the studies reported in Refs. [26,35,69–71] reviewed above, the evaluation of gear tooth mesh stiffness were conducted when gearboxes work under constant speed conditions, failing to involve time-varying speed conditions. However, in industrial applications, gearboxes oftentimes experience speed fluctuations. Therefore, the evaluation of gear tooth mesh stiffness under variable speed conditions needs to be conducted, which will be presented in Chapter 3 of this thesis.

1.2.1.3 Effect of tooth crack on gear tooth mesh stiffness

When there exists a tooth crack in a spur gearbox, the presence of a tooth crack in the spur gear pair will result in changes in gear tooth mesh stiffness since the tooth crack changes the tooth geometrical structure and its load-bearing capacity, consequently changing gearbox vibration characteristics. The changes in gear tooth mesh stiffness due to a tooth crack can be analytically represented using the potential energy method or calculated using the finite element method. This thesis will employ the potential energy method to study the effect of tooth cracks on the mesh stiffness of a spur gear pair. During the last few decades, many studies have been conducted to

evaluate the effect of a tooth crack on gear tooth mesh stiffness using the potential energy method, some representatives of which are reviewed in what follows.

For a spur gear pair consisting of a pinion and a gear, Tian [26] evaluated the gear tooth mesh stiffness for the case that there was a root crack on one pinion tooth and the gear was healthy. The reason for considering the pinion tooth crack was that the pinion had higher rotational frequency and was easier to experience tooth cracks. In Ref. [26], Tian only considered the case when the crack depth was less than half of the base chordal thickness of one pinion tooth, which corresponded to a shallow crack in the tooth, and assumed that the tooth crack extended through the whole tooth face width with a uniform depth. It was found that a pinion tooth crack did not affect the effective work surface of the tooth, therefore the Hertzian stiffness was not affected by tooth crack. Besides, although a tooth crack existed, the crack part still had the capacity of bearing the axial compressive force as if there was no crack, which made the axial compressive stiffness the same as that under the perfect tooth condition. However, the bending stiffness and the shear stiffness were affected by a tooth crack, calculation formulae of which for the cracked case were derived based on the beam theory [26]. Bending stiffness and shear stiffness decreased greatly due to the presence of a tooth crack and the affected mesh stiffness lasted for the entire mating duration of the tooth with a root crack, and the total mesh stiffness of a gear pair also decreased significantly accordingly. Later, Wu et al. [33] extended the work presented in Ref. [26] by considering the case that the tooth crack depth was greater than half of the base chordal thickness of one pinion tooth. Accordingly, the calculation formulae for the bending stiffness and the shear stiffness were refined to cover the newly considered case of crack depth. They also studied the effect of tooth crack growth on the total mesh stiffness of a spur gear pair and found that as the crack depth increased, the total mesh stiffness when the cracked pinion tooth was in meshing became much lower. This observation could be used for tooth crack detection and severity assessment. Besides, Chaari et al. [72] developed a mathematical model to analytically quantify the gear tooth mesh stiffness reduction due to the presence and severity progression of tooth crack.

In order to improve the accuracy of mesh stiffness of a spur gear pair with a tooth crack, the tooth crack propagation path needs to be modelled in a practical way. For the propagation path of a tooth crack, straight line segments were employed for crack modelling in Refs. [26,33]. However, Pandya and Parey [73] proposed a curved crack propagation path for representing tooth crack

severity progression and for evaluating gear tooth mesh stiffness. Besides, comparisons between the results of total mesh stiffness obtained using the proposed curved tooth crack propagation path and those obtained using the straight counterpart were made for two gear pairs with different contact ratios. For the gear pair with a contact ratio smaller than two, it was found that for early tooth crack, the total mesh stiffness results obtained using the two types of crack propagation were approximately equal. However, for advanced tooth crack, the total mesh stiffness obtained using the proposed curved tooth crack propagation path was smaller than that obtained using the straight one. On the contrary, for the gear pair with a contact ratio greater than two, the difference between the stiffness results for the straight and curved paths was insignificant [73]. In addition, various tooth crack propagation scenarios were also studied and compared in Refs. [35], including (1) tooth crack propagated in both the crack depth and the crack length directions simultaneously [74]; (2) tooth crack extended through the whole tooth width with a uniform crack depth distribution [26,33,71]; (3) tooth crack extended through the whole tooth width with a parabolic crack depth distribution [75]. It was found that the third scenario resulted in insignificant reflection on the decrease of gear tooth mesh stiffness.

Although the studies reviewed above have been conducted to study the effect of tooth crack on gear tooth mesh stiffness, they only considered the case that there exists one tooth crack in a spur gear pair, which is not always the case in the gearboxes used in industrial applications since multiple tooth cracks may occur in gearboxes in some scenarios. To overcome this drawback, Chapter 5 of this thesis will analytically evaluate the mesh stiffness of a spur gear pair with multiple tooth cracks on the pinion and/or on the gear and reveal the effects of multiple tooth cracks on the total mesh stiffness and gearbox vibration responses.

1.2.2 Vibration-based gear tooth fault diagnosis for fixed-axis spur gearboxes

In this subsection, the composition of vibration signals of fixed-axis spur gearboxes is first introduced, which helps us get a good understanding of the constitutive components of vibration signals of fixed-axis spur gearboxes, therefore contributing to the development of effective vibration signal analysis methods for gear fault diagnosis for fixed-axis spur gearboxes. This is complementary to the gearbox dynamic simulation for understanding gearbox vibration signals. Afterwards, vibration signal analysis methods for gear tooth crack detection and severity assessment for fixed-axis spur gearboxes reported in the literature are reviewed, including the

Condition Indicators (CIs) employed for gear fault diagnosis, the extraction of the Crack Induced Impulses (CII), and the removal of the Amplitude Modulation (AM) and Frequency Modulation (FM) caused by operating condition variations.

1.2.2.1 Composition of vibration signals of fixed-axis spur gearboxes

For a spur gear pair works under constant speed and constant load conditions, if each gear is an ideal gear that is free of geometry and manufacturing errors, the gear meshing vibration will comprise the fundamental gear meshing frequency and its multiples [76]. However, for the vibration signals generated from healthy fixed-axis spur gearboxes used in real industrial applications, they mainly consist of the gear meshing harmonics and the associated sidebands and environmental noise [76,77]. The sidebands around the gear meshing harmonics are usually low-order (first and second order) sidebands resulting from the AM and FM, which are caused by the transmission errors that are related to the manufacturing and assembly errors of the spur gear pairs.

When a tooth crack is present in a fixed-axis spur gearbox which is working under constant speed and constant load conditions, impulses will be produced by the cracked tooth when it contacts with other gear teeth [77–79], and the impulses are termed CII in this thesis. The CII possess a short-period property and have a comparatively low-energy level, which results in a cluster of high-order harmonic components with relatively low magnitudes spreading over the frequency spectrum of the gearbox vibration signal. The carrier frequencies of the CII are generally the resonant frequencies of a gearbox. Besides, the CII also induce additional AM and FM into the normal gear vibration where the carrier frequencies are the gear meshing harmonics, which modifies the original AM and FM of healthy gearbox vibration signals caused by the gear manufacturing and assembly errors. Therefore, for a practical fixed-axis spur gearbox with a tooth crack working under constant speed and constant load conditions, its vibration signal mainly consists of the gear meshing harmonics and the associated crack-related AM and FM, the CII, and environmental noises [77,79]. The crack-related AM and FM and the CII are the signal components which are closely related to the gear tooth crack, the information embedding in which can be extracted and used for gear tooth crack diagnosis. On this basis, many CIs have been developed using the crack-related AM and FM and the CII for gear tooth crack diagnosis, which will be reviewed later in Subsection 1.2.2.2. Besides, it was also found that the CII provided more valuable information for the tooth crack diagnosis than the crack-related AM and FM [77,79]. Therefore, the CII need to be

extracted from gearbox vibration signals for the development of more effective methods for tooth crack diagnosis. The reported studies on the extraction of the CII from gearbox vibration signals will be reviewed in Subsection 1.2.2.3.

When gearboxes work under time-varying operating conditions, where either the speed or the load or both vary with time, the speed and load variations will result in additional AM and FM into gear vibration signals [36,80,81], which are termed the operating condition variation-induced AM and FM in this thesis. Therefore, for a fixed-axis spur gearbox with a tooth crack which works under time-varying operating conditions, its vibration signal is a combination of the operating condition variation-induced AM and FM, gear meshing harmonics and the associated crack-related AM and FM, the CII, and environmental noises. However, the dependences of the operating condition variation-induced AM and FM on the time-varying operating conditions are unknown yet. Urbanek at al. [36] made an attempt to build a model of vibration signals that included the effects of time-varying speed and load conditions by assuming that the operating condition variation-related AM was a compound function of both speed and load, but only a graphic representation of the operating condition variation-induced AM was presented, failing to give its mathematical expression. Later, Schmidt and Heyns [80] assumed that the measured vibration signals for gearboxes working under time-varying operating conditions were a product of a function of operating condition variables (speed and load), which denoted the AM induced by operating condition variations, and a stationary signal. But the mathematical form of the function representing the AM induced by operating condition variations was not described as well. To overcome this drawback, Chapter 3 of this thesis will reveal the dependence of the AM induced by operating condition variations on the time-varying operating conditions. On this basis, a phenomenological model for the vibration signals of a fixed-axis spur gearbox with a tooth crack working under variable speed conditions will be introduced in Chapter 4 of this thesis.

In addition, because the operating condition variation-induced AM and FM are interfering factors in terms of gearbox fault diagnosis since they do not reflect the changes of health status of gears and can mask the presence of gear tooth faults, they need to be removed when processing gearbox vibration signals for gear fault diagnosis. The reported studies on the removal of the operating condition variation-induced AM and FM will be reviewed in Subsection 1.2.2.4.

1.2.2.2 Condition indicators for gear tooth crack diagnosis

During the last several decades, various CIs have been developed using raw gearbox vibration signals and gear TSA signals for gear tooth crack diagnosis. However, because raw gearbox vibration signals usually contain strong environmental noise that always masks the weak fault signature, CIs calculated using raw gearbox vibration signals are not effective enough for tooth crack diagnosis. To eliminate the effects of noise, the TSA signals of gears, which can be obtained by conducting the TSA operation on raw gearbox vibration signals, have been commonly employed for developing various CIs for gear tooth crack diagnosis. The CIs developed using the gear TSA signals are reviewed in the following.

FM0 was developed by Stewart [82] to detect vibration changes caused by tooth cracks. FM0 was defined as the ratio of the peak-to-peak value of the signal to the sum of RMS values of the Gear Meshing Frequency (GMF) and its harmonics. Subsequently, to boost the performance of FM0, FM4 was designed to detect cracks limited to a small number of gear teeth. To calculate FM4, the difference signal was first created by removing the GMF and its harmonics along with the first order sidebands around them from the TSA signal. FM4 was calculated by dividing the fourth statistical moment of the mean by the square of the variance of the difference signal [83]. If the tooth fault only propagates locally, FM4 would keep increasing. However, as the occurrences of tooth cracks progressed in both number and severity, FM4 became less sensitive to tooth crack growth. To overcome the deficiency of FM4, NA4 was developed by making two changes to the FM4 [83]. The first change was that FM4 was calculated using the difference signal while NA4 was calculated from the residual signal. The residual signal includes the first order sidebands that are removed from the difference signal. The second change was that trending was incorporated into the NA4 parameter. NA4 was more sensitive to tooth fault growth than FM4 [83,84]. NB4 was another CI developed to detect localized gear tooth cracks [85]. The calculation of NB4 was like that of NA4 since it adopted the same operation to normalize the kurtosis. However, unlike NA4, NB4 used the envelope of the signal obtained by band-pass filtering about the dominant GMF [85]. These four CIs have been employed for gear tooth crack diagnosis, but they can only indicate tooth cracks in the advanced stage (close to complete loss of tooth), failing to reliably and accurately detect early tooth cracks [84]. Later, another CI called PS-I was developed to track tooth crack severity progression [86]. It was designed as the ratio of RMS of the residual signal to that

of the regular signal. Using the PS-I, the presence of a tooth crack could be detected. In addition, PS-I has been shown to be more sensitive towards tooth crack severity progression than the FM0, FM4, NA4, and NB4 [86]. However, from the perspective of tracking tooth crack growth in the early stage, PS-I cannot achieve satisfactory performance since its increase was still small from healthy state to early crack stage [86]. The reason accounting for the failure of these CIs to track tooth crack growth in the early stage is that the signal components based on which they are calculated comprise little signature reflecting early tooth crack severity progression.

As discussed in Subsection 1.2.2.1, for a gearbox with a localized tooth crack, it has been reported that the CII in the gearbox vibration signal contain more valuable information for tooth crack diagnosis than the crack-related AM-FM [77]. Therefore, how to accurately extract the CII from the gear TSA signals and how to obtain tooth crack information from the CII are worth studying since it will contribute to early tooth crack diagnosis. Generally, for a gearbox with one tooth crack, there only exists one impulse induced by the tooth crack in one gear shaft revolution. Because a gear TSA signal has the length of one gear shaft revolution, it includes the average of the CII. For the consistency of nomenclature, the average of the CII included in a gear TSA signal is also termed "CII" in this thesis. However, the "CII" extracted from a gear TSA signal is the average of the "CII" obtained from the raw gearbox vibration signals, although they use the same abbreviation.

Wang [77] made an attempt to extract features related to the CII from TSA signals of gearboxes with a tooth crack using a resonance demodulation technique. Firstly, the GMF and its harmonics were removed from the TSA signal to obtain the residual signal. The residual signal was then band-pass filtered within the resonant frequency band in which the CII existed. However, in Ref. [77], the resonant frequency band was selected simply using visual inspection. Afterwards, the band-pass filtered residual signal was squared, and the squared signal was low pass filtered to get the squared envelope signal. The resulting envelope signal was expected to indicate the abrupt change caused by the tooth crack. Kurtosis of the squared envelope signal was calculated, and the results showed that it provided a good indication of tooth crack. However, kurtosis of the squared envelope signal was not so good for continuously monitoring tooth crack severity progression. This deficiency may be resulted from the existence of the crack-related AM-FM sidebands in the visually selected resonant frequency band. In order to overcome the drawback of the method reported in Ref. [77], Man et al. [87] proposed a multiple modulated sinusoidal model to represent

the TSA signals of both healthy and cracked gears. The batch learning of the least squares technique was adopted to optimize the sinusoidal model parameters. With the optimized model parameters, both the impulse vibration component induced by tooth cracking and the crack-related AM-FM in the TSA signal were identified. Besides, the identified impulse vibration component was further analyzed to get insight of tooth crack diagnosis. The energy of the identified impulse vibration component was employed as a CI to monitor the evolution of tooth cracking. Although the result presented in Ref. [87] showed that the energy of the impulse vibration component performed better than the energy of the residual signal in Ref. [77], it was still relatively stabilized when the tooth crack was in the early stage, which may result in poor performance on early tooth crack severity assessment. The problem of the methods reported in Refs. [77,87] is that the component of the CII that can effectively indicate early tooth crack severity progression is not identified and utilized for early tooth crack diagnosis.

To overcome the deficiencies of the CIs reviewed in this subsection in terms of tracking tooth crack severity progression in the early crack stage, Chapter 2 of this thesis proposes a new method for extracting the CII from gearbox vibration signals and conducts a comprehensive study on the extracted CII to propose two new CIs for early tooth crack severity assessment.

1.2.2.3 Extraction of crack induced impulses

As mentioned in Subsection 1.2.2.1, the CII in gearbox vibration signals contain more valuable information for tooth crack diagnosis than the crack-related AM-FM. Therefore, better results of gear fault diagnosis will be achieved if the CII are employed for gear fault diagnosis. To this end, one critical step is to extract the CII accurately and effectively from gearbox vibration signals. However, to extract the CII directly from gearbox vibration signals is very demanding. A feasible way is to transform the extraction of the CII to the reconstruction of the CII, thus achieving the goal of extracting the CII. In the literature, many studies that follow the idea of reconstructing the CII have been conducted to extract the CII from gearbox vibration signals, some representatives of which are reviewed as follows.

Wang [77] made an attempt to extract the CII from gearbox vibration signals using the band-pass filtering operation. To be specific, TSA was first conducted on gearbox vibration signals to get the gear TSA signals. Gear mesh harmonics were then removed from the gear TSA signal to generate

the residual signal. Afterwards, the residual signal was band-pass filtered with the pass band being the resonant frequency band to get the CII. Because the resonant frequency band was determined simply using the visual inspection, the extracted CII had many masking components related to gear mesh, which submerged the tooth crack information to some extent and undermined its effectiveness for early tooth crack diagnosis. Therefore, how to select the optimal resonant frequency band where the CII exist and extract the CII directly from TSA signals are very challenging and demanding. Later, Man et al. [87] used the idea of reconstruction to extract the CII via mathematical models. Specifically, the authors developed a multiple modulated sinusoidal model to represent the TSA signals of cracked gears, and the CII were reconstructed using the optimized model parameters of the multiple modulated sinusoidal models. However, it was difficult to determine the model order, and if the model order was not properly determined, the reconstructed CII could not cover all the information on tooth crack, thus failing to well extract the CII. To overcome the deficiencies of the studies reported in Refs. [77,87], in this thesis, Chapter 2 will propose a new method for extracting the CII from gearbox vibration signals, which follows the idea of reconstruction as well, and conduct a thorough study on the extracted CII. Details of the new method for the extraction of the CII will be presented in Chapter 2 of this thesis.

The CII can also be reconstructed using their corresponding frequency components. When a gearbox with a tooth crack is working under constant speed and constant load conditions, the CII are periodic in the time domain. Zhou et al. [88] observed that the CII resulted in a group of harmonics, namely a harmonic cluster, in the frequency spectrum of gearbox vibration signals, and the frequency interval between every two adjacent harmonics was the reciprocal of the repetition period of the CII. The authors also bridged the equivalence between the CII and the corresponding harmonic cluster via mathematical derivations [88]. On this basis, Zhou et al. [88] developed an Adaptive Harmonic Decomposition (AHD) method to extract all the harmonics in the frequency spectrum, which were related to the CII, using an iteration scheme. After all the harmonics related to the CII were obtained, they were further summed to reconstruct the CII, therefore achieving the goal of extracting the CII from gearbox vibration signals. The operations of the AHD method were conducted in the time and frequency domains, and the AHD method worked well in extracting the CII from gearbox vibration signals under constant speed and constant load conditions. However, when it comes to time-varying speed and load conditions, the CII are no longer periodic in the

time domain. In this case, the original AHD method becomes incompetent to extract the CII. To overcome this drawback, the original AHD method needs to be modified to extract the CII from vibration signals of gearboxes working under time-varying speed and load conditions. Details of the modified AHD method will be presented in Chapter 3 of this thesis.

Another way is to reconstruct the CII by selecting desirable components of gearbox vibration signals obtained using the signal decomposition methods for summation, thus achieving the goal of extracting the CII from gearbox vibration signals. In the context of reconstructing the CII, the desirable signal components to be selected refer to the constitutive components of the CII, while the other unselected signal components can be regarded as unwanted interference or noise components. Therefore, the reconstruction of the CII based on the signal decomposition and the selection of desirable signal components is also called signal denoising in some papers since the CII are highlighted and kept while the unwanted signal components are discarded as noise. During the last several decades, various signal decomposition methods have been developed for signal denoising, which include Wavelet Transform (WT) [45,89,90], Empirical Mode Decomposition (EMD) [47,91], Ensemble Empirical Mode Decomposition (EEMD) [92], Local Mean Decomposition (LMD) [93], Singular Value Decomposition (SVD) [94–97], and so forth. Among these signal decomposition methods, SVD has become increasingly popular since it is a non-parametric signal analysis method which can be implemented without defining prior basis functions and it has relatively high computation efficiency [97]. Due to these metrics of SVD, it has been widely used to extract the CII in the research field of gearbox condition monitoring and fault diagnosis. The main idea behind the studies which adopted SVD to extract the CII is to first decompose a gearbox vibration signal into several Singular Components (SCs) using SVD. Subsequently, the SCs which are the constitutive components of the CII need to be identified and selected. To this end, a selection criterion needs to be designed. Conventionally, researchers always employed the energy of an SC as the selection criterion to pick out the SCs for signal denoising. The idea behind the conventional energy-based SVD methods is that an SC with a higher energy value is assumed to be a main signal component and needs to be picked out and kept for signal reconstruction, while those with lower energy values are discarded as noise [98,99]. However, the conventional energy-based SVD methods did not work well in extracting the CII since the energy of the CII is relatively lower than those of other signal components such as gear

meshing harmonics. To overcome this drawback, recently, Zhao and Jia [97] developed a new selection criterion for picking out the SCs most related to the CII, which was based on an index termed Periodic Modulation Intensity (PMI). PMI can effectively evaluate the information on the CII included in an SC since it measures the strength of CII and represents the energy ratio between the CII and other signal components [97]. Although Zhao and Jia [97] demonstrated that their PMI-based SVD method outperformed the conventional energy-based SVD methods, performance of their method was affected by the gear meshing harmonics which were not removed in their study. Chen at al. [96] observed that the non-fault related baseline vibration components affected the PMI values and adopted an auto-regression model to remove the baseline vibration components (such as gear meshing harmonics) to get the so-called residual signal. Afterwards, the residual signal was processed using the SVD-PMI scheme. However, it is difficult to select a good model order for the auto-regression model. If the model order is not well determined, the auto-regression model cannot work well in removing the baseline vibration components. To overcome this disadvantage, a new method for extracting the CII using the SVD-PMI framework is proposed, which will be detailed in Chapter 5 of this thesis.

For the three kinds of methods for extracting the CII reviewed in this subsection, namely the reconstruction of the CII via mathematical models, the reconstruction of the CII via the corresponding frequency components, and the reconstruction of the CII via selecting the desirable signal components, each of them has its own advantages and disadvantages. It is difficult to tell which one is the best option. Each of the three methods has a room for further improvements to make itself more powerful and suitable to extract the CII. Therefore, in this thesis, the method adopted to extract the CII will be selected according to the application scenarios.

1.2.2.4 Removal of the operating condition variation-induced AM and FM

As discussed in Subsection 1.2.2.1, time-varying operating conditions of gearboxes induce additional operating condition variation-induced AM and FM into gearbox vibration signals, which can mask the presence of gear tooth faults. The reason is that due to the operating condition variation-induced AM and FM, changes in CIs may indicate the change of gear tooth health state, operating condition variations, or both. Therefore, in order to conduct effective and accurate gear tooth crack diagnosis under time-varying operating conditions, the operating condition variation-induced AM and FM need to be removed. Besides, during the removal process, the information on

tooth crack should not be attenuated. This subsection reviews the reported studies on the removal of the operating condition variation-induced AM and FM, some representatives of which are described in the following.

For the removal of the operating condition variation-induced FM, it can be easily done using the order tracking techniques, which have been widely adopted to compensate for the FM induced by speed variations [100]. Because the order tracking techniques have been well developed, the relevant studies are not reviewed herein. On the contrary, the research work on the removal of the operating condition variation-induced AM is not mature and has been developing all the time. Therefore, the reported studies on the removal of the operating condition variation-induced AM are reviewed herein. Stander et al. [81] developed a Load Demodulation Normalisation (LDN) procedure to reduce the AM induced by cyclic stationary load conditions, but it also attenuated the information on tooth crack severity progression. Urbanek et al. [36] came up with a method for normalizing the amplitude of gearbox vibration signal to get rid of the AM induced by time-varying speed conditions. However, this normalization method attenuated the information on gear tooth crack severity progression since the AM effect was estimated using the entire vibration signal. Abboud et al. [101] developed a method called Speed-Spectral Whitening (SSW) to reduce the amplitude fluctuation of frequency contents caused by variable speed conditions based on the Campbell diagram. However, the performance of the SSW method was highly dependent on the estimation of the Campbell diagram. Later, Abboud et al. [102] further proposed another method named Generalized Synchronous Average (GSA) to mitigate the AM induced by variable speed conditions. However, in the GSA method, estimation issues related to speed resolution, the number of regimes, and the repartition of the central frequencies were difficult to tackle [102], which makes the GSA method hard to implement in some applications.

Recently, another method called Normalization of the AM caused by Varying Operating Conditions (NAMVOC) has been developed to remove the AM induced by time-varying speed conditions [80]. In the NAMVOC method, the square root of the moving median filtered squared envelope of the entire raw vibration signal was calculated and seen as the AM, through which the entire raw vibration signal was normalized, thus removing the AM induced by variable speed conditions [80]. The analysis results of both simulated gearbox signals and experimental gearbox data showed that the NAMVOC outperformed the GSA for reducing the AM. Although the

NAMVOC method alleviated the AM caused by variable speed conditions, it still suffered from several problems. To be specific, firstly, the NAMVOC method possesses an inappropriate assumption that variable speed conditions induce the same AM into all components of the gearbox vibration signal. This assumption leads to a significant simplification of the original problem since variable speed conditions could result in different AM effects on different signal components [36]. The utilization of the estimated AM result obtained from the entire raw vibration signal to remove the AM attenuates the information on gear tooth crack severity progression. The second problem is that it is not an easy job to determine the optimal length of the moving median filter for the NAMVOC method. Improper values of moving median filter length can highly affect the performance of the NAMVOC method [80]. In addition, the performance of the NAMVOC method on the removal of the AM effect was only qualitatively evaluated and compared, rather than being quantitatively evaluated [80].

To overcome the deficiencies of the methods for removing the operating condition variation-induced AM reviewed above, in this thesis, Chapter 4 proposes a new normalization method which not only removes the AM and FM induced by variable speed conditions but also preserves the information on tooth crack severity progression. Details of the proposed normalization method will be presented in Chapter 4.

1.3 Thesis objective and outline

The overarching objective of this thesis is to get a good understanding of the vibration characteristics of fixed-axis spur gearboxes with tooth cracks under either constant and time-varying operating conditions, and develop effective vibration analysis methods for accurate tooth crack detection and severity assessment based on the obtained insights into gearbox vibration characteristics. The overarching objective is divided into four sub-objectives, which are described as follows.

1) To propose a novel method to effectively extract the CII from gearbox vibration signals and conduct a thorough study on the CII to propose two new CIs for accurate early tooth crack severity assessment.

2) To conduct a comprehensive study on how time-varying operating conditions affect the vibration characteristics of a fixed-axis spur gearbox with a tooth crack using dynamic simulation and develop effective CIs for tracking tooth crack severity progression under time-varying operating conditions.

3) To propose a novel normalization method to remove the speed variation-induced AM and FM without attenuating the tooth crack information and apply the proposed normalization method for tracking tooth crack severity progression under variable speed conditions.

4) To obtain insights into the vibration characteristics of a fixed-axis spur gearbox with multiple tooth cracks using dynamic simulation and propose a method for detecting the multiple tooth cracks.

The basic assumptions adopted in this thesis are listed in the following.

1) The components in a fixed-axis spur gearbox, such as gears, bearing, and shafts, have no geometric, manufacturing, and assembly errors.

2) The gearbox lubrication condition is perfect.

3) The gear mesh interaction is modelled as a mass-spring-damper system.

4) A gear tooth is regarded as a cantilever beam when calculating its potential energy.

5) The gearbox casing is considered as a rigid body when conducting gearbox dynamic modelling.

6) The effect of the transmission path on gearbox vibration signals is negligible.

7) Gearbox acceleration signals and tachometer signals can be acquired accurately using accelerometers and tachometers or encoders, respectively.

To achieve the four sub-objectives presented above, four research topics have been completed in this thesis, which are presented as follows.

In the first research topic (Topic #1), two new CIs are developed using the CII for early tooth crack severity assessment, which outperform the three ones reported in Refs. [77,86,87]. To this end, a novel method is proposed to extract the CII and conduct a thorough analysis on the CII. In the proposed method, TSA is first adopted to process gearbox vibration signal to get the gear TSA

signal. The GMF and its harmonics and the crack-related AM-FM are then removed from the gear TSA signal using comb notch filters. The notch filtered signal mainly contains components related to the CII. A modal model is adopted to fit the dominant resonances in the notch filtered signal and modal parameters are obtained using the matrix pencil method. With the modal parameter estimates, the dominant resonances, which are Single Degree-Of-Freedom Impulse Responses (SDOF IRs), are identified and used to reconstruct the CII. Besides, the SDOF IRs are grouped according to their carrier frequencies. The energy of the reconstructed CII and the sum of the energy of the SDOF IRs with carrier frequencies in a specific frequency band are proposed as two new CIs for tooth crack diagnosis. The effectiveness of the proposed method and the two new CIs for early tooth crack severity assessment are demonstrated using both simulated gearbox vibration signals and experimental gearbox vibration datasets. The materials of this research topic have been published partially in a conference paper [103] and as a whole in a journal paper [104].

In the second research topic (Topic #2), how time-varying operating conditions affect the vibration characteristics of a fixed-axis spur gearbox with a tooth crack is studied using dynamic simulation and signal processing. The limitations of the reported studies on dynamic simulation of fixed-axis spur gearboxes [26,33,49,66] have been overcome. To be specific, firstly, gear tooth mesh stiffness is evaluated considering both tooth crack severity progression and operating condition variations, through which gearbox vibration responses are generated under time-varying operating conditions. A signal analysis procedure is proposed with its focus placed on the CII, which are extracted from gearbox vibration signals using the AHD method or its modified version. Envelope analysis is conducted on the CII to study how the CII are affected by time-varying operating conditions, and a linear dependence of the AM of the CII on the time-varying operating condition is identified. Based on the identified linear dependence, a novel CI, which is sensitive to crack growth while insensitive to operating condition variations, is proposed to track tooth crack severity progression under time-varying operating conditions. The linear dependence of the AM of the CII on time-varying operating conditions and the effectiveness of the proposed CI for tooth crack diagnosis are demonstrated using both simulated gearbox vibration signals and experimental gearbox vibration datasets. The materials of this topic have been presented in a journal paper [105] which is under review at present.

In the third research topic (Topic #3), a novel normalization method for removing the speed variation-induced AM and FM without attenuating the tooth crack information is proposed to track tooth crack severity progression under variable speed conditions. The proposed normalization method outperforms the reported studies [36,80,81] in terms of removing the speed variation-induced AM and FM without attenuating the tooth crack information. Specifically, order tracking techniques are used to remove the FM induced by variable speeds. For the removal of the speed variation-induced AM, a novel normalization method focusing on the CII is proposed to remove the AM effect without attenuating the tooth crack information. The modified AHD method is adopted to obtain the CII under variable speed conditions. The peak envelope of the CII is determined using spline interpolation of its envelope peaks and is further employed to remove the AM of the CII by normalization. Two metrics are introduced to quantitatively evaluate the performance of the proposed normalization method on removing the AM and preserving the tooth crack information. The effectiveness of the proposed normalization method is demonstrated using both simulated gearbox signals and experimental gearbox datasets. The proposed method benefits tracking gear tooth crack severity progression under variable speed conditions. The materials of this topic have been published partially in a conference paper [106] and as a whole in a journal paper [107].

In the fourth research topic (Topic #4), the vibration characteristics of a fixed-axis spur gearbox with multiple tooth cracks are investigated and a novel method focusing on the CII is proposed for the detection of multiple tooth cracks. The limitations of the reported studies [26,33,64] that involved only one tooth crack have been overcome. To be specific, insights into the vibration characteristics of a fixed-axis spur gearbox with multiple tooth cracks are procured using dynamic simulation. Three scenarios of multiple tooth cracks are considered, including two nonadjacent tooth cracks on the pinion and a healthy gear, two adjacent tooth cracks on the pinion and a healthy gear, and one tooth crack on the pinion and one tooth crack on the gear. Gear tooth mesh stiffness is analytically evaluated using the potential energy method and is further inserted into the spur gearbox dynamic model to generate vibration responses. Analyses of gear tooth mesh stiffness and vibration responses are conducted in both time and frequency domains. Besides, a novel method focusing on the CII is proposed to detect the number and locations of multiple tooth cracks. Firstly, the CII are extracted from gearbox vibration signals using a new strategy based on the SVD. TSA

is conducted on the CII to get the TSA signals for both the pinion and the gear. Afterwards, detection of the number and locations of multiple tooth cracks is achieved via analyzing the squared envelopes of the TSA signals for both the pinion and the gear. The obtained insights into vibration characteristics of a fixed-axis spur gearbox with multiple tooth cracks and the effectiveness of the proposed method for detecting the number and locations of multiple tooth cracks are demonstrated using both simulated gearbox vibration signals and experimental gearbox vibration datasets. The materials of this topic have been documented in a journal paper [108] which is under review.

The novel contributions of this thesis are summarized as follows.

1) A novel method has been proposed to well extract the CII from gearbox vibration signals and conduct a thorough study on the CII, through which two new CIs have been developed for early tooth crack severity assessment. The effectiveness of the proposed method and the two new CIs for early tooth crack severity assessment are demonstrated using both simulated gearbox vibration signals and experimental gearbox vibration datasets.

2) A comprehensive study has been conducted to investigate how time-varying operating conditions affect the vibration characteristics of a fixed-axis spur gearbox with a tooth crack. A linear dependence of the AM of the CII on the time-varying operating condition has been identified. The identified linear dependence has been employed to develop a new CI to track tooth crack severity progression under time-varying operating conditions. The correctness of the linear dependence of the AM of the CII on time-varying operating conditions, and the effectiveness of the proposed CI method for tracking tooth crack severity progression are demonstrated using both simulated gearbox vibration signals and experimental gearbox vibration datasets.

3) A novel normalisation method focusing on the CII has been proposed to remove the speed variation-induced AM and FM of the CII without attenuating the tooth crack information, which benefits tracking tooth crack severity progression under variable speed conditions. The effectiveness of the proposed normalization method for tracking tooth crack severity progression is demonstrated using both simulated gearbox vibration signals and experimental gearbox vibration datasets.

4) A good understanding of the vibration characteristics of a fixed-axis spur gearbox with multiple tooth cracks has been procured and a novel method has been proposed to detect the number and locations of multiple tooth cracks in fixed-axis spur gearboxes. The obtained insights into vibration characteristics of spur gearboxes with multiple tooth cracks are validated, which fills the knowledge gaps in the field of gearbox tooth crack diagnosis. The effectiveness of the proposed method for the detection of multiple tooth cracks is demonstrated using both simulated gearbox vibration signals and experimental gearbox vibration datasets.

The rest of this thesis is organized as follows. Chapter 2, Chapter 3, Chapter 4, and Chapter 5 present the details of the four research topics, namely Topic #1, Topic #2, Topic #3, and Topic #4, respectively. Lastly, in Chapter 6, the research studies conducted in this thesis are summarized and the future explorations are also discussed.

This thesis is written using the paper-based template which meets the formatting requirements of the Faculty of Graduate Studies and Research at the University of Alberta.

Chapter 2: Development of crack induced impulse-based condition indicators for early tooth crack severity assessment

As mentioned in Section 1.3, the focus of this chapter is placed on early tooth crack severity assessment, which is covered by the first research topic (Topic #1). In this chapter, a novel method is proposed to extract the CII from gearbox vibration signals and conduct a thorough study on the CII. In addition, two new CIs are developed using the CII for early tooth crack severity assessment. The organization of this chapter is as follows. In Section 2.1, an introduction to the tooth crack severity assessment is presented. Section 2.2 introduces the fundamentals of the two techniques used in the proposed method. In Section 2.3, the proposed method, and the development of the two new CIs are described in detail. The effectiveness of the proposed method and the two new CIs is demonstrated with spur gearbox dynamic responses and experimental gearbox vibration datasets in Section 2.4 and Section 2.5, respectively. Lastly, Section 2.6 concludes the conducted study in this chapter. The results of this chapter have been published partially in a conference paper [103] and as a whole in a journal paper [104].

2.1 Introduction

Due to their harsh working environment, gearboxes might suffer from various faults, such as tooth cracks and tooth pitting [23]. Tooth cracks are a kind of gearbox failure mode commonly seen in real industrial applications [109]. It is important to conduct gear tooth crack diagnosis, especially in the early stage of crack propagation. If early tooth crack severity is well assessed, precautions and maintenance activities could be scheduled as early as possible, thus improving gearbox system reliability and reducing operation and maintenance costs [110].

For gearbox fault diagnosis, the TSA has been widely employed as a powerful tool [111]. TSA is capable of removing background noise and the vibration components that are not synchronous with the target gear shaft [42]. If the gearbox vibration signal is processed using the TSA technique, the obtained TSA signal will be an estimate of the average meshing vibration of the gear of interest over a complete gear shaft revolution [42]. For healthy gears, their TSA signals mainly consist of

gear meshing frequency (GMF) and its harmonics [77]. In addition, due to the transmission errors in the gear mesh pairs, there will also be low-order AM-FM sidebands around the GMF and its harmonics. However, when a localized gear tooth crack occurs, for the TSA signal, the AM-FM will be modified. Besides, a tooth crack will induce impulsive vibration components with a short period, reflecting the localized transient vibration around the tooth cracking area, into the gear meshing vibration [77,87]. Therefore, the crack-related AM-FM and the CII in the TSA signal comprise early tooth crack information.

During the past several decades, various CIs developed using the gear TSA signals for tooth crack diagnosis have been reported, which have been reviewed in Subsection 1.2.2.2. The CIs reviewed in Subsection 1.2.2.2 include FM0 [82], FM4 [83], NA4 [83], NB4 [85], *PS-I* [86], the energy of the envelope of the resonant vibration in Ref. [77] (E_{CIIEnv}), and the energy of the impulse vibration component in Ref. [87] (E_{ImpVC}). All these existing CIs failed to work well in assessing early tooth crack severity levels.

To overcome the deficiencies of the CIs reviewed above, this chapter proposes a modification and improvement of the reported studies. Inspired by the findings obtained from the study focusing on how the CII is affected by tooth crack severity progression, which was conducted via dynamic simulation in Ref. [103], in the proposed method, the CII is thoroughly studied. Firstly, the proposed method conducts TSA on the gearbox vibration signals to get the gear TSA signal and removes the GMF and its harmonics along with sidebands around them from the gear TSA signal using comb notch filters. The notch filtered signal mainly consists of frequency components related to the CII. Afterwards, the notch filtered signal is fitted using a modal model to identify the dominant resonances, which are the Single Degree-Of-Freedom Impulse Responses (SDOF IRs), excited by the tooth crack. The modal parameters are obtained using the Matrix Pencil Method (MPM) [112,113]. With the obtained modal parameters, the SDOF IRs can be regenerated. The SDOF IRs are combined to get the Reconstructed CII (RecCII) without background masking components. The energy of the RecCII is used to track early tooth crack severity progression. In addition, the sum of the energy of the SDOF IRs with carrier frequencies in a specific frequency band is also adopted to track early tooth crack severity progression, which provides additional promising tooth crack prognosis information. These energy metrics are proposed as new CIs in this chapter. The effectiveness of the proposed method and the new CIs for early tooth crack

severity assessment is demonstrated using both simulated gearbox vibration signals and experimental gearbox vibration datasets.

The novel contributions of this chapter include: 1) By using the proposed method, dominant SDOF IRs have been identified from the gear TSA signal and the CII has been reconstructed without masking components by combining the SDOF IRs; 2) Two new CIs have been proposed for early tooth crack severity assessment, the first CI is the energy of the RecCII and the second one is the sum of the energy of SDOF IRs with carrier frequencies in a specific frequency band.

The remainder of this chapter is organized as follows: the fundamentals of TSA and MPM, which are used in the proposed method, are introduced in Section 2.2. Section 2.3 describes the proposed method and the development of the new CIs. Effectiveness of the proposed method and the new CIs is demonstrated using spur gearbox dynamic responses and experimental gearbox vibration datasets in Sections 2.4 and 2.5, respectively. Lastly, conclusions are made in Section 2.6.

2.2 Fundamentals of TSA and MPM

In two key steps of the proposed method to be presented in Section 2.3, TSA and MPM are adopted to analyze gearbox vibration signals. Therefore, for the ease of reference later when describing the proposed method in Section 2.3, brief introductions to TSA and MPM are presented in this section.

2.2.1 Time synchronous average

TSA is a powerful signal processing technique widely used to extract periodic components from noisy vibration data [42,111]. Because TSA can separate the target gear fault signature under analysis from vibration sources of other components and environmental noise in the gearbox which are not synchronous with the gear to be monitored, it has been shown to be very suitable to conduct gearbox fault diagnosis [114,115]. To remove signal components which are not synchronous with the gear to be monitored, the entire vibration signal is divided into separate segments using the tachometer signal of the target gear shaft, and then the segments are averaged out. The ensemble average of all the divided segments is the resultant signal obtained by TSA, which always has the length of one target gear shaft revolution [42]. The signal that is synchronous with the target gear shaft rotation gets enhanced while the non-synchronous components get cancelled out. To conduct TSA on experimental gearbox vibration signals, pulse times are always needed. Pulse times can

be calculated by analyzing the signals obtained from tachometers. Because TSA technique has been widely used for gearbox fault detection and diagnosis during the last several decades, its fundamental theory and algorithms are not introduced herein for brevity. Those who are interested in the details of TSA can refer to Ref. [42] for more detailed information.

2.2.2 Matrix pencil method

The fundamental theory of MPM is presented herein [112,113]. Before introducing MPM, the concept of "matrix pencil" is explained. The matrix pencil of two N × M matrices P, Q, is defined as the matrix shown in Eq. (2.1) [112]. Although "$P - \lambda Q$" is not an equation, it is still treated as an equation herein for the convenience of description.

$$P - \lambda Q \tag{2.1}$$

where λ is a parameter.

For the matrix pair {P, Q}, its generalized eigenvalues are those values of λ that make "$P - \lambda Q$" to reduce its rank. A generalized eigenvector corresponding to such a λ is a vector in the null space $N(P - \lambda Q)$, so a matrix pencil is seen as a generalization of the eigenvalue concept to non-square matrices. Define two $(N - L) \times L$ matrices Y_1 and Y_2 based on the 1-D input signal y as follows.

$$[Y_2] = \begin{bmatrix} y(1) & y(2) & \cdots & y(L) \\ y(2) & y(3) & \cdots & y(L+1) \\ \vdots & \vdots & & \vdots \\ y(N-L) & y(N-L+1) & \cdots & y(N-1) \end{bmatrix}_{(N-L)\times L} \tag{2.2}$$

$$[Y_1] = \begin{bmatrix} y(0) & y(1) & \cdots & y(L-1) \\ y(1) & y(2) & \cdots & y(L) \\ \vdots & \vdots & & \vdots \\ y(N-L-1) & y(N-L) & \cdots & y(N-2) \end{bmatrix}_{(N-L)\times L} \tag{2.3}$$

where L is referred to as the pencil parameter, $y(i)$ $(i = 1, 2, \ldots, N-1)$ is an element of the 1-D input signal y.

Also, matrices Y_1 and Y_2 can be rewritten as the following forms.

$$[Y_2] = [Z_1][R][Z_0][Z_2] \tag{2.4}$$

$$[Y_1] = [Z_1][R][Z_2] \tag{2.5}$$

where

$$[Z_1] = \begin{bmatrix} 1 & 1 & \cdots & 1 \\ z_1 & z_2 & \cdots & z_M \\ \vdots & \vdots & & \vdots \\ z_1^{N-L-1} & z_2^{N-L-1} & \cdots & z_M^{N-L-1} \end{bmatrix}_{(N-L)\times M} \tag{2.6}$$

$$[Z_2] = \begin{bmatrix} 1 & z_1 & \cdots & z_1^{L-1} \\ 1 & z_2 & \cdots & z_2^{L-1} \\ \vdots & \vdots & & \vdots \\ 1 & z_M & \cdots & z_M^{L-1} \end{bmatrix}_{\mathrm{M}\times L} \tag{2.7}$$

$$[Z_0] = diag[z_1 \quad z_2 \quad , \dots , \quad z_M] \tag{2.8}$$

$$[R] = diag[R_1 \quad R_2 \quad , \dots , \quad R_M] \tag{2.9}$$

The matrix pencil of matrices Y_1 and Y_2 is constructed and listed as follows:

$$[Y_2] - \lambda[Y_1] = [Z_1][R]\{[Z_0] - \lambda[I]\}[Z_2] \tag{2.10}$$

where $[I]$ is the $M \times M$ identity matrix.

If $\lambda = z_i$, the rank of $[Y_2] - \lambda[Y_1]$ is $M - 1$. Therefore, z_i in Eq. (2.6) through Eq. (2.8) could be obtained as the generalized eigenvalues of the matrix pair $\{[Y_2]; [Y_1]\}$. In other words, the problem of solving for z_i can be converted into an ordinary eigenvalue problem listed in Eq. (2.11).

$$\{[Y_1]^+[Y_2] - \lambda[\mathrm{I}]\} \tag{2.11}$$

where $[Y_1]^+$ is the Moore-Penrose pseudoinverse of $[Y_1]$ and is calculated using Eq. (2.12).

$$[Y_1]^+ = \{[Y_1]^H[Y_1]\}^{-1}[Y_1]^H \tag{2.12}$$

where the superscript "*H*" represents the conjugate transpose.

To eliminate the effect of environmental noise in the input signal y, the MPM constructs the data matrix $[Y]$ by combining matrices $[Y_1]$ and $[Y_2]$ as

$$[Y] = \begin{bmatrix} y(0) & y(1) & \cdots & y(L) \\ y(1) & y(2) & \cdots & y(L+1) \\ \vdots & \vdots & & \vdots \\ y(N-L-1) & y(N-L) & \cdots & y(N-1) \end{bmatrix}_{(N-L)\times(L+1)} \tag{2.13}$$

To remove noise, the pencil parameter L is chosen between $N/3$ to $N/2$. Next, the singular value decomposition is applied to the matrix $[Y]$.

$$[Y] = [\mathrm{U}][\Sigma][\mathrm{V}]^H \tag{2.14}$$

where [U] and [V] are unitary matrices, and [Σ] is a diagonal matrix containing the singular values of $[Y]$, i.e.

$$[U]^H[Y][V] = [\Sigma] \tag{2.15}$$

The determination of the parameter M is made by checking the ratio of the various singular values to the largest one. By specifying a proper threshold for the ratio, the dominant resonance modes excited by the CII can be selected out [112]. After determining the value of M, $\left[V^{'}\right]$ is constructed so that it contains only M dominant right-singular vectors of $[V]$:

$$[V'] = [v_1, v_2, \dots, v_M] \tag{2.16}$$

Therefore,

$$[Y_1] = [U][\Sigma'][V_1']^H \tag{2.17}$$

$$[Y_2] = [U][\Sigma'][V_2']^H \tag{2.18}$$

where $[\mathrm{V}_1']$ is obtained from $[\mathrm{V}']$ with the last row of $[\mathrm{V}']$ deleted; $[\mathrm{V}_2']$ obtained by removing the first row of $[\mathrm{V}']$; and $[\Sigma']$ obtained from the first M columns of [Σ] corresponding to the first M dominant singular values. Then for the noiseless case,

$$[Y_1]^+[Y_2] = \{[\mathrm{V}_1']^H\}^+[\mathrm{V}_2']^H = [\mathrm{V}_2']^H\{[\mathrm{V}_1']^H\}^+ \tag{2.19}$$

Calculating the eigenvalues of $[\mathrm{V}_2']^H\{[\mathrm{V}_1']^H\}^+$ can lead to all z_i $(i = 1, 2, \dots, M)$. So far, M and all z_i are known. R_i are calculated by solving the least-squares problem listed in the following.

$$\begin{bmatrix} y(0) \\ y(1) \\ \vdots \\ y(N-1) \end{bmatrix} = \begin{bmatrix} 1 & 1 & \cdots & 1 \\ z_1 & z_2 & \cdots & z_M \\ \vdots & \vdots & & \vdots \\ z_1^{N-1} & z_2^{N-1} & \cdots & z_M^{N-1} \end{bmatrix} \begin{bmatrix} R_1 \\ R_2 \\ \vdots \\ R_M \end{bmatrix} \tag{2.20}$$

Eq. (2.20) can be re-written as

$$[y] = [\mathrm{z}][R] \tag{2.21}$$

In Eq. (2.21), $[R]$ is a column vector, which is different from the diagonal matrix $[R]$ in Eq. (2.9), but their non-zero elements are the same. The least-squares solution of Eq. (2.21) is

$$[R] = [\mathrm{z}]^{+}[y] \tag{2.22}$$

Based on all the formulae listed above, the values of M, z_i, and R_i could be estimated. The values of M, z_i, and R_i will be used to estimate the modal parameters of the SDOF IRs, which is to be presented in Section 2.3.

2.3 The proposed method and development of new condition indicators

In this section, the proposed method is introduced. The scope of the proposed method is limited to the case where only one gear has a tooth crack, although there may be multiple gear pairs in the gearbox. This is the same case considered in Refs. [77,86,87]. In this study, the gear with a tooth crack is seen as the "target gear" and the shaft on which the target gear is mounted is the "target shaft". As claimed in Refs. [77,87], a tooth crack induces both the crack-related AM-FM and the CII into gearbox vibration signals, and the CII provides more significant crack signature than the crack-related AM-FM. Thus, the proposed method focuses on the thorough analysis of the CII.

As claimed in Ref. [116], the CII in the vibration signal of a gearbox with a localized tooth crack has a transient nature and could be modelled using the Impulse Response (IR) of the gearbox system, the frequency spectrum of which is dominated by resonance peaks. For a SDOF vibration system considering the effect of damping, its IR is represented with one Exponentially Damped Sinusoid (EDS), which results in one resonance peak in the frequency spectrum. For a gearbox system with multiple degrees-of-freedom, its IR could be represented using the sum of several EDSs [117], which results in several resonance peaks in the frequency spectrum. In other words, for the CII, it consists of several resonance peaks and each of them is seen as a SDOF IR, which can be modelled as an EDS [117,118]. Several SDOF IRs forms a CII component. Besides, an individual SDOF IR may react uniquely to tooth crack growth. Specifically, some SDOF IRs are more sensitive to crack severity progression in the early crack stage while others have more obvious changes in the advanced crack stage [117]. The constitutive SDOF IRs of the CII will be identified from the TSA signal using the MPM and used to reconstruct the CII. In addition, the SDOF IRs will be grouped according to their carrier frequencies. The energy of the reconstructed CII and the sum of the energy of SDOF IRs with their carrier frequencies in a specific frequency band are proposed as new CIs to assess early tooth crack severity.

2.3.1 Procedure of the proposed method

Procedure of the proposed method is illustrated in Fig. 2.1, from which it is seen that there are 5 steps in total. The novelty of the proposed method is that a modal model is used to identify the dominant resonance peaks of the gear TSA signal as SDOF IRs, through which the CII is reconstructed without masking components. Besides, the identified SDOF IRs are grouped, and the sum of the energy of the grouped SDOF IRs provide promising tooth crack diagnosis information. The proposed method conducts a thorough analysis of the CII, reduces the masking effects caused by gear mesh components and crack-related AM-FM, and extracts signatures that can well indicate early tooth crack severity progression. These are the advantages of the proposed method over the studies reported in Refs [77,86,87].

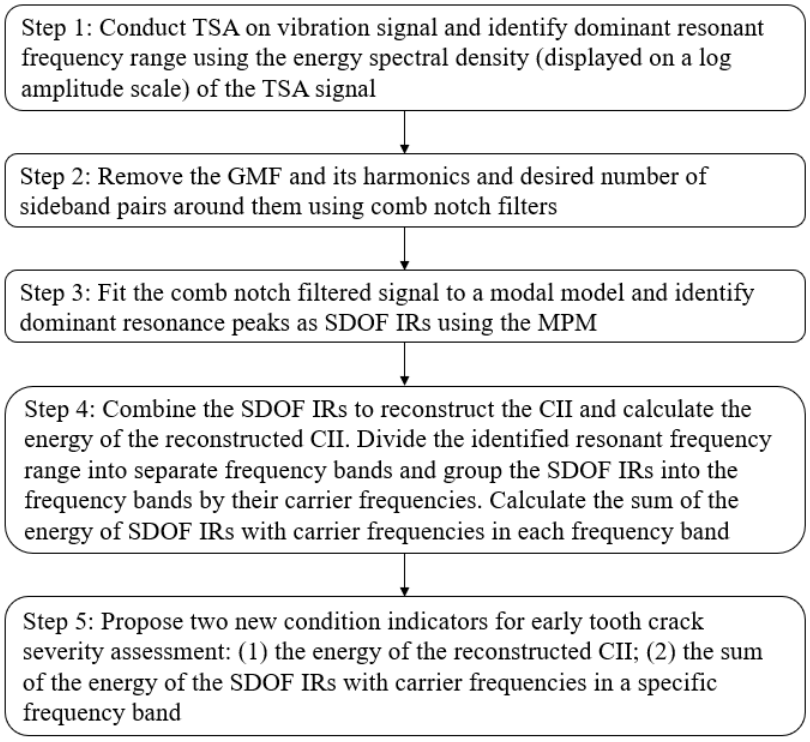

Fig. 2.1: The procedure for the proposed method

In Step 1, the TSA technique is applied to the gearbox vibration signal to remove the background noise and vibration components that are not synchronous with the target shaft. If only one gear with a tooth crack is mounted on the target shaft for which TSA is carried out, the obtained TSA signal mainly includes the GMF and its harmonics of the gear with a tooth crack, the crack-related AM-FM and the CII. If there are more than one gear on the target shaft, such as a gear with a tooth

crack and several other healthy gears, the TSA signal would also include the meshing harmonics of the other healthy gears. Based on the energy spectral density of the TSA signal displayed on a log amplitude scale, the frequency range in which the evident resonance peaks excited by the gear tooth crack exist is identified. The identified resonant frequency range will be used in Step 4.

In Step 2, the GMF and its harmonics alongside the sidebands around them for all gears on the target shaft are removed from the TSA signal using comb notch filters of the Infinite Impulse Response (IIR) type. The number of comb notch filters is equal to the number of gears on the target shaft. A comb notch filter is a series of band-stop filters with same bandwidth but with different center frequencies. Center frequencies of a comb notch filter are set as the GMF and its harmonics of the target gear. Bandwidth of a notch filter is defined by the width of the notch. The order of a comb notch filter is specified as $n = round(F_s/f_{mesh})$, where F_s is the sampling frequency and f_{mesh} is the GMF of the target gear. Number of the notches of a comb notch filter is $n + 1$. After conducting the comb notch filtering on the TSA signal, the resulting signal mainly comprises the CII caused by the gear with a tooth crack. The CII excites resonance peaks in the frequency domain.

In Step 3, dominant resonance peaks in the comb notch filtered signal obtained in Step 2 are fitted to a modal model. The dominant resonant peaks are selected by specifying a threshold for the ratio to the highest peak. As reviewed at the beginning of Section 2.3, the CII can be represented as a sum of several EDSs. Each EDS is an SDOF IR, which results in a resonance peak in the frequency domain. Therefore, the CII is represented by the modal model shown in Eq. (2.23).

$$y(\mathrm{t}) = \sum_{i=1}^{M} A_i e^{(-D_i t)} \cos\left(2\pi f_i t + \theta_i\right);\ t \geq 0 \tag{2.23}$$

where $y(\mathrm{t})$ is the CII, M is the number of the EDSs (or SDOF IRs); A_i is the amplitude, D_i the damping factor, f_i the carrier (resonance) frequency, and θ_i the phase of the i^{th} EDS, respectively.

To obtain modal model parameters, several operational modal analysis methods could be adopted, such as the Hankel Total Least Square Method (HTLSM) [119], the Prony's Method (PM) [120], and the MPM [112]. In Ref. [121], MPM was demonstrated to be more computationally efficient than HTLSM and PM. Therefore, MPM is used to obtain modal model parameters. As described in Subsection 2.2.2, MPM can be used to estimate the parameters of each SDOF IR in Eq. (2.23). For Eq. (2.23), after sampling with the sampling period T_s, the time variable t is replaced by nT_s, where n is the sampling point. Then Eq. (2.23) can be rewritten as

$$y(nT_s) = \sum_{i=1}^{M} A_i e^{(-D_i nT_s)} \cos\left(2\pi f_i nT_s + \theta_i\right), \text{ for } n = 0,1,\dots,N-1. \tag{2.24}$$

Rewrite the signal in Eq. (2.24) into its complex form, and it yields:

$$y(n) = \sum_{i=1}^{M} R_i \, z_i^n \tag{2.25}$$

where

$$R_i = \frac{A_i}{2} e^{j\theta_i} \tag{2.26}$$

$$z_i = e^{(-D_i + j2\pi f_i)T_s} \tag{2.27}$$

Because R_i and z_i can be determined using the formulae presented in Subsection 2.2.2, parameters A_i, D_i, f_i, and θ_i of each SDOF IR are calculated as follows.

$$A_i = 2\text{abs}(R_i) \tag{2.28}$$

$$\theta_i = \arctan\left(\frac{\text{imag}(R_i)}{\text{real}(R_i)}\right) \tag{2.29}$$

$$D_i = -\ln\big(\text{abs}(z_i)\big)/T_s \tag{2.30}$$

$$f_i = \arctan\left(\frac{\text{imag}(z_i)}{\text{real}(z_i)}\right)/(2\pi T_s) \tag{2.31}$$

As shown in Eq. (2.28) to Eq. (2.31), the modal model parameters, namely amplitude A_i, initial phase θ_i, damping factor D_i and carrier frequency f_i of each SDOF IR, are calculated. Their accuracy can be verified using the results obtained via modal tests. Based on these parameters, each SDOF IR is regenerated, thus being identified. Because the identified SDOF IRs are excited by the tooth crack on a particular gear, their carrier frequencies should be close to the natural frequencies of that gear and its associated torsional and radial springs. If the natural frequencies of all the gears on the target shaft are known, by comparing the carrier frequencies of the SDOF IRs to the natural frequencies of each gear, it will help decide which gear is the one with a tooth crack, that is, the target gear, that causes the CII in the vibration signal. Besides, if natural frequencies of all the gears on the target shaft are unknown, the target gear can be decided by inspecting the differences between the frequency spectrum of the vibration signal for the healthy gear case and that for the cracked gear case, especially by inspecting if there are newly emerged sidebands around the gear mesh harmonics of a particular gear in the frequency spectrum of the cracked gear signal. If there are newly emerged sidebands, that gear is the target gear.

In Step 4, the identified SDOF IRs are summed to reconstruct the CII. The Reconstructed CII (RecCII) is expected to get rid of the masking effects caused by extraneous frequency components. The energy of the RecCII is calculated, which is named E_{RecCII}. For a continuous-time signal $x(t)$, its energy can be numerically estimated using its discrete-time counterpart $x[n]$ ($x[n] = x(t_n)$, $t_n = nT_s$, T_s is the sampling period) and is calculated using Eq. (2.32).

$$E_x = T_s \sum_{n=1}^{N} (x[n])^2 \tag{2.32}$$

where n is the index of $x[n]$ and $N = length(x[n])$.

Therefore, based on Eq. (2.32), E_{RecCII} is calculated using Eq. (2.33).

$$E_{RecCII} = T_s \sum_{n=1}^{N} (RecCII[n])^2 \tag{2.33}$$

The resonant frequency range identified in Step 1 is divided into separate frequency bands. Harmonics of the GMF of the target gear decided in Step 3 are used as dividers and the width of each frequency band equals the GMF. If K frequency bands are obtained, the i^{th} one is named FB_i ($i = 1, \dots, K$). The obtained frequency bands are used to group the SDOF IRs. If the carrier frequency of a SDOF IR, i.e., f_i, is in the frequency band FB_i, that SDOF IR is classified into the group related to the FB_i. Several SDOF IRs will be grouped together if their carrier frequencies are in the same frequency band. The sum of the energy of the SDOF IRs with carrier frequencies in the frequency band FB_i is named SE_{FB_i} ($i = 1, \dots, K$) and is calculated using Eq. (2.34).

$$SE_{FB_i} = \sum_{m=1}^{M} E_m, (m = 1, 2, \dots, M) \tag{2.34}$$

where M is the number of the SDOF IRs with carrier frequencies in the frequency band FB_i, E_m is the energy of the m^{th} SDOF IR, i.e. $SDOF\ IR_m$, and is calculated using Eq. (2.35).

$$E_m = T_s \sum_{n=1}^{N} (SDOF\ IR_m[n])^2 \tag{2.35}$$

For different gearboxes, the number of SE_{FB_i} may be different. Besides, not all the SE_{FB_i} can well track tooth crack growth. However, some of them can provide additional promising crack diagnosis information, which can be proposed as new CIs for early tooth crack severity assessment.

In Step 5, two new CIs are proposed for early tooth crack severity assessment. The first CI is the energy of the RecCII, i.e., E_{RecCII}. The second CI is selected from the SE_{FB_i} ($i = 1, \dots, K$) which

are obtained in Step 4. The SE_{FB_i} with the best ability to track early tooth crack severity progression is employed as the second CI. This will be illustrated in Section 2.4 and Section 2.5.

2.3.2 Performance comparison criteria

To compare the performance on early tooth crack severity assessment of the proposed CIs to that of the three reported ones in Refs. [77,86,87], the Average Increase Rate (AIR) [106] and tooth crack severity assessment accuracy are used as two comparison criteria. The three reported CIs are: (1) energy of the envelope of the resonant vibration, namely E_{CIIEnv} [77]; (2) energy of the impulse vibration component, namely E_{ImpVC} [87]; and (3) *PS-I* [86]. AIR is used to measure the sensitivity of a CI towards tooth crack severity progression. A higher value the AIR has, the more sensitive a CI is towards tooth crack severity progression. The AIR is calculated using Eq. (2.36).

$$\mathrm{AIR}(v) = (((v_{end-}v_1)/v_1)/(cl_{end} - cl_1)) \times 100\% \tag{2.36}$$

where v is the value vector of a CI; and cl is the value vector of the tooth crack level; subscripts "1" and "end" denote the first and last elements of a vector, respectively.

Tooth crack severity assessment accuracy is a numerical metric to evaluate the ability of a CI to separate different tooth crack levels, which is measured with the Linear Discriminant Analysis (LDA) classifier [122]. A higher accuracy means that a CI has better separating ability. Since the LDA classifier is a supervised classification model, tooth crack levels need to be labelled. Inputs of a LDA classifier are CIs and outputs are the predicted labels for tooth crack levels. Tooth crack severity assessment accuracy is measured by comparing the predicted labels to their true values and is illustrated using confusion matrices. The more tooth crack information a CI has, a higher tooth crack severity assessment accuracy a LDA classifier can obtain. Therefore, tooth crack severity assessment accuracy can be used as a metric to evaluate the performance of a CI on early tooth crack severity assessment. For different CIs, their values may differ greatly. To illustrate how CIs track crack severity progression in the same scale, CIs are normalized using Eq. (2.37).

$$V_{norm} = ln\big(V/V_{ref}\big) \tag{2.37}$$

where V is the value of a CI for a specific tooth crack level, V_{ref} denotes the CI value for the reference crack level (healthy case or 0% crack level), $ln(\cdot)$ is the natural logarithm, V_{norm} is normalized result of V.

2.4 Illustration of the proposed method using simulated gearbox vibration data

In this section, simulated gearbox vibration responses are used to demonstrate the effectiveness of the proposed method and the new CIs for early tooth crack severity assessment. Each step of the proposed method is illustrated by analyzing the simulated gearbox vibration responses.

2.4.1 Generation of simulated vibration response using a gearbox dynamic model

The dynamic model of a one-stage fixed-axis spur gearbox system reported in Refs. [26,49], which has been experimentally validated using a real one-stage gearbox system in Ref. [67], is adopted to generate simulated vibration responses. Schematic of the gearbox system is shown in Fig. 2.2. The cracked tooth is on the pinion m_1, so the pinion is the target gear. Its acceleration signal in the y direction is studied. Number of pinion teeth is $N_p = 19$. The pinion shaft rotating frequency is $f_s = 30$ Hz and the torque load applied on the load motor M_2 is 48.8 Nm. Thus, GMF is $f_{mesh} = 570$ Hz and the pinion shaft rotating period is $T_p = 1/f_s = 0.033$ s.

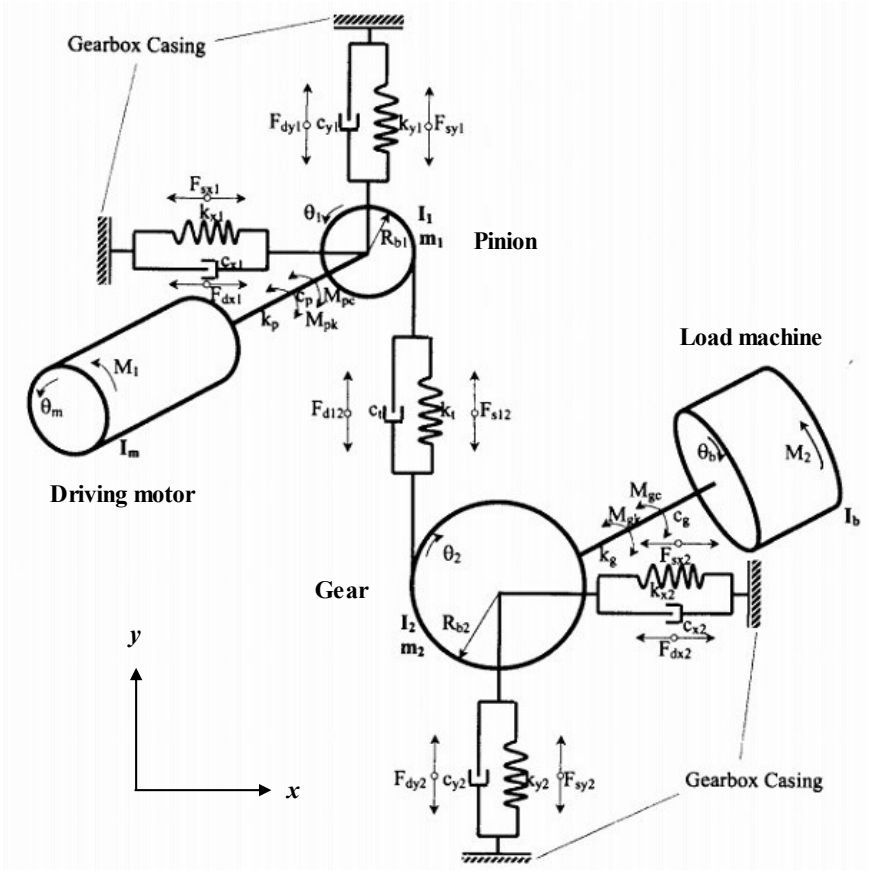

Fig. 2.2: The schematic of the model of a spur gearbox system [26,49]

The cracked tooth model displayed in Fig. 2.3 is used to simulate the root crack of one tooth of the pinion m_1. Tooth crack propagation path is simplified as a straight line starting from the tooth root fillet. In Fig. 2.3, the line segment q_p denotes the crack depth. To simulate the early tooth crack, the considered maximum value of q_p is set to 3 mm. The percentage of a crack depth to the theoretical maximum crack depth is defined as the crack level (*cl*), which is given by Eq. (2.38).

$$cl = \left(q_p / q_{max}\right) \times 100\% \tag{2.38}$$

where q_p is the pinion tooth crack depth; q_{max} denotes the value of the maximum tooth crack depth that the cracked tooth can have theoretically, which is 7.8 mm (complete loss of tooth).

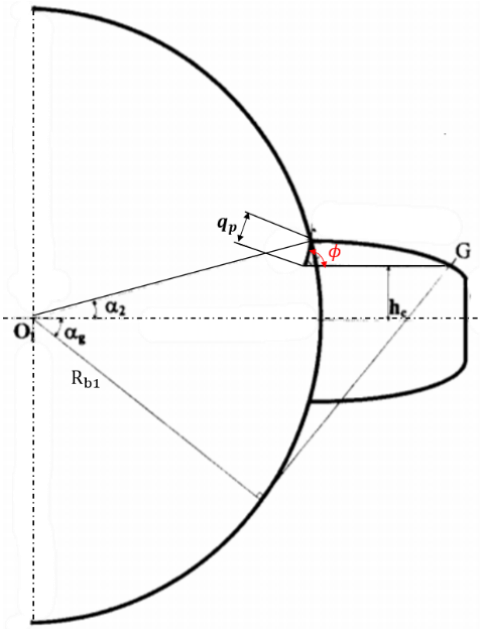

Fig. 2.3: The schematic of the cracked pinion tooth model [26,33]

Based on Eq. (2.38), the crack level corresponding to an arbitrary crack depth is calculated. When $q_{\mathrm{p}} = 0$ mm, it is the healthy gear case and $cl = 0\%$. When $q_p = 3.0$ mm, it is the maximum tooth crack depth considered in this study and $cl = 38.46\%$. To mimic the environmental noise, a white Gaussian noise with SNR=10 dB is added to the simulated gearbox vibration responses. Fig. 2.4 shows the time domain waveforms of the simulated vibration responses for four different tooth crack levels.

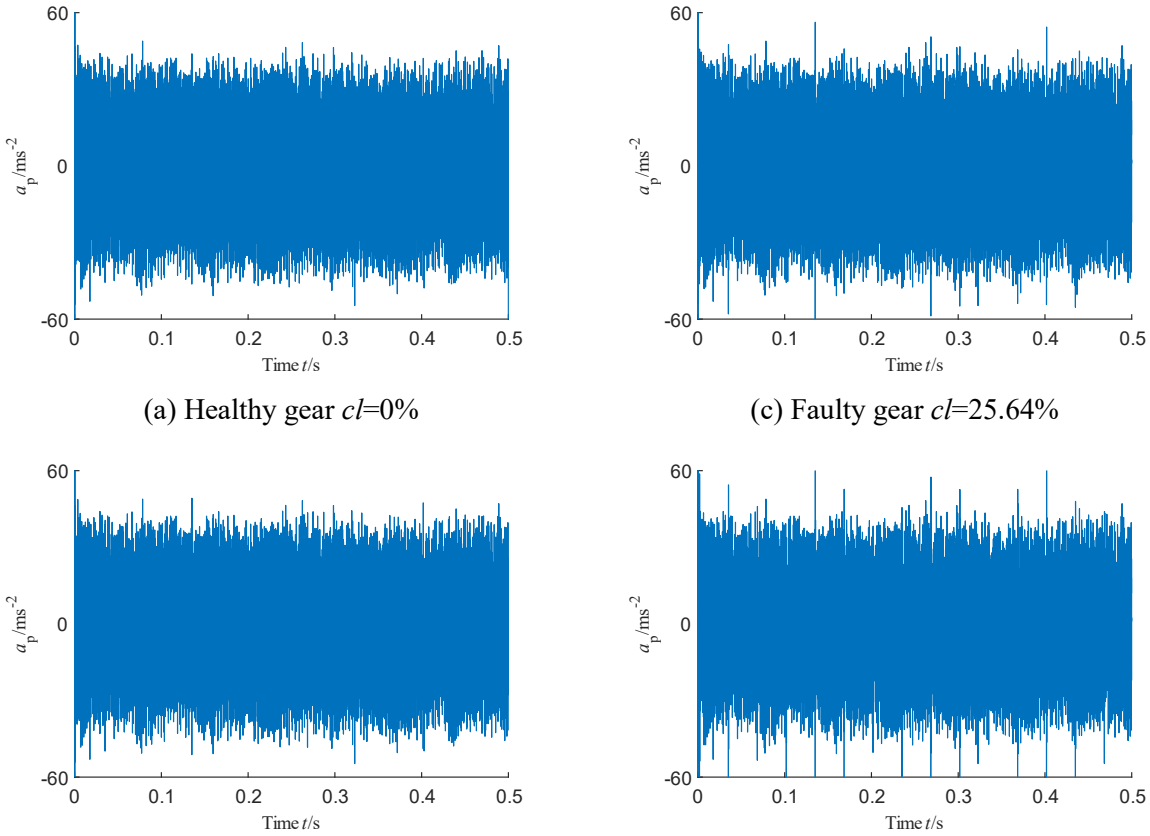

(a) Healthy gear *cl*=0%

(c) Faulty gear *cl*=25.64%

(b) Faulty gear *cl*=12.82%

(d) Faulty gear *cl*=38.46%

Fig. 2.4: Time waveforms of simulated vibration signals for four tooth crack levels

2.4.2 Application of the proposed method to the simulated gearbox vibration response

In this subsection, the simulated gearbox vibration response for 38.46% crack level is used as an example to illustrate the procedure of the proposed method shown in Fig. 2.1. In Step 1, the TSA technique is used to process the simulated vibration responses. The TSA signal and its energy spectral density are shown in Fig. 2.5. From Fig. 2.5(a), it is seen that there is an abrupt change between 10 and 50 degrees of the shaft angle, which is caused by the CII. Further examining the energy spectral density (displayed on log amplitude scale) shown in Fig. 2.5(b), it is found that there are evident resonance peaks located in the frequency range [1710, 4560] Hz. Therefore, the dominant resonant frequency range in which the CII exists is identified as [1710, 4560] Hz. For the vibration responses of other tooth crack levels, this conclusion still holds.

In Step 2, a comb notch filter of the IIR type is adopted to remove the GMF and its harmonics alongside the sidebands of the pinion from the TSA signal. The bandwidth of the notch filter is set

as 5 sideband pairs, which covers the sidebands caused by the crack-related AM-FM, thus removing the crack-related AM-FM. The comb notch filtering operates in time-domain, but the operation has a corresponding effect in the frequency domain. After conducting the comb notch filtering, the resulting signal mainly includes components related to the CII. The removal of 5 pairs of sidebands around the GMF and its harmonics causes distortion to the resulting spectrum, but the distortion impact on the dominant resonance peaks is not significant. The reason is that the harmonics of the CII spread over a wide frequency range and have relatively lower amplitudes and the removal of 5 pairs of sidebands does not affect the harmonics of the CII too much. The time domain waveform and energy spectral density of the notch filtered signal are shown in Fig. 2.6. From Fig. 2.6(a), it is seen that the notch filtered signal has a transient impact with short-period nature, which results in a broadband frequency property. As shown in Fig. 2.6(b), the frequency range dominated by the dominant resonance peaks is also about [1710, 4560] Hz, which is the same as the one identified in Step 1. It is also seen that the resonance peaks in Fig. 2.6(b) have lower damping than the original ones in Fig. 2.5(b), which is resulted from the removal of GMF and its harmonics and 5 pairs of sidebands around them using the comb notch filters.

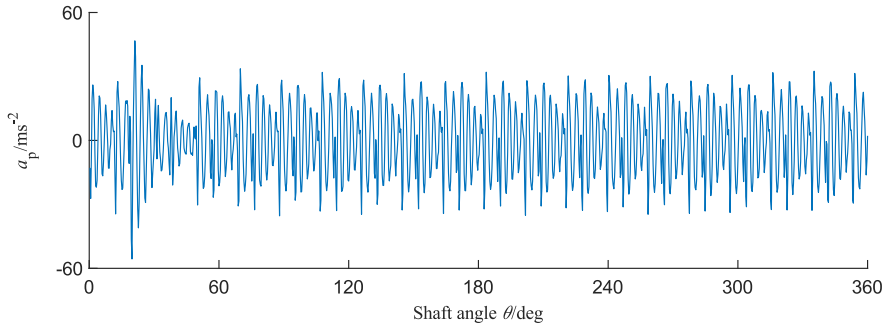

(a) TSA signal

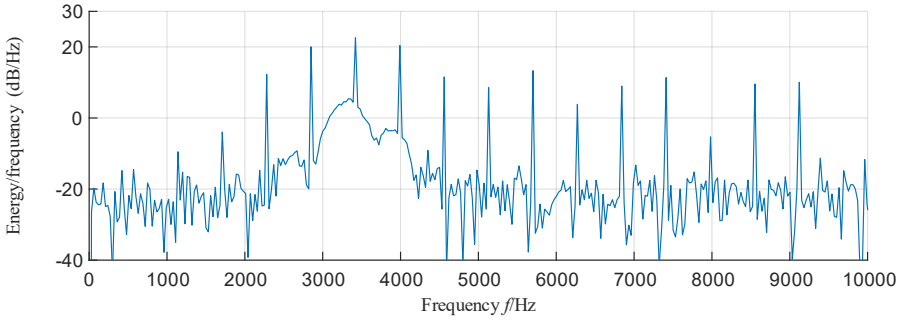

(b) Energy spectral density of TSA signal

Fig. 2.5: TSA signal and its energy spectral density (Faulty gear $cl = 38.46\%$)

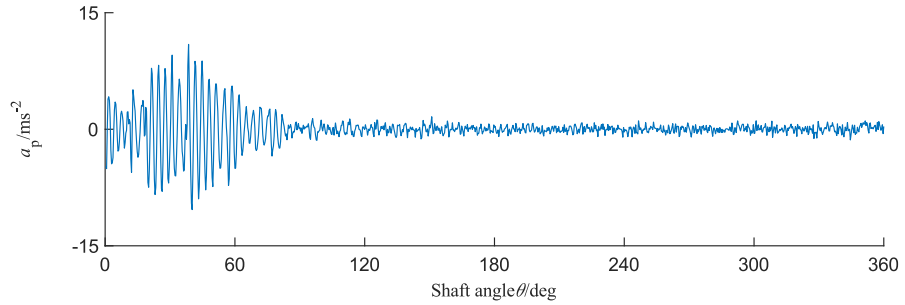

(a) Notch filtered signal

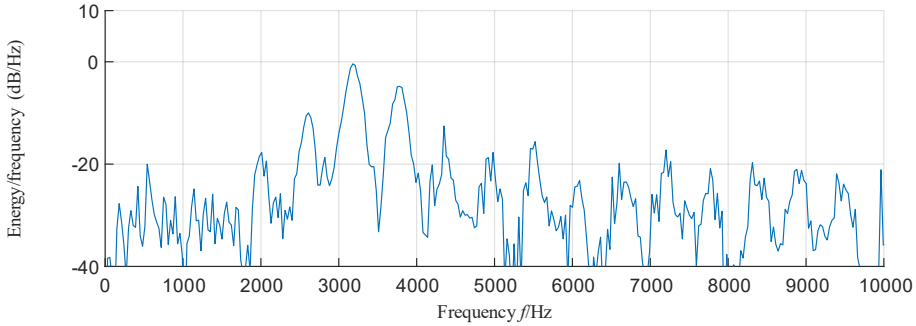

(b) Energy spectral density of notch filtered signal

Fig. 2.6. Time waveform and energy spectral density of notch filtered signal (Faulty gear $cl = 38.46\%$)

In Step 3, the modal model shown in Eq. (2.23) is used to fit the dominant resonance peaks of the notch filtered signal displayed in Fig. 2.6(b). The dominant resonance peaks are defined as those within about 20 dB of the highest one. Each resonance peak is identified as an SDOF IR. Modal parameters of the SDOF IRs are obtained using the MPM. Ten dominant SDOF IRs are obtained, the amplitudes, carrier frequencies, phases, damping factors and energy of which are displayed in Table 2.1, in which the unit of phase is "rad". Based on the estimated modal parameters tabulated in Table 2.1, each SDOF IR is regenerated. The ten identified SDOF IRs are shown in Fig. 2.7.

In Step 4, by summing the ten SDOF IRs shown in Fig. 2.7, the CII is reconstructed. For comparison, time waveforms and energy spectral densities of the reconstructed CII and the notch filtered signal obtained in Step 2 are plotted in Fig. 2.8 and Fig. 2.9, respectively. As shown in Fig. 2.8, the reconstructed CII matches the notch filtered signal very well. The coefficient of determination is used to measure their difference, and its value is 0.903, indicating that the difference between the reconstructed CII and the notch filtered signal is very small. As shown in Fig. 2.9, dominant resonance peaks are identified from the notch filtered signal. All these indicate

that the MPM works well in identifying dominant resonances in the notch filtered signal as SDOF IRs and estimating the modal parameters of each SDOF IR.

Table 2.1: Amplitudes, carrier frequencies, phases, damping factors, and energy of the ten identified SDOF IRs (Faulty gear $cl = 38.46\%$)

	1st SDOF IR	2nd SDOF IR	3rd SDOF IR	4th SDOF IR	5th SDOF IR	6th SDOF IR	7th SDOF IR	8th SDOF IR	9th SODF IR	10th SDOF IR
Amplitude	1.58	2.75	16.44	34.90	30.47	1.00	5.58	11.06	4.38	0.75
Carrier frequency	2026.8	2599.9	3063.9	3167.2	3289.4	3410.6	3477.8	3767.7	3926.6	4348.8
Phase	4.84	11.79	16.40	12.32	14.46	14.98	15.72	15.69	11.63	9.23
Damping factor	386.0	203.6	619.0	441.3	654.7	130.7	507.8	400.8	503.5	99.46
Energy	0.0016	0.0094	0.1085	0.7141	0.3616	0.0019	0.0158	0.0783	0.0098	0.0014

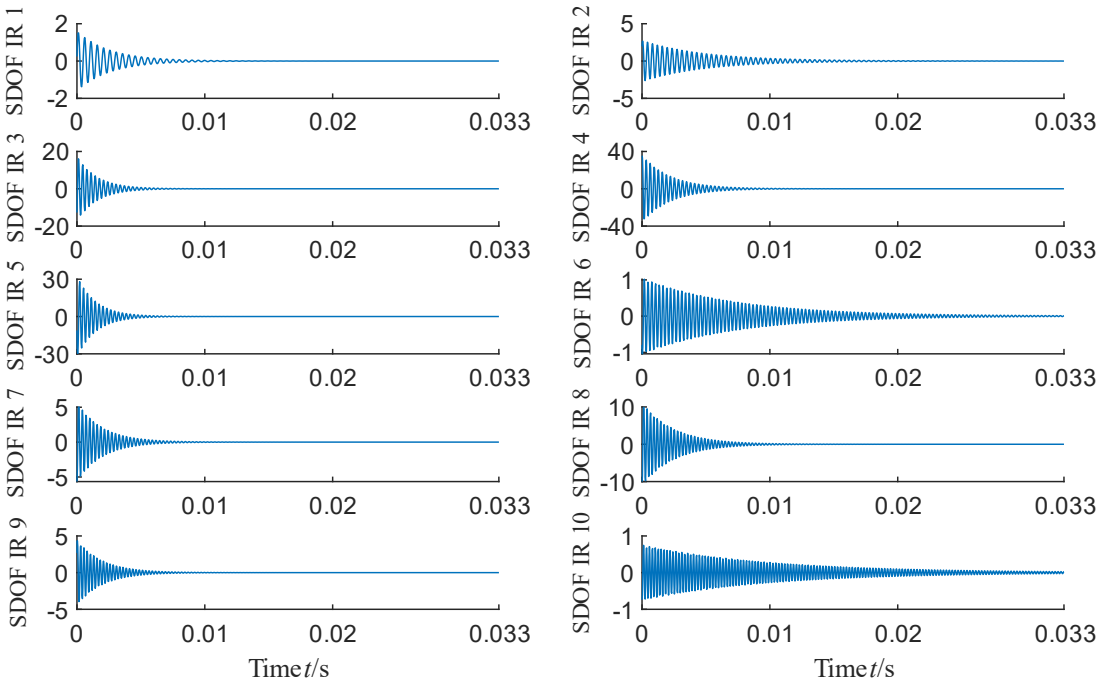

Fig. 2.7. Time waveforms of the ten identified SDOF IRs (Faulty gear $cl = 38.46\%$)

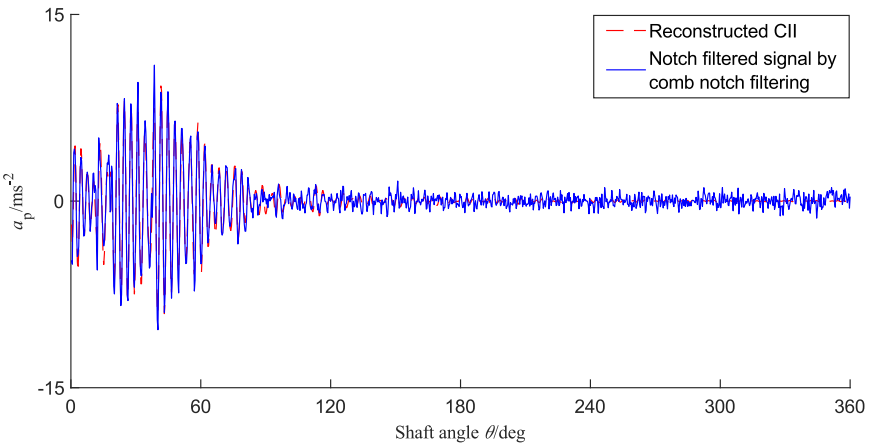

Fig. 2.8: Time waveforms of the reconstructed CII and the notch filtered signal obtained by comb notch filtering (Faulty gear $cl = 38.46\%$)

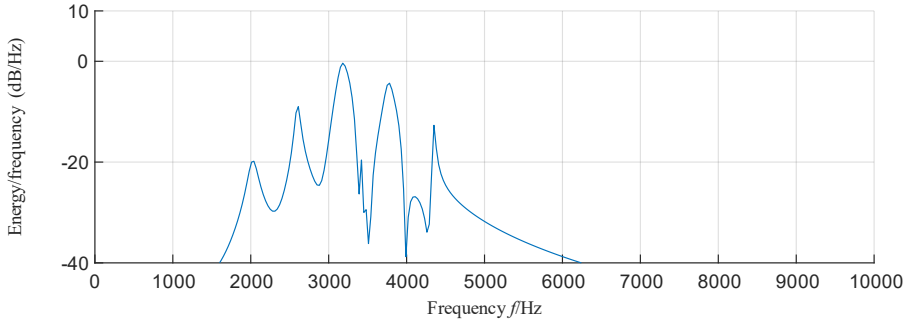

(a) Energy spectral density of reconstructed CII

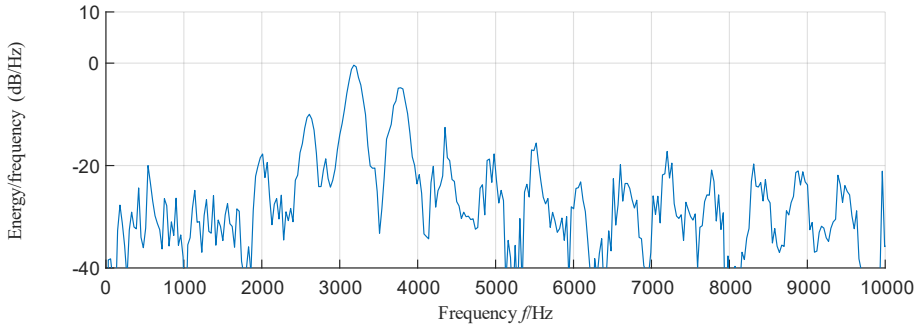

(b) Energy spectral density of notch filtered signal

Fig. 2.9: Energy spectral densities of the reconstructed CII and the notch filtered signal obtained by comb notch filtering (Faulty gear $cl = 38.46\%$)

In addition, the resonant frequency range identified in Step 1, i.e. [1710, 4560] Hz, is divided into five separate frequency bands, namely FB_i $(i = 1, \dots, 5)$. Harmonics of the GMF of the pinion ($f_{mesh} = 570$ Hz) are used as dividers and the width of each frequency band is equal to the GMF.

The five frequency bands are tabulated in Table 2.2. Based on these five frequency bands, the identified SDOF IRs shown in Fig. 2.7 are grouped by their carrier frequencies. For example, for the 3rd, 4th, 5th, and 6th SDOF IRs, their carrier frequencies are 3063.9 Hz, 3167.2 Hz, 3289.4 Hz, and 3410.6 Hz (shown in Table 2.1), respectively, which are in the third frequency band FB_3 [2850, 3420] Hz. Therefore, these four SDOF IRs are grouped together, and this group is related to the FB_3. Likewise, other SDOF IRs shown in Fig. 2.7 are also grouped into the groups related to specific frequency bands. The grouping results are shown in Table 2.3.

Table 2.2: Five frequency bands (simulated analysis)

Frequency band	FB_1	FB_2	FB_3	FB_4	FB_5
Range/Hz	[1710, 2280]	[2280, 2850]	[2850, 3420]	[3420, 3990]	[3990, 4560]

Table 2.3: Grouping result for the ten identified SDOF IRs (Faulty gear $cl = 38.46\%$)

Group	group related to FB_1	group related to FB_2	group related to FB_3	group related to FB_4	group related to FB_5
SDOF IR	1st	2nd	3rd, 4th, 5th, 6th	7th, 8th, 9th	10th

Afterwards, the energy of the RecCII is calculated using Eq. (2.33), and the result is $E_{RecCII} = 0.12$. Besides, the sums of the energy of the SDOF IRs in the groups shown in Table 2.3 are calculated using Eq. (2.34). For example, $SE_{FB_3} = 0.1085 + 0.7141 + 0.3616 + 0.0019 \approx 1.2$. Likewise, the sums of the energy of the SDOF IRs in other groups are also calculated. The energy results are tabulated in Table 2.4, from which it is seen that SE_{FB_3} is much greater than E_{RecCII} for a specific crack level. This means that some certain SE_{FB_i} can provide additional tooth crack diagnosis information, which can be utilized as promising CIs for early crack severity assessment.

Table 2.4: Results of the SE_{FB_i} and E_{RecCII} (Faulty gear $cl = 38.46\%$)

Energy	SE_{FB_1}	SE_{FB_2}	SE_{FB_3}	SE_{FB_4}	SE_{FB_5}	E_{RecCII}
Value	0.0016	0.0094	1.2	0.11	0.0014	0.12

In Step 5, repeating Steps 1-4 of the proposed method shown in Fig. 2.1 for the simulated vibration responses of other crack levels, E_{RecCII} and SE_{FB_i} $(i = 1, \dots, 5)$ for all the considered crack levels

are calculated. To compare them in the same scale, their values are first normalized using Eq. (2.37), and the normalized values of E_{RecCII} and SE_{FB_i} $(i = 1, \dots, 5)$ with regard to the crack level are shown in Fig. 2.10. It is seen that E_{RecCII} has a good performance on tracking early tooth crack severity progression. Besides, SE_{FB_3} has the best ability to track crack growth among the SE_{FB_i} $(i = 1,2,3,4,5)$, which provides additional promising crack diagnosis information. Therefore, the energy of the RecCII, i.e., E_{RecCII}, and the sum of the energy of the SDOF IRs with their carrier frequencies in the frequency band FB_3, i.e., SE_{FB_3}, are proposed as two new CIs for early tooth crack severity assessment.

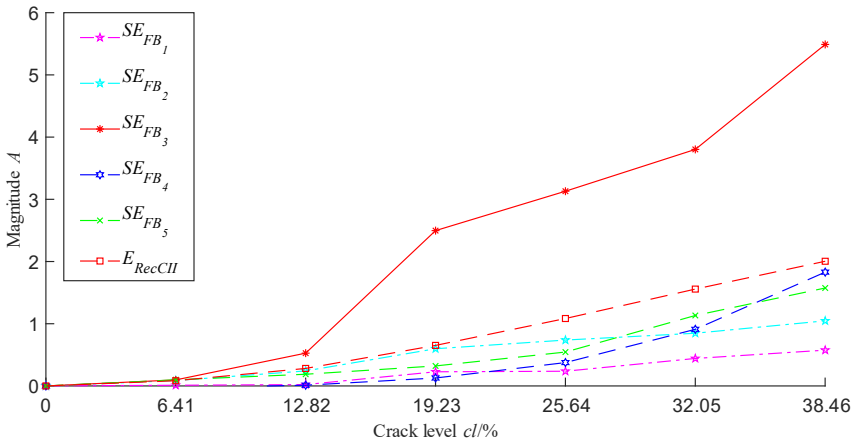

Fig. 2.10: Energy metrics versus crack level (simulated analysis)

2.4.3 Performance comparison

To make performance comparison, the CIs reported in Refs. [77,86,87] are also calculated using the simulated gearbox vibration responses. The two comparison criteria presented in Subsection 2.3.2 should be adopted. However, for the simulated signal analysis, it can only generate one result for each CI at a specific crack level, which makes it impossible to conduct crack severity assessment. The reason is that conducting tooth crack severity assessment needs more than one dataset, some of which are used to train the classification model while others for assessment. Therefore, for simulated gearbox vibration responses, only the AIR values of the CIs are calculated for comparison. AIR values of the two proposed CIs, i.e., E_{RecCII} and SE_{FB_3}, and the three reported ones, namely E_{CIIEnv}, E_{ImpVC}, and *PS-I*, are tabulated in Table 2.5. As shown in Table 2.5, SE_{FB_3} and E_{RecCII} have higher AIR values, which means that they outperform the three reported CIs for

tracking early tooth crack severity progression. SE_{FB_3} has the highest AIR value, indicating that it performs best. This means that the sum of the energy of SDOF IRs with carrier frequencies in a specific frequency band can provide additional promising crack diagnosis information.

Table 2.5: AIR values of the condition indicators (simulated analysis)

Condition indicator	E_{CIIEnv} [77]	E_{ImpVC} [87]	$PS-I$ [86]	SE_{FB_3} (proposed)	E_{RecCII} (proposed)
AIR value (%)	8.54	6.66	2.36	626.81	16.69

Besides, to visually illustrate how the CIs track tooth crack growth, the normalized values of these CIs are calculated using Eq. (2.37). The normalized CIs versus tooth crack level are shown in Fig. 2.11, from which it is seen that SE_{FB_3} and E_{RecCII} are more sensitive to early tooth crack severity progression than the three reported ones. Based on the higher AIR values of the two proposed CIs, it is expected that they can also achieve higher accuracy for early tooth crack severity assessment, which will be validated using experimental gearbox vibration datasets in Section 2.5.

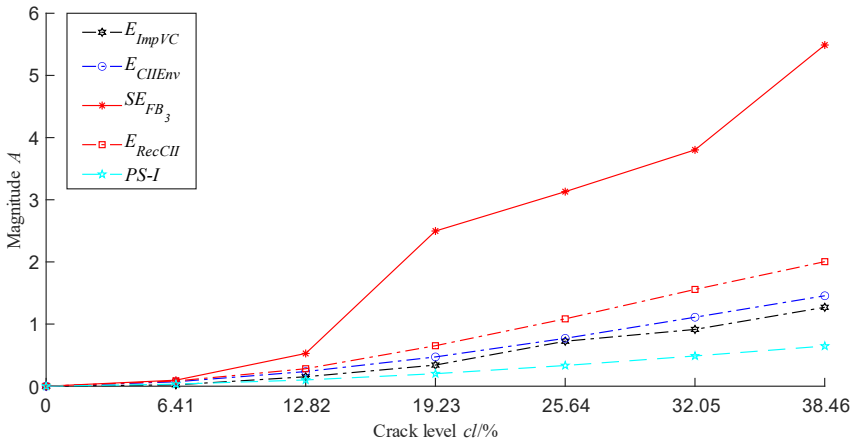

Fig. 2.11: Condition indicators versus crack level (simulated analysis)

2.5 Application to experimental gearbox vibration dataset

In this section, to further validate the effectiveness of the proposed method and the newly proposed CIs, they are applied to the experimental vibration datasets of a fixed-axis spur gearbox with a tooth crack in the early crack stage. The three reported CIs, namely E_{CIIEnv}, E_{ImpVC}, and *PS-I*, are also calculated using the experimental vibration datasets for comparison.

2.5.1 Experimental setup

The experimental vibration datasets were collected using the planetary gearbox test rig in the Reliability Research Lab at the University of Alberta. The planetary gearbox test rig, schematic of the target fixed-axis spur gearbox, and locations of accelerometers are shown in Fig. 2.12. As shown in Fig. 2.12(a), the test rig includes a drive motor, a bevel gearbox, a two-stage planetary gearbox, two speed-up fixed-axis gearboxes, and a load motor. In the experiment, the 2nd stage Speed-up gearbox was used as the target gearbox. Its schematic is shown in Fig. 2.12(b), from which it is seen that the target gearbox has two gear mesh pairs: input mesh pair and output mesh pair. The input pinion with 18 teeth was selected as the target gear in the experiment and its specifications are tabulated in Table 2.6. As shown in Fig. 2.12(c), accelerometer 1 is installed on gearbox casing, accelerometer 2 is vertically installed on the bearing cab, accelerometer 3 is parallelly installed on the bearing cab, accelerometer 4 is laterally installed on the bearing cab.

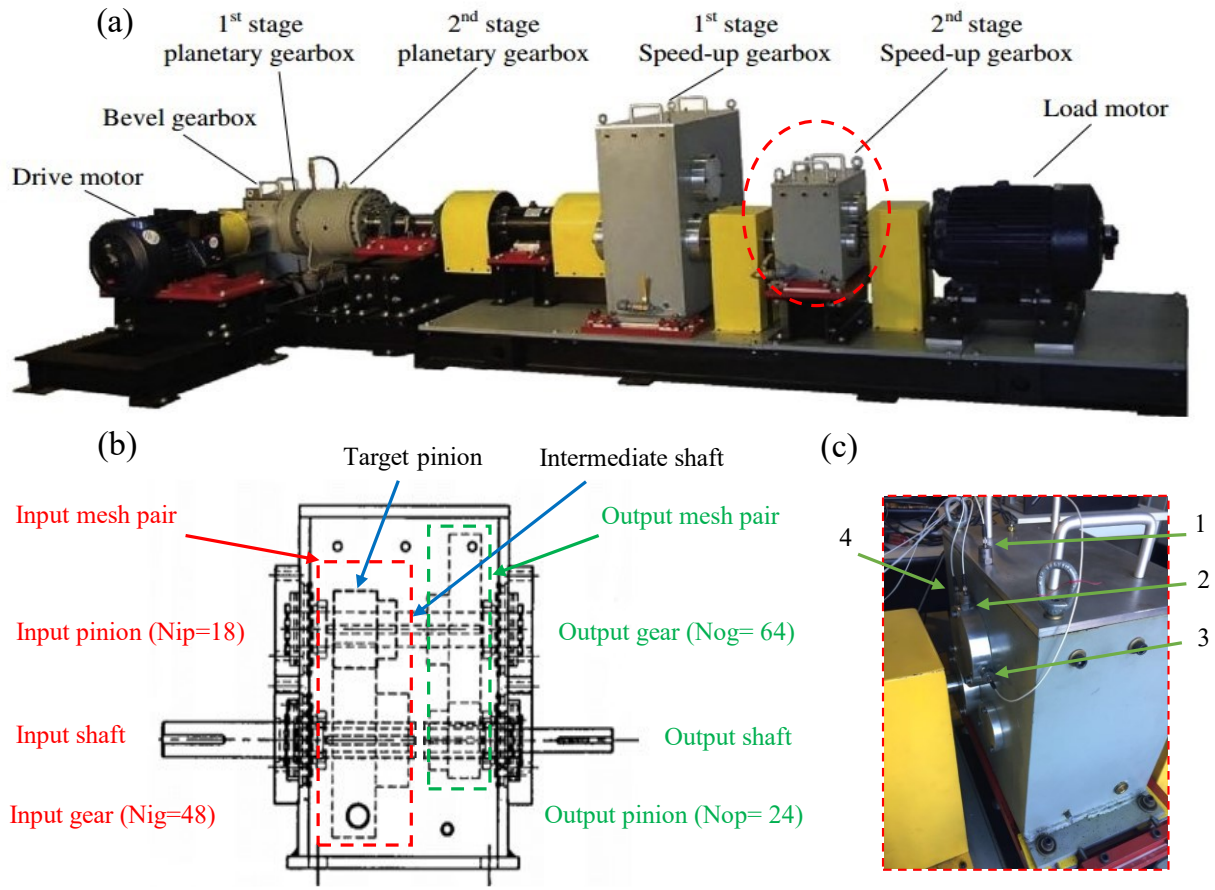

Fig. 2.12: Experimental setup: (a) Planetary gearbox test rig, (b) Schematic of the target fixed-axis spur gearbox, (c) Accelerometer locations

Table 2.6: Specifications of the target pinion

Parameter	Value
Face width (cm)	5.08
Pitch diameter (cm)	7.62
Diametral pitch (DP)	6
Pressure angle (Deg)	20
Number of teeth	18

A localized tooth crack was artificially seeded on the root fillet of one tooth of the 18-tooth input pinion in Fig. 12 (b) with an electric discharge machine. Tooth crack propagation of the target pinion is illustrated in Fig. 2.13, in which w is whole tooth face width, w_0 is tooth crack length, q is half-length of the tooth chordal thickness, q_0 is crack depth, and α_c is crack angle. In the experiment, 4 health conditions including a healthy case and 3 cracked cases were considered, which are tabulated in Table 2.7. In Table 2.7, the crack level is defined as the product of the crack length ratio w_0/w and the crack depth ratio $q_0/(2q)$, namely $cl = \frac{w_0}{w} \times \frac{q_0}{2q} \times 100\%$. When $w_0 =$ w and $q_0 = 2q$, which corresponds to the case of complete loss of tooth, $cl = 100\%$. Crack levels of the three faulty cases are figured out as 2%, 8%, and 18%. For the healthy case, its crack level is 0% since there is no crack seeded on the tooth root fillet. The considered crack levels belong to the early tooth crack stage.

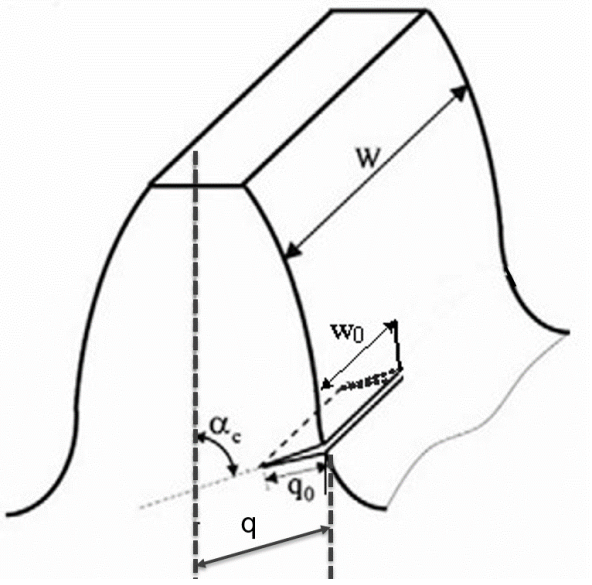

Fig. 2.13: Tooth crack propagation scenario for the target pinion

Table 2.7: Tooth crack levels considered in the experiment

Health condition (Label)	Crack parameters	Crack level (cl)
Healthy (F0)	$w_0 = 0$; $q_0 = 0$;	0%
Faulty 1 (F1)	$w_0 = 0.2$w; $q_0 = 0.2q$; $\alpha_c = 60°$	2%
Faulty 2 (F2)	$w_0 = 0.4$w; $q_0 = 0.4q$; $\alpha_c = 60°$	8%
Faulty 3 (F3)	$w_0 = 0.6$w; $q_0 = 0.6q$; $\alpha_c = 60°$	18%

In the experiment, gearbox vibration datasets were collected when the target pinion run at a constant rotational frequency of 2.955 Hz and the applied torque on the load motor was 80 Nm. GMF of the input gear mesh pair (the one with the cracked pinion) is $\mathrm{GMF_{in}} = 53.19$ Hz, and GMF of the output gear mesh pair is $\mathrm{GMF_{out}} = 189.12$ Hz. The sampling frequency was set to 25.6 kHz to avoid frequency aliasing. Vibration signals were collected for the four health conditions shown in Table 2.7. Time length of each signal sample was 10 s, and 10 signal samples were collected for each health condition. Four accelerometers (model: PCB 352B, sensitivity is 1000 mv/g, frequency range is 1 to 15000 Hz with an error range of $\pm 10\%$) were used for signal acquisition and their mounting locations are shown in Fig. 2.12 (c). Without loss of generality, the vibration signals collected by the accelerometer 3 are analyzed in this paper. Besides, a tachometer signal was also acquired using an encoder simultaneously with vibration signal collection. The collected experimental vibration signals of the target gearbox under each health condition are shown in Fig. 2.14. It is seen that there are strong environmental noise and random impacts in the experimental vibration signals. It is difficult to assess tooth crack severity by observing the time waveforms since tooth crack signatures are completely submerged in the vibration signals.

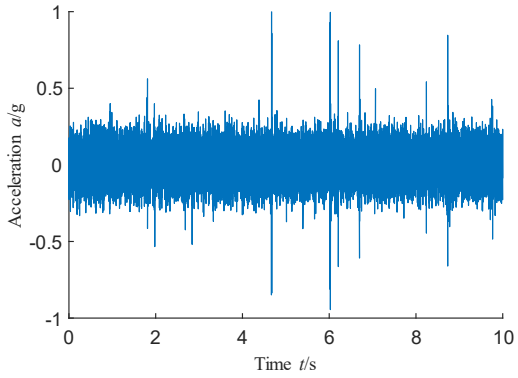

(a) "Healthy" case

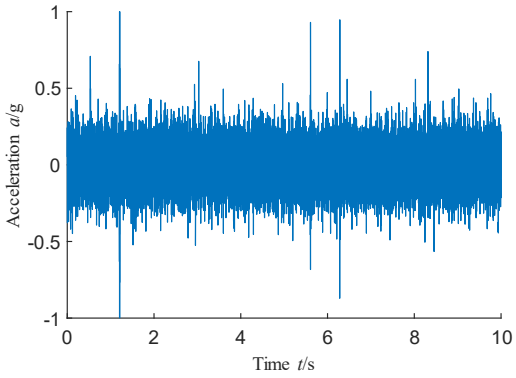

(c) "Faulty 2" case

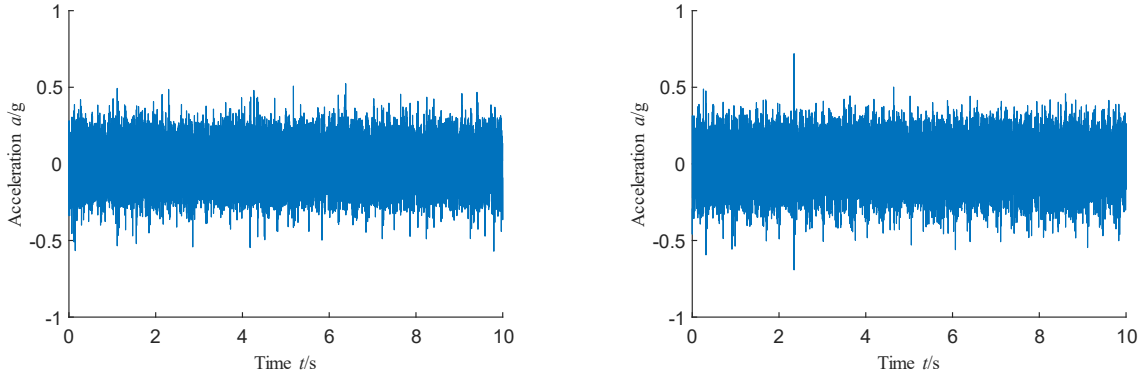

(b) “Faulty 1” case (d) “Faulty 3” case

Fig. 2.14: Time waveforms of experimental gearbox vibration signals

2.5.2 Application of the proposed method and new condition indicators

As illustrated in Section 2.4, the effectiveness of the proposed method and the proposed CIs has been verified with simulated gearbox vibration responses. In this section, their effectiveness is further validated with experimental gearbox vibration signals. One sample of the experimental gearbox vibration signals for the health condition case “Faulty 3” is used as an example to show the analysis results obtained using the proposed method.

In Step 1 of the proposed method, the TSA signal and its energy spectral density are obtained, which are shown in Fig. 2.15. From Fig. 2.15(a), no obvious abrupt change caused by the tooth crack is observed due to the existence of the masking effect of the regular meshing components of both the target input pinion and the output gear. From Fig. 2.15(b), it is seen that there are evident resonance peaks located in the frequency range from about 212.7 Hz to 425.5 Hz. Therefore, the dominant resonant frequency range in which the CII exists is identified as [212.7, 425.5] Hz. For experimental vibration signals for other health conditions, this conclusion still holds.

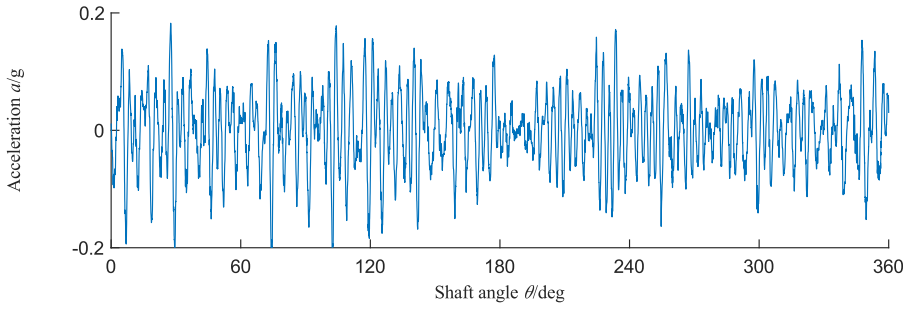

(a) TSA signal

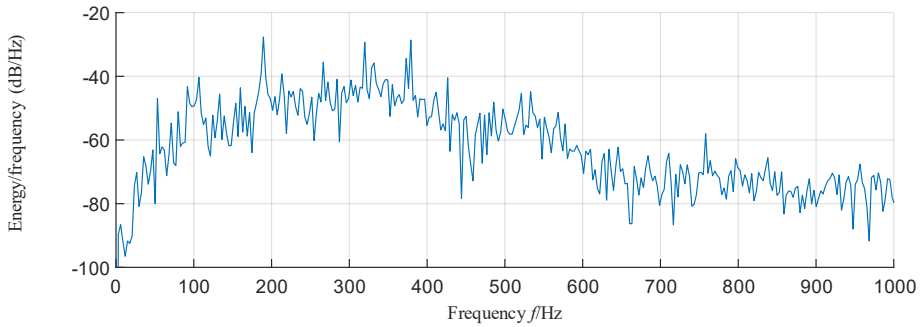

(b) Energy spectral density of TSA signal

Fig. 2.15: The TSA signal and its energy spectral density (Faulty 3 case)

In Step 2, the comb notch filter of the IIR type is used to remove the GMF and its harmonics alongside the sidebands from the TSA signal. There are two gear mesh pairs in the target gearbox shown in Fig. 2.12(b), so two comb notch filters are used to remove the meshing components of the two gears on the target shaft: (1) $\mathrm{GMF}_{\mathrm{in}}$ and its harmonics and the associated sidebands for the 18-tooth input pinion; (2) $\mathrm{GMF}_{\mathrm{out}}$ and its harmonics and the associated sidebands for the 64-tooth output gear. For the comb notch filter used to remove the meshing components of the input pinion, its center frequencies are set to $\mathrm{GMF}_{\mathrm{in}}$ and its harmonics, and its bandwidth is set to 5 sideband pairs. For the comb notch filter used to remove the meshing components of the output gear, its center frequencies are set to $\mathrm{GMF}_{\mathrm{out}}$ and its harmonics, and its bandwidth is set to 5 sideband pairs. After conducting comb notch filtering, the gear meshing components and sidebands of the two gears are removed. The removal of 5 pairs of sidebands causes distortion to the resulting spectrum, but the distortion impact on the main resonance peaks excited by the CII is insignificant. The reason is that harmonics of the CII spread over a wide frequency range and have low amplitudes and the removal of 5 pairs of sidebands does not affect the harmonics of the CII too much. The notch filtered signal mainly includes components related to the CII. The notch filtered signal and its energy spectral density are shown in Fig. 2.16. As shown in Fig. 2.16(b), frequency range [212.7, 425.5] Hz is dominated by the resonance peaks, which is the same as the one identified in Step 1.

In Step 3, the modal model shown in Eq. (2.23) is employed to fit the dominant resonance peaks of the notch filtered signal displayed in Fig. 2.16(b). The dominant resonance peaks are defined as those within about 20dB of the highest one. The model parameters of the resonance peaks, i.e., SDOF IRs, are obtained using the MPM. Eight dominant SDOF IRs are obtained, the amplitudes,

carrier frequencies, phases, damping factors and energy values of which are displayed in Table 2.8, in which the unit of phase is “rad”. Based on the estimated modal parameters tabulated in Table 2.8, each SDOF IR is identified. The eight identified SDOF IRs are shown in Fig. 2.17.

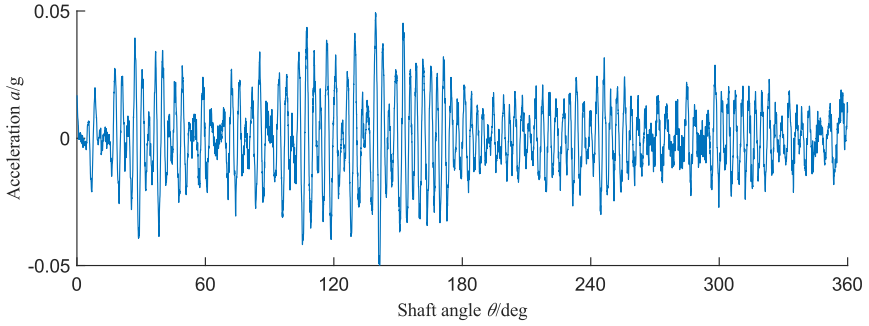

(a) Notch filtered signal

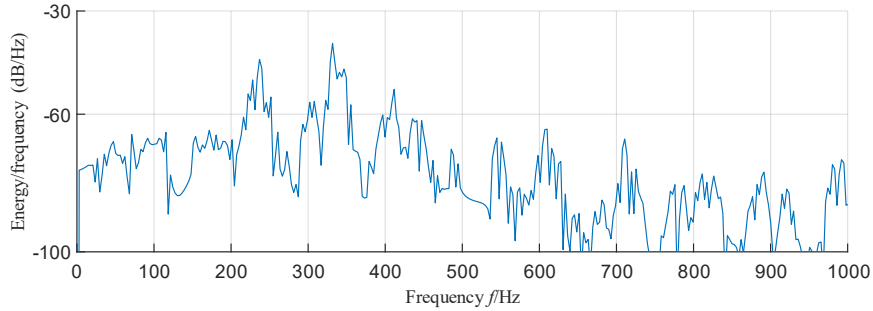

(b) Energy spectral density of notch filtered signal

Fig. 2.16: Time waveform and energy spectral density of the notch filtered signal obtained by comb notch filtering (Faulty 3 case)

Table 2.8: Amplitudes, frequencies, phases, damping factors and energy of the eight identified SDOF IRs (Faulty 3 case)

	1st SDOF IR	2nd SDOF IR	3rd SDOF IR	4th SDOF IR	5th SDOF IR	6th SDOF IR	7th SDOF IR	8th SDOF IR
Amplitude	0.0055	0.0158	0.0148	0.0038	0.0173	0.0328	0.0113	0.0026
Frequency	228.05	235.28	240.39	303.27	327.01	330.49	337.33	411.30
Phase	-11.32	-10.98	-8.16	-9.87	-9.97	-8.10	-6.62	-6.15
Damping factor	2.51	6.10	7.90	4.66	9.12	5.54	3.01	0.50
Energy	2.4E-06	1.0E-05	1.7E-05	7.3E-07	8.3E-06	4.7E-05	9.2E-06	9.9E-07

As stated in Subsection 2.3.1, if the natural frequencies of the two gears on the intermediate shaft shown in Fig. 2.12(b) are known, the comparison of the carrier frequencies of the SDOF IRs in Table 2.8 to the natural frequencies of the two gears would help determine which gear is the one with a tooth crack, i.e., the target gear. Specifically, if the carrier frequencies of the SDOF IRs are close to the natural frequencies of the 18-tooth input pinion, the input pinion is the target gear. Otherwise, the 64-tooth output gear is the target gear. But in this study, since the natural frequencies of the two gears are unknown, we need to resort to the method of inspecting the frequency spectrum differences. By comparing the frequency spectrum of the vibration signal for the "Healthy" case to that for the "Faulty 3" case, it is found that in the spectrum for the "Faulty 3" case, there are newly emerged sidebands located around the $\mathrm{GMF}_{\mathrm{in}}$ (53.19 Hz) and its harmonics while there are no newly emerged sidebands around the $\mathrm{GMF}_{\mathrm{out}}$ (189.12 Hz) and its harmonics, which means that the 18-tooth input pinion has a tooth crack. This agrees with the fact that the tooth crack was seeded on one tooth of the 18-tooth input pinion in the experiment, which was presented in Subsection 2.5.1. This indicates that the target gear can be determined by inspecting the differences between the frequency spectrum of the healthy gear vibration signal and that of the cracked gear case, even in the actual cases where the gear with a tooth crack is unknown.

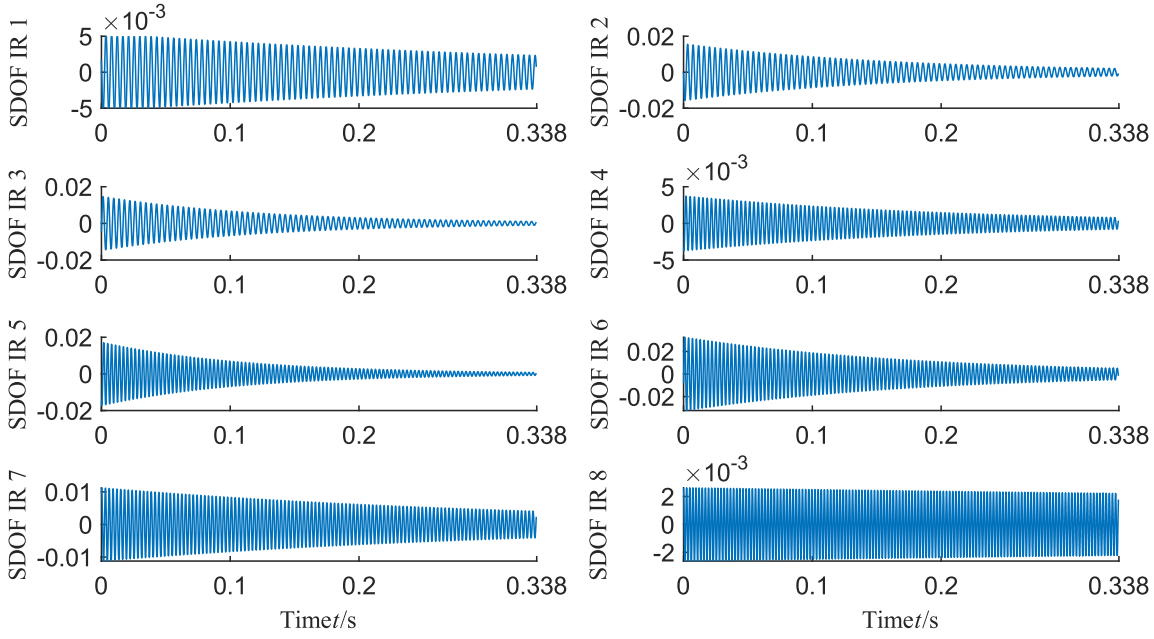

Fig. 2.17: Time waveforms of the eight identified SDOF IRs (Faulty 3 case)

In Step 4, by summing the eight identified SDOF IRs shown in Fig. 2.17, the CII was reconstructed. The time waveform and energy spectral density of the reconstructed CII are plotted in Fig. 2.18. From Fig. 2.18(a), it is seen that the reconstructed CII has a maximum amplitude between 90 and 150 degrees of the target input pinion shaft rotational angle, although the beginning of the reconstructed CII is at time zero. The maximum amplitude of the reconstructed CII is resulted from the interaction of the amplitudes and phases of all the identified SDOF IRs used to reconstruct the CII. For comparison, time waveforms of the reconstructed CII and the notch filtered signal obtained in Step 2 are plotted in Fig. 2.19, and their energy spectral densities are plotted in Fig. 2.20. From these two figures, it is found that there are much less extraneous masking components in the reconstructed CII. In addition, the resonant frequency range identified in Step 1, i.e. [212.7, 425.5] Hz, is divided into four separate frequency bands, namely FB_i ($i = 1, \dots, 4$). Because the 18-tooth input pinion is the target gear, harmonics of $\mathrm{GMF_{in}}$ ($\mathrm{GMF_{in}} = 53.19$ Hz) are used as dividers and the width of each frequency band is equal to $\mathrm{GMF_{in}}$. The four frequency bands are tabulated in Table 2.9. Based on these four frequency bands, the identified SDOF IRs shown in Fig. 2.17 are grouped by their carrier frequencies. For example, for the 1st, 2nd, and 3rd SDOF IRs, their frequencies are 228.05 Hz, 235.28 Hz, 240.39 Hz (shown in Table 2.8), respectively, which are in the first frequency band FB_1 [212.7, 265.9] Hz. Therefore, these three SDOF IRs are grouped together, and this group is related to the FB_1. Likewise, other SDOF IRs shown in Fig. 2.17 are grouped into the groups related to other frequency bands by their carrier frequencies. The grouping results are shown in Table 2.10.

Table 2.9: Four frequency bands (experimental analysis)

Frequency band	FB_1	FB_2	FB_3	FB_4
Range/Hz	[212.7, 265.9]	[265.9, 319.1]	[319.1, 372.3]	[372.3, 425.5]

Table 2.10: Grouping result for the identified SDOF IRs (Faulty 3 case)

Group	group related to FB_1	group related to FB_2	group related to FB_3	group related to FB_4
SDOF IR	1st, 2nd, 3rd	4th	5th, 6th, 7th	8th

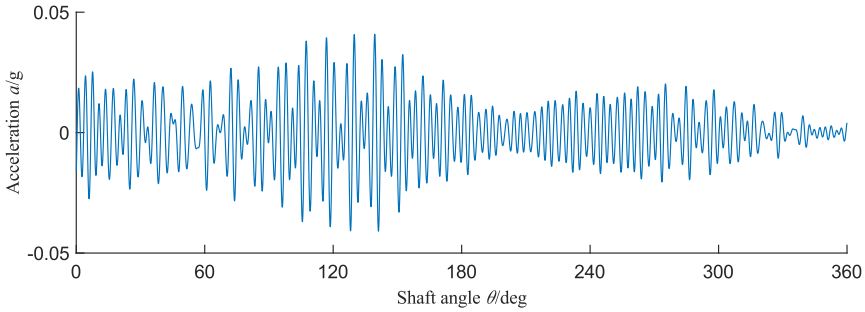

(a) Reconstructed CII

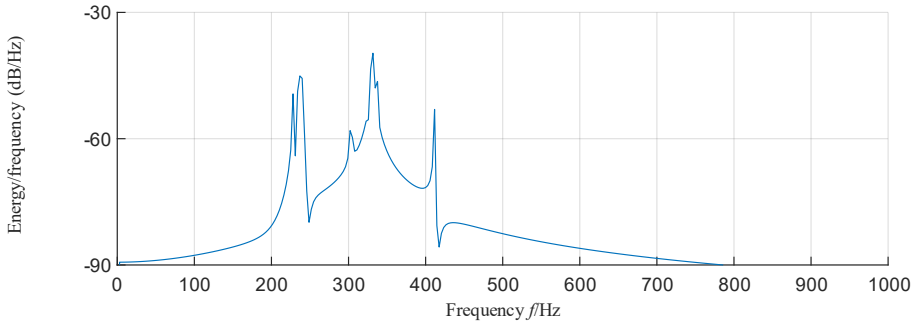

(b) Energy spectral density of reconstructed CII

Fig. 2.18: Time waveform and energy spectral density of the reconstructed CII (Faulty 3 case)

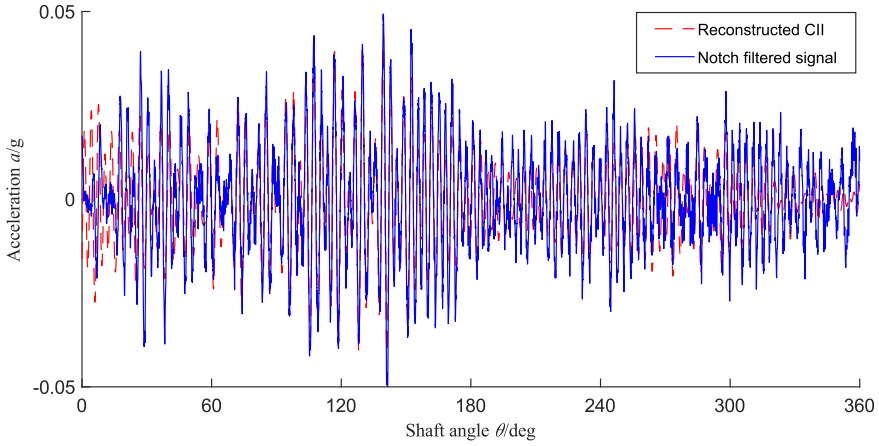

Fig. 2.19: The reconstructed CII and the notch filtered signal (Faulty 3 case)

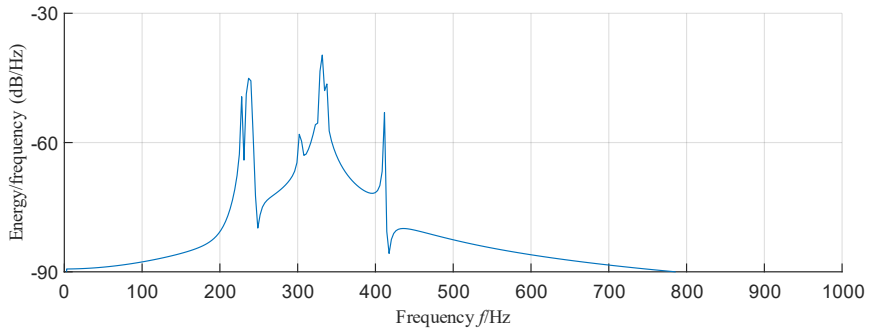

(a) Energy spectral density of reconstructed CII

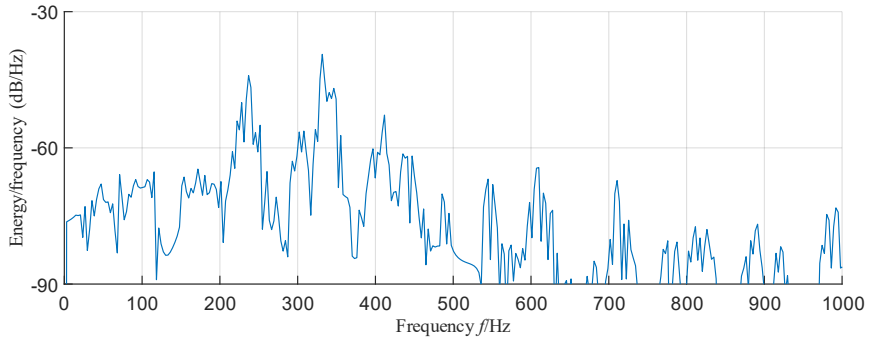

(b) Energy spectral density of notch filtered signal

Fig. 2.20: Energy spectral densities of the reconstructed CII and the notch filtered signal (Faulty 3 case)

The energy of reconstructed CII is calculated using Eq. (2.33), which is $E_{RecCII} = 6.1 \times 10^{-5}$. The sum of the energy of the SDOF IRs in each group shown in Table 2.10 is calculated using Eq. (2.34). For example, $SE_{FB_3} = 8.3 \times 10^{-6} + 4.7 \times 10^{-5} + 9.2 \times 10^{-6} = 6.5 \times 10^{-5}$. Likewise, the sums of the energy of the SDOF IRs in the other groups are also calculated. The energy results are tabulated in Table 2.11, from which it is seen that SE_{FB_3} is greater than E_{RecCII}. This means that SE_{FB_3} can give additional promising crack diagnosis information.

Table 2.11: Results of the SE_{FB_i} and E_{RecCII} (Faulty 3 case)

Energy	SE_{FB_1}	SE_{FB_2}	SE_{FB_3}	SE_{FB_4}	E_{RecCII}
Value	2.9×10^{-5}	7.3×10^{-7}	6.5×10^{-5}	9.9×10^{-7}	6.1×10^{-5}

In Step 5, repeating all Steps 1-4 of the proposed method for the experimental gearbox vibration signals of all health conditions, E_{RecCII} and SE_{FB_i} $(i = 1, \ldots, 4)$ are calculated. To study the repeatability of the proposed method, for each health condition, the collected 10 datasets were used to calculate the energy metrics. The boxplots of the energy metrics are shown in Fig. 2.21, in which

the central red mark on the box denotes the median value of the 10 values of a CI, the edges of the box represent the 25th and 75th percentiles, whiskers extend to the most extreme data points, and outliers are plotted as red crosses. As shown in Fig. 2.21, E_{RecCII} shows better ascending trend towards early tooth crack severity progression. SE_{FB_3} has the best ability to track crack growth among SE_{FB_i} $(i = 1,2,3,4)$, which provides promising crack diagnosis information. Therefore, SE_{FB_3} is proposed as a new CI together with E_{RecCII} for early tooth crack severity assessment.

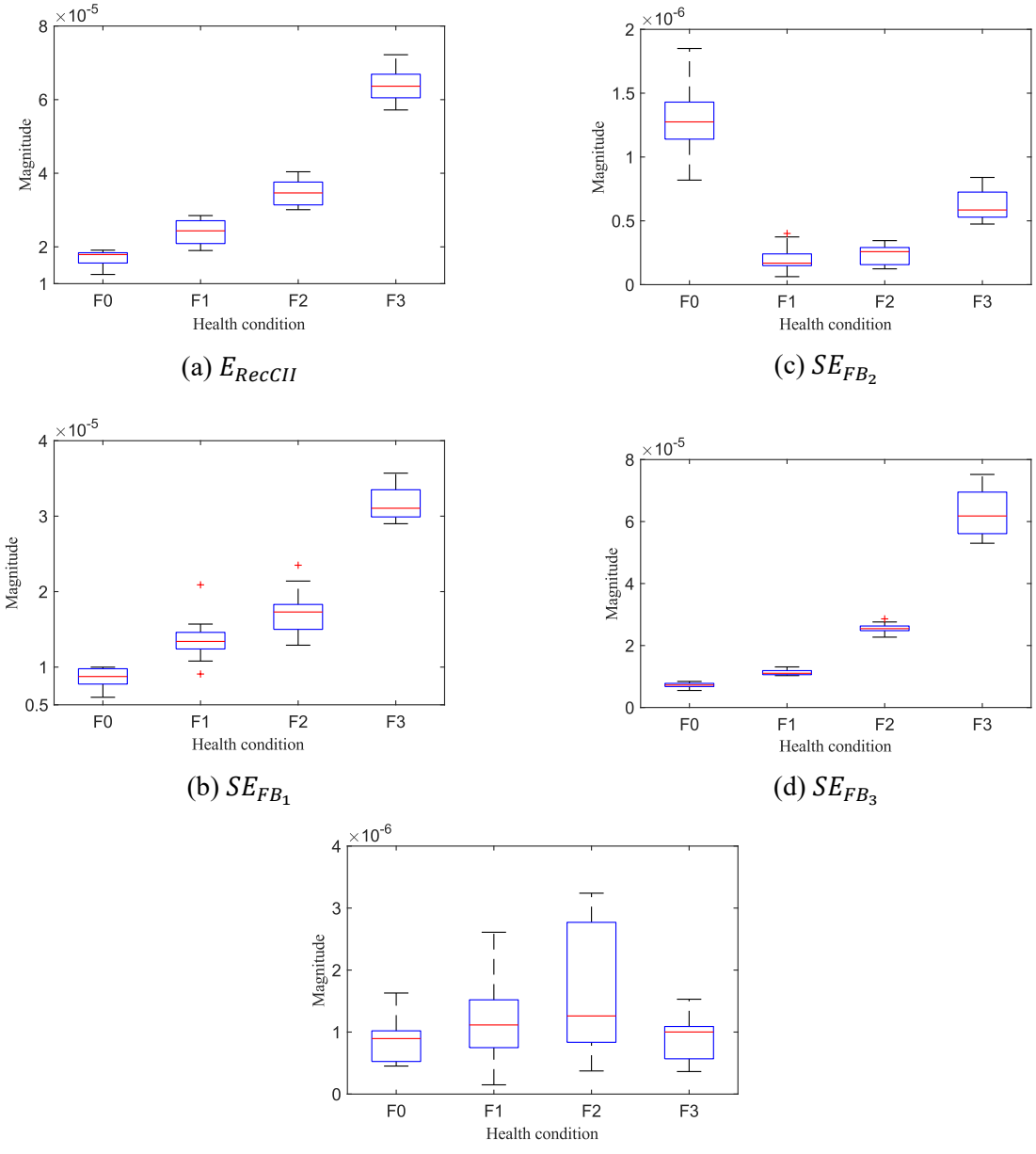

(a) E_{RecCII}

(c) SE_{FB_2}

(b) SE_{FB_1}

(d) SE_{FB_3}

(e) SE_{FB_4}

Fig. 2.21: Boxplots for E_{RecCII} and SE_{FB_i} (for $i = 1, \dots, 4$)

2.5.3 Performance comparison

As mentioned in Subsection 2.3.2, the AIR and tooth crack severity assessment accuracy are used for performance comparison between the two proposed CIs, namely E_{RecCII} and SE_{FB_3}, and the three reported ones, i.e., E_{CIIEnv} [77], E_{ImpVC} [87], and *PS-I* [86]. In the experiment, 10 data samples were collected for each health condition. Therefore, for each health condition, 10 results were obtained for each CI, which were used to calculate the median values. Median values of the CIs were adopted to calculate their AIR values, which are tabulated in Table 2.12. As shown in Table 2.12, E_{RecCII} and SE_{FB_3} have much higher AIR values than the three reported CIs, which means that they are more sensitive towards early tooth crack severity progression. To illustrate this visually, the obtained median values are normalized using Eq. (2.37). The normalized median values of the CIs with regard to the gear healthy conditions are plotted in Fig. 2.22, from which it is seen that E_{RecCII} outperforms the three reported CIs, and SE_{FB_3} has the best performance in terms of tracking early tooth crack severity progression.

Table 2.12: AIR values of the condition indicators (experimental analysis)

Condition indicator	E_{CIIEnv} [77]	E_{ImpVC} [87]	$PS-I$ [86]	SE_{FB_3} (proposed)	E_{RecCII} (proposed)
AIR value (%)	678.76	716.44	275.35	4180.08	1419.93

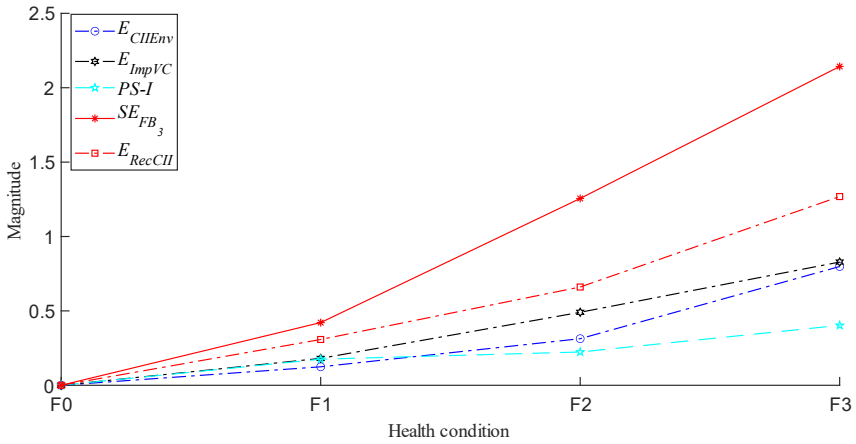

Fig. 2.22: Normalized median values of condition indicators versus health condition

To obtain the tooth crack severity assessment accuracy, an LDA classifier [122] was trained. The data was randomly partitioned into training and testing datasets where the training set holds 60%

and the testing set 40%. Classification result was converted into tooth crack severity assessment accuracy using the confusion matrix. Three trials of tooth crack severity assessment were conducted, which resulted in three overall accuracy values for each CI. Confusion matrices of the CIs for the third trial are shown in Fig. 2.23 for illustration. As shown in Fig. 2.23, the overall accuracy is displayed in the last cell at the bottom rightmost corner of the confusion matrix.

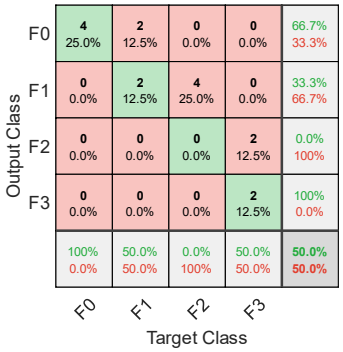

(a) Confusion matrix for E_{CIIEnv}

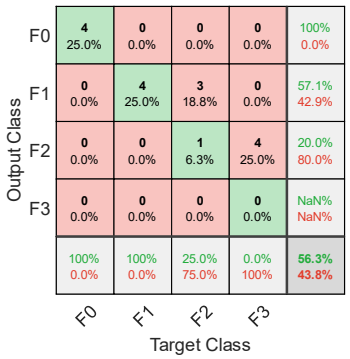

(c) Confusion matrix for *PS-I*

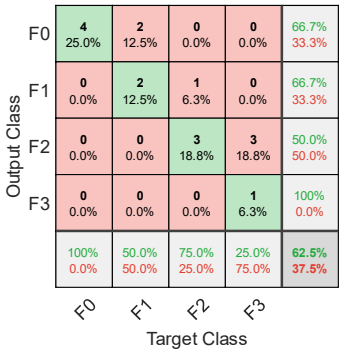

(b) Confusion matrix for E_{ImpVC}

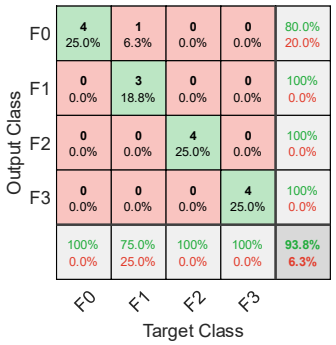

(d) Confusion matrix for SE_{FB_3}

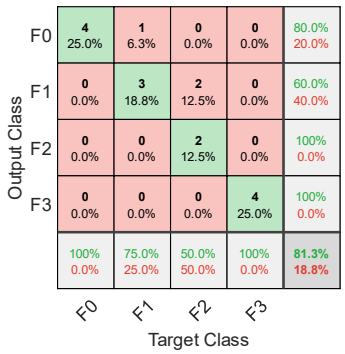

(e) Confusion matrix for E_{RecCII}

Fig. 2.23: Confusion matrices for all the five condition indicators (third trial)

The average overall accuracy of these three trials is used as the final assessment accuracy. The overall assessment accuracy for each CI in each trial and their average values are tabulated in Table 2.13, from which it is found that the average accuracy values of E_{RecCII} and SE_{FB_3} for early tooth crack severity assessment are 87.5% and 91.7%, which are much higher than those of E_{CIIEnv}, E_{ImpVC}, and *PS-I*, i.e. 56.3%, 60.4%, 52.1%, respectively. On this basis, it is concluded that when the inputs of the LDA classifier are the proposed CIs, i.e., E_{RecCII} and SE_{FB_3}, it can result in much higher accuracy values for early tooth crack severity assessment than those for the three reported ones. This indicates that the proposed method can extract better signatures of early tooth cracks from gearbox vibration signals and the two proposed CIs can better track early tooth crack severity progression, thus resulting in better performance on early tooth crack severity assessment.

Table 2.13: Early tooth crack severity assessment accuracy results for the condition indicators

Condition indicator	E_{CIIEnv} [77]	E_{ImpVC} [87]	$PS-I$ [86]	SE_{FB_3} (proposed)	E_{RecCII} (proposed)
Trial 1 accuracy	62.5%	68.8%	50.0%	93.8%	93.8%
Trial 2 accuracy	56.3%	50.0%	50.0%	87.5%	87.5%
Trial 3 accuracy	50.0%	62.5%	56.3%	93.8%	81.3%
Average accuracy	56.3%	60.4%	52.1%	91.7%	87.5%

2.6 Conclusions

In this chapter, a novel method is proposed to conduct a thorough analysis of the CII extracted from gearbox vibration signals and two new CIs are proposed to assess tooth crack severity in the early crack stage. The proposed method focuses on the CII since it consists of structural resonances and provides more crack information than other vibration components. There are five steps in the proposed method. Firstly, the TSA technique is adopted to remove the components that are not synchronous with the gear with a tooth crack from gearbox vibration signals. The resonant frequency range in which the CII exists is identified from the energy spectral density of the TSA signal. Afterwards, the GMF and its harmonics and the sidebands around them of all gears on the target shaft are removed using comb notch filters. A modal model is used to identify the dominant

resonances as SDOF IRs, and modal parameters are estimated using the MPM. The identified SDOF IRs are used to reconstruct the CII. In addition, the resonant frequency range is divided into separate frequency bands, through which the SDOF IRs are grouped. Lastly, the energy of the reconstructed CII and the sum of the energy of SDOF IRs with their carrier frequencies in a specific frequency band are proposed as two new CIs for early tooth crack severity assessment.

The effectiveness of the proposed method and the proposed CIs is demonstrated with both simulated gearbox vibration responses and experimental gearbox vibration signals. In addition, a comparison of performance on assessing early tooth crack severity is made between the proposed CIs, i.e., E_{RecCII} and SE_{FB_3}, and the three reported ones, namely E_{CIIEnv} [77], E_{ImpVC} [87], and *PS-I* [86]. The AIR and tooth crack severity assessment accuracy are used as two comparison criteria. Comparative results show that the proposed CIs perform much better than the three reported ones in terms of early tooth crack severity assessment with larger AIR values and higher tooth crack severity assessment accuracy values. By conducting a thorough analysis of the CII, the proposed method can extract signatures that well indicate early tooth crack severity progression, which demonstrates the superiority of the proposed CIs in terms of assessing early tooth crack severity.

In this chapter, the proposed method and the new CIs were developed under constant speed and constant load conditions. Future studies will explore the scenarios of early tooth crack diagnosis under time-varying working conditions.

Chapter 3: The effect of time-varying operating condition on the crack induced impulses and its application to gearbox tooth crack diagnosis

This chapter focuses on studying how time-varying operating conditions affect vibration characteristics of a fixed-axis spur gearbox with a tooth crack. The effect of time-varying operating condition on the CII is identified and is further adopted to develop a new CI for tracking tooth crack severity progression under time-varying operating conditions. The materials in this chapter are covered by the second research topic (Topic #2), which is introduced in Section 1.3. The organization of this chapter is as follows. In Section 3.1, an introduction to the reported studies on fixed-axis spur gearbox dynamics involving operating condition variations is made. Section 3.2 presents the proposed methodology for conducting a comprehensive study on how time-varying operating conditions affect vibration signals of fixed-axis spur gearbox with a tooth crack. Simulation analysis and experimental validation for the proposed methodology are presented in Section 3.3 and Section 3.4, respectively. Discussions of the proposed CI are presented in Section 3.5 and the conducted study is concluded in Section 3.6. Results of this chapter are documented in a journal paper [105] which is under review at present.

3.1 Introduction

During the last several decades, tooth crack diagnosis has been a research hotspot since it can prevent gearboxes failures, but many reported studies only focused on tooth crack diagnosis under constant operating conditions [33,77,103,104,123,124]. However, gearboxes oftentimes work under time-varying operating conditions, which makes tooth crack diagnosis methods for constant operating conditions incompetent. Time-varying operating conditions indicate that either the applied load (torque) or the rotating speed is variable, or both are variable. When gearboxes work under time-varying operating conditions, operating condition variations induce AM and FM into gearbox vibration signals [66,125,126]. For the operating condition variation-induced AM, it results in difficulties in distinguishing between changes of tooth crack severity and operating

condition variations [80]. For the operating condition variation-induced FM, it causes frequency smearing, which makes it hard to capture crack characteristic frequencies. Therefore, the AM and FM induced by time-varying operating conditions may lead to incorrect results of tooth crack diagnosis if not properly tackled.

To effectively conduct tooth crack diagnosis under time-varying operating conditions, the operating condition variation-induced AM and FM of gearbox vibration signals need to be well interpreted. To this end, dynamic model-based methods are preferred since they can eliminate the interferences of environmental noise and isolate the effects of time-varying operating conditions on vibration signals. Bartelmus et al. [125] adopted a dynamic model of a spur gearbox to study gearbox vibration responses under piecewise constant load conditions. They found that there was a linear relation between the load and the arithmetic sum of spectral components in the limited load range. However, they did not involve tooth cracks and how the load affects raw gearbox vibration signals was not revealed. Chaari et al. [66] studied the effect of a variable load on gearbox vibration signals using a dynamic model of a gearbox transmission system. They observed that load variation induced an AM into gear mesh harmonics. However, the relation between the variable load and the AM of gear mesh harmonics was not explicitly and mathematically described, and they also did not consider tooth cracks. Besides, a square waveform was used to represent the gear tooth mesh stiffness, which leaded to a significant simplification of the tooth meshing process. Later, another two studies have been conducted to study gearbox vibration responses under time-varying operation conditions [127,128]. Although tooth cracks were considered in these two studies, they still shared some common drawbacks: (1) square waveforms were used to approximate the gear tooth mesh stiffness, which made it difficult to evaluate the mesh stiffness of a gear mesh pair considering tooth crack severity progression under time-varying operating conditions; (2) the relations among the operating condition variation-induced AM and FM of the gearbox vibration signals, the time-varying operating conditions, and tooth crack severity progression were not identified.

Recently, Shu et al. [21] studied the dynamic properties of a gearbox in a multi-motor driving system under time-varying operating conditions. For the variable load and constant speed condition, gearbox accelerations changed as the load varied. For the variable load and variable speed condition, gearbox accelerations were the result of the interaction between the load and the

speed. However, in Ref. [21], the effects of variable load and speed on gearbox vibration signals were only qualitatively described, no mathematical representations were provided. Besides, vibration signals of gearboxes with tooth cracks were not studied. Bachar et al. [24] studied the effects of operating conditions on gearbox vibration signals. They examined the effects of operating conditions on healthy gearbox vibration signatures using constant loads and constant speeds and found that the energy of the signal component including the FM sidebands depended mainly on speed variation but was least affected by load variation. The energy of the signal component comprising the FM sidebands was adopted to track tooth fault growth under various constant speeds. However, in Ref. [24], tooth cracks were not involved and the relation between the operation condition variations and the AM and FM was not identified. Besides, in these studies, only conventional CIs, such as RMS and kurtosis, were used to differentiate tooth fault severity levels, failing to propose novel CIs to track tooth crack severity progression under time-varying operating conditions.

To overcome the deficiencies of the studies reviewed above, this chapter conducts a comprehensive study on how time-varying operating conditions affect vibration signals of a fixed-axis spur gearbox with a tooth crack. A gearbox system including a driving motor, a spur gear mesh pair, and a load machine is first modelled. For the time-varying operating conditions, two scenarios are considered, i.e., the variable load and constant speed condition, and the constant load and variable speed condition. As an internal excitation of the gearbox system, the gear tooth mesh stiffness is evaluated using the potential energy method under time-varying operating conditions. The gear tooth mesh stiffness is inserted into the gearbox dynamic model to simulate gearbox vibration signals under time-varying operating conditions. Because the CII contain more tooth crack information [77,104], the focus of signal analysis is placed on the CII extracted from gearbox vibration signals using the Adaptive Harmonic Decomposition (AHD) method or its modified counterpart. The AM of the CII is obtained using the envelope analysis and a linear dependence of the AM of the CII on the time-varying operating condition is identified. The identified linear dependence is used to propose a novel CI which is sensitive to tooth crack severity progression while insensitive to operating condition variations. By analyzing both simulated gearbox vibration signals and experimental gearbox vibration datasets, the linear dependence of the AM of the CII

on the time-varying operating condition and the effectiveness of the proposed CI for tracking tooth crack severity progression under time-varying operating conditions are demonstrated.

The novel contributions of this chapter include: (1) Evaluation of gear tooth mesh stiffness considering tooth crack severity progression under time-varying operating conditions, which is achieved by deriving gear tooth mesh stiffness obtained using the potential energy method as an implicit function of time. On this basis, gearbox dynamic responses for different tooth crack severity levels under time-varying operating conditions are generated; (2) A new procedure is proposed to analyze gearbox vibration signals, and a linear dependence of the AM of the CII on time-varying operating condition (variable load or variable speed) is identified; (3) Based on the identified linear dependence of the AM of the CII on the time-varying operating condition, a novel CI is proposed to track tooth crack severity progression under time-varying operating conditions.

The remainder of this chapter is organized as follows. Section 3.2 describes the proposed methodology, mainly including the gearbox dynamic simulation under time-varying operating conditions, the signal analysis procedure, and the development of a novel CI. The demonstration of the linear dependence of the AM of the CII on the time-varying operating condition and the effectiveness of the proposed CI for tooth crack diagnosis using simulated gearbox vibration signals and experimental gearbox vibration datasets are presented in Section 3.3 and Section 3.4, respectively. Discussions of the proposed CI are presented in Section 3.5 and the work conducted in this study is finally concluded in Section 3.6.

3.2 The proposed methodology

The proposed methodology consists of four parts, including the generation of simulated vibration signals of a spur gearbox with a tooth crack under time-varying operating conditions, the procedure for analyzing gearbox vibration signals, the development of a novel CI for tracking tooth crack severity progression under time-varying operating conditions, and the quantitative evaluation of the performance of the proposed CI on tooth crack diagnosis.

3.2.1 Gearbox dynamic simulation under time-varying operating conditions

In this subsection, simulated vibration signals of a spur gearbox involving tooth crack severity progression under time-varying operating conditions are generated. To this end, a spur gearbox

system with a tooth crack subject to a variable load or a variable speed is modeled, and the gear tooth mesh stiffness is obtained using the potential energy method and is further expressed as a function of time to consider tooth crack severity progression and operating condition variations.

3.2.1.1 Dynamic model of a spur gearbox transmission system

A spur gearbox system subject to time-varying operating conditions is modelled, and the fixed-axis spur gearbox shown in Fig. 2.2 in Section 2.4 is used as the spur gearbox system herein. As shown in Fig. 2.2, the gearbox system includes a driving motor, a pinion, a gear, and a load machine. A tooth crack is seeded on the pinion. The gearbox system is driven by the driving motor with a torque M_1 and a speed SPD, and the torque exerted on the load machine is M_2. The values of the load machine torque M_2 and the driving motor speed SPD are controlled to achieve the time-varying operating conditions. The driving motor shaft and the pinion shaft are directly coupled with a flexible coupling, so their speeds are the same. In Section 2.4, gearbox dynamic responses are generated under constant operating conditions, which has already been completed in Refs. [26,33], so gearbox motion equations are not introduced in Section 2.4. However, in this subsection, gearbox dynamic responses will be generated under time-varying operating conditions, which is different from the work conducted in Refs. [26,33]. To facilitate generating gearbox dynamic responses under time-varying operating conditions, gearbox system motion equations introduced in Refs. [26,33] are rearranged into the Lagrange formulation herein, which is shown in Eq. (3.1).

$$M\ddot{u} + C\dot{u} + Ku = F \tag{3.1}$$

where M is the mass matrix, C the damping matrix, K the stiffness matrix, u the displacement vector, and F the force vector.

The mass matrix M is a diagonal matrix, which is expressed in Eq. (3.2).

$$M = \begin{bmatrix} m_1 & & & & & & & & \\ & m_2 & & & & & 0 & & \\ & & m_1 & & & & & & \\ & & & m_2 & & & & & \\ & & & & I_1 & & & & \\ & & & & & I_2 & & & \\ & & 0 & & & & I_m & & \\ & & & & & & & I_b & \end{bmatrix} \tag{3.2}$$

where m_1 and I_1 are the mass and the mass moment of inertia of the pinion, respectively; m_2 and I_2 are the mass and the mass moment of inertia of the gear, respectively; I_m is the mass moment of inertia of the driving motor; I_b is the mass moment of inertia of the load machine.

The displacement vector u is shown in Eq. (3.3).

$$u = \{x_p \quad x_g \quad y_p \quad y_g \quad \theta_p \quad \theta_g \quad \theta_m \quad \theta_b\}^T \tag{3.3}$$

where superscript "T" is the vector transposition; x_p and x_g are linear displacements of the pinion and gear in the x direction, respectively; y_p and y_g are the pinion and gear linear displacements in the y direction, respectively; θ_p and θ_g are the pinion and gear angular displacements, respectively; θ_m and θ_b are angular displacements of the driving motor and load machine, respectively.

The force vector F is expressed using Eq. (3.4).

$$F = \{0 \quad 0 \quad 0 \quad 0 \quad 0 \quad 0 \quad M_1 \quad -M_2\}^T \tag{3.4}$$

where M_1 is the driving motor torque, M_2 the load machine torque.

The stiffness matrix K is expressed in Eq. (3.5).

$$K = K_{bc} + K_{mesh} \tag{3.5}$$

where K_{bc} is the stiffness matrix for the bearings and couplings, and K_{mesh} is the matrix for the gear tooth mesh stiffness, which are shown in Eq. (3.6) and Eq. (3.7), respectively.

$$K_{bc} = \begin{bmatrix} k_{x1} & 0 & 0 & 0 & 0 & 0 & 0 & 0 \\ 0 & k_{x2} & 0 & 0 & 0 & 0 & 0 & 0 \\ 0 & 0 & k_{y1} & 0 & 0 & 0 & 0 & 0 \\ 0 & 0 & 0 & k_{y2} & 0 & 0 & 0 & 0 \\ 0 & 0 & 0 & 0 & k_p & 0 & -k_p & 0 \\ 0 & 0 & 0 & 0 & 0 & k_g & 0 & -k_g \\ 0 & 0 & 0 & 0 & -k_p & 0 & k_p & 0 \\ 0 & 0 & 0 & 0 & 0 & -k_g & 0 & k_g \end{bmatrix} \tag{3.6}$$

where k_{x1} and k_{x2} are the horizontal radial stiffness of the input and output bearings, respectively; k_{y1} and k_{y2} are the vertical radial stiffness of the input and output bearings, respectively; k_p and k_g are the torsional stiffness of the input and output couplings, respectively. Values of these parameters can be determined through experimental measurements and theoretical calculations.

$$K_{mesh} = k_t \begin{bmatrix} 0 & 0 & 0 & 0 & 0 & 0 & 0 & 0 \\ 0 & 0 & 0 & 0 & 0 & 0 & 0 & 0 \\ 0 & 0 & 1 & -1 & -R_{b1} & R_{b2} & 0 & 0 \\ 0 & 0 & 1 & -1 & -R_{b1} & R_{b2} & 0 & 0 \\ 0 & 0 & -R_{b1} & R_{b1} & {R_{b1}}^2 & -R_{b1}R_{b2} & 0 & 0 \\ 0 & 0 & R_{b2} & -R_{b2} & -R_{b1}R_{b2} & {R_{b2}}^2 & 0 & 0 \\ 0 & 0 & 0 & 0 & 0 & 0 & 0 & 0 \\ 0 & 0 & 0 & 0 & 0 & 0 & 0 & 0 \end{bmatrix} \tag{3.7}$$

where k_t is the gear tooth mesh stiffness, which is to be evaluated in Section 3.2.1.2; R_{b1} and R_{b2} are the base circle radii of the pinion and the gear, respectively.

The damping matrix C is expressed using Eq. (3.8).

$$C = C_{bc} + C_{mesh} \tag{3.8}$$

where C_{bc} is the damping coefficient matrix for the bearings and couplings, and C_{mesh} is the gear tooth mesh damping coefficient matrix, which are shown in Eq. (3.9) and Eq. (3.10), respectively.

$$C_{bc} = \begin{bmatrix} c_{x1} & 0 & 0 & 0 & 0 & 0 & 0 & 0 \\ 0 & c_{x2} & 0 & 0 & 0 & 0 & 0 & 0 \\ 0 & 0 & c_{y1} & 0 & 0 & 0 & 0 & 0 \\ 0 & 0 & 0 & c_{y2} & 0 & 0 & 0 & 0 \\ 0 & 0 & 0 & 0 & c_p & 0 & -c_p & 0 \\ 0 & 0 & 0 & 0 & 0 & c_g & 0 & -c_g \\ 0 & 0 & 0 & 0 & -c_p & 0 & c_p & 0 \\ 0 & 0 & 0 & 0 & 0 & -c_g & 0 & c_g \end{bmatrix} \tag{3.9}$$

where c_{x1} and c_{x2} are the horizontal radial damping coefficients of the input and output bearings, respectively; c_{y1} and c_{y2} the vertical radial damping coefficients of the input and output bearings, respectively; c_p and c_g the damping coefficients of the input and output couplings, respectively.

$$C_{mesh} = c_t \begin{bmatrix} 0 & 0 & 0 & 0 & 0 & 0 & 0 & 0 \\ 0 & 0 & 0 & 0 & 0 & 0 & 0 & 0 \\ 0 & 0 & 1 & -1 & -R_{b1} & R_{b2} & 0 & 0 \\ 0 & 0 & 1 & -1 & -R_{b1} & R_{b2} & 0 & 0 \\ 0 & 0 & -R_{b1} & R_{b1} & {R_{b1}}^2 & -R_{b1}R_{b2} & 0 & 0 \\ 0 & 0 & R_{b2} & -R_{b2} & -R_{b1}R_{b2} & {R_{b2}}^2 & 0 & 0 \\ 0 & 0 & 0 & 0 & 0 & 0 & 0 & 0 \\ 0 & 0 & 0 & 0 & 0 & 0 & 0 & 0 \end{bmatrix} \tag{3.10}$$

where c_t is the time-varying tooth mesh damping coefficient, which is calculated using Eq. (3.11).

$$c_t = \mu k_t \tag{3.11}$$

where μ is a scale constant with the unit of *second* (s).

3.2.1.2 Evaluation of gear tooth mesh stiffness

To overcome the drawback of using square waveforms to represent gear tooth mesh stiffness in the reported studies [66,127,128], the potential energy method [26,33] is modified to evaluate the mesh stiffness k_t in order to involve tooth crack severity progression and time-varying conditions. To evaluate the mesh stiffness for a gear pair with a pinion tooth crack, the cracked tooth model shown in Fig. 2.3 in Section 2.4 is used to simulate the pinion tooth crack. In this chapter, crack depth q_p is used to represent tooth crack severity level, and seven tooth crack depths are considered, namely the values of q_p are 0mm, 1mm, 2mm, 3mm, 4mm, 5mm, and 6mm, respectively.

The total potential energy stored in a gear mesh pair was assumed to include four parts: the Hertzian energy, the bending energy, the axial compressive energy, and the shear energy. For the single-tooth-pair meshing duration, the gear tooth mesh stiffness is expressed in Eq. (3.12) [33].

$$k_t = \frac{1}{1/k_h + 1/k_{b1} + 1/k_{a1} + 1/k_{s1} + 1/k_{b2} + 1/k_{a2} + 1/k_{s2}} \tag{3.12}$$

where k_h, k_b, k_a, and k_s are Hertzian stiffness, bending stiffness, axial compressive stiffness, and shear stiffness, respectively; subscripts 1 and 2 denote the pinion and the gear, respectively.

For the double-tooth-pair meshing duration, gear tooth mesh stiffness is shown in Eq. (3.13) [33].

$$k_t = \sum_{i=1}^{2} \frac{1}{1/k_{h,i} + 1/k_{b1,i} + 1/k_{a1,i} + 1/k_{s1,i} + 1/k_{b2,i} + 1/k_{a2,i} + 1/k_{s2,i}} \tag{3.13}$$

where $i = 1$ represents the first pair of meshing teeth, $i = 2$ the second pair of meshing teeth.

Formulae of k_h, k_b, k_a, and k_s are not presented herein, those who are interested in their derivations can refer to Refs. [26,33]. In Refs. [26,33], k_t was only evaluated under constant speed conditions, and the relation between k_t and time was not described. To overcome these drawbacks, derivation of k_t as an implicit function of time is conducted herein, through which k_t can be evaluated considering tooth crack severity progression under time-varying operating conditions. k_t is a periodic function of the pinion angular displacement, which is shown in Eq. (3.14).

$$k_t = G\left(\Phi_{pin}\right) \tag{3.14}$$

where G denotes a periodic function; Φ_{pin} is the angular displacement of the pinion, which is calculated by Eq. (3.15).

$$\Phi_{pin} = 2\pi \int SPD(t)dt \tag{3.15}$$

where SPD is the rotational speed of the pinion.

Therefore, k_t can be expressed as an implicit function of time t, which is shown in Eq. (3.16).

$$k_t = G\left(\Phi_{pin}\right) = G(2\pi \int SPD(t)dt) = H(t) \tag{3.16}$$

From Eq. (3.16), it is seen that for either the variable load and constant speed condition, i.e., SPD is constant, or for the constant load and variable speed condition, i.e., SPD is time varying, k_t can be expressed as a function of time t. Besides, under the constant load and variable speed condition, the effect of speed variation on k_t is included in the function $k_t = H(t)$. Therefore, k_t includes information on both tooth crack severity progression and time-varying operating conditions.

3.2.2 Procedure for analyzing gearbox vibration signal

3.2.2.1 Overall implementation procedure

A new procedure displayed in Fig. 3.1 is proposed to study how time-varying operating conditions affect gearbox vibration signals. The procedure consists of several parts: (1) time-frequency analysis of gearbox vibration signals; (2) extraction of the CII; (3) envelope analysis of the CII. Descriptions of each part of the procedure are presented in the following subsections.

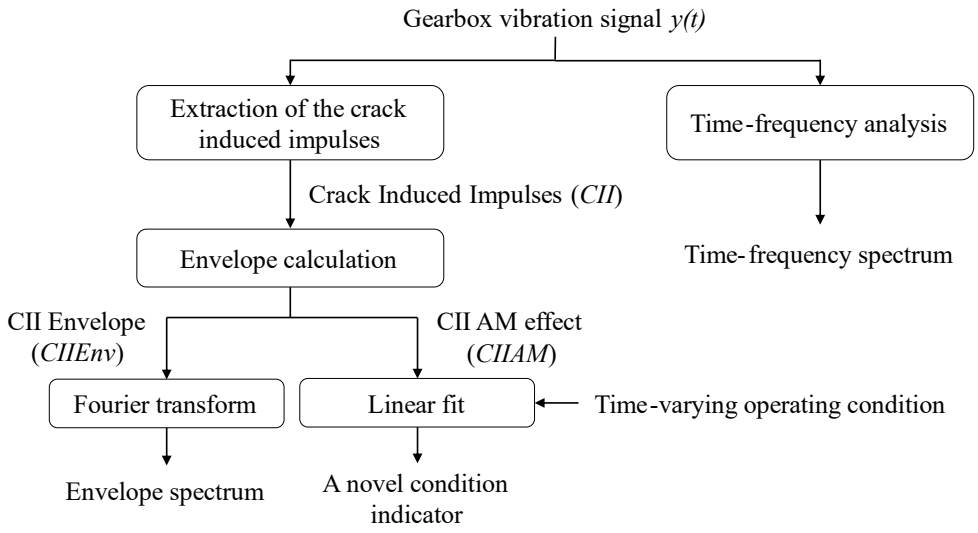

Fig. 3.1: The proposed procedure for analyzing gearbox vibration signals

3.2.2.2 Time-frequency analysis

To illustrate how time-varying operating conditions affect gearbox vibration signals, the time-frequency spectra of gearbox vibration signals are obtained using the Short Time Fourier Transform (STFT). The STFT is a Fourier transform-related operation that can be used to simultaneously represent the time, frequency, and amplitude properties of a signal. The STFT result of a continuous signal $y(t)$ is calculated using Eq. (3.17).

$$STFT(t,w) = \int_{-\infty}^{+\infty} y(t)w(t-\tau)e^{-jwt}dt \tag{3.17}$$

where $w(t)$ is a window function.

3.2.2.3 Extraction of the crack induced impulses

In this chapter, the focus of signal analysis is placed on the CII since the CII contain more tooth crack information than other signal components [77,104], so the CII are extracted from gearbox vibration signals and are further analyzed for tooth crack diagnosis. As mentioned in Subsection 1.2.2, for a spur gearbox with a tooth crack, its vibration signal consists of the gear meshing harmonics and the associated crack-related AM and FM, the CII, and the environmental noise. The gear meshing harmonics and the associated crack-related AM and FM have no direct relationship with the CII, so they need to be removed before extracting the CII, which can be achieved using comb notch filters. Afterwards, the CII are extracted from the comb notch filtered signal. To this end, it is necessary to get a good understanding of the spectral property of the CII under the two considered scenarios of time-varying operating conditions, i.e., the variable load and constant speed condition, and the constant load and variable speed condition.

For the variable load and constant speed condition, the CII result in a harmonic-cluster in the frequency spectrum. A harmonic-cluster is a group of frequencies with a uniform interval of the tooth crack characteristic frequency. The tooth crack characteristic frequency is the rotational frequency of the gear with a tooth crack. Zhou et al. [88] demonstrated the equivalence between the CII and the harmonic-cluster under constant speed conditions, which is shown in Eq. (3.18).

$$s(t) = \sum_{i=1}^{I} s_i(t) = \sum_{i=1}^{I} a_i \cos(2\pi f_i t + b_i) \tag{3.18}$$

where $s(t)$ denotes the CII; $s_i(t)$ is the i^{th} harmonic of the harmonic-cluster; a_i, f_i, and b_i are the amplitude, frequency, and initial phase of $s_i(t)$, respectively.

Based on the equivalence shown in Eq. (3.18), Zhou et al. [88] developed a method called the Adaptive Harmonic Decomposition (AHD) to extract all the CII-related harmonics, i.e., $s_i(t)$, and the CII was reconstructed by summing all the $s_i(t)$. However, how to extract the CII under constant load and variable speed conditions was not involved in Ref. [88].

For the constant load and variable speed condition, the CII cannot result in a harmonic-cluster in the frequency spectrum due to the FM effect caused by speed variation, so the AHD method is incapable of obtaining the CII in this case. However, if the CII is resampled in the angle domain to remove the FM effect, the resampled CII would result in an order-cluster in the order spectrum. An order-cluster is a group of orders with a uniform interval of the tooth crack characteristic order, and the tooth crack characteristic order is the rotational order of the gear with a tooth crack. There is an equivalence between the resampled CII and the order-cluster, which is shown in Eq. (3.19).

$$srem(\theta) = \sum_{k=1}^{K} s_k(\theta) = \sum_{k=1}^{K} A_k(\theta)\cos\big(R_k\theta + B_k(\theta)\big) \tag{3.19}$$

where $srem(\theta)$ is the resampled CII; R_k is the k^{th} order in the order-cluster; $s_k(\theta)$ corresponds to the R_k in the order spectrum; $A_k(\theta)$ and $B_k(\theta)$ are the amplitude and phase of $s_k(\theta)$, respectively.

Enlightened by the idea that the AHD method in Ref. [88] was used to extract $s_i(t)$ of the CII shown in Eq. (3.18) under constant speed conditions, a modified AHD method is developed in this chapter to extract $s_k(\theta)$ of the resampled CII shown in Eq. (3.19) under variable speed conditions. This strategy will also be used to obtain the CII from gearbox vibration signals generated using a phenomenological model of gearbox signals under variable speed conditions in Chapter 4. The modified AHD method focuses on the operations for the resampled CII in the angle domain. If an initial estimate of the k^{th} order is specified as $\widetilde{R_k}$, $s_k(\theta)$ in Eq. (3.19) is expressed as

$$s_k(\theta) = A_k(\theta)\cos\big(R_k\theta + B_k(\theta)\big) = u_k(\theta)\cos\big(\widetilde{R_k}\theta\big) + v_k(\theta)\sin\big(\widetilde{R_k}\theta\big) \tag{3.20}$$

where $u_k(\theta)$ and $v_k(\theta)$ are two demodulated signal components, which are shown in Eq. (3.21).

$$\begin{cases} u_k(\theta) = A_k(\theta)\cos\Big((R_k - \widetilde{R_k})\theta + B_k(\theta)\Big) \\ v_k(\theta) = -A_k(\theta)\sin\Big((R_k - \widetilde{R_k})\theta + B_k(\theta)\Big) \end{cases} \tag{3.21}$$

When $\widetilde{R_k} = R_k$, $u_k(\theta)$ and $v_k(\theta)$ are shifted to zero-order positions in the order spectrum. The amplitude and phase of $s_k(\theta)$ are calculated using Eq. (3.22), based on which $s_k(\theta)$ is reconstructed.

$$\begin{cases} A_k(\theta)|_{\widetilde{R_k}=R_k} = \sqrt{\left(u_k(\theta)\right)^2 + \left(v_k(\theta)\right)^2} \\ B_k(\theta)|_{\widetilde{R_k}=R_k} = \arctan\left[{-v_k(\theta)}\Big/{u_k(\theta)}\right] \end{cases} \tag{3.22}$$

To calculate $A_k(\theta)$ and $B_k(\theta)$, $u_k(\theta)$, $v_k(\theta)$, and $\widetilde{R_k}$ need to be obtained, which can be achieved by solving the optimization problem shown in Eq. (3.23).

$$\min_{\{u_k, v_k, \widetilde{R_k}\}} \left\{ \left\| \frac{d^2 u_k}{d\theta^2} \right\|_2^2 + \left\| \frac{d^2 v_k}{d\theta^2} \right\|_2^2 + \lambda \left\| \mathrm{z} - \left(u_k \cos\left(\widetilde{R_k}\theta\right) + v_k \sin\left(\widetilde{R_k}\theta\right) \right) \right\|_2^2 \right\} \tag{3.23}$$

where $\|\cdot\|_2$ is the L_2-norm, λ is the penalty coefficient, z is the comb notch filtered signal with gear meshing harmonics and the associated crack-related AM and FM removed in the angle domain.

To numerically solve the optimization problem shown in Eq. (3.23), it needs to be discretized into the form shown in in Eq. (3.24).

$$\hat{Q} = arg \min_{Q} \{ \|\boldsymbol{D u_k}\|_2^2 + \|\boldsymbol{D v_k}\|_2^2 + \lambda \|\mathbf{z} - (\boldsymbol{C_k u_k} + \boldsymbol{L_k v_k})\|_2^2 \} \tag{3.24}$$

where $Q = \left(u_k, v_k, \widetilde{R_k}\right)$ are the variables to be estimated; $\boldsymbol{D}$ is a matrix for the second-order difference operator, the square of the L_2-norm of $\boldsymbol{D}$ is used to quantify the smoothness of the demodulated components $u_k(\theta)$ and $v_k(\theta)$.

The variables sampled at different angle values $\{\theta_1, \theta_2, \dots, \theta_m, \dots, \theta_M\}$ are expressed as

$$\mathbf{z} = [\mathrm{z}(\theta_1), \mathrm{z}(\theta_2), \dots, \mathrm{z}(\theta_M)\,]^T \tag{3.25}$$

$$\begin{cases} \boldsymbol{u_k} = [u_k(\theta_1), u_k(\theta_2), \dots, u_k(\theta_M)\,]^T \\ \boldsymbol{v_k} = [v_k(\theta_1), v_k(\theta_2), \dots, v_k(\theta_M)\,]^T \end{cases} \tag{3.26}$$

$$\begin{cases} \boldsymbol{C_k} = \mathrm{diag}\left[cos\left(\widetilde{R_k}\theta_1\right), cos\left(\widetilde{R_k}\theta_2\right), \dots, cos\left(\widetilde{R_k}\theta_M\right)\right] \\ \boldsymbol{L_k} = \mathrm{diag}\left[sin\left(\widetilde{R_k}\theta_1\right), sin\left(\widetilde{R_k}\theta_2\right), \dots, sin\left(\widetilde{R_k}\theta_M\right)\right] \end{cases} \tag{3.27}$$

The algorithm used to solve the discretized form of the optimization problem in Eq. (3.24) is presented in Algorithm 1, in which η is the penalty parameter used to control the smoothness of order correction, q is the iteration count, and ε is the tolerance used to stop the iteration. When

implementing Algorithm 1, the value of the parameter ε is set to 1×10^{-8} for analyzing both simulated and experimental gearbox vibration signals, while the values of parameters λ and η are determined through trial and error. The optimization problem shown in Eq. (3.24) will be solved iteratively until the preset conditions are satisfied, and the order estimate $\widetilde{R_k}$ and the order component $s_k(\theta)$ will be obtained. Likewise, conducting Algorithm 1 on the residual signal $\mathbf{z} - s_k(\theta)$ recursively, all the other desired order components can also be obtained. Afterwards, the reconstruction of the CII in the angle domain is conducted by summing all the obtained order components, therefore realizing the goal of extracting the CII from gearbox vibration signals under constant load and variable speed conditions.

Algorithm 1. The modified AHD method

1: Input the comb notch filtered signal $\boldsymbol{z}$ obtained in the angle domain, set the values for the tolerance ε and the penalty parameters λ and η;

2: Initialize the values for the variables related to the order component $s_k(\theta)$

$q = 1, \quad \widetilde{R_k}^1, \quad \boldsymbol{C}_k^1 = \mathrm{diag}\left[cos\left(\widetilde{R_k}^1 \theta_m\right)\right], \quad \boldsymbol{L}_k^1 = \mathrm{diag}\left[sin\left(\widetilde{R_k}^1 \theta_m\right)\right],$

$\boldsymbol{u}_k^1 = \left[\frac{\boldsymbol{D}^T\boldsymbol{D}}{\lambda} + (\boldsymbol{C}_k^1)^T\boldsymbol{C}_k^1\right]^{-1}(\boldsymbol{C}_k^1)^T\mathbf{z}, \quad \boldsymbol{v}_k^1 = \left[\frac{\boldsymbol{D}^T\boldsymbol{D}}{\lambda} + (\boldsymbol{L}_k^1)^T\boldsymbol{L}_k^1\right]^{-1}(\boldsymbol{L}_k^1)^T\mathbf{z},$

$s_k(\theta)^1 = \boldsymbol{C}_k^1\boldsymbol{u}_k^1 + \boldsymbol{L}_k^1\boldsymbol{v}_k^1;$

3: **While** $\left\|s_k(\theta)^{q+1} - s_k(\theta)^q\right\|_2^2 \Big/ \left\|s_k(\theta)^q\right\|_2^2 > \varepsilon$, **do**

4: Iteration count $q = q + 1$;

5:
$$\begin{cases} \boldsymbol{u}_k^q = \left[\frac{\boldsymbol{D}^T\boldsymbol{D}}{\lambda} + \left(\boldsymbol{C}_k^{q-1}\right)^T\boldsymbol{C}_k^{q-1}\right]^{-1}\left(\boldsymbol{C}_k^{q-1}\right)^T\left(\mathbf{z} - \boldsymbol{L}_k^{q-1}\boldsymbol{v}_k^{q-1}\right) \\ \boldsymbol{v}_k^q = \left[\frac{\boldsymbol{D}^T\boldsymbol{D}}{\lambda} + \left(\boldsymbol{L}_k^{q-1}\right)^T\boldsymbol{L}_k^{q-1}\right]^{-1}\left(\boldsymbol{L}_k^{q-1}\right)^T\left(\mathbf{z} - \boldsymbol{C}_k^{q-1}\boldsymbol{u}_k^{q-1}\right) \\ \Delta\boldsymbol{R}_k^q = \left[\boldsymbol{v}_k^q\left(d\boldsymbol{u}_k^q \Big/ d\theta\right) - \boldsymbol{u}_k^q\left(d\boldsymbol{v}_k^q \Big/ d\theta\right)\right] \Big/ \left[\left(\boldsymbol{u}_k^q\right)^2 + \left(\boldsymbol{v}_k^q\right)^2\right] \end{cases};$$

6: $\widetilde{R_k}^q = \widetilde{R_k}^{q-1} + \left(\boldsymbol{I} + \boldsymbol{D}^T\boldsymbol{D}/\eta\right)^{-1}\Delta\boldsymbol{R}_k^q;$

7: $\boldsymbol{C}_k^q = \mathrm{diag}\left[cos\left(\widetilde{R_k}^q \theta_m\right)\right], \quad \boldsymbol{L}_k^q = \mathrm{diag}\left[sin\left(\widetilde{R_k}^q \theta_m\right)\right], \quad s_k(\theta)^q = \boldsymbol{C}_k^q\boldsymbol{u}_k^q + \boldsymbol{L}_k^q\boldsymbol{v}_k^q;$

8: **End while**;

9: Output the the k^{th} order component $s_k(\theta)$=$s_k(\theta)^q$ and its order $R_k = \widetilde{R_k}^q$, and the resulting residual signal $\boldsymbol{z} - s_k(\theta)$.

3.2.2.4 Envelope analysis of the crack induced impulses

For the envelope analysis of the CII, two kinds of envelopes of the CII are calculated, i.e., the upper envelope of the CII and the peak envelope of the CII. The upper envelope of the CII is called the CII Envelope (*CIIEnv*), while the peak envelope of the CII is the AM effect of the CII (*CIIAM*) since it is induced by time-varying operating conditions. For the CII obtained under variable load and constant speed conditions, which is denoted as $s(t)$ shown in Eq. (3.18), its Hilbert Transform is expressed in Eq. (3.28).

$$\mathrm{HT}(s(t)) = \sum_{i=1}^{I} a_i \sin(2\pi f_i t + b_i) \tag{3.28}$$

Therefore, the corresponding analytical signal of $s(t)$ is expressed as [47]

$$d(t) = s(t) + j\mathrm{HT}(s(t)) = A_d(t)\exp(j\Psi(t)) \tag{3.29}$$

where $A_d(t)$ is the upper envelope of the CII, which is calculated using Eq. (3.30).

$$A_d(t) = \sqrt{\left(s(t)\right)^2 + (\mathrm{HT}(s(t)))^2} \tag{3.30}$$

Therefore, $A_d(t)$ is the CII Envelope, i.e., *CIIEnv*, under variable load and constant speed conditions. Based on $A_d(t)$, the local maxima of the *CIIEnv* can be identified. Afterwards, by joining all the identified local maxima of the *CIIEnv* using the cubic spline interpolation, the peak envelope of the CII is obtained. The obtained peak envelope is further smoothed via the moving median filtering, and the smoothed peak envelope is regarded as the AM of the CII, i.e., *CIIAM*.

For the constant load and variable speed conditions, by implementing the above operations to the resampled CII obtained in the angle domain, the corresponding *CIIEnv* and *CIIAM* can also be obtained. Besides, the relationship between the *CIIAM* and the time-varying operating condition is further studied in the next subsection.

3.2.3 Development of a new condition indicator

As reviewed in Section 3.1, in Refs. [21,24,125,127,128], only some conventional CIs were adopted for tooth crack diagnosis, failing to propose novel CIs to track tooth crack severity progression under time-varying operating conditions. This is attributed to the fact that the relations among tooth crack severity progression, time-varying operating conditions, and the operating condition variation-induced AM on the gearbox vibration signal were not identified. Some

researchers have tried to study how time-varying operating conditions affect vibration signals of gearboxes with tooth cracks, but not explicitly. Bartelmus et al. [129] studied the relation between the envelope of the first gear meshing harmonic component and the variable load, and found that the envelope was proportional to the load variation. Besides, they observed that gearboxes in good condition and bad condition had different load susceptibilities, based on which fault detection was achieved. However, no explicit representation of the relation between the load susceptibility and gearbox health condition was presented, and no new CIs were proposed. Later, Bartelmus et al. extended the idea of load susceptibility in Ref. [129] and discovered a linear dependence between a diagnostic feature, i.e. the sum of amplitudes of 10 meshing components, and the operation condition variations [130]. The slope of the linear dependence was used as a new CI to detect gearbox fault, but its effectiveness for tracking tooth crack growth was not demonstrated.

In this section, a novel CI is proposed using the *CIIAM* obtained in Subsection 3.2.2, which contains information on tooth crack severity progression. Inspired by the studies reported in Refs. [129,130], we propose a hypothesis that there is a linear dependence of *CIIAM* on the time-varying operating condition, which is mathematically expressed as

$$Y = A \cdot X + B \tag{3.31}$$

where Y denotes the *CIIAM*; X represents the time-varying operating condition, which refers to either a variable load or a variable speed; A and B are the model parameters.

Because the linear model shown in Eq. (3.31) represents the linear relation between the *CIIAM* and the time-varying operating condition, and the *CIIAM* includes the information on tooth crack severity progression, it is expected that the model parameter A (slope of the linear relation) is sensitive to tooth crack severity progression while insensitive to operating condition variations. Therefore, the model parameter A is proposed as a novel CI to track tooth crack severity progression under time-varying operating conditions, and it is named Ratio of *CIIAM* to Operating Condition Variation (RCOCV). The correctness of the hypothesis shown in Eq. (3.31) and the effectiveness of RCOCV in terms of tracking tooth crack severity progression under time-varying operating conditions will be first verified using simulated gearbox vibration signals in Section 3.3 and be further validated using experimental gearbox vibration datasets in Section 3.4.

3.2.4 Performance comparison metrics

Performance comparisons are made between the RCOCV and the RMS of the CII in terms of tracking tooth crack severity progression under time-varying operating conditions. The reason why the RMS is selected for performance comparison is that it has shown its effectiveness for tooth crack diagnosis under both constant and time-varying operating conditions [24,33]. To make quantitative performance comparisons, two aspects are measured. The first aspect is the sensitivity of a CI to tooth crack severity progression and the second one is the insensitivity of a CI to operating condition variations. The sensitivity of a CI to tooth crack severity progression is measured with the AIR, which has been introduced in Subsection 2.3.2 and can be calculated using Eq. (2.36). The bigger the AIR value is, the more sensitive a CI is to tooth crack severity progression. The insensitivity of a CI to operating condition variations is measured by the Frechet Distance (FD) [131,132], which is calculated using Eq. (3.32).

$$\mathrm{FD}(P,Q) = min\{max(d(P,Q))\} \tag{3.32}$$

where P is the CI curve obtained under an operating condition, Q is the CI curve obtained under another operating condition, $d(P,Q)$ is the distance operator.

FD is a metric to measure the similarity between two curves. When two curves are the same, FD is 0. When the dissimilarity between two curves becomes larger, FD value gets bigger. If a CI is completely insensitive to operating condition variations, the curves of this CI with regard to crack severity level under different operating conditions should be the same, and the FD values are 0. On the contrary, if a CI is sensitive to operating condition variations, the resulting FD are not 0. The smaller value the FD is, the more insensitive a CI is to operating condition variations. To sum up, if a CI is sensitive to tooth crack severity progression while insensitive to time-varying operating conditions, it will result in a high AIR value and a small FD value.

3.3 Simulation analysis

3.3.1 Generation of simulated gearbox vibration signals

To simplify dynamic simulation, some assumptions are made [26]: (1) the bearing radial stiffnesses k_{x1}, k_{x2}, k_{y1}, and k_{y2} are equal to a constant k_r; (2) the bearing radial damping

coefficients c_{x1}, c_{x2}, c_{y1}, and c_{y2} are equal to a constant c_r; (3) the coupling torsional stiffnesses k_p and k_g are equal to a constant k_c; (4) the coupling damping coefficients c_p and c_g are equal to a constant c_c. Main parameters of the one-stage fixed-axis spur gearbox system are tabulated in Table 3.1. The gear tooth mesh stiffness is calculated using the potential energy method described in Section 3.2.1.2. Afterwards, the gear tooth mesh stiffness and time-varying operating conditions are substituted into the gearbox system motion equation shown in Eq. (3.1), and gearbox vibration responses are calculated using the Newmark integration algorithm. Because one tooth crack is seeded on the pinion, the y-direction acceleration signal of the pinion is used as the simulated gearbox vibration signal. To mimic the environmental noise, a white Gaussian noise with SNR of 10 dB is added into simulated gearbox vibration signals.

Table 3.1: Main parameters of the gearbox transmission system [26]

Parameter	value
Gear type	standard involute spur gear
Modulus of elasticity	$E = 2.068 \times 10^{11}$ Pa
Poisson's ratio	$\upsilon = 0.3$
Number of teeth	pinion $N_p = 19$; gear $N_g = 48$
Pressure angle	$\alpha_0 = 20^{\circ}$
Diametral pitch	$P = 8\ inch^{-1}$
Base radius of the pinion	$R_{b1} = 0.02834\ m$
Base radius of the gear	$R_{b2} = 0.07160\ m$
Width of teeth	$L = 0.016\ m$
Mass of the pinion	$m_1 = 0.96\ kg$
Mass of the gear	$m_2 = 2.88\ kg$
Mass moment of inertia of the pinion	$I_1 = 4.3659 \times 10^{-4}\ kgm^2$
Mass moment of inertia of the gear	$I_2 = 8.3602 \times 10^{-4}\ kgm^2$
Mass moment of inertia of the drive motor	$I_m = 0.0021\ kgm^2$
Mass moment of inertia of the load machine	$I_b = 0.0105\ kgm^2$
Torsional stiffness of the coupling	$k_c = 4.4 \times 10^4\ Nm/rad$
Radial stiffness of the bearing	$k_r = 6.56 \times 10^7\ N/m$
Damping coefficient of the coupling	$c_c = 5.0 \times 10^5\ Nms/rad$
Damping coefficient of the bearing	$c_r = 1.8 \times 10^5\ Ns/m$
Scale constant	$\mu = 3.99 \times 10^{-6} s$

3.3.2 Simulated signal analysis for the variable load and constant speed condition

For the variable load and constant speed condition, four variable loads (torque M_2) are exerted on the load machine of the gearbox transmission system shown in Fig. 2.2, which are the sinusoidal (sin), run-up (run), coast-down (coa), and harmonic (har) load profiles. The formulae of the four

load profiles are shown in Eq. (3.33) and the profiles are plotted in Fig. 3.2. The driving motor speed is set to $SPD = 30$ Hz, which is equal to the pinion rotational speed.

$$\begin{cases} \text{sin: } M_2 = 30 + 24\,sin(2\pi \cdot 8 \cdot t) \\ \text{run: } M_2 = 10 + 70t \\ \text{coa: } M_2 = 60 - 100t \\ \text{har: } M_2 = 30 + 12\,sin(2\pi \cdot 8 \cdot t) + 12\,sin(2\pi \cdot 4 \cdot t) \end{cases} \tag{3.33}$$

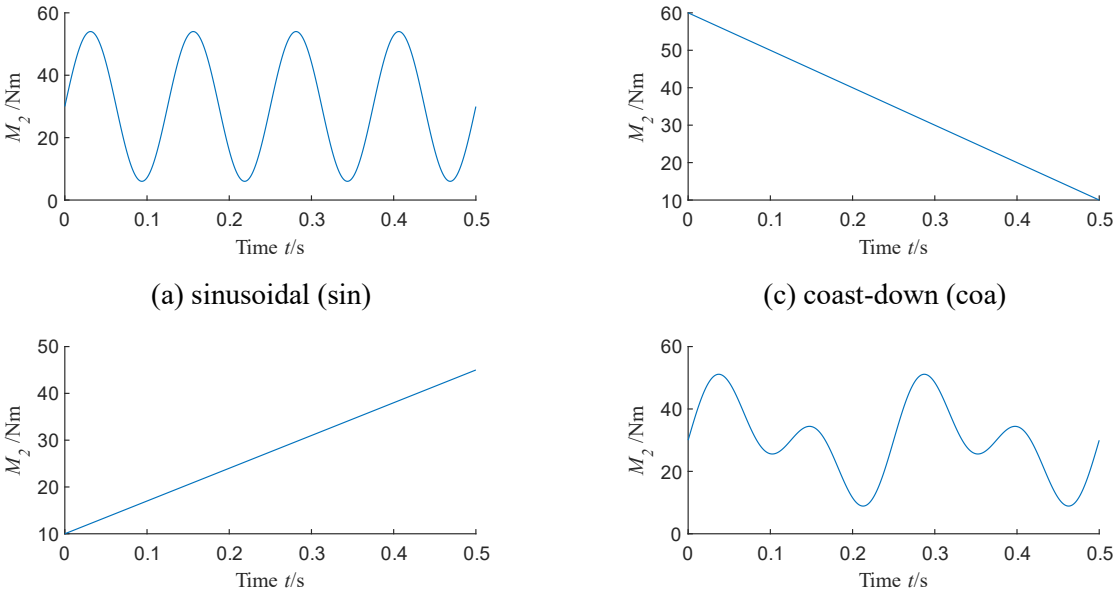

(a) sinusoidal (sin)

(c) coast-down (coa)

(b) run-up (run)

(d) harmonic (har)

Fig. 3.2: Four profiles for the load machine torque M_2

The dynamic simulation results for the case that the pinion tooth crack depth is 6 mm under the sinusoidal load profile and constant speed condition are used for illustration. The gear tooth mesh stiffness is shown in Fig. 3.3. It is seen that the frequency spectrum is dominated by the pinion rotational speed (30 Hz) and its multiples and gear mesh harmonics (570 Hz and its multiples). No frequency smearing phenomenon is observed, and no sidebands are found around either pinion rotational speed and its multiples or gear mesh harmonics. Therefore, it is concluded that variable load and constant speed conditions do not induce any AM or FM into the gear tooth mesh stiffness. The simulated gearbox vibration signal is shown in Fig. 3.4. From Fig. 3.4(a), it is seen that there is an AM in the signal. The frequency spectrum is dominated by the gear mesh harmonics, and no frequency smearing phenomenon is observed, which indicates that there is no FM effect in the signal. There are several clusters of harmonics located in the frequency range [2280, 4560] Hz,

which are caused by the CII. By checking the zoomed-in view of the frequency spectrum shown in Fig. 3.4(b), it is found that there are sidebands around the harmonics, and the interval between a harmonic and its nearest sideband is 8 Hz. For example, for the harmonic 3420 Hz, there are two nearest sidebands around it, i.e., 3412 Hz and 3428 Hz, and both intervals are 8 Hz (3420-3412=8 Hz, 3428-3420=8 Hz). 8 Hz is equal to the frequency of the sinusoidal load profile shown in Eq. (3.33), which means that the sidebands around the harmonics are induced by the AM effect resulting from the variable load. Therefore, the variable load and constant speed condition only induces an AM into the simulated gearbox vibration signal. The reason why a variable load induces an AM effect is due to the load dependence of the tooth deflection effect and gearbox vibration amplitude is sensitive to the tooth loading, when the torque load varies, amplitude of gearbox vibration will vary in sympathy, thus resulting in an AM of gearbox vibration signals [78,81].

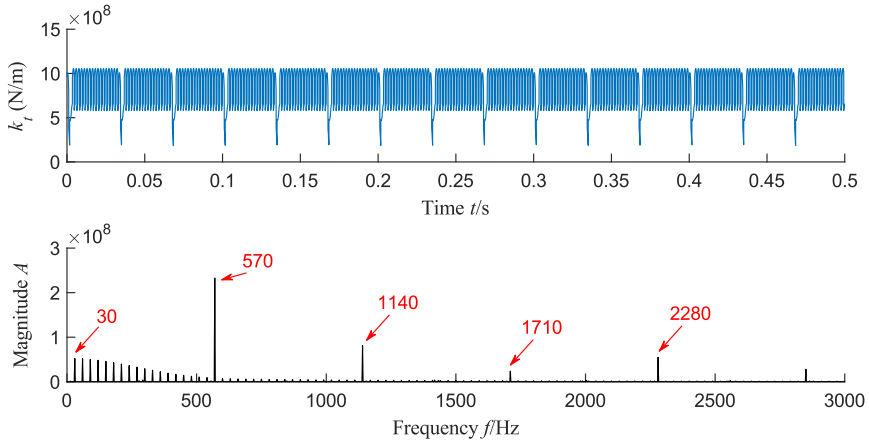

Fig. 3.3: The gear tooth mesh stiffness (crack depth 6mm, sinusoidal load profile and *SPD*=30Hz)

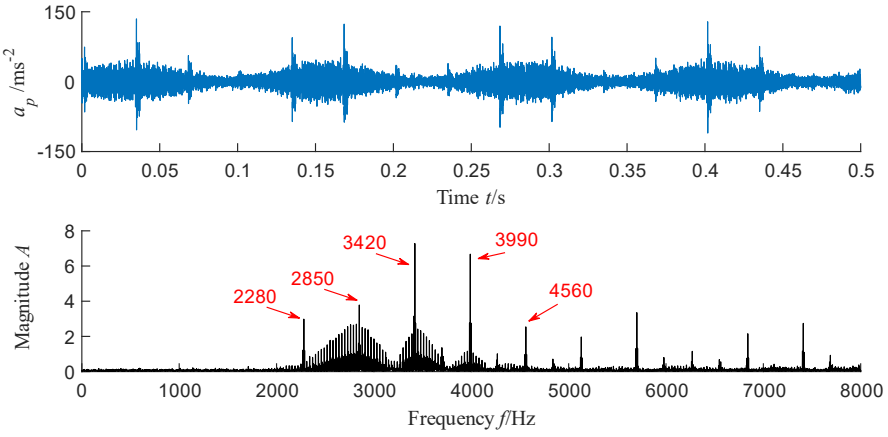

(a) Time waveform and frequency spectrum of the simulated signal

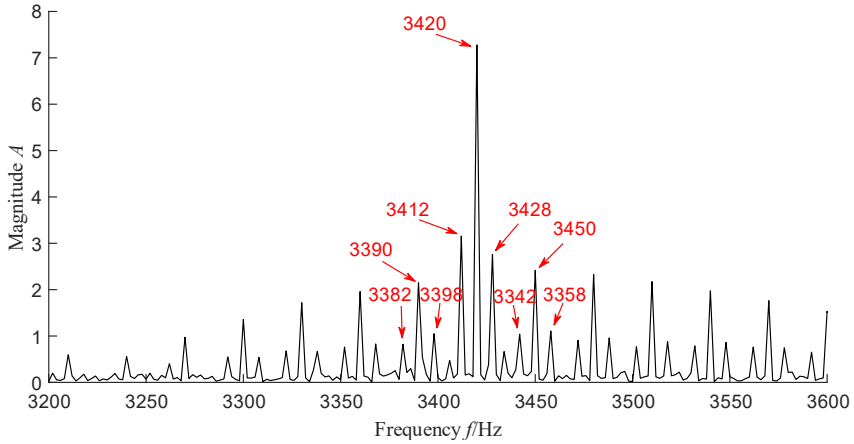

(b) Zoomed-in view of the frequency spectrum of the simulated signal in [3200, 3600] Hz

Fig. 3.4: The simulated signal (crack depth 6mm, sinusoidal load profile and *SPD*=30Hz)

The gear meshing components are first removed from gearbox vibration signal using a comb notch filter, and the AHD method is conducted on the comb notch filtered signal with the parameters λ, η, and ε being set to 10^{-10}, 10^{-11}, and 10^{-8}, respectively, to extract the CII. The obtained CII is shown in Fig. 3.5, from which it is seen there is no FM and the CII amplitude is modulated. The upper envelope of the CII, i.e., *CIIEnv*, is shown in Fig. 3.6. Frequency spectrum of *CIIEnv* is dominated by pinion shaft rotational speed (30 Hz) and its multiples, which are the characteristic frequencies for the pinion tooth crack. There is a spectral line at 8 Hz, which is the same as the frequency of the applied sinusoidal load. There are symmetric sidebands around 30 Hz and its multiples with an interval of 8 Hz, such as 30-22=8 Hz and 38-30=8 Hz. These observations indicate that the AM of the CII is induced by the sinusoidal load M_2 shown in Fig. 3.2(a).

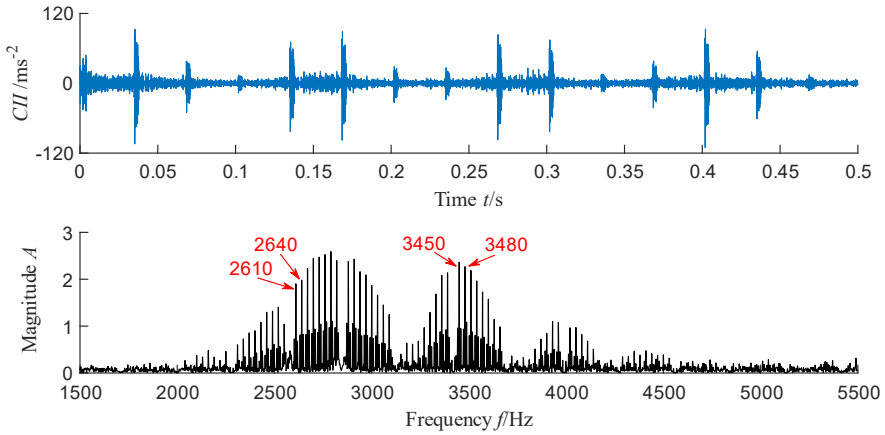

Fig. 3.5: The CII and its frequency spectrum (crack depth 6mm, sinusoidal load profile and *SPD*=30Hz)

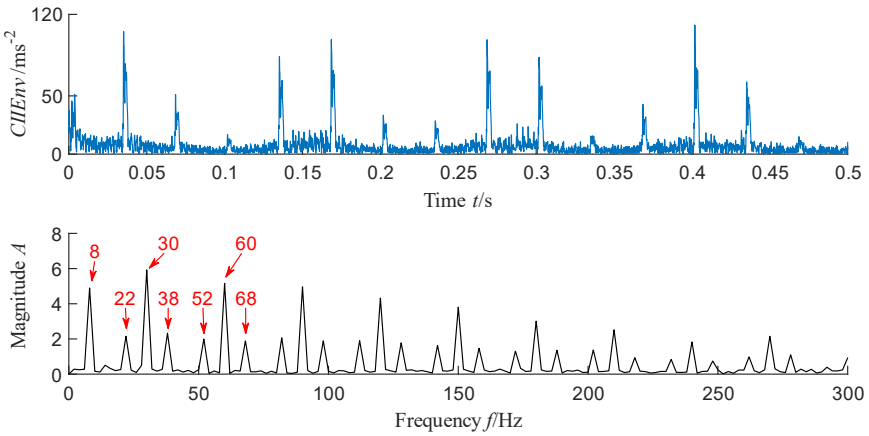

Fig. 3.6: *CIIEnv* and its frequency spectrum (crack depth 6mm, sinusoidal load profile and *SPD*=30Hz)

The *CIIAM* is obtained and is shown in Fig. 3.7 alongside the CII and the sinusoidal load M_2. As shown in Fig. 3.7(a), the *CIIAM* has a sinusoidal variation pattern. Comparing Fig. 3.7(b) to Fig. 3.7(c), it is found that the frequency of the *CIIAM* is 8 Hz, which is equal to that of the load M_2. This means that there exists a linear dependence of the *CIIAM* on M_2, which verifies the correctness of the hypothesis shown in Eq. (3.31). This observation reveals that the variable load induces an AM effect on the CII and the AM effect is linearly dependent on the variable load. The linear model shown in Eq. (3.31) is used to fit the linear relation between the *CIIAM* and the load M_2, and the fitting result is shown in Fig. 3.8. It is seen that the relation between the *CIIAM* and M_2 is well fitted and the fitting result is $CIIAM = 1.651M_2 + 3.028$ (with 95% confidence bounds). The coefficient of determination is $R^2 = 0.9944$, which indicates a high goodness of the linear fit. In this case, the proposed condition indicator RCOCV is equal to 1.651.

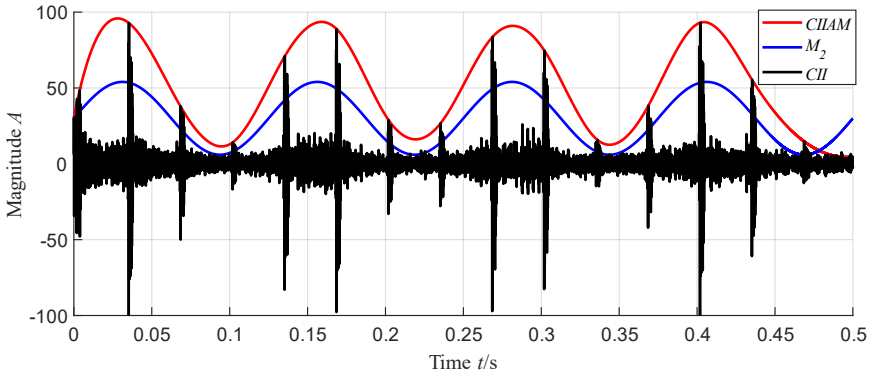

(a) Waveforms of the *CIIAM*, sinusoidal load M_2, and the *CII*

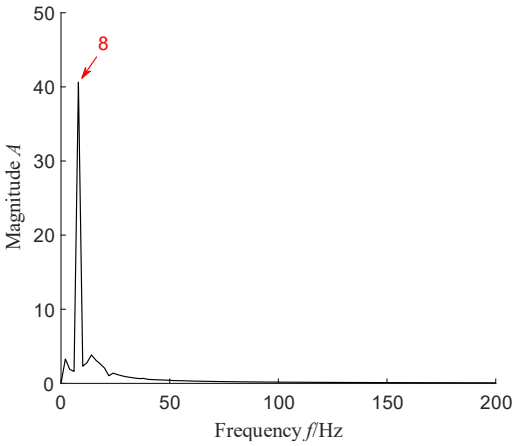

(b) Frequency spectrum of *CIIAM*

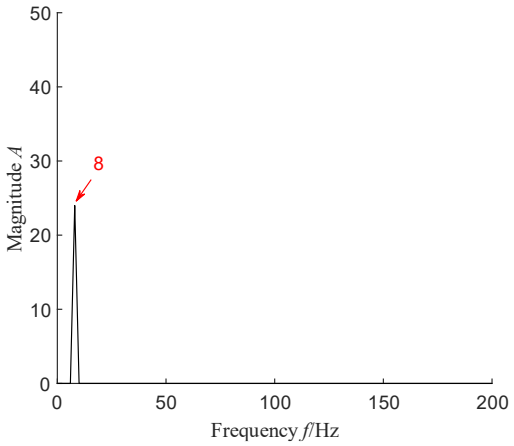

(c) Frequency spectrum of sinusoidal load M_2

Fig. 3.7: The *CIIAM*, M_2, and *CII* (crack depth 6mm, sinusoidal load profile and *SPD*=30Hz)

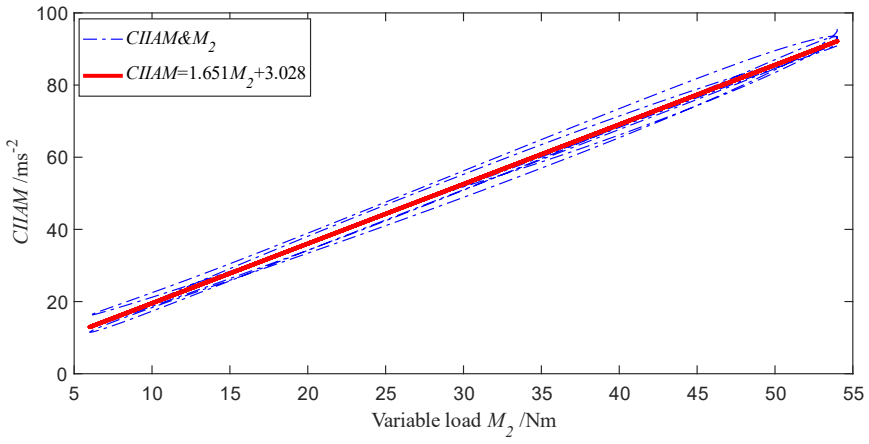

Fig. 3.8: The linear fitting result for the *CIIAM* and the sinusoidal load M_2

After analyzing the simulated signals for all the tooth crack depths under the four variable load and constant speed conditions, RCOCV results are obtained. The results of RCOCV versus tooth crack depth are shown in Fig. 3.9. For comparison, the results of RMS of the CII versus tooth crack depth are shown in Fig. 3.10. In these two figures, the subscript "sin" means that the CI results are for the sinusoidal load profile, "run" the run-up profile, "coa" the coast-down profile, and "har" the harmonic profile. From Fig. 3.9, it is seen that the RCOCV is not only sensitive to tooth crack severity progression, but also insensitive to load variation. On the contrary, as shown in Fig. 3.10, the RMS of the CII is very sensitive to load changes due to the big spreads among the four curves.

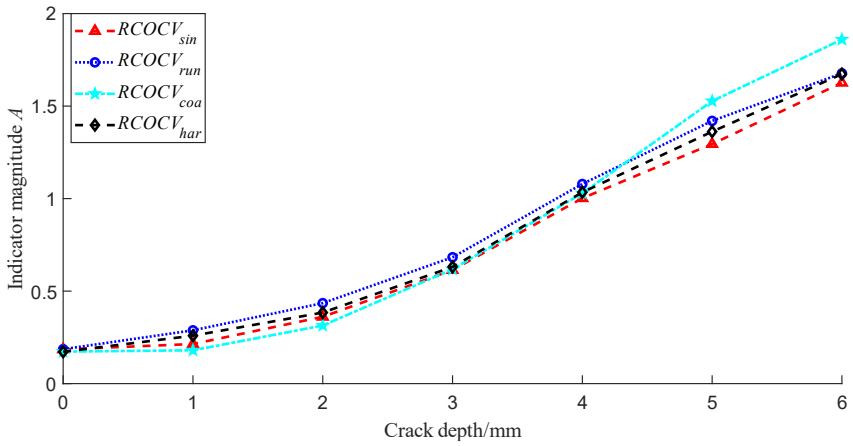

Fig. 3.9: RCOCV versus tooth crack depth (variable load and constant speed condition)

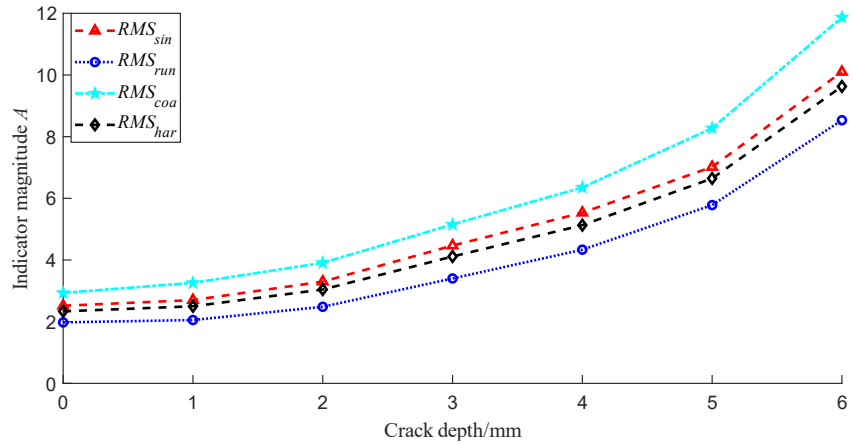

Fig. 3.10: RMS of the CII versus tooth crack depth (variable load and constant speed condition)

To make quantitative performance comparison between RCOCV and RMS of the CII in terms of tracking tooth crack severity progression, the AIR and FD metrics in Section 3.2.4 are calculated. The AIR and FD results for the RCOCV are shown in Table 3.2 and Table 3.3, respectively, and those for the RMS of the CII are shown in Table 3.4 and Table 3.5, respectively. In Tables 3.2 and 3.4: the suffix "_sin" denotes the sinusoidal load profile, "_run" run-up, "_coa" coast-down, and "_har" harmonic. In Tables 3.3 and 3.5: the suffix "_sr" denotes the FD between the CI curve for the sinusoidal load profile and that for the run-up profile, "_sc" sinusoidal and coast-down, "_sh" sinusoidal and harmonic, "_rc" run-up and coast-down, "_rh" run-up and harmonic, "_ch" coast-down and harmonic.

Table 3.2: AIR results for the RCOCV (variable load and constant speed condition)

RCOCV	Average Increase Rate (AIR %)
RCOCV_sin	129.82
RCOCV_run	133.60
RCOCV_coa	162.52
RCOCV_har	145.45
Average:	142.85

Table 3.3: FD results for the RCOCV (variable load and constant speed condition)

RCOCV	Frechet Distance (FD)
RCOCV_sr	0.1997
RCOCV_sc	0.3359
RCOCV_sh	0.1036
RCOCV_rc	0.2795
RCOCV_rh	0.1084
RCOCV_ch	0.2712
Average:	0.2164

Table 3.4: AIR results for the RMS of the CII (variable load and constant speed condition)

RMS	Average Increase Rate (AIR %)
RMS_sin	50.24
RMS_run	55.27
RMS_coa	50.78
RMS_har	52.06
Average:	52.09

Table 3.5: FD results for the RMS of the CII (variable load and constant speed condition)

RMS	Frechet Distance (FD)
RMS_sr	2.8179
RMS_sc	2.5911
RMS_sh	0.8894
RMS_rc	5.3771
RMS_rh	1.9301
RMS_ch	3.4574
Average:	2.8438

By comparing the AIR and FD results shown in Tables 3.2 through 3.5, two results are obtained: (1) Higher sensitivity of the RCOCV to tooth crack severity progression. Comparing Table 3.2 and Table 3.4, it is seen that the RCOCV has a higher average AIR value than the RMS (142.85%>52.09%), which indicates that the RCOCV is more sensitive to tooth crack severity

progression than the RMS; (2) Higher insensitivity of the RCOCV to load variation. Comparing Table 3.3 and Table 3.5, it is seen that the RCOCV has a much smaller average FD value than the RMS (0.2164<2.8438), which means that the RCOCV is much more insensitive to load variations than the RMS. Therefore, it is concluded that the RCOCV is not only sensitive to tooth crack severity progression but also insensitive to load variations, which demonstrates its effectiveness of tracking tooth crack severity progression under variable load and constant speed conditions.

3.3.3 Simulated signal analysis for the constant load and variable speed condition

For the constant load and variable speed condition, four variable speeds of the driving motor are considered, including the sinusoidal (sin), run-up (run), coast-down (coa), and harmonic (har) speed profiles. Their formulae are shown in Eq. (3.34) and they are plotted in Fig. 3.11. The pinion rotational speed is equal to the driving motor speed. The load machine torque is set to $M_2 = 48$ Nm.

$$\begin{cases} \text{sin: } SPD = 20 + 15\,sin(2\pi \cdot 5 \cdot t) \\ \text{run: } SPD = 10 + 80t \\ \text{coa: } SPD = 85 - 65t \\ \text{har: } SPD = 20 + 3\,sin(2\pi \cdot 10 \cdot t) + 12\,sin(2\pi \cdot 5 \cdot t) \end{cases} \tag{3.34}$$

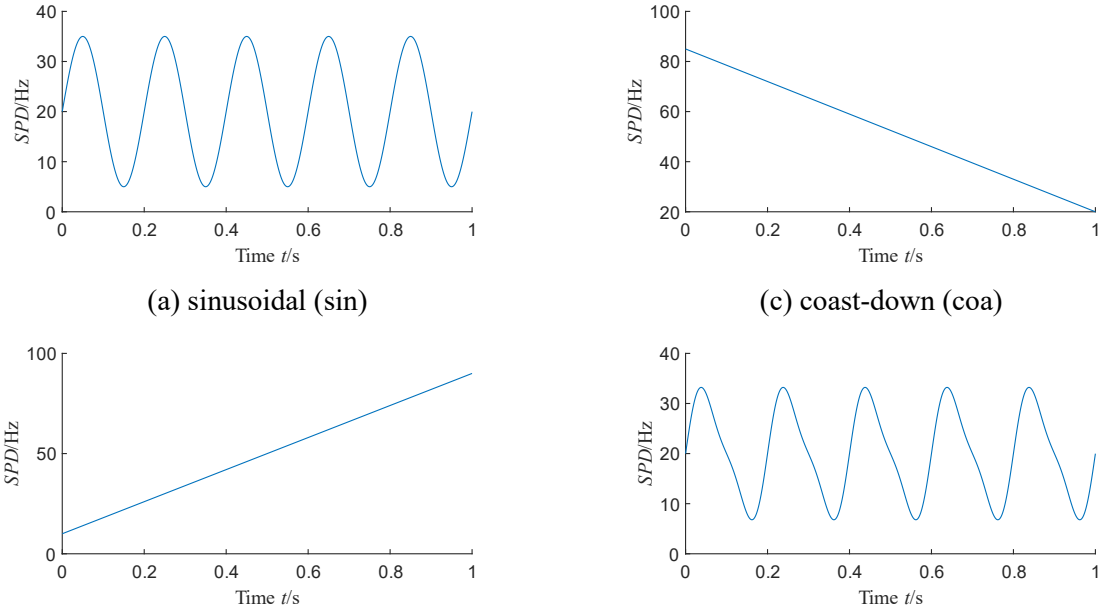

(a) sinusoidal (sin)

(c) coast-down (coa)

(b) run-up (run)

(d) harmonic (har)

Fig. 3.11: Four profiles for the driving motor speed SPD

The dynamic simulation results for the case that the pinion tooth crack depth is 6 mm under the constant load and sinusoidal speed profile are used for illustration. Gear tooth mesh stiffness is shown in Fig. 3.12. It is seen that there exists frequency smearing in the frequency spectrum, indicating that the variable speed induces an FM effect in the mesh stiffness. The spectrogram of the mesh stiffness is shown in Fig. 3.13, from which it is seen that there are sinusoidal frequency ridges. The resampled mesh stiffness is shown in Fig. 3.14. It is seen that the order spectrum is dominated by the pinion rotational order (1) and its multiples and gear mesh orders (19 and its multiples). Therefore, it is concluded that the constant load and variable speed condition only induces an FM effect into the gear tooth mesh stiffness.

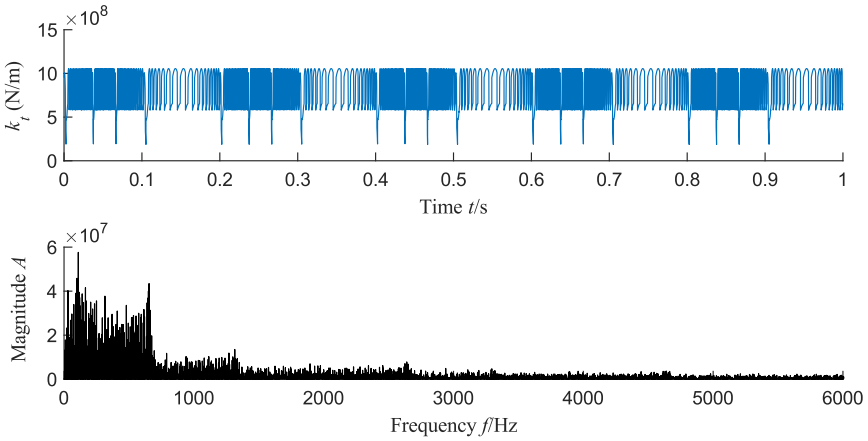

Fig. 3.12: The gear tooth mesh stiffness (crack depth 6mm, $M_2 = 48$Nm and sinusoidal speed profile)

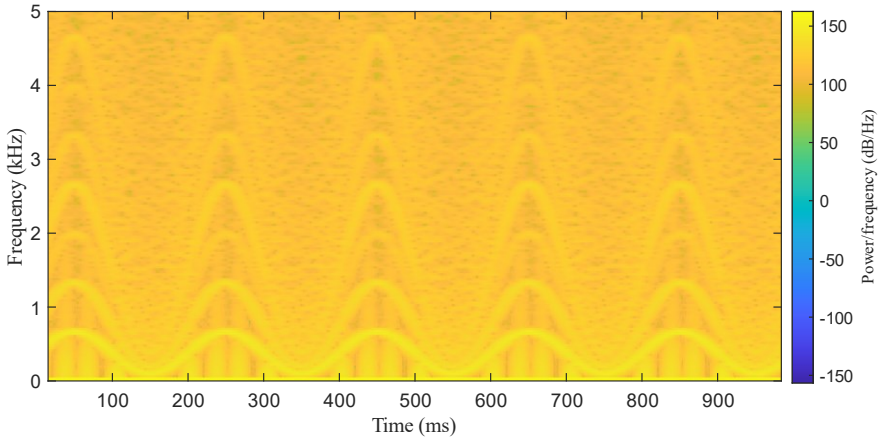

Fig. 3.13: Spectrogram of mesh stiffness (crack depth 6mm, $M_2 = 48$Nm and sinusoidal speed profile)

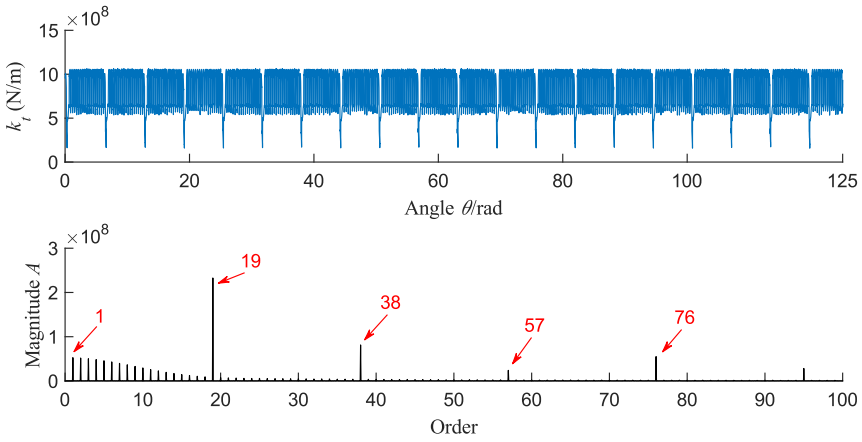

Fig. 3.14: The resampled mesh stiffness (crack depth 6mm, $M_2 = 48$Nm and sinusoidal speed profile)

The simulated gearbox vibration signal is shown in Fig. 3.15, and it is seen that the signal amplitude is modulated and there exists an FM in the signal. As shown in Fig. 3.16, there are sinusoidal ridges in the spectrogram. The resampled signal is shown in Fig. 3.17. From Fig. 3.17(a), it is seen that there are gear mesh orders (19 and its multiples) and several clusters of orders located in the order range [57, 171]. By checking the zoomed-in view of the order spectrum shown in Fig. 3.17(b), it is seen that there are sidebands around the orders and the interval between an order and its nearest sideband is 0.25 order. For example, there are two nearest sidebands around the order 95, i.e., 94.75 and 95.25, and both intervals are 0.25 (95-94.75=0.25, 95.25-95=0.25). The interval 0.25 is equal to the ratio of the frequency of the sinusoidal speed profile shown in Eq. (3.34) to the mean value of the sinusoidal speed, i.e., 5/20=0.25, indicating that the sidebands are resulting from the speed variation-induced AM. Therefore, the constant load and variable speed condition induces both AM and FM into the simulated gearbox vibration signal. Under CLVS conditions, the reasons why a variable speed induces AM and FM effects into gearbox vibration signals include: (a) when the gearbox rotational speed varies over a reasonable range, the frequency components may pass through resonances, or experience variation in the transfer function [107]. Therefore, not only do the response signals vary in the frequency (FM), but also vary in amplitude (AM); (b) a variable speed causes variations of gearbox system power intake, which induces an AM into gearbox vibration signals as well [102].

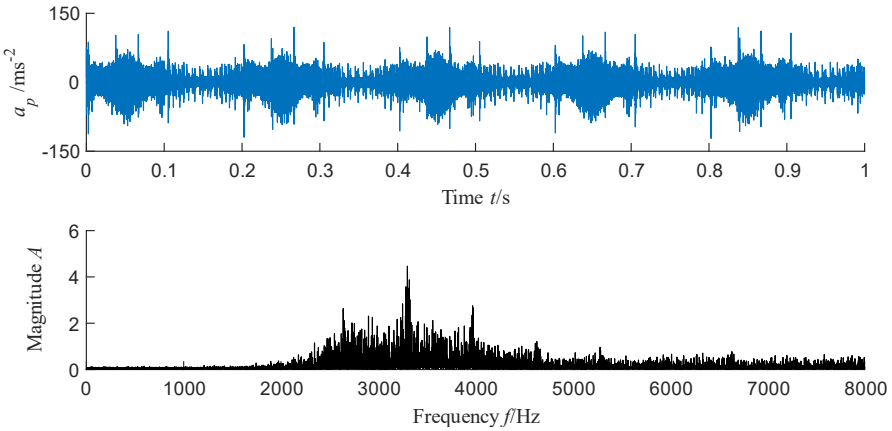

Fig. 3.15: The simulated signal (crack depth 6mm, $M_2 = 48$Nm and sinusoidal speed profile)

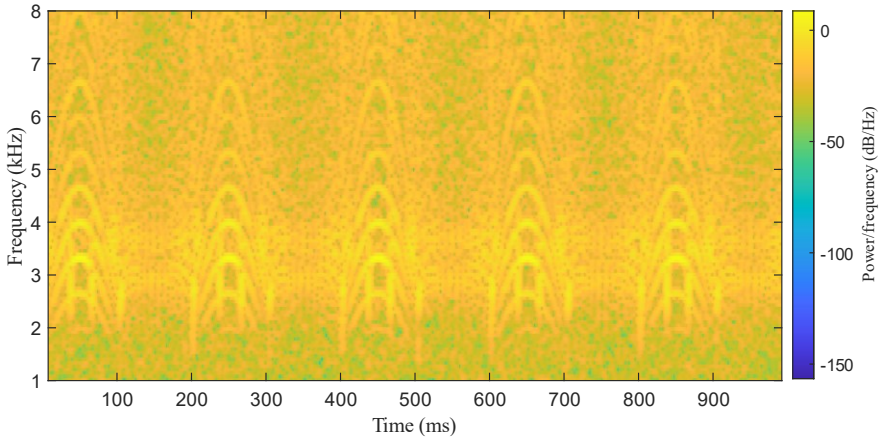

Fig. 3.16: Spectrogram of simulated signal (crack depth 6mm, $M_2 = 48$Nm and sinusoidal speed profile)

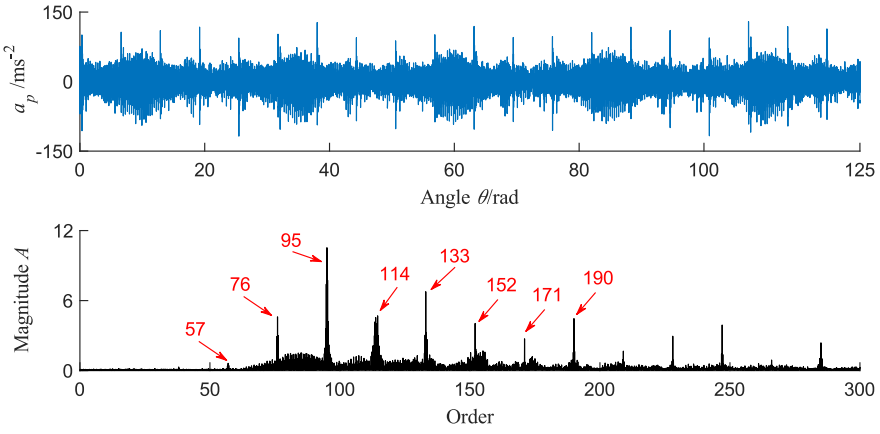

(a) Angle domain waveform and order spectrum of the resampled simulated signal

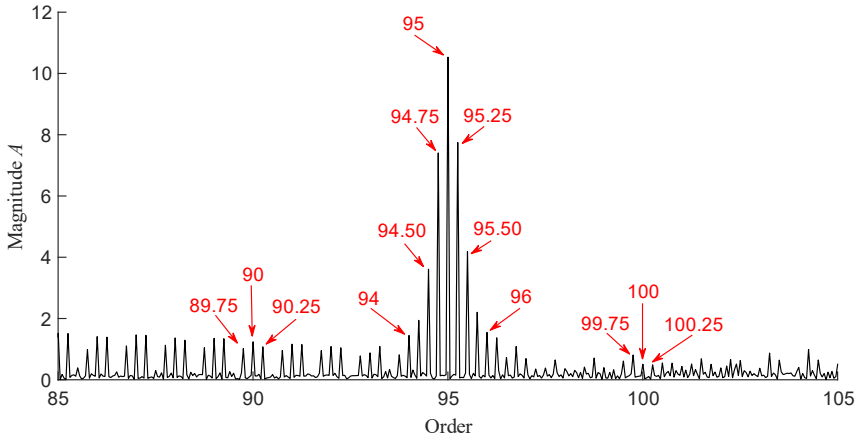

(b) The zoomed-in view of the order spectrum of the resampled simulated signal

Fig. 3.17: The resampled simulated signal (crack depth 6mm, $M_2 = 48$Nm and sinusoidal speed profile)

The gear meshing orders are removed from the resampled signal shown in Fig. 3.17(a) with a comb notch filter. Afterwards, the modified AHD method shown in Algorithm 1 is conducted on the comb notch filtered signal with the parameters λ, η, and ε being set to 10^{-10}, 10^{-11}, and 10^{-8}, respectively, to extract the CII. The obtained CII is shown in Fig. 3.18, from which it is seen that the CII amplitude is modulated. The *CIIEnv* is calculated and is shown in Fig. 3.19 together with its order spectrum. As shown in Fig. 3.19, the order spectrum of *CIIEnv* is dominated by the pinion rotational order (1) and its multiples, which are the crack characteristic orders. There is a spectral line at 0.25 order, which is the order of the sinusoidal speed. There are sidebands around the tooth crack characteristic orders with an interval of 0.25 order, such as 1-0.75=0.25 and 1.25-1=0.25. These observations indicate that the AM effect of the CII is induced by the sinusoidal speed SPD shown in Fig. 3.11(a).

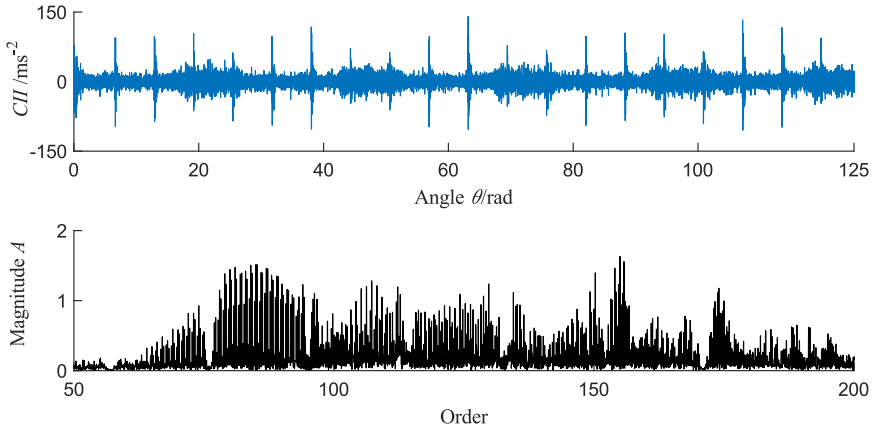

Fig. 3.18: CII and its order spectrum (crack depth 6mm, $M_2 = 48$Nm and sinusoidal speed profile)

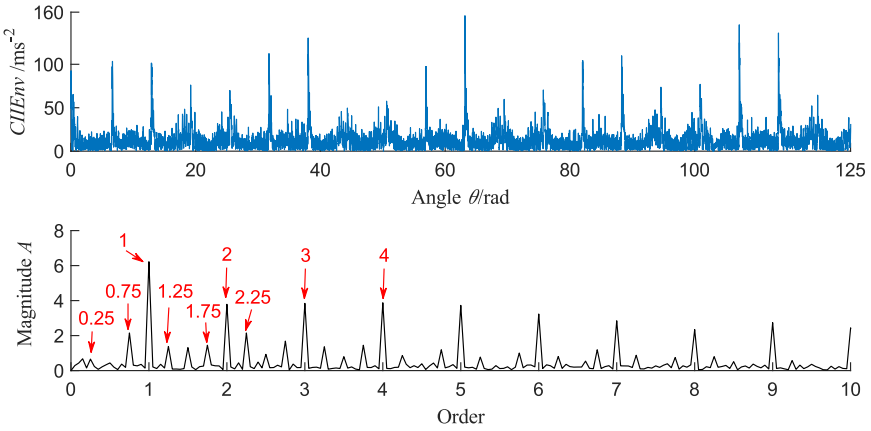

Fig. 3.19: *CIIEnv* and its order spectrum (crack depth 6mm, $M_2 = 48$Nm and sinusoidal speed profile)

The *CIIAM* is calculated and is shown in Fig. 3.20 alongside the CII and the sinusoidal speed SPD. From Fig. 3.20(a), it is seen that the *CIIAM* has a quasi-sinusoidal pattern. Comparing Fig. 3.20(b) to Fig. 3.20(c), it is found that frequency of the *CIIAM* is 5Hz, which is equal to that of the SPD. This means that there exists a linear dependence of the *CIIAM* on the speed SPD, which verifies the correctness of the hypothesis presented in Eq. (3.31). This observation reveals that the variable speed induces an AM effect on the CII and the AM effect is linearly dependent on the variable speed. The linear model shown in Eq. (3.31) is adopted to fit the linear relation between the *CIIAM* and the SPD, and the fitting result is shown in Fig. 3.21. The ellipse pattern is caused by the big phase difference between the the *CIIAM* and the SPD. As shown in Fig. 3.21, the relation between the *CIIAM* and the sinusoidal speed SPD is properly fitted and the fitting result is $CIIAM = 1.792SPD + 47.87$ (with 95% confidence bounds). In this case, the RCOCV is equal to 1.792.

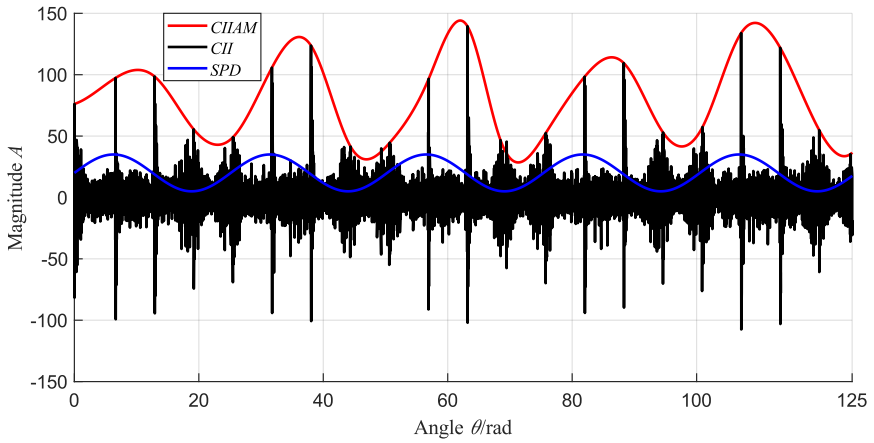

(a) Waveforms of the *CIIAM*, sinusoidal speed SPD, and the *CII*

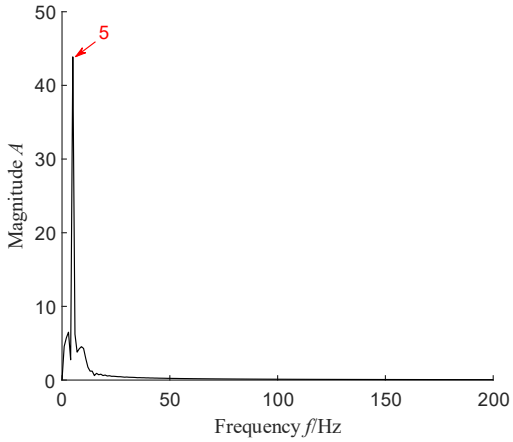

(b) Frequency spectrum of the *CIIAM*

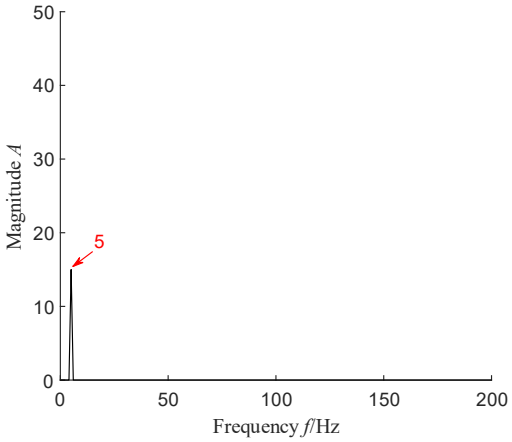

(c) Frequency spectrum of the SPD

Fig. 3.20: The *CIIAM*, SPD, and *CII* (crack depth 6mm, $M_2 = 48$Nm and sinusoidal speed profile)

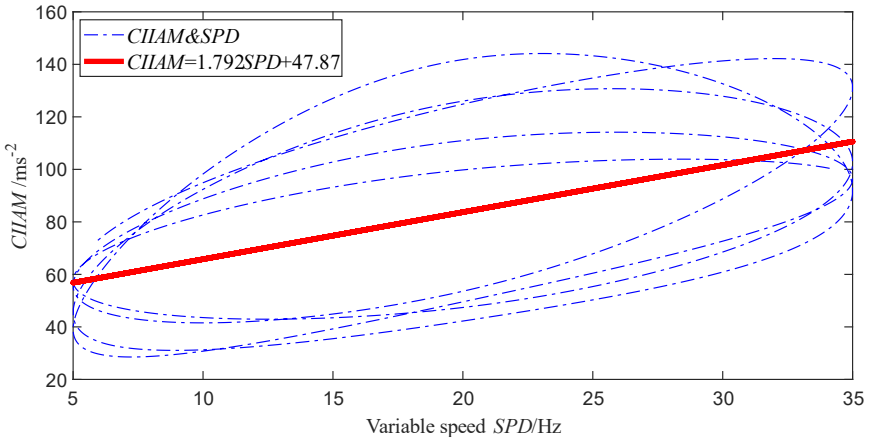

Fig. 3.21: The linear fitting result for the *CIIAM* and the sinusoidal speed SPD

After analyzing simulated gearbox vibration signals for all tooth crack depths under the four considered constant load and variable speed conditions, the RCOCV results are obtained, which are plotted versus tooth crack depth in Fig. 3.22. RMS of the CII versus tooth crack depth are shown in Fig. 3.23. In these two figures, the subscript "sin" means that the CI results are obtained for the sinusoidal speed profile, "run" run-up, "coa" coast-down, and "har" harmonic. To make quantitative performance comparison between RCOCV and RMS of the CII, AIR and FD metrics are calculated. AIR and FD results for RCOCV are tabulated in Table 3.6 and Table 3.7, respectively, and those for RMS of the CII are shown in Table 3.8 and Table 3.9, respectively.

Comparing Table 3.6 and Table 3.8, it is seen that the RCOCV has a higher average AIR value than the RMS of the CII (235.89%>42.22%), which means that RCOCV is more sensitive to tooth

crack severity progression than RMS of the CII. Comparing Table 3.7 and Table 3.9, it is seen that the RCOCV has a much smaller average FD value than the RMS (0.2788<11.7285), which means that RCOCV is more insensitive to speed variations than RMS of the CII. Therefore, the RCOCV is not only sensitive to tooth crack severity progression but also insensitive to speed variations, which demonstrates its effectiveness of tracking tooth crack severity progression under constant load and variable speed conditions.

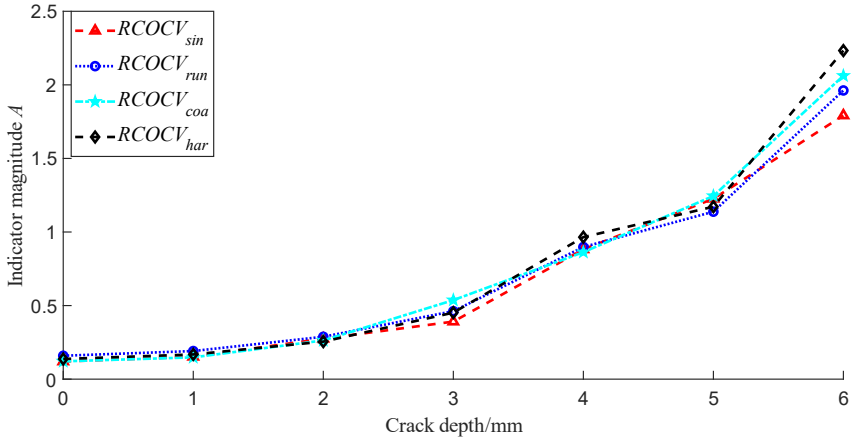

Fig. 3.22: RCOCV versus tooth crack depth (constant load and variable speed condition)

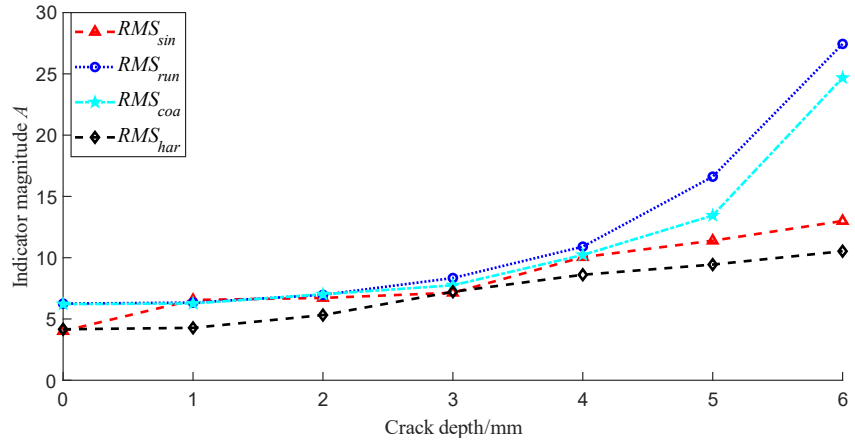

Fig. 3.23: RMS of the CII versus tooth crack depth (constant load and variable speed condition)

Table 3.6: AIR results for the RCOCV (constant load and variable speed condition)

RCOCV	Average Increase Rate (AIR %)
RCOCV_sin	232.22
RCOCV_run	188.99
RCOCV_coa	267.36
RCOCV_har	254.99
Average:	235.89

Table 3.7: FD results for the RCOCV (constant load and variable speed condition)

RCOCV	Frechet Distance (FD)
RCOCV_sr	0.2125
RCOCV_sc	0.3084
RCOCV_sh	0.4571
RCOCV_rc	0.1795
RCOCV_rh	0.2851
RCOCV_ch	0.2300
Average:	0.2788

Table 3.8: AIR results for the RMS of the CII (constant load and variable speed condition)

RMS	Average Increase Rate (AIR %)
RMS_sin	37.33
RMS_run	56.48
RMS_coa	49.54
RMS_har	25.51
Average:	42.22

Table 3.9: FD results for the RMS of the CII (constant load and variable speed condition)

RMS	Frechet Distance (FD)
RMS_sr	15.5965
RMS_sc	12.0858
RMS_sh	4.3699
RMS_rc	4.3008
RMS_rh	18.8492
RMS_ch	15.1688
Average:	11.7285

3.4 Experimental validation

In this section, the identified linear dependence of the *CIIAM* on the variable load or variable speed, and the effectiveness of the proposed condition indicator RCOCV in terms of tracking tooth crack severity progression under time-varying operating conditions are further validated using the experimental gearbox vibration datasets.

3.4.1 Experiment setup

The experimental gearbox vibration datasets were collected from a fixed-axis spur gearbox of the test rig shown in Fig. 2.12 in Section 2.5. The details of the experimental fixed-axis spur gearbox, the locations of the accelerometers, and the specifications of the pinion on which a tooth crack was seeded have been introduced in Subsection 2.5.1. The tooth crack propagation path of the target pinion has been illustrated in Fig. 2.13. In the experiment, 5 health conditions of the pinion corresponding to 5 tooth crack levels were considered, which are tabulated in Table 3.10. The tooth crack severity level is defined as the product of the crack length ratio w_0/w and the crack depth ratio $q_0/(2q)$, namely $cl = \frac{w_0}{w} \times \frac{q_0}{2q} \times 100\%$, so the crack severity levels of the 5 cases are figured out as 2%, 8%, 18%, 32%, and 50%. The target pinions with 5 different tooth crack severity levels are shown in Fig. 3.24.

Table 3.10: Five health conditions of the target pinion considered in the experiment

Pinion health condition	Tooth crack parameters	Crack severity level (cl)
Faulty 1 (F1)	w_0 = 0.2w; q_0 = 0.2q; α_c = 60°	2%
Faulty 2 (F2)	w_0 = 0.4w; q_0 = 0.4q; α_c = 60°	8%
Faulty 3 (F3)	w_0 = 0.6w; q_0 = 0.6q; α_c = 60°	18%
Faulty 4 (F4)	w_0 = 0.8w; q_0 = 0.8q; α_c = 60°	32%
Faulty 5 (F5)	w_0 = 1.0w; q_0 = 1.0q; α_c = 60°	50%

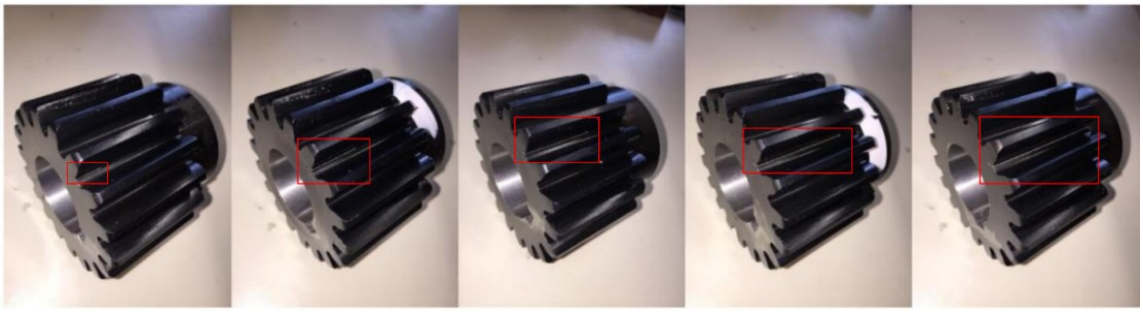

Fig. 3.24: Five tooth crack severity levels of the target pinion (from left to right: Faulty 1 to Fault 5)

In the experiment, the target fixed-axis spur gearbox was operating under two scenarios of time-varying operating conditions: (1) variable load and constant speed condition, (2) constant load and variable speed condition, which were controlled using a variable frequency drive. For the variable load and constant speed condition, the drive motor speed was set to 20 Hz, and the target pinion rotational speed was 2.955 Hz. In this case, the gear mesh frequency of the input mesh pair (the

one with the cracked pinion) is $\mathrm{GMF}_{\mathrm{in}} = 53.19$ Hz, and that of the output mesh pair is $\mathrm{GMF}_{\mathrm{out}} = 189.12$ Hz. Two types of load (torque) profiles were applied to the load motor to generate the variable load conditions, namely the Load Profile I (LPI) and the Load Profile II (LPII), and the measured torque signals are shown in Fig. 3.25. For the constant load and variable speed condition, the torque applied to the load motor was set to 13% of the full torque, which generated a torque of 120 Nm to the target pinion shaft. Two types of speed profiles were applied to the drive motor to generate the variable speed conditions, namely the Speed Profile I (SPI) and the Speed Profile II (SPII), and the measured speed signals are shown in Fig. 3.26.

Acceleration signals of the target fixed-axis spur gearbox for the 5 pinion health conditions defined in Table 3.10 were collected with the four accelerometers shown in Fig. 2.12(c) under the two considered scenarios of time-varying operating conditions. The accelerometer model is PCB 352B and its sensitivity is 1000 mv/g. The sampling frequency was set to 25.6 kHz. For each pinion health condition under each load profile, 5 data samples were collected, each sample had a time length of 20 seconds. For each pinion health condition under each speed profile, 5 data samples were collected, each sample had a time length of 40 seconds. In this study, without loss of generality, the acceleration signals acquired by the accelerometer 3 shown in Fig. 2.12(c) are analyzed.

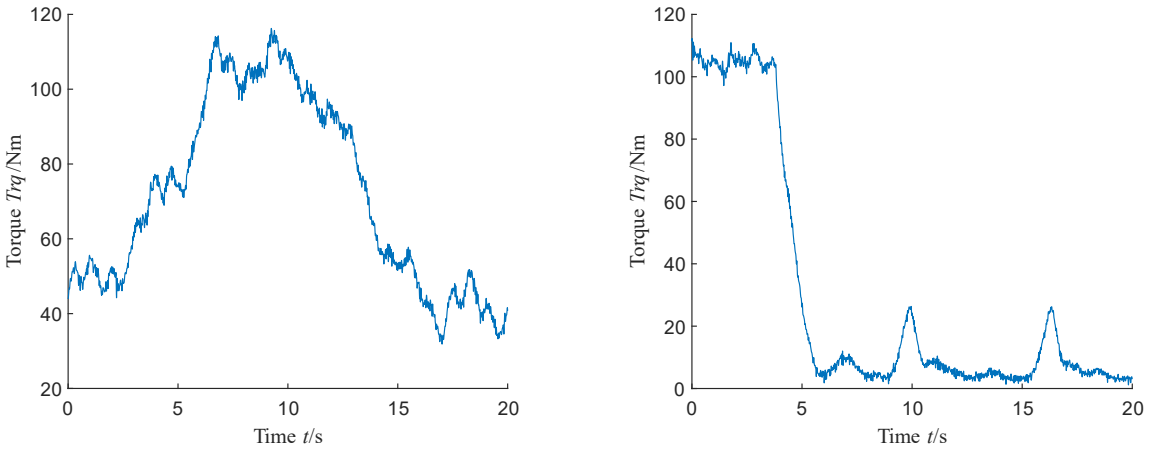

(a) Load Profile I (LPI) (b) Load Profile II (LPII)

Fig. 3.25: Measured torque signals of the target pinion shaft for the LPI and LPII load profiles

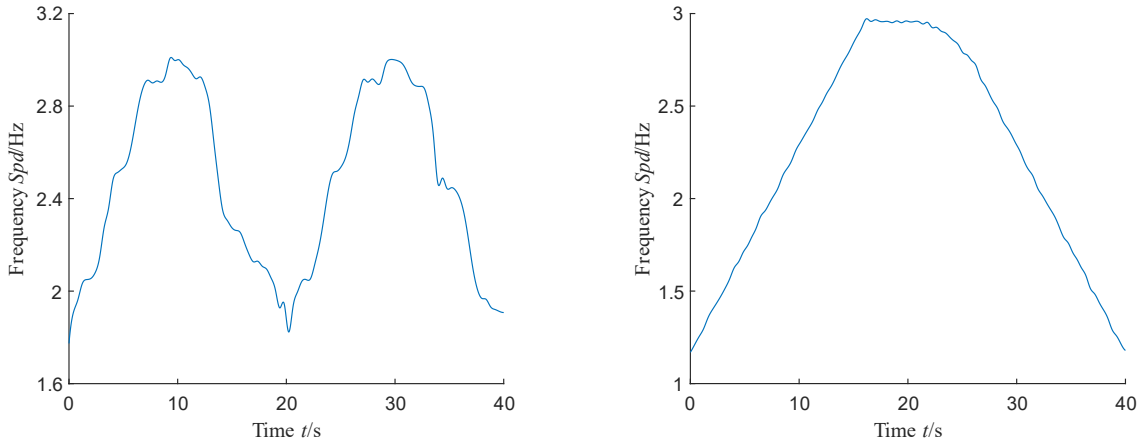

(a) Speed Profile I (SPI) (b) Speed Profile II (SPII)

Fig. 3.26: Measured speed signals of the target pinion shaft for the SPI and SPII speed profiles

3.4.2 Experimental signal analysis for the variable load and constant speed condition

For this scenario, the vibration signal for the pinion health condition "Faulty 5" collected under the variable load (LPI) and constant speed condition is used as an example to show the analysis results. From Fig. 3.27, it is seen that the frequency spectrum is dominated by gear mesh harmonics of the two gear mesh pairs of the target gearbox, i.e., $\mathrm{GMF}_{\mathrm{in}} = 53.19$ Hz, $\mathrm{GMF}_{\mathrm{out}} = 189.12$ Hz, and their multiples, and there is no frequency smearing phenomenon. Besides, the signal amplitude is modulated, although the AM is not obvious due to the strong noise. Therefore, the variable load and constant speed condition only induces an AM into the gearbox vibration signal.

The meshing components of the two mesh pairs are removed from the vibration signal using comb notch filters. Afterwards, the AHD method is conducted on the comb notch filtered signal to obtain the CII, and the obtained CII is shown in Fig. 3.28. As shown in the top plot of Fig. 3.28, the time interval between every two neighbouring pulses is about 0.34 s, such as 4.32-3.98=0.34 s, which is the reciprocal of the target pinion rotational speed, i.e., $0.34\ \mathrm{s} \approx 1/2.955$ Hz. Therefore, the CII result in a group of harmonics with a uniform interval of 2.955Hz in the frequency spectrum, such as $209.81 - 206.86 \approx 2.955$ Hz . There is no frequency smearing in the spectrum, indicating that there is no FM in the CII. The CII amplitude is modulated. Therefore, the variable load and constant speed condition only induces an AM into the CII. The *CIIEnv* and its frequency spectrum are shown in Fig. 3.29. As shown in Fig. 3.29, the spectrum is dominated by the crack characteristic frequencies, i.e., the target pinion rotational speed (2.955 Hz) and its multiples. There are two

spikes at 0.05 Hz and 0.35 Hz, which equal the frequencies of LPI, i.e., the torque Trq shown in Fig. 3.25(a). There are sidebands around the crack characteristic frequencies with an interval of 0.05 Hz or 0.35 Hz, which means that the AM of the CII is induced by the variable torque Trq.

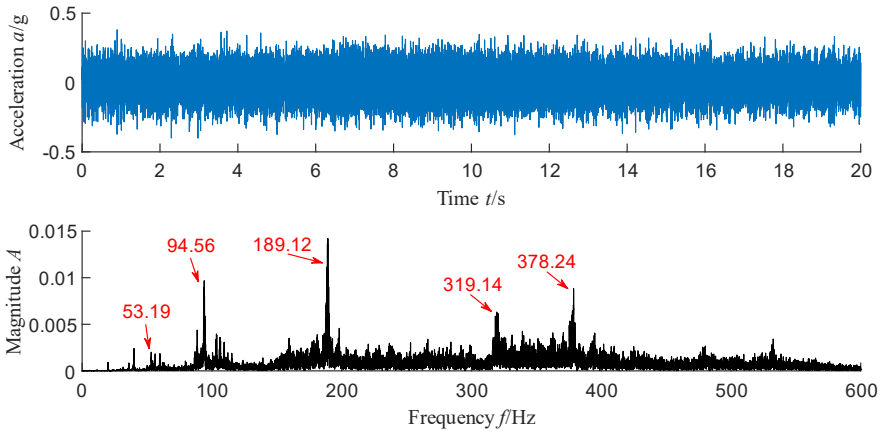

Fig. 3.27: Vibration signal (health condition "Faulty 5", variable load (LPI) and constant speed)

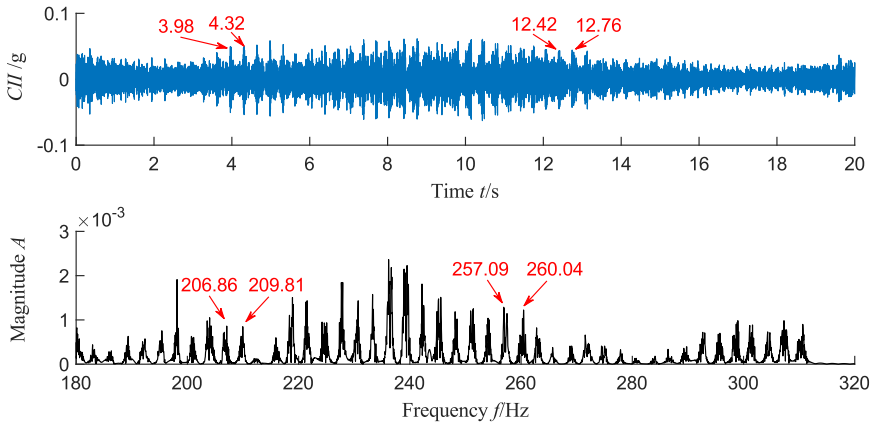

Fig. 3.28: The obtained CII (health condition "Faulty 5", variable load (LPI) and constant speed)

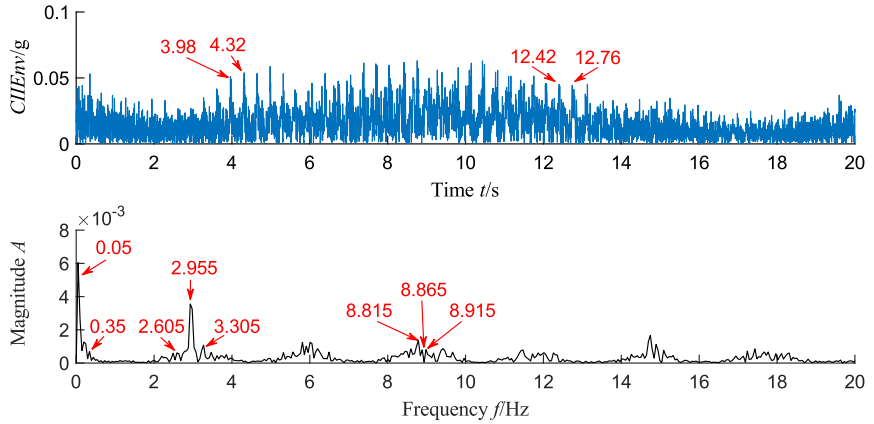

Fig. 3.29: The *CIIEnv* (health condition "Faulty 5", variable load (LPI) and constant speed)

The *CIIAM* is shown in Fig. 3.30 alongside CII and torque Trq. *CIIAM* and Trq are scaled to make them on the same scale of CII, which is shown in Fig. 3.30(a). Comparing Fig. 3.30(b) to Fig. 3.30(c), it is seen that two main frequencies of *CIIAM* are 0.05 Hz and 0.35 Hz, which are equal to those of Trq. This means that there is a linear dependence of *CIIAM* on Trq, which validates the correctness of the hypothesis shown in Eq. (3.31). This observation reveals that the variable load induces an AM on the CII, and the AM is linearly dependent on the variable load. A linear model is used to fit the linear relation between *CIIAM* and Trq, and the fitting result is shown in Fig. 3.31. The relation between *CIIAM* and Trq is well fitted and the result is $CIIAM = 0.00016Trq + 0.0032$ (with 95% confidence bounds). The coefficient of determination is $R^2 = 0.85$, indicating a high goodness of the linear fit. In this case, the RCOCV is equal to 0.00016.

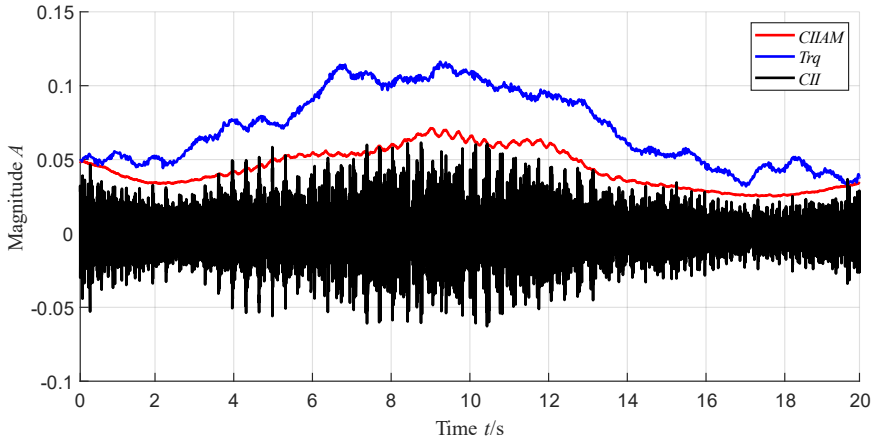

(a) Waveforms of the *CIIAM*, the applied LPI torque Trq, and the *CII*

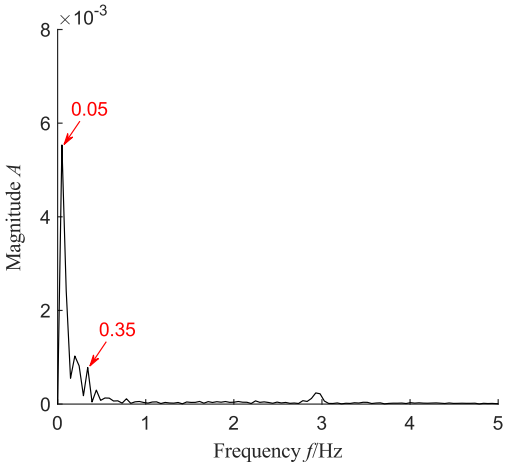

(b) Frequency spectrum of the *CIIAM*

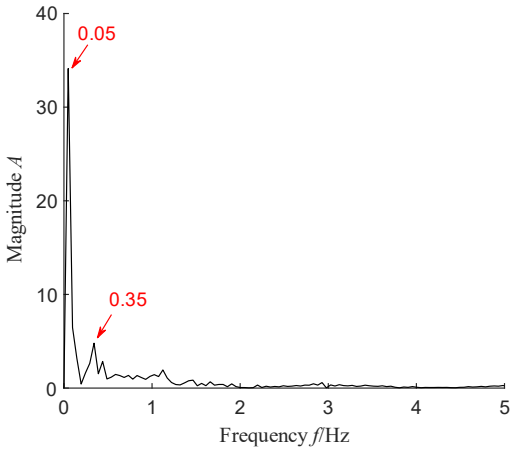

(c) Frequency spectrum of the torque Trq

Fig. 3.30: The *CIIAM*, Trq, and *CII* (health condition "Faulty 5", variable load (LPI) and constant speed)

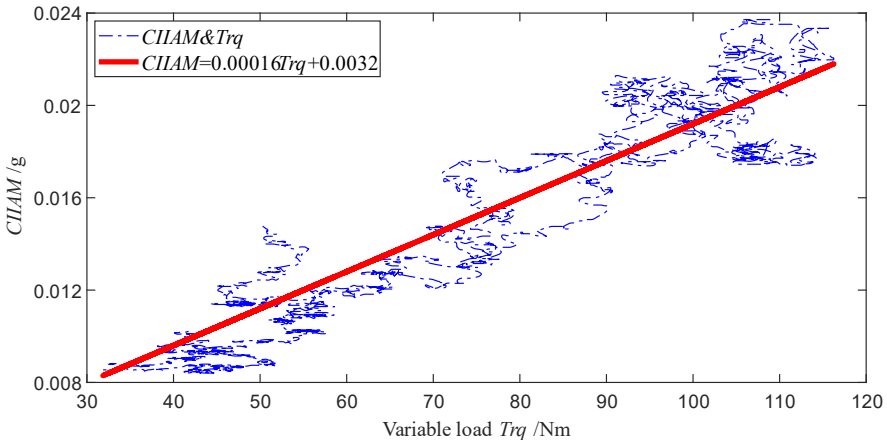

Fig. 3.31: The linear fitting result for the *CIIAM* and the applied torque Trq

After analyzing vibration signals for all tooth crack severity levels under the two considered variable load and constant speed conditions, the RCOCV results are obtained. For each pinion health condition under each load profile, 5 data samples were collected, so 5 results are obtained for the RCOCV for each tooth crack severity level under each load profile. The median value of the 5 results is used as the final value of the RCOCV. Likewise, the final value of RMS of the CII is also calculated for performance comparison. The results for RCOCV versus crack severity level are shown in Fig. 3.32 and those for RMS of the CII versus crack severity level are shown in Fig. 3.33. In these two figures, the subscript "LPI" denotes the results are obtained for the torque LPI, "LPII" the torque LPII. As shown in Fig. 3.32, RCOCV is not only sensitive to tooth crack severity progression but also insensitive to load variation. On the contrary, as shown in Fig. 3.33, the RMS of the CII is not insensitive to load changes due to the big spread between the two curves.

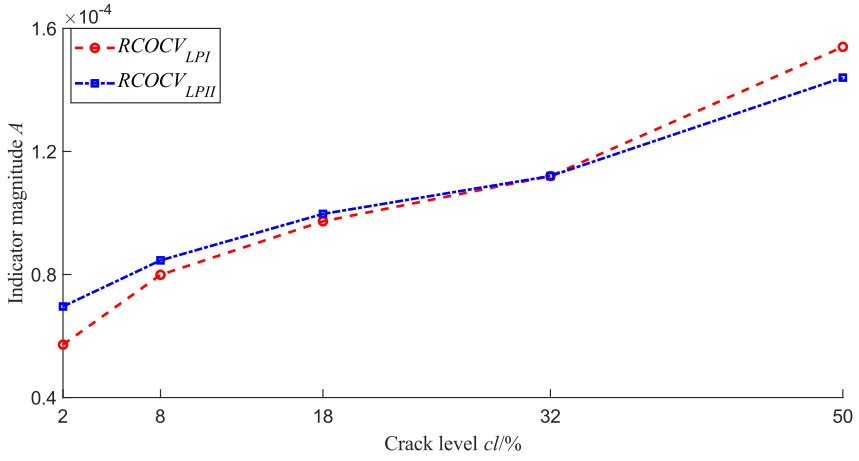

Fig. 3.32: RCOCV versus tooth crack severity level (variable load and constant speed condition)

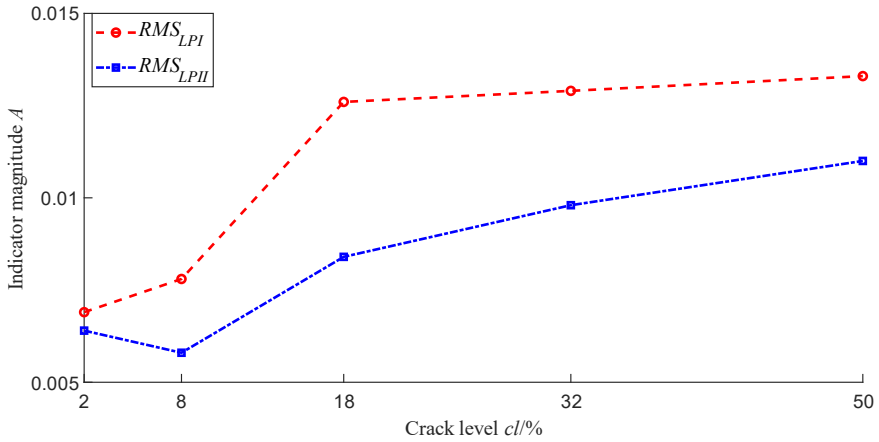

Fig. 3.33: RMS of the CII versus tooth crack severity level (variable load and constant speed condition)

To make quantitative performance comparison, AIR and FD results for RCOCV and RMS of the CII are calculated and tabulated in Table 3.11 and Table 3.12, in which suffix "_LPI" denotes the LPI load profile, "_LPII" the LPII load profile. By comparing the AIR and FD values shown in Table 3.11 and Table 3.12, two conclusions are made: (1) Higher sensitivity of RCOCV to tooth crack severity progression. From Table 3.11, it is seen that RCOCV has a higher average AIR value than the RMS (296.74%>171.49%), indicating that RCOCV is more sensitive to tooth crack severity progression than RMS; (2) Higher insensitivity of RCOCV to load variation. As shown in Table 3.12, the RCOCV has a much smaller average FD value than the RMS (0.000020<0.0061), which means that RCOCV is much more insensitive to the load variation than RMS.

Table 3.11: AIR for the median values of RCOCV and RMS of the CII (variable load and constant speed)

Condition indicator for a load profile	Average Increase Rate (AIR %)
RCOCV_LPI	370.78
RCOCV_LPII	222.70
Average for RCOCV	296.74
RMS_LPI	193.24
RMS_LPII	149.74
Average for RMS	171.49

Table 3.12: FD for the median values of RCOCV and RMS of the CII (variable load and constant speed)

Condition indicator	Frechet Distance (FD)
RCOCV	0.000020
RMS	0.0061

3.4.3 Experimental signal analysis for the constant load and variable speed condition

For this scenario, the vibration signal for the pinion health condition “Faulty 5” collected under the constant load and variable speed (SPI) condition is used as an example to show the analysis results. As shown in Fig. 3.34, the signal amplitude is modulated and there exists a frequency smearing effect in the frequency spectrum. Therefore, the constant load and variable speed condition induces both AM and FM into gearbox vibration signals. The signal spectrogram is shown in Fig. 3.35, from which it is seen that there are ridges with variation patterns similar to that of the SPI shown in Fig. 3.26(a). The vibration signal is resampled in the angle domain and the resampled result is shown in Fig. 3.36, from which it is seen that the order spectrum is dominated by the mesh orders of the input gear mesh pair (order 18 and its multiples) and the output gear mesh pair (order 64 and its multiples).

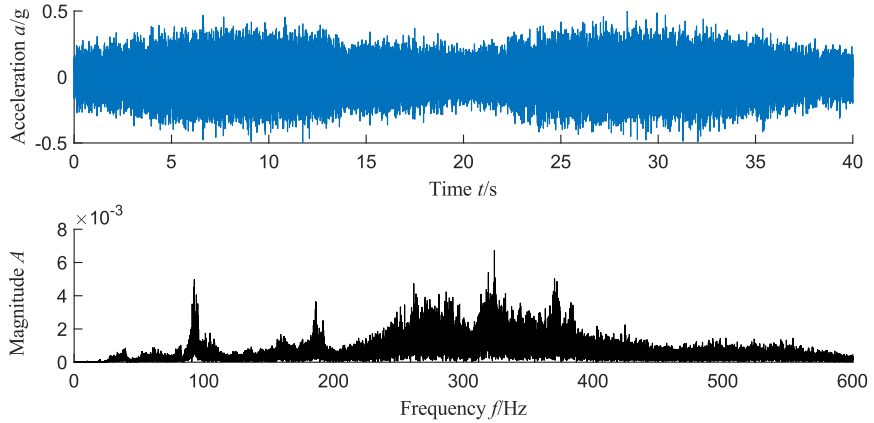

Fig. 3.34: Vibration signal (health condition “Faulty 5”, constant load and variable speed (SPI))

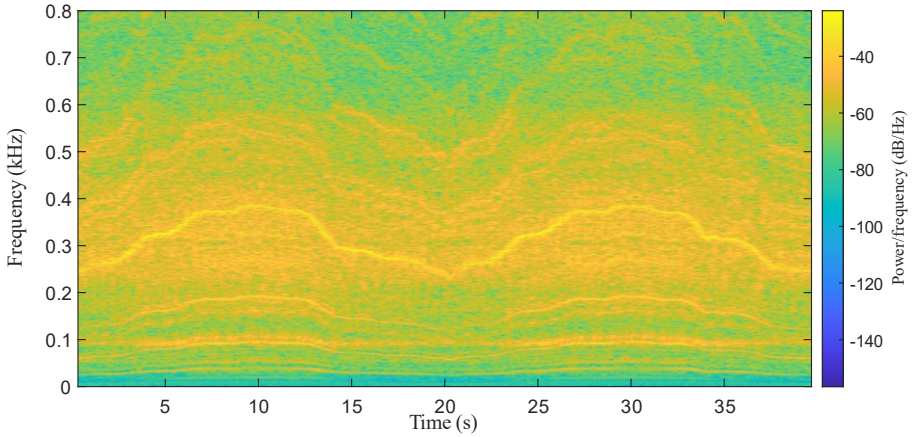

Fig. 3.35: Signal spectrogram (health condition “Faulty 5”, constant load and variable speed (SPI))

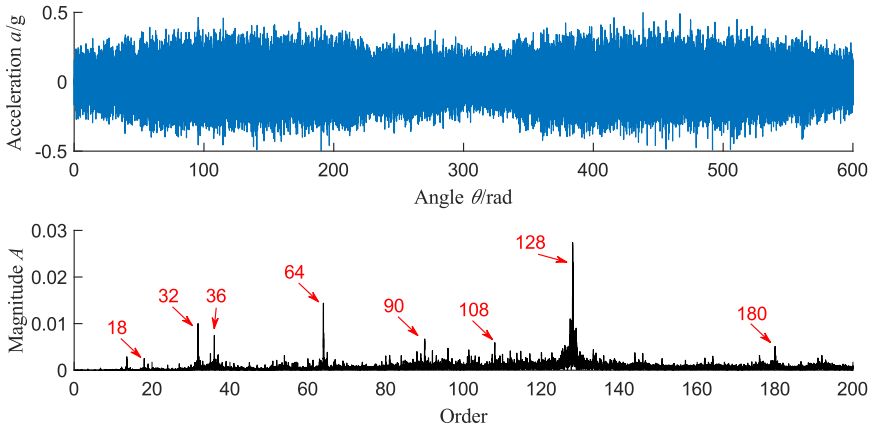

Fig. 3.36: Resampled signal (health condition "Faulty 5", constant load and variable speed (SPI)).

Before extracting the CII, the mesh orders of the two gear mesh pairs are first removed from the resampled vibration signal shown in Fig. 3.36 using comb notch filters. Afterwards, the modified AHD method shown in Algorithm 1 is conducted on the comb notch filtered signal to obtain the CII, and the obtained CII is shown in Fig. 3.37. As shown in the top plot of Fig. 3.37, the angle interval between every two neighbouring pulses is 6.28 rad, such as 140.1-133.82=6.28 rad and 485.58-479.3=6.28 rad, which is the angular displacement of the target pinion in one revolution. This means that the pulses are induced by the pinion tooth crack. The CII result in a group of orders with a uniform interval of 1 order in the order spectrum, which is shown in the bottom plot of Fig. 3.37. Besides, the CII amplitude is modulated. Therefore, the constant load and variable speed condition induces both AM and FM into the CII.

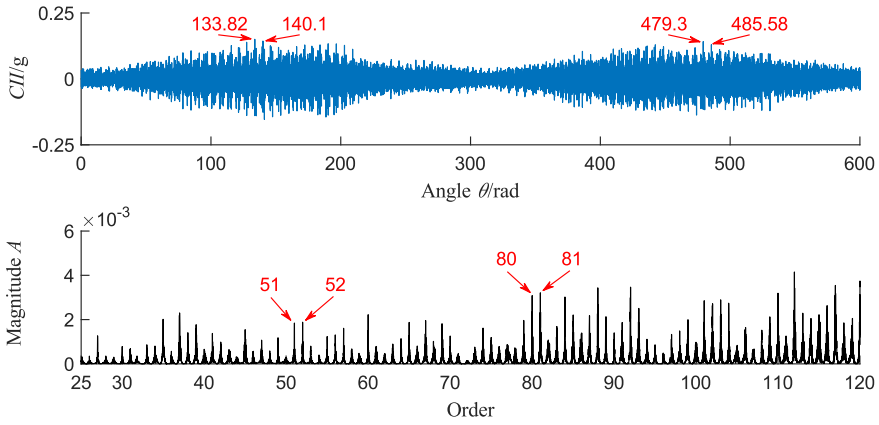

Fig. 3.37: The obtained CII (health condition "Faulty 5", constant load and variable speed (SPI))

The *CIIEnv* is shown in Fig. 3.38 alongside its order spectrum. As shown in the bottom plot of Fig. 3.38(a), the order spectrum is dominated by the pinion shaft rotational order (order 1) and its multiples, which are the tooth crack characteristic orders. There are two spikes at 0.02 order and 0.069 order, which are the equivalent orders of the variable speed SPI, i.e., the Spd shown in Fig. 3.26(a), i.e., 0.05/2.48=0.02 order and 0.17/2.48=0.069 order (0.05 Hz and 0.17 Hz are the frequencies of the variable speed Spd, 2.48 Hz is the mean value of the variable speed Spd). Besides, as shown in Fig. 3.38(b), there are sidebands around the tooth crack characteristic orders with intervals of 0.02 order or 0.069 order, which means that the AM of the CII is induced by the variable speed Spd.

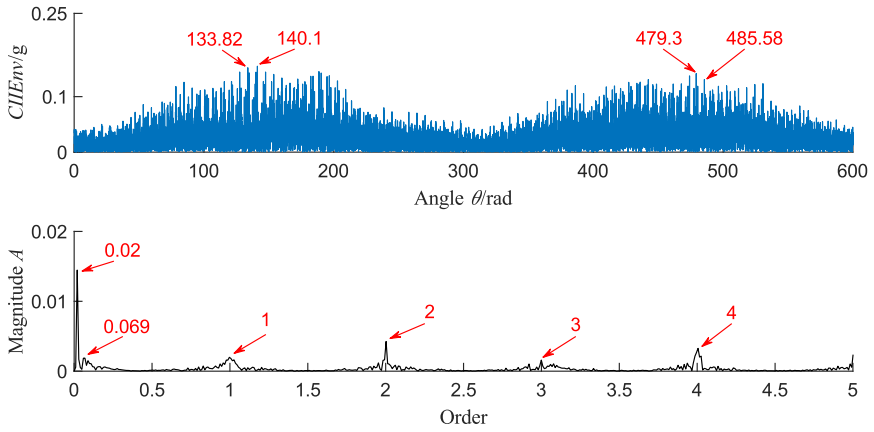

(a) The CII envelope and its order spectrum

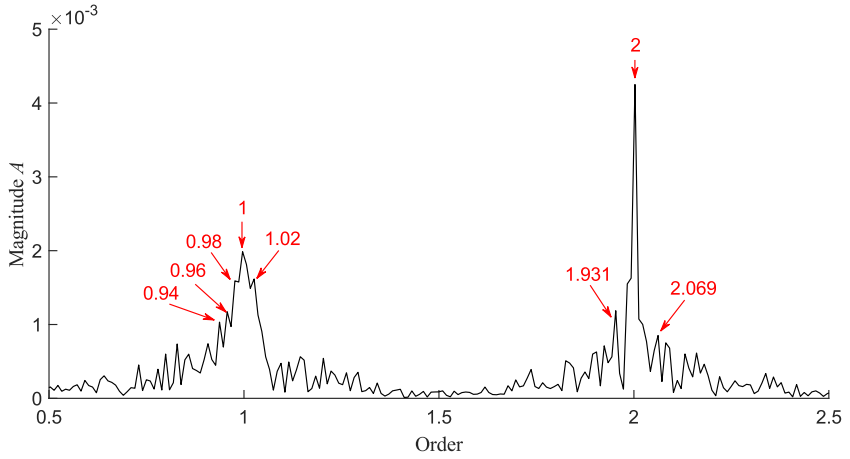

(b) The zoomed-in view of the CII envelope order spectrum

Fig. 3.38: The *CIIEnv* (health condition "Faulty 5", constant load and variable speed (SPI))

The *CIIAM* is shown in Fig. 3.39 together with CII and speed Spd. Because *CIIAM*, Spd, and CII have different magnitudes, *CIIAM* and Spd are scaled to make them on the same scale of CII. Comparing Fig. 3.39(b) to Fig. 3.39(c), it is found that two main frequencies of *CIIAM* are 0.05 Hz and 0.17 Hz, which are equal to those of Spd. This means that there exists a linear dependence of the *CIIAM* on the Spd, which validates the correctness of the hypothesis shown in Eq. (3.31). This observation reveals that the variable speed induces an AM on the CII and the AM is linearly dependent on the variable speed. A linear model is used to fit the relation between the *CIIAM* and Spd, and the fitting result is shown in Fig. 3.40, from which is seen that the relation between the *CIIAM* and the Spd is well fitted and the fitting result is $CIIAM = 0.024Spd - 0.031$ (with 95% confidence bounds). The coefficient of determination is $R^2 = 0.96$, which indicates a high goodness of the linear fit. In this case, the proposed condition indicator RCOCV is equal to 0.024.

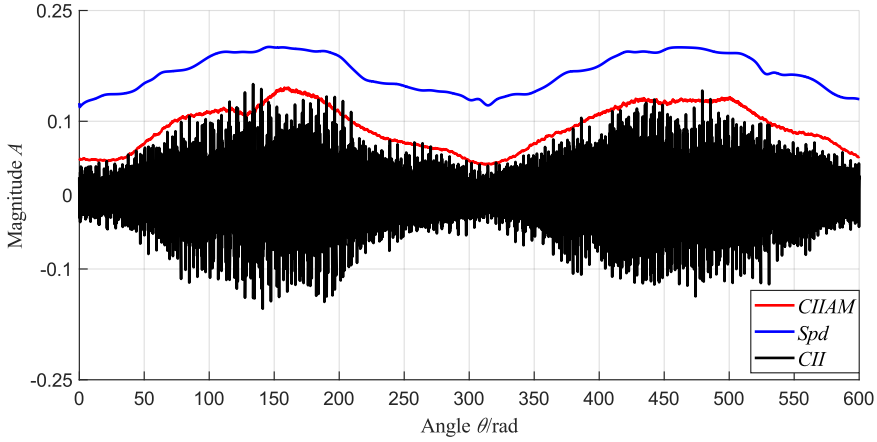

(a) Waveforms of the *CIIAM*, speed Spd, and the *CII*

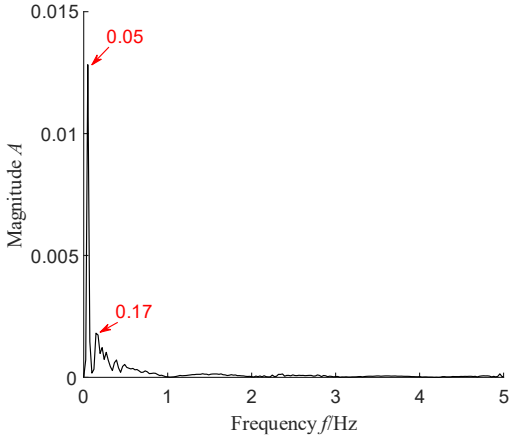

(b) Frequency spectrum of the *CIIAM*

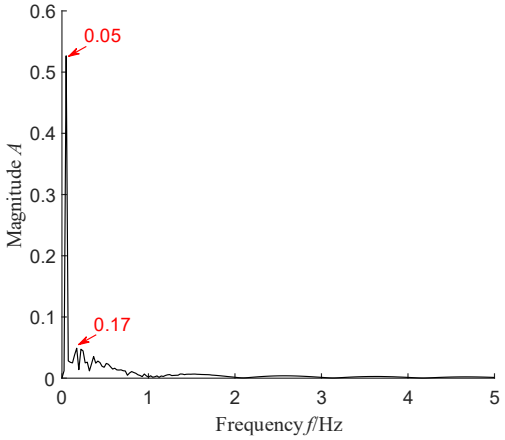

(c) Frequency spectrum of the speed Spd

Fig. 3.39: The *CIIAM*, Spd, and *CII* (health condition "Faulty 5", constant load and variable speed (SPI))

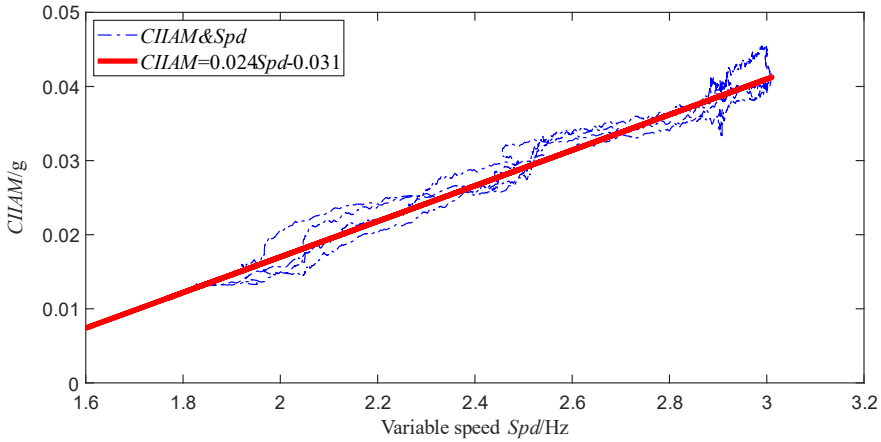

Fig. 3.40: The linear fitting result for the *CIIAM* and the variable speed Spd

After analyzing the vibration signals for all the considered tooth crack severity levels under the two constant load and variable speed conditions, the RCOCV results are obtained. For each pinion health condition under each speed profile, 5 data samples were collected, so 5 results are obtained for the RCOCV for each tooth crack severity level under each speed profile. The median value of the 5 results is used as the final value of the RCOCV. Likewise, the final value of the RMS of the CII is also calculated for performance comparison. The results for the RCOCV versus tooth crack severity level are shown in Fig. 3.41 and those for the RMS of the CII versus tooth crack severity level are shown in Fig. 3.42. In these two figures, the subscript "SPI" means that the results are obtained for the speed SPI, "SPII" the speed SPII.

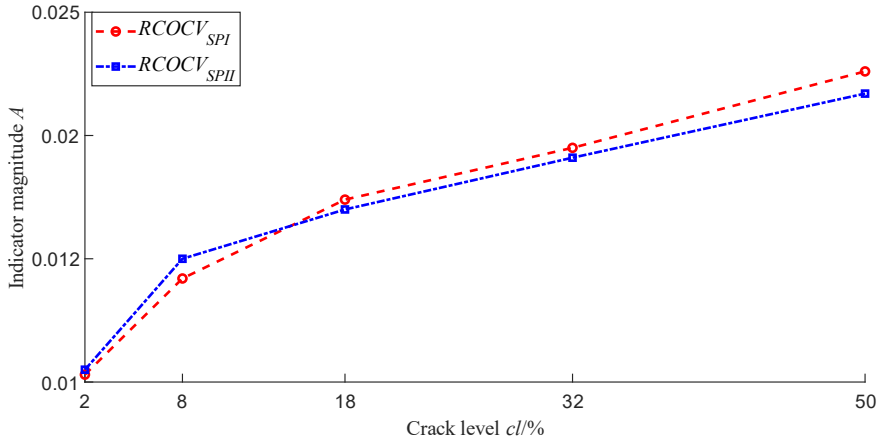

Fig. 3.41: RCOCV versus tooth crack severity level (constant load and variable speed condition)

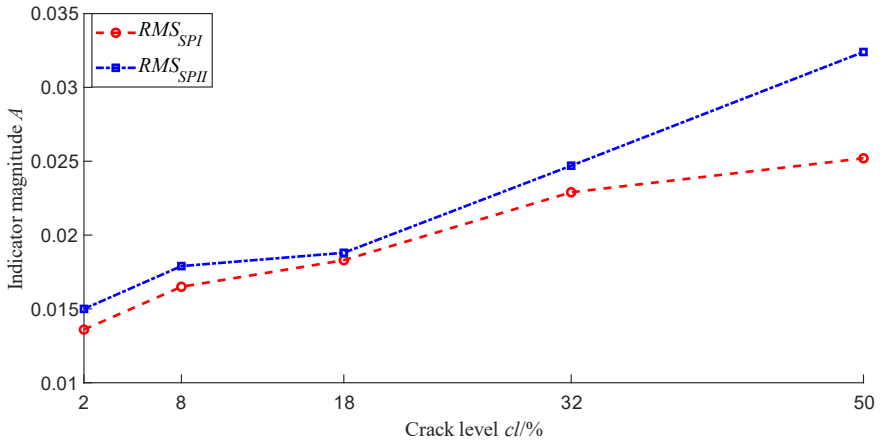

Fig. 3.42: RMS of the CII versus tooth crack severity level (constant load and variable speed condition)

To make quantitative performance comparison, AIR and FD results for RCOCV and RMS of the CII are calculated and tabulated in Table 3.13 and Table 3.14, in which the suffix "_SPI" denotes the SPI speed profile, "_SPII" the SPII speed profile. Comparing the AIR and FD results shown in Table 3.13 and Table 3.14, two conclusions are made: (1) Higher sensitivity of RCOCV to tooth crack severity progression. From Table 3.13, it is seen that RCOCV has a higher average AIR value than the RMS of the CII (235.51%>209.69%), indicating that RCOCV is more sensitive to tooth crack severity progression than RMS; (2) Higher insensitivity of RCOCV to speed variation. From Table 3.14, it is seen that RCOCV has a smaller average FD value than RMS of the CII (0.0013<0.0077), which means that RCOCV is more insensitive to the speed variation than RMS.

Table 3.13: AIR for the median values of RCOCV and RMS of the CII (constant load and variable speed)

Condition indicator for a speed profile	Average Increase Rate (AIR %)
RCOCV_SPI	248.79
RCOCV_SPII	222.22
Average for RCOCV	235.51
RMS_SPI	177.70
RMS_SPII	241.67
Average for RMS	209.69

Table 3.14: FD for the median values of RCOCV and RMS of the CII (constant load and variable speed)

Condition indicator	Frechet Distance (FD)
RCOCV	0.0013
RMS	0.0077

3.5 Discussion of the proposed condition indicator RCOCV

The effectiveness of the RCOCV in terms of tracking tooth crack severity progression under time-varying operating conditions has been demonstrated using simulated gearbox vibration signals in Section 3.3 and experimental gearbox vibration datasets in Section 3.4. In this section, the advantages, requirements, and limitations of RCOCV are discussed by qualitatively comparing to other conventional tooth crack diagnosis techniques. Besides, the way to use RCOCV for the diagnosis of gearboxes with unknown tooth crack levels is also briefly described.

Many tooth crack diagnosis techniques have been reported in the literature, a large proportion of which are the CIs developed for crack diagnosis. Generally, CIs were developed using raw gearbox vibration signals or their pre-processed results such as those obtained using the TSA. Typical CIs which have been widely used for tooth crack diagnosis include RMS, Kurtosis, FM0 [82], FM4 [83], NA4 [83,84], NB4 [85], and so on. Although these conventional CIs have been used for tooth crack diagnosis, they still have some drawbacks. Firstly, they were initially developed under constant load and constant speed conditions, therefore their performance on tooth crack diagnosis will deteriorate significantly if gearboxes work under time-varying operating conditions. Besides, they were not developed using the signal components which can well reflect tooth crack severity progression, so their sensitivities to tooth crack growth were not so good.

On the contrary, as compared to the conventional tooth crack diagnosis techniques described above, the RCOCV performs better in terms of tracking tooth crack severity progression under time-varying operating conditions due to its advantages. Advantages of the RCOCV include: (1) RCOCV is defined as the ratio of *CIIAM* to the operating condition variation and *CIIAM* is obtained from the CII which contain more valuable information on tooth crack, therefore RCOCV is more sensitive to tooth crack severity progression than the conventional CIs; (2) RCOCV is not only sensitive to tooth crack severity progression but also insensitive to operating condition variations since it keeps tooth crack information and removes the interferences of operating condition variations. The advantages of RCOCV have been demonstrated by its better performance than the RMS on tracking tooth crack severity progression under time-varying operating conditions, which has been illustrated by analyzing simulated gearbox vibration signals and experimental gearbox vibration datasets in Section 3.3 and Section 3.4, respectively. To guarantee

the good performance of the RCOCV, some requirements need to be met. To be specific, *CIIAM* needs to be calculated accurately if an accurate value of RCOCV is required. To this end, advanced signal processing methods are needed to pre-process gearbox vibration signals to extract the CII with a high SNR, through which the *CIIAM* can be obtained accurately. In the present study, the AHD method and its modified version and envelope analysis are used to meet these requirements. However, these requirements in turn result in one limitation of RCOCV, which is that if the CII cannot be well extracted from raw gearbox vibration signals and *CIIAM* cannot be accurately calculated using the extracted CII, the performance of RCOCV on tooth crack diagnosis under time-varying operating conditions may deteriorate to some degree.

Besides, if the mapping relationship between RCOCV and gear tooth crack severity levels can be obtained by analyzing vibration signals of gearboxes with known tooth crack sizes using advanced data processing approaches such as neural networks, the obtained mapping relationship can be adopted to tell tooth crack level. To be specific, RCOCV is first calculated using the vibration signals of a gearbox with an unknown tooth crack level, through which the tooth crack level can be inferred together with the obtained mapping relationship.

3.6 Conclusions

This chapter proposes a new methodology to study the effects of time-varying operating conditions on vibration signals of gearboxes with tooth cracks comprehensively and explicitly. Firstly, a fixed-axis spur gearbox system with a tooth crack subject to time-varying operating conditions is modelled. Two scenarios of time-varying operating conditions of the gearbox system are considered, namely the variable load and constant speed condition, and the constant load and variable speed condition. The relation between the gear tooth mesh stiffness and time is derived, thus facilitating the evaluation of the mesh stiffness of a gear mesh pair considering tooth crack severity progression under time-varying operating conditions. By substituting the tooth mesh stiffness and the time-varying operating conditions into the gearbox system motion equation, gearbox vibration responses under the two considered scenarios of time-varying operating conditions are generated. A signal analysis procedure with its focus placed on the CII is proposed. The CII are extracted from gearbox vibration signals using the modified AHD method or its original counterpart. The findings obtained from signal analysis are summarized in the following.

(1) For the variable load and constant speed condition, it induces neither AM nor FM into the gear tooth mesh stiffness, and it only induces an AM into the gearbox vibration signal and the CII. There is a linear dependance of the AM of the CII on the variable load.

(2) For the constant load and variable speed condition, it induces an FM into the gear tooth mesh stiffness, and it induces both AM and FM into the gearbox vibration signal and the CII. There is a linear dependance of the AM of the CII on the variable speed.

The identified linear dependence of the AM of the CII on the time-varying operating condition, i.e., the variable load or the variable speed, can be well fitted using a linear model. The model parameter specifying the slope of the linear dependence is proposed as a novel CI, which is named RCOCV, to track gear tooth crack severity progression under time-varying operating conditions. The RCOCV is not only sensitive to tooth crack severity progression but also insensitive to operating condition variations. The correctness of the identified linear dependence and the effectiveness of RCOCV in terms of tracking tooth crack severity progression under time-varying operating conditions have been demonstrated using both simulated gearbox vibration signals and experimental gearbox vibration datasets. Besides, quantitative comparisons of performance on tracking tooth crack severity progression are made between the RCOCV and the RMS of the CII, and the AIR and FD are adopted as two comparison metrics. Comparative results show that the RCOCV outperforms the RMS of the CII with a higher AIR value and a smaller FD value, which demonstrates the superiority of the RCOCV in terms of tracking tooth crack severity progression under time-varying operating conditions.

In this chapter, only two scenarios of time-varying operating conditions are considered, i.e., the variable load and constant speed condition, and the constant load and variable speed condition. In the future, tooth crack diagnosis under variable load and variable speed conditions will be conducted.

Chapter 4: Normalization of gearbox vibration signal for tooth crack diagnosis under variable speed conditions

As revealed in Chapter 3, when gearboxes work under variable speed conditions, speed variations induce AM and FM into gearbox vibration signals, which may lead to incorrect results of tooth crack diagnosis if the speed variation-induced AM and FM are not removed. To overcome this problem, this chapter proposes a novel normalization method to remove the speed variation-induced AM and FM without attenuating the tooth crack information, which benefits tracking tooth crack severity progression under variable speed conditions. The materials in this chapter are covered by the third research topic (Topic #3), which is introduced in Section 1.3. The organization of this chapter is as follows. In Section 4.1, an introduction to the reported methods for removing the speed variation-induced AM and FM is presented. Section 4.2 presents the proposed normalization method for removing the speed variation-induced AM and FM. Analysis of simulation gearbox vibration signals and experimental validation for the proposed normalization method are presented in Section 4.3 and Section 4.4, respectively. Lastly, conclusions of the conducted study are made in Section 4.5. The results of this chapter have been published partially in a conference paper [106] and as a whole in a journal paper [107].

4.1 Introduction

In industrial applications, gearboxes oftentimes work under variable speed conditions and speed variations induce AM and FM into gearbox vibration signals [36,66]. The speed variation-induced AM and FM can mask the existence of a tooth crack and make it difficult to distinguish between changes of tooth crack severity and speed variations [80]. The reason accounting for this difficulty is that due to the speed variation-induced AM and FM, changes in CIs may indicate gear tooth crack severity progression, speed changes, or both. In such cases, reported methods for gearbox tooth crack diagnosis under constant speed conditions become incompetent.

In order to conduct gear tooth crack diagnosis under variable speed conditions, the speed variation-induced AM and FM need to be removed from gearbox vibration signals. However, the

information on tooth crack severity progression should not be attenuated when removing the speed variation-induced AM and FM. Order tracking techniques have been well developed and widely adopted to compensate for the FM induced by speed variation [100]. Under variable speed conditions, the passage through resonances or the changes of static transmission errors will induce AM into the gear mesh harmonics. Besides, the speed variation also changes the forcing function of the gearbox system, thus changing the amplitudes of the repetitive impact responses caused by tooth cracks. For the speed variation-induced AM, it also needs to be removed since it makes CIs sensitive to changes of rotating speed, which undermines the effectiveness of CIs to track gear tooth crack severity progression. Some studies on removing the speed variation-induced AM [36,101,102] have been reported during the last decades, which are reviewed in Subsection 1.2.2.4. These reported studies did not work well in tackling the speed variation-induced AM since they attenuated the tooth crack information greatly in the removal process. Recently, another method called NAMVOC has been developed to remove the speed variation-induced AM [80]. The NAMVOC method outperformed the GSA method in terms of reducing the speed variation-induced AM, but it still suffers from some problems, which are discussed in Subsection 1.2.2.4.

To overcome the deficiencies of the NAMVOC method, this chapter proposes a new normalization method to remove the AM and FM induced by variable speed conditions. In order to remove the speed variation-induced AM without attenuating the information on tooth crack severity progression, the focus of the proposed normalization method in this chapter is placed on the CII since they have more valuable information on tooth crack than other components of gearbox vibration signals, which follows the idea of signal analysis adopted in Chapter 3. Firstly, the raw vibration signal is processed using the computed order tracking technique to remove the speed variation-induced FM [100]. Afterwards, the modified AHD method presented in Chapter 3 is employed to extract the CII from vibration signals of gearboxes working under variable speed conditions. Lastly, the peak envelope of the CII is obtained via the envelope analysis scheme presented in Chapter 3. The peak envelope of the CII is regarded as the AM induced by variable speed conditions, through which the normalization process is conducted on the CII, thus removing speed variation-induced AM of the CII. In addition, quantitative evaluations of the performance of the proposed normalization method on the removal of the speed variation-induced AM and the preservation of tooth crack information are made.

The contributions of this chapter are summarized as follows: (1) A new normalization method is proposed, which not only removes the speed variation-induced AM and FM but also preserves the information on tooth crack severity progression; (2) Two evaluation metrics are introduced to make quantitative evaluation of performance of the proposed normalization method on removing the speed variation-induced AM and preserving the tooth crack information; (3) The superiority of the proposed normalization method over the NAMVOC method is demonstrated using both simulated gearbox vibration signals and experimental gearbox vibration datasets.

The remainder of this chapter is organized as follows. In Section 4.2, the proposed normalization method for removing the AM and FM induced by variable speed conditions is introduced. Section 4.3 presents the analysis results of simulated gearbox vibration signals. The validation of the effectiveness of the proposed normalization method using experimental gearbox vibration datasets is conducted in Section 4.4. Lastly, conclusions are made in Section 4.5.

4.2 The proposed normalization method

In this section, the proposed normalization method for removing the AM and FM induced by variable speed conditions is presented with a detailed description. Because the proposed normalization method is adopted to process gearbox vibration signals to track tooth crack severity progression, it is necessary to first introduce the composition of vibration signals of gearboxes working under variable speed conditions. Afterwards, the procedure of the proposed normalization method is illustrated. In addition, two metrics are introduced for quantitative evaluation of the performance of the proposed normalization method on removing the speed variation-induced AM and preserving the tooth crack information.

4.2.1 Phenomenological model of gearbox vibration signals

As reviewed in Subsection 1.2.2.1, when a gearbox works under variable speed conditions, speed variations induce AM and FM into gearbox vibration signals. However, the mathematical forms of the speed variation-induced AM and FM have not been known yet. The research outcomes obtained in Chapter 3 indicate that there exists a linear dependence of the speed variation-induced AM of the CII on the variable speed condition. Besides, some studies on the composition of vibration signals of a gearbox with a tooth crack have also been reported [36,77,133]. Based on

these preliminary research work, a phenomenological model for the vibration signals of a fixed-axis spur gearbox with a tooth crack working under variable speed conditions is introduced herein, which is shown in Eq. (4.1).

$$y(t) = y_{AF}(t) + \beta y_{Imp}(t) + N(t) \tag{4.1}$$

where $y_{AF}(t)$ denotes the gear mesh-related components; $\beta y_{Imp}(t)$ is the CII and β is the CII magnification factor representing the tooth crack severity level; $N(t)$ is the background noise.

Under variable speed conditions, $y_{AF}(t)$ can be expressed using Eq. (4.2).

$$y_{AF}(t) = \sum_{m=1}^{M} Q_m^{AF}(t)[1 + a_m(t)] \cos\left[2\pi m N_g \int f_s dt + \theta_m + b_m(t) + P_m^{AF}(t)\right] \tag{4.2}$$

where $Q_m^{AF}(t)$ and $P_m^{AF}(t)$ denote the AM and FM induced by variable speed conditions, respectively; $a_m(t)$ and $b_m(t)$ are the tooth crack-related AM and FM, respectively; θ_m is the initial phase, N_g is the number of gear teeth, f_s is the variable rotational frequency of the gear shaft.

Under variable speed conditions, $\beta y_{Imp}(t)$ is expressed using Eq. (4.3).

$$\beta y_{Imp}(t) = H(t - t_{oc}) \sum_{i=1}^{I} Q_i^{Imp}(t - t_{oc}) X_i e^{-D_i(t - t_{oc})} \cos\left[2\pi f_{ri}(t - t_{oc}) + \theta_i^{Imp}\right] \tag{4.3}$$

where *I* is the number of terms; $Q_i^{Imp}(t)$ denotes the AM induced by variable speed conditions; t_{oc} is the occurrence time vector of the CII pulses (effect of the speed variation-induced FM is included in t_{oc}); $H(t)$ denotes the Heaviside function; X_i, D_i, and θ_i^{Imp} represent the amplitude, damping factor and initial phase, respectively; f_{ri} is the i^{th} resonance frequency.

From Eq. (4.1), it is seen that for a gearbox with one tooth crack, its vibration signal includes three parts, namely the gear mesh-related components, the CII, and the background noise. Based on the gearbox vibration signal composition shown in Eq. (4.1), each part of the proposed normalization method is illustrated in the next subsection. Besides, the phenomenological model shown in Eq. (4.1) will be used to generate simulated vibration signals of a fixed-axis spur gearbox with a tooth crack for the simulation analysis presented in Section 4.3.

4.2.2 Procedure of the proposed normalization method

The procedure of the proposed normalization method is shown in Fig. 4.1, from which it is seen that the proposed normalization method consists of three parts: removal of FM, extraction of CII, and removal of AM. Each part is introduced in the following.

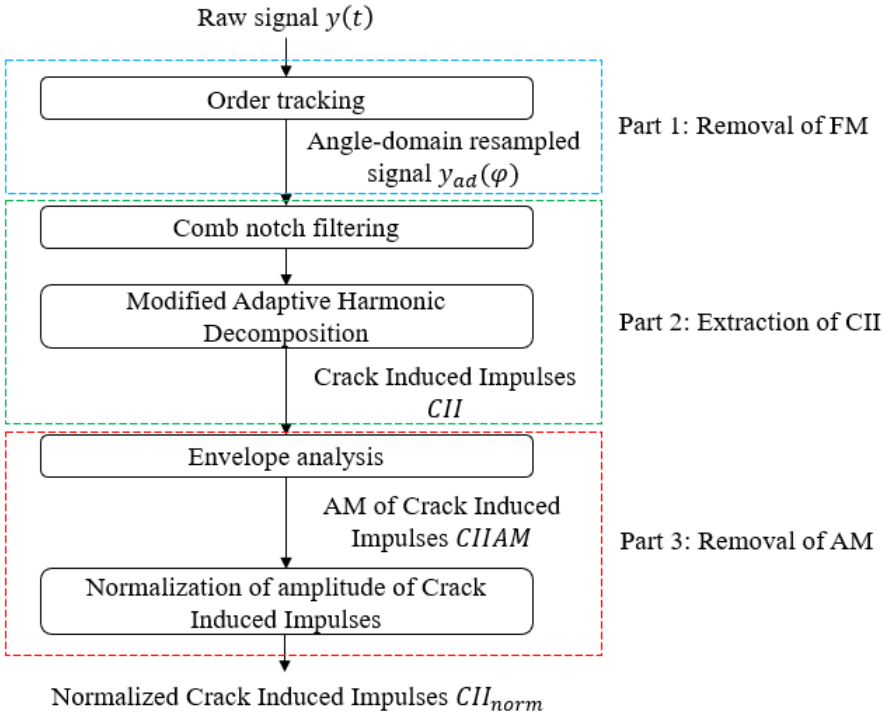

Fig. 4.1: Procedure of the proposed normalization method

4.2.2.1 Part 1: Removal of FM

The variable speed condition induces an FM into gearbox vibration signals. The speed variation-induced FM effect needs to be removed, which can be done using the well-developed computed order tracking technique [100]. To compensate for the speed variation-induced FM, a speed signal is required for angle domain resampling, which can be obtained using a collected tachometer signal. After removing the FM, the original gearbox vibration signal in the time domain is converted into its counterpart in the angle domain, namely $y(t)$ is converted into $y_{ad}(\varphi)$.

4.2.2.2 Part 2: Extraction of CII

For the vibration signal of a fixed-axis gear with a tooth crack with its FM effect removed, its order spectrum is mainly dominated by gear mesh order and its multiples and the sidebands around them,

which is related to the angle-domain resampled counterpart of y_{AF} in Eq. (4.1), and the order-cluster resulting from the CII (βy_{Imp} in Eq. (4.1)). The order-cluster is a group of characteristic orders of the tooth crack, with uniform spacing in the order spectrum. The gear mesh order and its multiples and the sidebands around them have no direct relationships with the order-cluster resulting from the CII, even though they may overlap in the order spectrum. Therefore, they need to be removed before extracting the CII, which can be done using comb notch filtering. Afterwards, the resulting signal is supposed to include the CII and environmental noise. But due to the strong environmental noise, it is still hard to extract the CII from the resulting signal. In this chapter, the modified AHD method presented in Subsection 3.2.2.3 of Chapter 3, which is a modified version of the original AHD method [88], is adopted to extract the CII from gearbox vibration signals under variable speed conditions, which is briefly introduced in the following.

Under constant speed conditions, the CII, which is the $\beta y_{Imp}(t)$ in Eq. (4.1), are periodic in the time domain. In addition, the CII can be equivalently represented as the summation of their corresponding harmonic-cluster [88], which is shown in Eq. (4.4). This is the same as Eq. (3.18) in Chapter 3.

$$\beta y_{Imp}(t) = \sum_{p=1}^{P} s_p(t) = \sum_{p=1}^{P} a_p \cos\left(2\pi f_p t + \theta_p\right) \tag{4.4}$$

where $s_p(t)$ denotes the p^{th} harmonic of the harmonic-cluster resulting from the CII; a_p, f_p, and θ_p are the amplitude, frequency, and initial phase of the p^{th} harmonic, respectively; the difference of f_p and f_{p-1} is the same, which is the tooth crack repetition frequency.

The original AHD method was used to obtain each harmonic harmonic $s_p(t)$ in Eq. (4.4) [88]. After all the desired harmonics are obtained by AHD recursively, the CII is reconstructed by adding all the obtained harmonics together, thus achieving the goal of extracting the CII from gearbox vibration signals under constant speed conditions.

Under variable speed conditions, the CII is shown in Eq. (4.3). In this situation, it has an FM due to speed variation and is no longer periodic in the time domain, thus cannot be represented as the summation of a group of harmonics. Therefore, the original AHD algorithm [88] is no longer suitable to extract the CII under variable speed conditions. To tackle this problem, the CII is first resampled in the angle domain to remove the FM caused by the variable speed conditions. Without

loss of generality, one term is considered in Eq. (4.3) for simplicity of derivation, namely $i = 1$. Similar to the case of constant speed conditions, for the variable speed conditions, the resampled CII become quasi-periodic in the angle domain, which means that the repetition angles of the pulses of the CII are equally spaced while the resonance frequency and the damping factor are variable in the angle domain. The resampled CII result in an order-cluster in the order domain, i.e., the equivalent tooth crack characteristic order and its multiples in the order spectrum. For different variable speed conditions, their corresponding equivalent tooth crack characteristic orders may be different. The equivalent conversion between the resampled CII and its corresponding order-cluster can be expressed using Eq. (4.5), which shares the same mathematical representation as Eq. (3.19).

$$\beta y_{Imp\_ad}(\varphi) = \sum_{k=1}^{K} s_k(\varphi) = \sum_{k=1}^{K} a_k(\varphi)\cos\left(R_k\varphi + \theta_k(\varphi)\right) \tag{4.5}$$

where K is the number of orders in the order-cluster; $R_k = k * ORC$ denotes the k^{th} order in the order-cluster, i.e. k^{th} multiple of the ORC, and the ORC is the equivalent tooth crack characteristic order; $s_k(\varphi)$ is the component of the resampled CII, which corresponds to the R_k in the order spectrum; $a_k(\varphi)$ and $\theta_k(\varphi)$ are the amplitude and phase of $s_k(\varphi)$, respectively.

The modified AHD method presented in in Subsection 3.2.2.3 of Chapter 3 is adopted to obtain each order component $s_k(\varphi)$ of CII in E. (4.5) under variable speed conditions. For simplicity, details of the modified AHD method are not introduced herein. After all the other desired order components $s_k(\varphi)$ are obtained, the reconstruction of the CII in the angle domain can be completed by summing them, thus achieving the goal of extracting the CII from gearbox vibration signal under variable speed conditions.

4.2.2.3 Part 3: Removal of AM

The speed variation-induced AM of the CII is the peak envelope of the CII, which is the same as the *CIIAM* presented in Subsection 3.2.2.4 in Chapter 3. To remove the *CIIAM*, two steps need to be completed, namely the calculation of the *CIIAM* and the implementation of amplitude normalization. The calculation of *CIIAM* can be conducted using the envelope analysis method presented in Subsection 3.2.2.4 in Chapter 3. Afterwards, the obtained *CIIAM* is used to normalize the CII, thus removing the speed variation-induced AM of the CII. The normalized CII is calculated using Eq. (4.6), which not only removes the speed variation-induced AM of the CII but also preserves the crack information.

$$CII_{norm} = (CII/CIIAM) \cdot M_{CIIAM} \tag{4.6}$$

where CII_{norm} is the normalized CII with the speed variation-induced AM removed; M_{CIIAM} is the mean value of $CIIAM$, which contains tooth crack growth information.

After completing all steps of the procedure shown in Fig. 4.1, the normalized CII is obtained and is further utilized to calculate CIs to track tooth crack severity progression. In this study, the RMS and the Envelope Harmonic-to-Noise Ratio (EHNR) [134] are employed to track tooth crack severity progression since they have shown their effectiveness in the condition monitoring and fault diagnosis of rotary machinery. Therefore, RMS and EHNR of the normalized CII (CII_{norm}) are calculated to track tooth crack severity progression under variable speed conditions. In Ref. [80], the CII were also extracted from the normalized raw vibration signal by removing the gear meshing-related components in the angle-domain. For comparison, the CII obtained using the NAMVOC method in Ref. [80] is also used to calculate CIs for tracking tooth crack severity progression under variable speed conditions.

4.2.3 Metrics for quantitative performance comparison

In Ref. [80], the performance of the NAMVOC method on removing the speed variation-induced AM was only evaluated qualitatively, failing to obtain accurate evaluation results. This chapter aims to make a quantitative evaluation of the performance of either the proposed normalization method or the NAMVOC method in terms of removing the speed variation-induced AM and not attenuating the crack information. To this end, its performance is evaluated in two aspects. The first aspect is the extent of removing the speed variation-induced AM. A higher extent of removing the speed variation-induced AM indicates a better performance. The second aspect is the degree of attenuating the tooth crack information. A lower degree of attenuating the crack information indicates a better performance. Because RMS and EHNR are used to track tooth crack severity progression, the first aspect of performance evaluation is equivalently achieved using the insensitivities of RMS and EHNR values to speed changes and the second one by the sensitivities of RMS and EHNR values to crack severity progression.

In this chapter, the FD metric, which is introduced in Subsection 3.2.4 in Chapter 3, is adopted quantitatively measure the insensitivity of RMS or EHNR values to speed changes. The Overall

Increase Rate (OIR) metric is introduced to quantitatively measure the sensitivity of RMS or EHNR values to tooth crack severity progression, which is calculated using Eq. (4.7).

$$OIR(v) = ((v_{end} - v_1)/(\beta_{end} - \beta_1)) \times 100\% \tag{4.7}$$

where v is the value vector of a CI; β is the magnification factor vector representing tooth crack severity level; subscripts "1" and "end" denote the first and last elements of a vector, respectively; v_1 is the CI value calculated using the signal of a gearbox with a tooth crack of crack level β_1.

The bigger the OIR value is, the more sensitive a CI is to tooth crack growth, thus indicating a lower degree of attenuating the information on tooth crack severity progression.

4.3 Simulated gearbox vibration signal analysis

In this section, simulated gearbox vibration signals under variable speed conditions, with constant torque load, are generated using the gearbox vibration signal model shown in Eq. (4.1). The proposed normalization method is applied to analyze the simulated signals. Each part of the proposed normalization method is illustrated during the analysis process. In addition, the NAMVOC method is also applied to process the simulated signals. Lastly, performance comparison is quantitatively made between the proposed normalization method and the NAMVOC method using the FD and OIR metrics

4.3.1 Generation of simulated gearbox vibration signal

To mimic the variable speed conditions, three speed profiles are adopted, namely coast-down (COA), run-up (RUN), and harmonic (HAR) profiles. COA and RUN speed profiles can represent the stop and start process of a gearbox used in a metro train. HAR speed profile can represent the speed variations encountered in the wind turbine gearboxes. The three speed profiles, i.e., COA, RUN and HAR, are expressed using Eq. (4.8), Eq. (4.9), and Eq. (4.10), respectively, and are plotted in Fig. 4.2.

$$f_s = 12 - 3t \tag{4.8}$$

$$f_s = 7 + 2t \tag{4.9}$$

$$f_s = 9 + 3\,sin(\pi t) + sin(4\pi t) \tag{4.10}$$

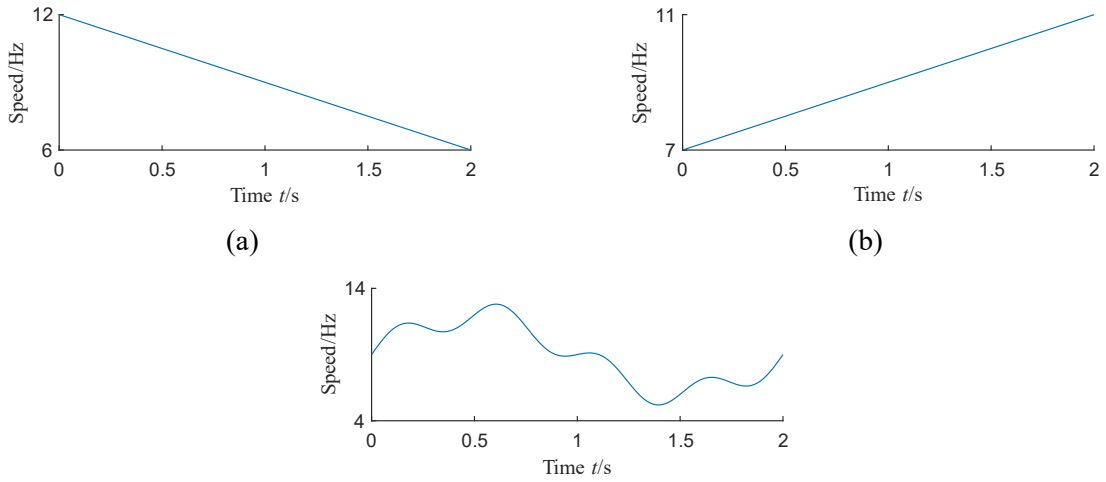

Fig. 4.2: Three variable speed profiles: (a) COA; (b) RUN; (c) HAR

Gearbox vibration signals for variable speed and constant load (load means the torque applied to the gearbox) conditions are generated using Eqs. (4.1), (4.2), and (4.3). Without loss of generality, for the gearbox vibration signal model shown in Eq. (4.1), two terms in Eq (4.2) and one term in Eq. (4.3) are considered to generate simulated signals. Parameters for each term of $y_{AF}(t)$ are listed in Eqs. (4.11) through (4.15) and those for $y_{Imp}(t)$ are shown in Eq. (4.16). In these equations, the unit for amplitude variables is "ms^{-2}", the unit for phase variables is "rad", the unit for damping factor is "$\mathrm{rad/s}$", the unit for frequency variables is "Hz", and the unit for the time variables is "s". A white Gaussian noise with SNR=10 dB is added to mimic environmental noise.

$$Q_1^{AF}(t) = 0.01f_s^3 + 0.1f_s; \qquad Q_2^{AF}(t) = 0.02f_s^3 + 0.2f_s \tag{4.11}$$

$$P_1^{AF}(t) = 0.1\cos(2\pi \int f_s dt); \qquad P_2^{AF}(t) = 0.2\cos(4\pi \int f_s dt) \tag{4.12}$$

$$a_1(t)=0.4\,sin(2\pi \int f_s dt); \qquad a_2(t)=0.8\sin(4\pi \int f_s dt) \tag{4.13}$$

$$b_1(t)=0.1\,sin(2\pi \int f_s dt); \qquad b_2(t)=0.2\sin(4\pi \int f_s dt) \tag{4.14}$$

$$\theta_1=0.5\pi\,; \qquad \theta_2=0.25\pi\,; \qquad N_g=100 \tag{4.15}$$

$$Q_1^{Imp}(t) = f_s;\ X_1=1;\ \theta_1^{Imp}=0;\ D_1=0.5;\ f_{r1}=1000 \tag{4.16}$$

To mimic different gear tooth crack severity levels, the magnification factor β in Eq. (4.1) is ranging from 0 to 6 with an increment of 1 and ranging from 6 to 12 with an increment of 2. Therefore, 10 tooth crack severity levels are considered. For the HAR speed profile shown in Fig. 4.2(c), its

simulated vibration signals are displayed in Fig. 4.3 as an example. Simulated vibration signals for COA and RUN speed profiles are not shown herein for brevity.

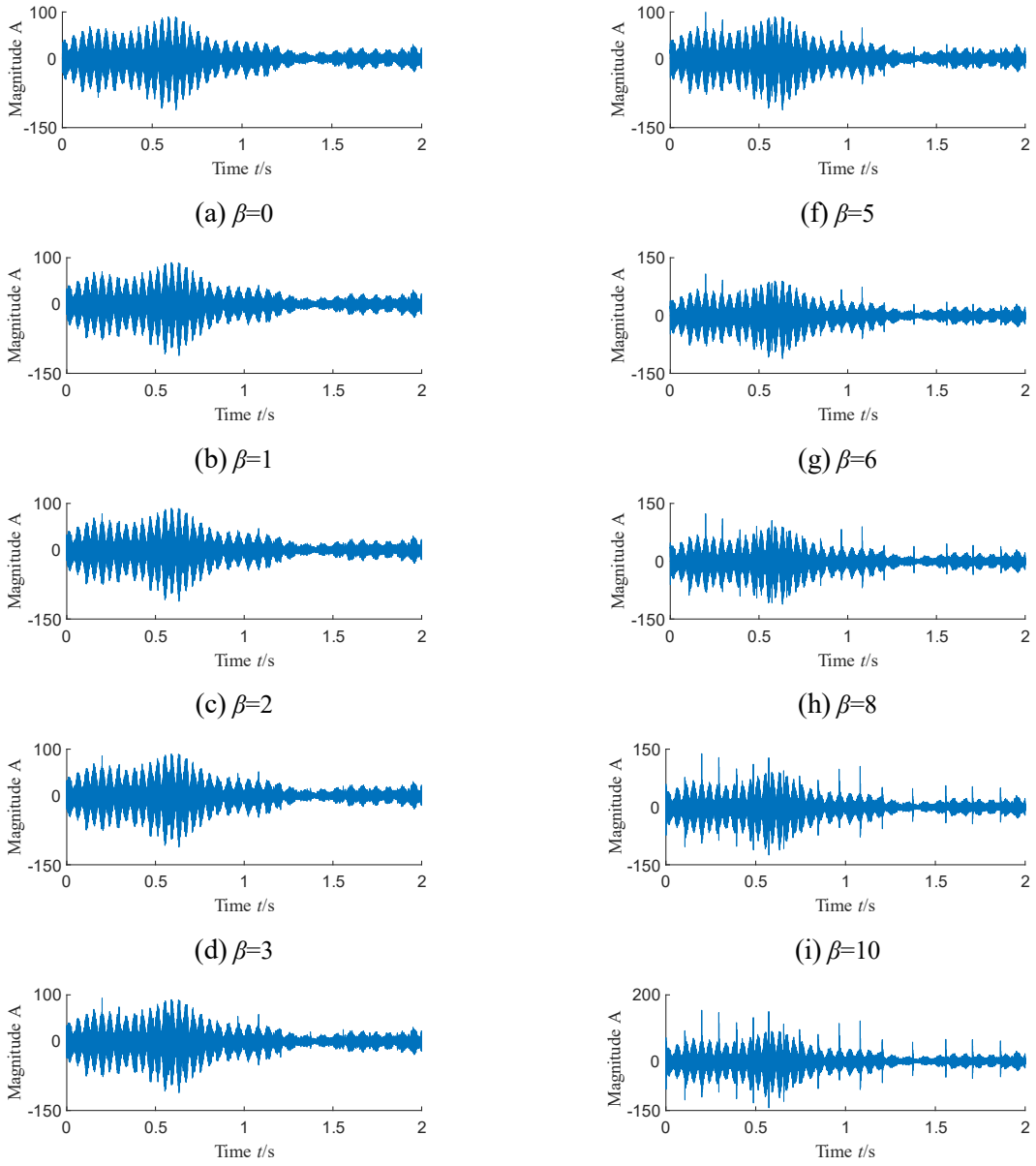

Fig. 4.3: Simulated gearbox vibration signals under harmonic speed profile for 10 crack severity levels

The RMS results of the raw simulated vibration signals under the three considered speed profiles are calculated and are shown in Fig. 4.4, from which it is seen that although the crack severity levels (β values) are the same, the RMS results are different for the three speed profiles. This means that other than gear tooth crack severity progression, variable speed conditions also result in changes in

the RMS values. Therefore, it will be hard to distinguish between changes of tooth crack severity and speed changes using the CIs if the AM induced by variable speed conditions is not removed.

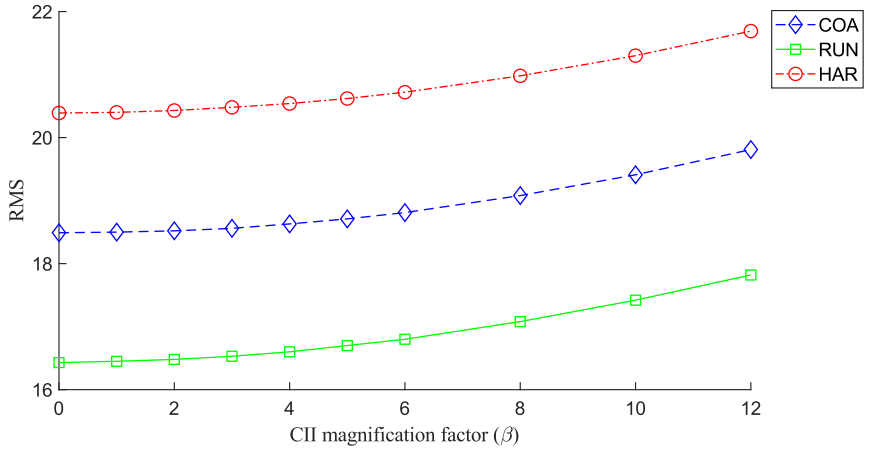

Fig. 4.4: The RMS values for the raw simulated vibration signals under three speed profiles

4.3.2 Analysis results

To remove the AM induced by variable speed conditions, the proposed normalization method is used to process the simulated vibration signals. Analysis results are presented to illustrate each part of the proposed normalization method. The simulated signal for β=5 under the HAR speed profile shown in Fig. 4.5 is used as an example for illustration. From Fig. 4.5, it is seen that there exists a frequency smearing phenomenon due to the FM effect induced by speed variation.

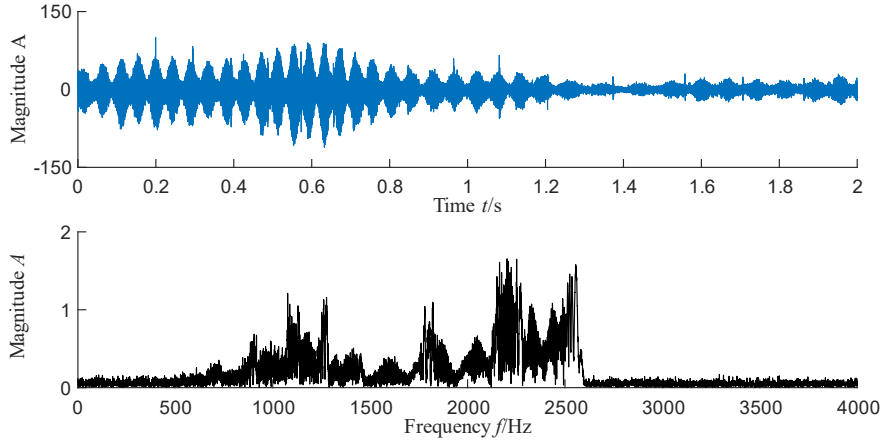

Fig. 4.5: Time waveform and frequency spectrum for raw simulated vibration signal (β=5, HAR)

In Part 1 of the proposed normalization method shown in Fig. 4.1, the FM induced by speed variation is removed using the order tacking technique. The obtained signal with FM effect removed and its order spectrum are displayed in Fig. 4.6. The order spectrum in the bottom plot of Fig. 4.6 is displayed on a log amplitude scale. This can benefit identifying the resonance excited by the tooth crack, which is in the order band from 50 to 120. As shown in the bottom plot of Fig. 4.6, the gear mesh related orders are clearly seen in the order spectrum, which means that the FM is well removed. In Part 2, the comb notch filter is first adopted to remove the gear mesh order and its multiples and the sidebands around them. Subsequently, the modified AHD is utilized to extract the CII. For the modified AHD algorithm, parameters λ, η, and ε are set to be 10^{-12}, 10^{-14}, and 10^{-8}, respectively. The extracted CII is shown in Fig. 4.7 together with its zoomed-in view from 32 rad to 42 rad, from which it is seen that the CII are well extracted without distortion and amplitude attenuation. This is due to the robustness of the modified AHD to interfering factors, such as the strong background noise, and its suitability for CII extraction. In addition, from the zoomed-in view of the CII shown in Fig. 4.7(b), it is found that for each pulse (or impact response) of the CII, its angular duration is about 0.3rad, which means that one tooth crack affects about 5 tooth mesh cycles. In Part 3, the first step is to calculate the peak envelope of the extracted CII shown in Fig. 4.7(a). The peak envelope of the CII is seen as the AM induced by variable speed conditions, namely the *CIIAM*. The identified envelope peaks and the *CIIAM* are plotted in Fig. 4.8. The *CIIAM* is used to normalize the CII. The normalized CII is shown in Fig. 4.9. Comparing Fig. 4.9 to Fig. 4.7(a), it is seen that after normalization, the AM of the CII is removed and the information on the tooth crack severity is not attenuated.

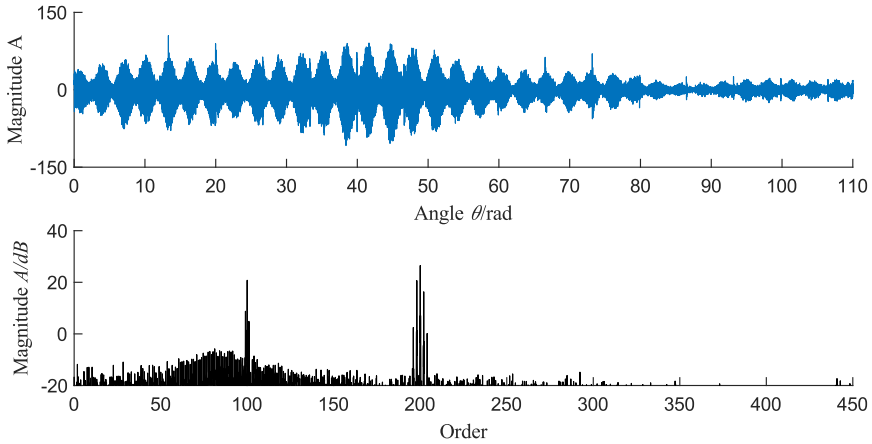

Fig. 4.6: Raw simulated vibration signal with the FM effect removed and its order spectrum

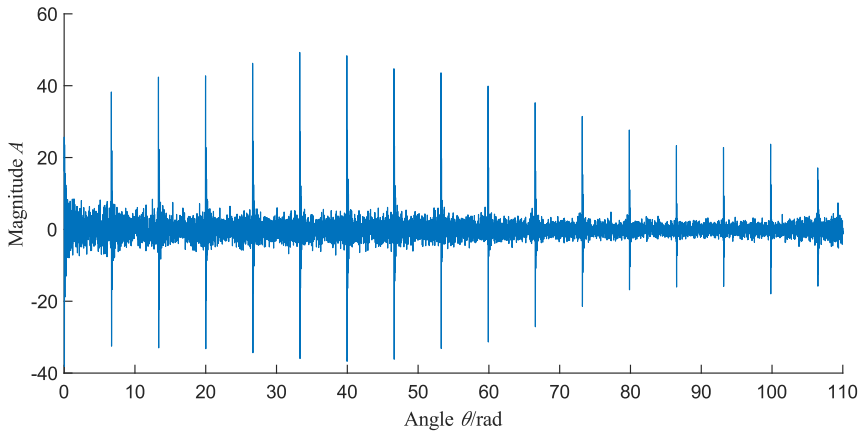

(a) Full-scale view

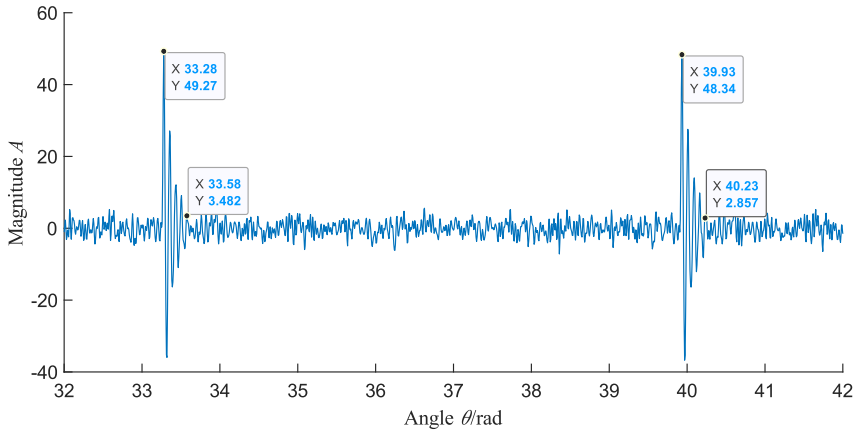

(b) Zoomed-in view in the angle range [32, 42] rad

Fig. 4.7: The CII obtained using the modified AHD method

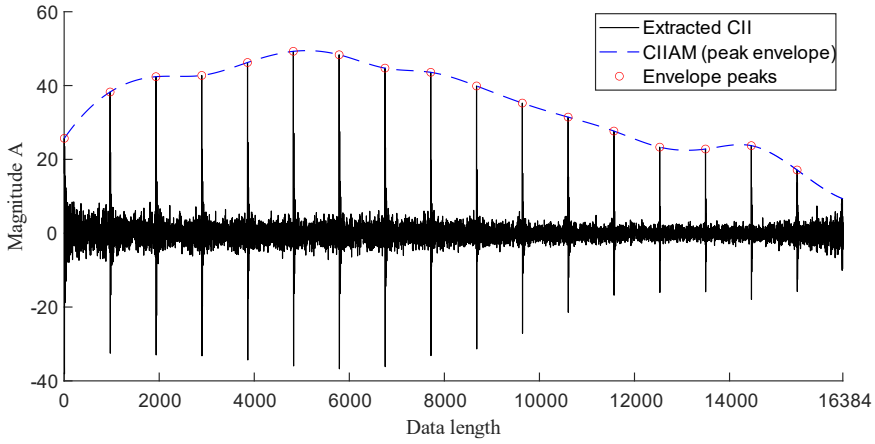

Fig. 4.8: The *CIIAM* (speed variation-induced AM of the CII) and envelope peaks

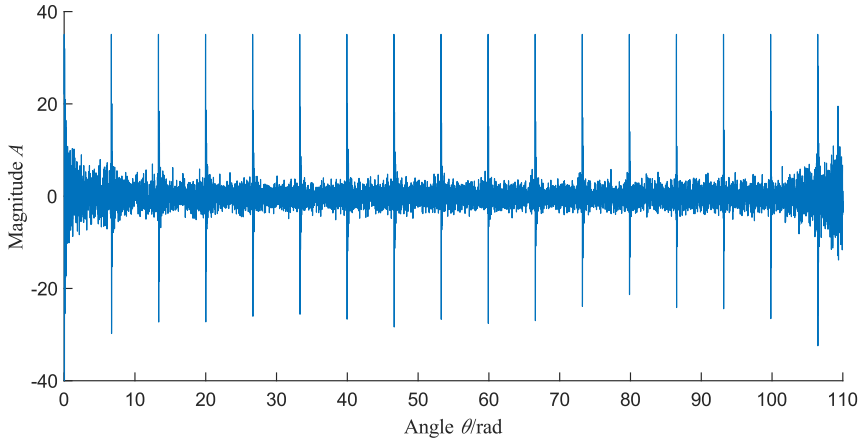

Fig. 4.9: The normalized CII (with AM effect removed) obtained by the proposed method

4.3.3 Performance comparison

To make performance comparison between the proposed normalization method and the NAMVOC method, the latter is also applied for simulated signal analysis. The length of the moving median filter is set to be 1 second. The speed variation-induced AM obtained by the NAMVOC method is shown in Fig. 4.10(a) and the normalized raw signal is shown in Fig. 4.10(b). From Fig. 4.10(b), it is seen that the speed variation-induced AM is not completely removed since these still exists amplitude fluctuation in the normalized raw signal. The normalized raw signal is resampled in the angle domain to remove the FM induced by speed changes. Gear meshing-related components are removed from the resampled normalized raw signal using comb notch filtering to obtain the CII. The obtained CII is shown in Fig. 4.11, from which it is found that the CII obtained by the NAMVOC method still has large amplitude fluctuation induced by variable speed conditions, which means that the speed variation-induced AM is not well removed.

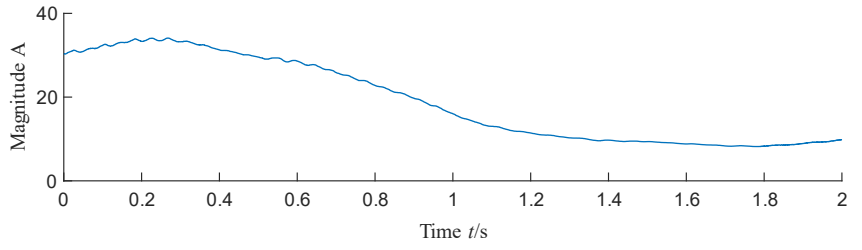

(a) The AM

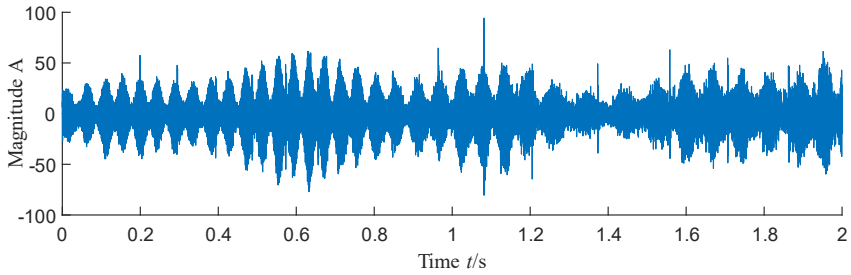

(b) The normalized raw signal

Fig. 4.10: The AM and the normalized raw signal obtained by the NAMVOC method

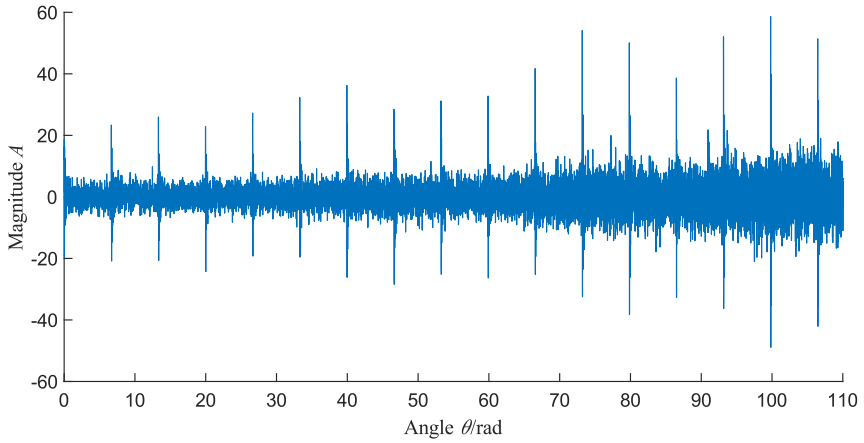

Fig. 4.11: The CII obtained by the NAMVOC method

After adopting both the proposed normalization method and the NAMVOC method for simulation analysis, two kinds of CIIs are obtained: (1) the CII obtained by the proposed normalization method, which is named CII-Proposed, (2) the CII obtained by the NAMVOC method, which is named CII-NAMVOC. Based on these two types of CIIs, RMS and EHNR values are calculated. RMS and EHNR results for CII-Proposed are plotted in Fig. 4.12 and those for CII-NAMVOC are plotted in Fig. 4.13. As shown in Fig. 4.12, RMS and EHNR results for the CII-Proposed are not only sensitive to crack severity progression due to the monotonic increasing trend of CIs, but also are insensitive to speed changes since there is almost no spread between the three curves. On the contrary, as shown in Fig. 4.13, the RMS values for the CII-NAMVOC are less sensitive to tooth crack severity progression and the EHNR values are sensitive to speed changes due to bigger spread between curves of EHNR. These observations are obtained based on qualitative evaluations.

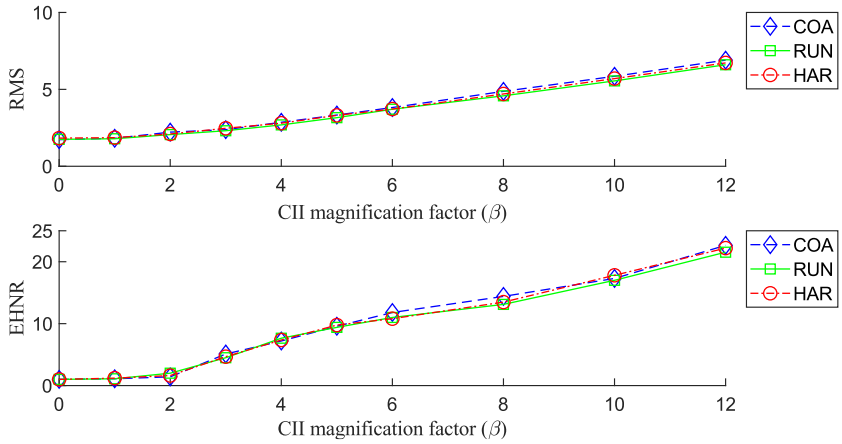

Fig. 4.12: The RMS and EHNR values calculated using the CII-Proposed

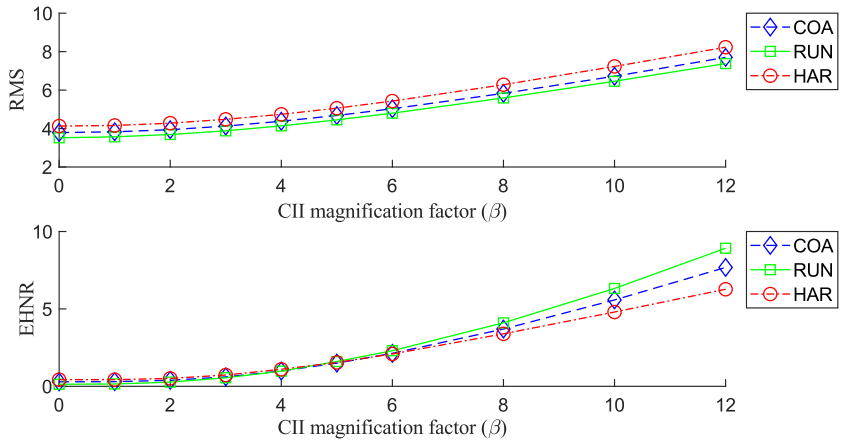

Fig. 4.13: The RMS and EHNR values calculated using the CII-NAMVOC

In addition, to make quantitative evaluation of the performance on removing the speed variation-induced AM and preserving the tooth crack information, the OIR and FD metrics are adopted to measure the sensitivities of the RMS and EHNR values to the changes of tooth crack severity and their insensitivities to speed changes, respectively. The OIR and FD values calculated using the RMS and EHNR results of the CII-Proposed are tabulated in Table 4.1 and Table 4.2, respectively. The OIR and FD values calculated using the RMS and EHNR results of the CII-NAMVOC are shown in Table 4.3 and Table 4.4, respectively. It should be noted that in Table 4.2 and Table 4.4, suffix "_CH" denotes the FD between CI curves for coast-down and harmonic speed profiles, "_RC" the FD between CI curves for run-up and coast-down speed profiles, "_RH" the FD between CI curves for run-up and harmonic speed profiles.

Table 4.1: The OIR values for RMS and EHNR of the CII-Proposed (simulated signal)

CI for CII-Proposed under a speed profile	OIR (%)
RMS_CII-Proposed_COA	43.08
RMS_CII-Proposed_RUN	40.42
RMS_CII-Proposed_HAR	40.75
Average of OIR of RMS_CII-Proposed	41.42
EHNR_CII-Proposed_COA	180.42
EHNR _CII-Proposed_RUN	171.17
EHNR _CII-Proposed_HAR	176.67
Average of OIR of EHNR_CII-Proposed	176.08

Table 4.2: The FD values for RMS and EHNR of the CII-Proposed (simulated signal)

CI curves for CII-Proposed under two speed profiles	FD
RMS_CII-Proposed_CH	0.3632
RMS_CII-Proposed_RC	0.6048
RMS_CII-Proposed_RH	0.3528
Average of FD of RMS_CII-Proposed	0.4403
EHNR_CII-Proposed_CH	1.6155
EHNR _CII-Proposed_RC	2.1376
EHNR _CII-Proposed_RH	1.2934
Average of FD of EHNR_CII-Proposed	1.6822

Table 4.3: The OIR values for RMS and EHNR of the CII-NAMVOC (simulated signal)

CI for CII- NAMVOC under a speed profile	OIR (%)
RMS_CII- NAMVOC _COA	32.58
RMS_CII- NAMVOC _RUN	32.17
RMS_CII- NAMVOC _HAR	34.17
Average of OIR of RMS_CII- NAMVOC	32.97
EHNR_CII- NAMVOC _COA	61.58
EHNR _CII- NAMVOC _RUN	73.25
EHNR _CII- NAMVOC _HAR	48.67
Average of OIR of EHNR_CII- NAMVOC	61.17

Table 4.4: The FD values for RMS and EHNR of the CII- NAMVOC (simulated signal)

CI curves for CII- NAMVOC under two speed profiles	FD
RMS_CII- NAMVOC _CH	1.2807
RMS_CII- NAMVOC _RC	0.8102
RMS_CII- NAMVOC _RH	2.0854
Average of FD of RMS_CII- NAMVOC	1.3921
EHNR_CII- NAMVOC _CH	1.6653
EHNR _CII- NAMVOC _RC	1.5331
EHNR _CII- NAMVOC _RH	3.1871
Average of FD of EHNR_CII- NAMVOC	2.1285

By comparing Table 4.1 and Table 4.3, it is seen that for either RMS or EHNR of the CII-Proposed, its average OIR value is greater than that of the CII-NAMVOC. Specifically, the average OIR value for RMS: 41.42%>32.97%, the average OIR value for EHNR: 176.08%>61.17%. This means that the RMS and EHNR of the CII-Proposed are more sensitive to crack severity progression than those of the CII-NAMVOC, indicating that the proposed normalization method results in a lower degree of attenuating the crack information than the NAMVOC method in the normalization process.

By comparing Table 4.2 and Table 4.4, it is seen that for either RMS or EHNR of the CII-Proposed, its average FD value is smaller than that of the CII-NAMVOC. To be specific, the average FD value for RMS: 0.4403<1.3921, the average FD value for EHNR: 1.6822<2.1285. This means that RMS and EHNR of the CII-Proposed are more insensitive to speed changes than those of the CII-NAMVOC, thus indicating that the proposed normalization method results in a higher degree of removing the AM effect induced by variable speed conditions than the NAMVOC method.

Therefore, based on the quantitative performance comparisons for the simulated signal analysis, it can be concluded that the proposed normalization method outperforms the NAMVOC method in terms of removing the AM induced by variable speed conditions and preserving the information on tooth crack severity progression.

4.4 Experimental validation

In this section, the effectiveness of the proposed normalization method in terms of removing the AM and FM induced by variable speed conditions and preserving the crack information is further validated using experimental gearbox vibration datasets.

4.4.1 Experiment setup

Details of experiment setup have been introduced in Subsection 3.4.1, including the introduction to the experimental fixed-axis spur gearbox, the considered pinion tooth crack severity levels, the specifications of variable speed conditions, and the configurations of data collection. The experimental gearbox vibration signals collected under the constant load and variable speed conditions shown in Fig. 3.26 are used in this chapter.

4.4.2 Analysis results

The proposed normalization method is adopted to analyze the experimental datasets of the fixed-axis gearbox with a pinion tooth crack collected under both SPI and SPII speed conditions shown in Fig. 3.26. The raw acceleration signal for "Faulty 3" pinion health state under SPI speed condition, which is shown in Fig. 4.14, is used as an example to illustrate the proposed normalization method. As shown in the bottom plot of Fig. 4.14, there exists a frequency smearing phenomenon in the frequency spectrum, which means that the variable speed condition causes an FM into the gearbox vibration signal. The raw vibration signal is resampled in the angle domain to compensate for the FM effect using the order track technique. The obtained signal with the FM effect removed and its order spectrum are displayed in Fig. 4.15, from which the gear mesh related orders are clearly seen in the order spectrum, which means that the speed variation-induced FM is well removed.

The comb notch filter is adopted to remove the gear mesh order and its multiples and the sidebands around them. There are two gear mesh pairs in the target fixed-axis gearbox as shown in Fig. 2.12(b): (1) the input gear mesh pair with mesh order of 18; (2) the output mesh pair with order of 64. To remove all the gear mesh related components, both two groups of mesh orders and their multiples and the associated sidebands around them are removed using comb notch filters. The comb notch filtered signal mainly contains the components related to the CII and the

environmental noise. Subsequently, the modified AHD is employed to extract the order components resulting from the CII, by which the CII can be reconstructed. For the modified AHD algorithm, parameters λ, η, and ε are set to be 10^{-14}, 10^{-15}, and 10^{-8}, respectively. The obtained CII is shown in Fig. 4.16 together with the zoomed-in view from 130 order to 150 order. From Fig. 4.16(b), it is found that the CII is well extracted since the angle difference between two adjacent pulses is about 2π rad, which is the angular displacement of one pinion shaft revolution. For the pinion with one tooth crack, there exists one pulse in one pinion shaft revolution. This demonstrates the advantages of the modified AHD algorithm of extracting CII in the angle domain. Although the CII is well extracted, it still has large amplitude fluctuation caused by the variable speed conditions.

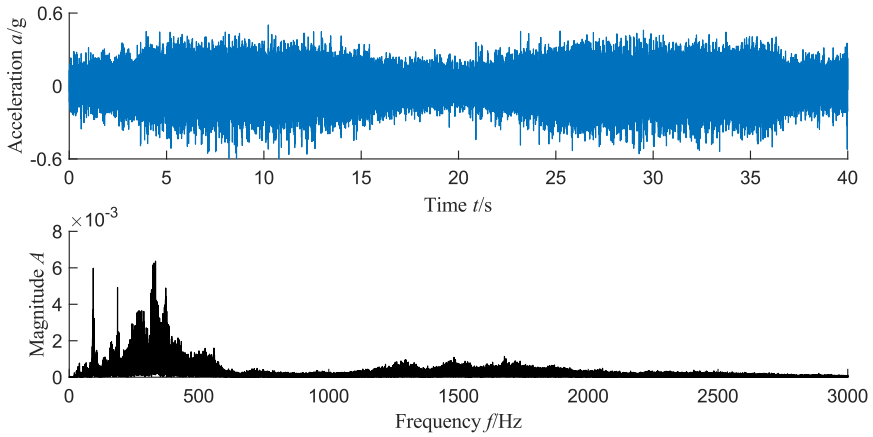

Fig. 4.14 Raw vibration signal (Faulty 3, SPI speed condition)

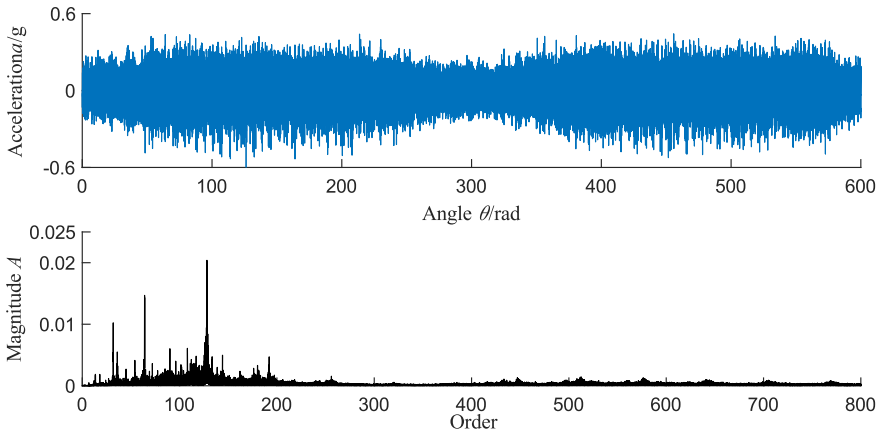

Fig. 4.15: Angle-domain resampled vibration signal (Faulty 3, SPI speed condition)

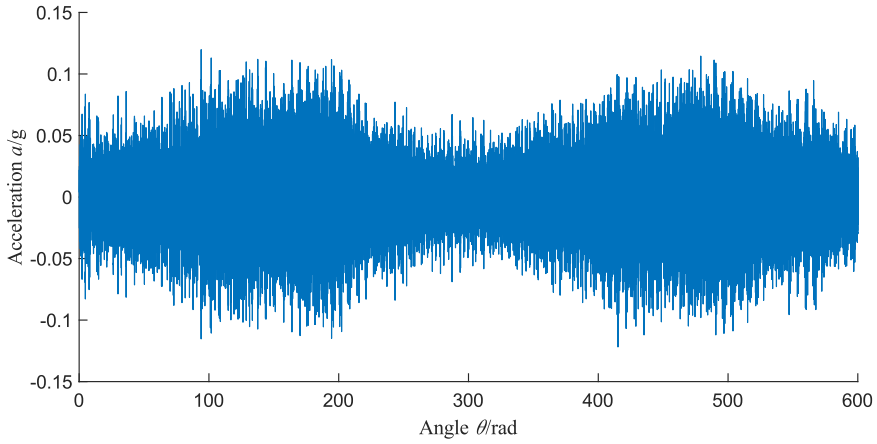

(a) Full-scale view

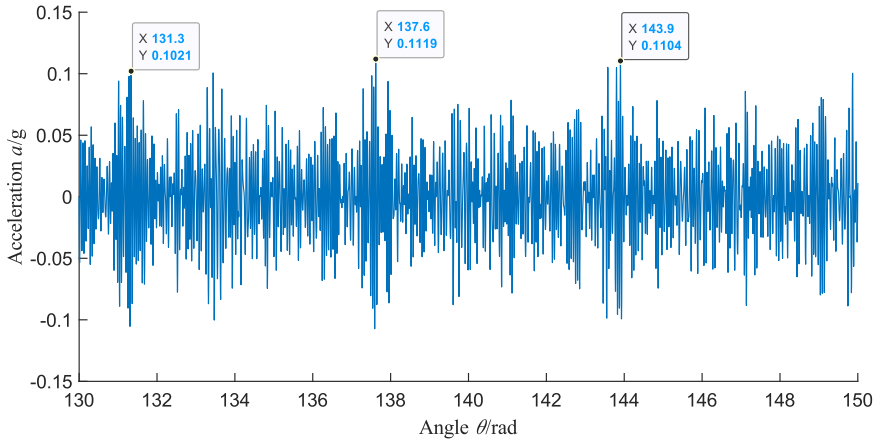

(b) Zoomed-in view in the angle range [130, 150] rad

Fig. 4.16: The extracted CII (Faulty 3, SPI speed condition)

Envelope peaks of the extracted CII are identified and are interpolated to get the peak envelope of CII. Besides, the peak envelope is smoothed. The smoothed peak envelope is regarded as the speed variation-induced AM of CII, namely *CIIAM*. The identified envelope peaks and *CIIAM* are shown in Fig. 4.17 together with the CII. The *CIIAM* is used to normalize the CII. The normalized CII is named "CII-Proposed" and is shown in Fig. 4.18. Comparing Fig. 4.18 to Fig. 4.16, it is seen that the speed variation-induced AM is removed by the proposed normalization method to a great extent since there is almost no amplitude fluctuation in the CII-Proposed in Fig. 4.18. The CII-Proposed will be used to calculate the RMS and EHNR values to track tooth crack severity progression.

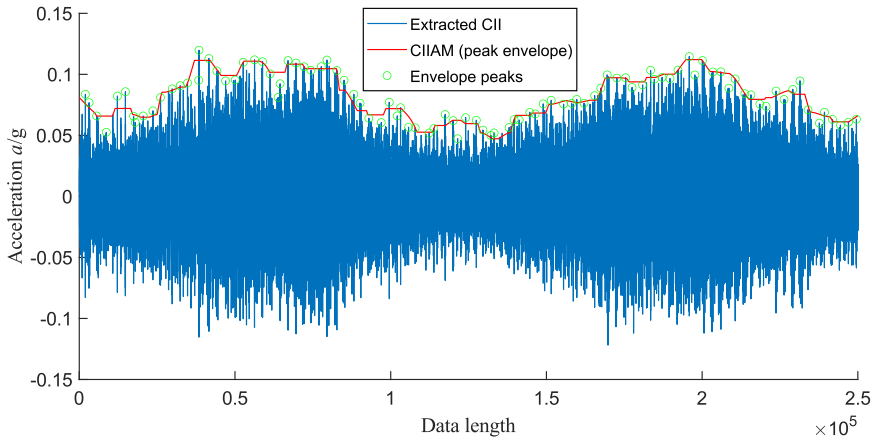

Fig. 4.17: The *CIIAM* and envelope peaks (Faulty 3, SPI speed condition)

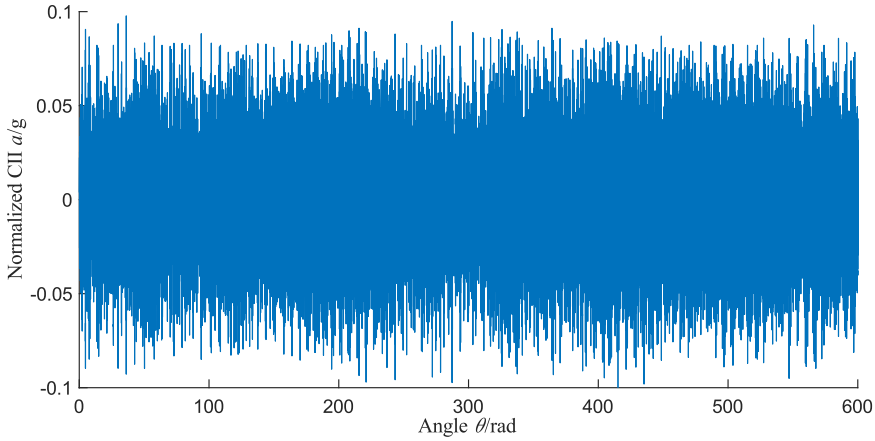

(a) Full-scale view

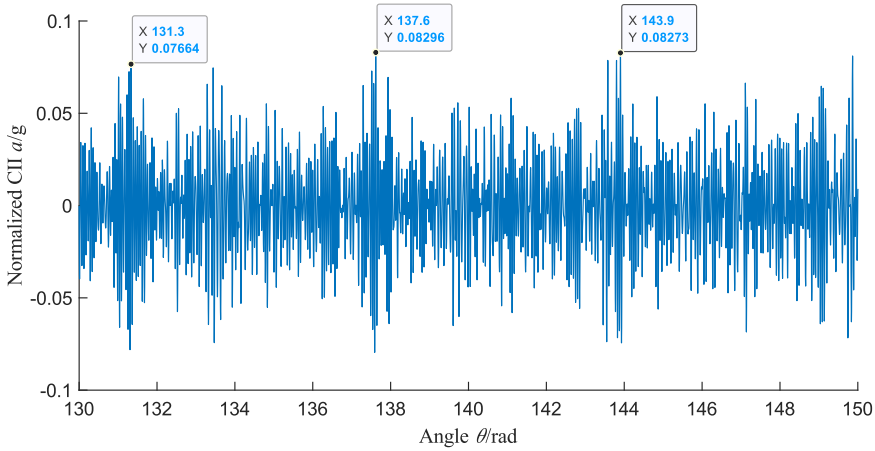

(b) Zoomed-in view in the angle range [130, 150] rad

Fig. 4.18: The normalized CII by the proposed method: CII-Proposed (Faulty 3, SPI speed condition)

4.4.3 Performance comparison

To make performance comparison between the proposed normalization and the NAMVOC method, the latter is also applied to process the experimental gearbox datasets. The length of the moving median filter is set to be 1 second as well. The speed variation-induced AM obtained by the NAMVOC method is shown in Fig. 4.19(a) and the normalized raw signal is shown in Fig. 4.19(b), from which it is seen that the speed variation-induced AM is not completely removed since there still exists amplitude fluctuation in the normalized raw signal. The normalized raw signal is resampled in angle domain to remove the FM resulting from speed variation. Gear mesh order and its multiples and the associated sidebands are removed from the resampled normalized raw signal using comb notch filters, thus obtaining the CII. The obtained CII is named "CII-NAMVOC" and is shown in Fig. 4.20, from which it is seen that the CII-NAMVOC still has large amplitude fluctuation induced by variable speed conditions, which means that the AM effect is not well removed by the NAMVOC method.

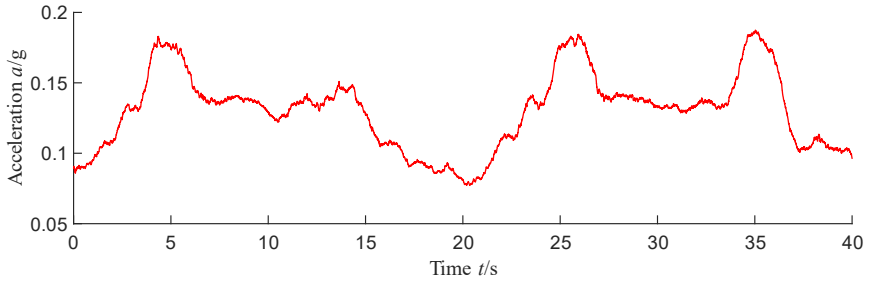

(a) The AM

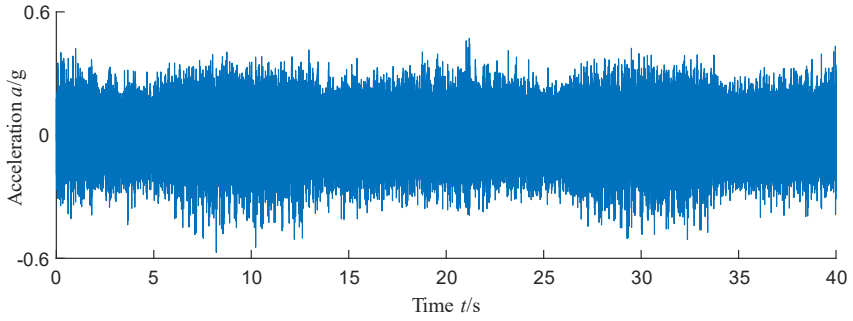

(b) The normalized raw signal

Fig. 4.19: The AM and the normalized raw signal obtained by NAMVOC method (Faulty 3, SPI speed condition)

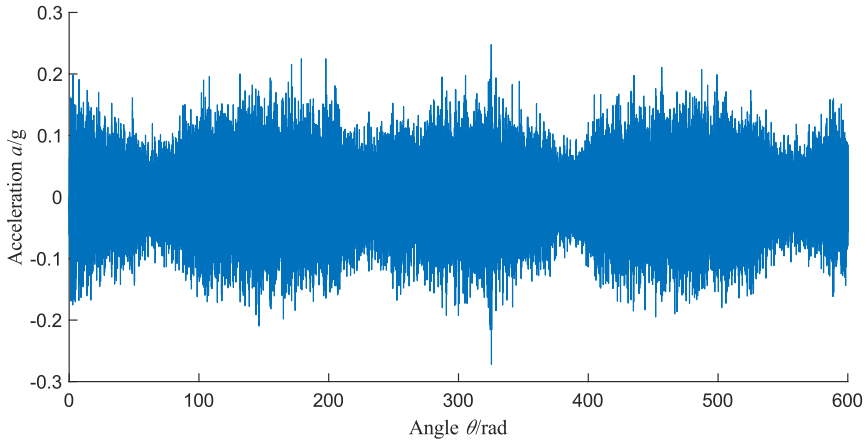

Fig. 4.20: The normalized CII obtained by the NAMVOC method: CII-NAMVOC (Faulty 3, SPI speed condition)

After adopting the proposed normalization method and the NAMVOC method to process the experimental gearbox datasets, two kinds of CIIs are obtained for each dataset, namely CII-Proposed and CII-NAMVOC. Based on them, the RMS and EHNR results are calculated. Because in the experiment, for each pinion health state, five data samples were collected under either the SPI or the SPII speed condition, five results are obtained for either RMS or EHNR for each pinion health state under each speed condition. The median value of the five results is calculated and is used to track tooth crack severity progression. Fig. 4.21 shows the median values of RMS and EHNR for the CII-Proposed versus pinion health state under both SPI and SPII speed conditions. Fig. 4.22 shows the median values of RMS and EHNR for the CII-NAMVOC versus pinion health state under both SPI and SPII speed conditions. As shown in Fig. 4.21, the RMS and EHNR values of the CII-Proposed are not only sensitive to tooth crack severity progression, but also insensitive to speed variation since the spread between the two curves in each plot is very small. On the contrary, as shown in Fig. 4.22, RMS values of the CII-NAMVOC are more sensitive to speed changes and EHNR values are less sensitive to tooth crack severity progression.

In addition, quantitative comparisons of the performance of the proposed normalization method and the NAMVOC method are also made. The OIR and FD metrics are adopted to measure the sensitivities of the RMS and EHNR values to the changes of tooth crack severity and their insensitivities to speed changes, respectively. The OIR and FD values calculated using the RMS and EHNR results of the CII-Proposed are tabulated in Table 4.5 and Table 4.6, respectively. The

OIR and FD values calculated using the RMS and EHNR results of the CII-NAMVOC are shown in Table 4.7 and Table 4.8, respectively.

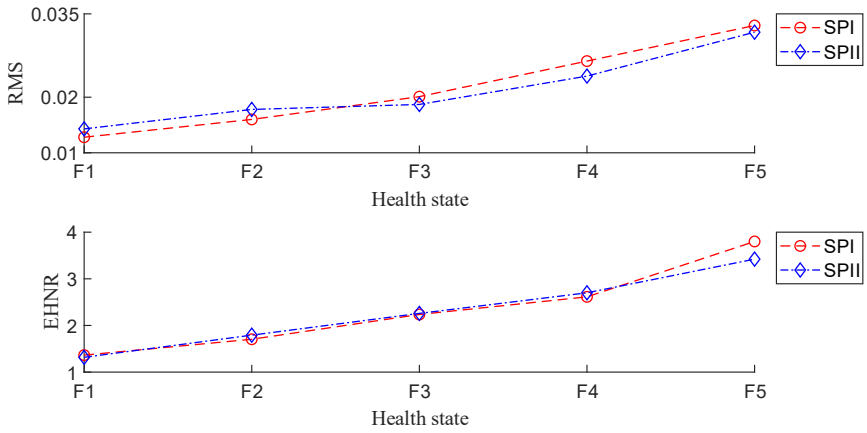

Fig. 4.21: Median values of RMS and EHNR results versus pinion health state (CII-Proposed)

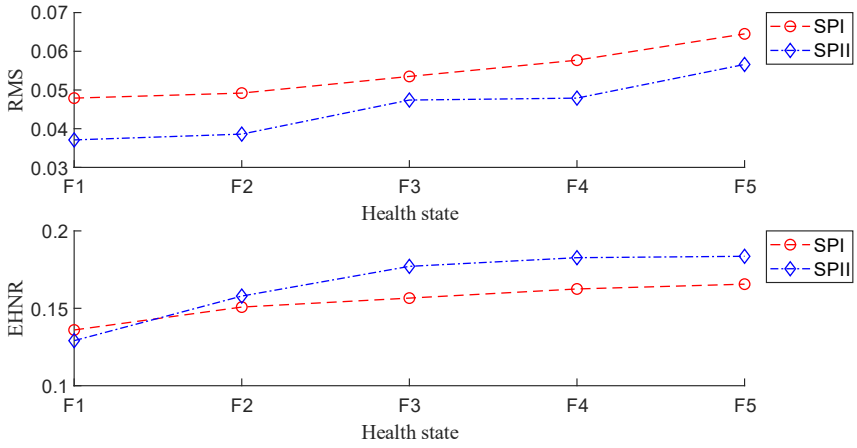

Fig. 4.22: Median values of RMS and EHNR results versus pinion health state (CII-NAMVOC)

Table 4.5: The OIR values for RMS and EHNR of the CII-Proposed (experimental data)

CI for CII-Proposed under a speed profile	OIR (%)
RMS_CII-Proposed_SPI	4.1875
RMS_CII-Proposed_SPII	3.6250
Average of OIR of RMS_CII-Proposed	3.9603
EHNR_CII-Proposed_SPI	507.6042
EHNR _CII-Proposed_SPII	438.5833
Average of OIR of EHNR_CII-Proposed	473.0937

Table 4.6: The FD values for RMS and EHNR of the CII-Proposed (experimental data)

CI curves for CII-Proposed under two speed profiles	FD
RMS_CII-Proposed	0.0040
EHNR_CII-Proposed	0.4017

Table 4.7: The OIR values for RMS and EHNR of the CII-NAMVOC (experimental data)

CI for CII- NAMVOC under a speed profile	OIR (%)
RMS_CII- NAMVOC _SPI	3.4583
RMS_CII- NAMVOC _SPII	4.0623
Average of OIR of RMS_CII- NAMVOC	3.7604
EHNR_CII- NAMVOC _SPI	6.1667
EHNR _CII- NAMVOC _SPII	11.3542
Average of OIR of EHNR_CII- NAMVOC	8.7604

Table 4.8: The FD values for RMS and EHNR of the CII- NAMVOC (experimental data)

CI curves for CII- NAMVOC under two speed profiles	FD
RMS_CII- NAMVOC	0.0206
EHNR_CII- NAMVOC	0.0354

By comparing Table 4.5 and Table 4.7, it is found that for either RMS or EHNR calculated using the CII-Proposed, its average OIR value is greater than that using the CII-NAMVOC. To be specific, the average OIR value for RMS: 3.9063%>3.7604%, the average OIR value for EHNR: 473.0937%>8.7604%. This means that the RMS and EHNR values of the CII-Proposed are more sensitive to tooth crack severity progression than those of the CII-NAMVOC, thus indicating that the proposed normalization method results in a lower degree of attenuating the information on crack severity progression than the NAMVOC method.

By comparing Table 4.6 and Table 4.8, it is observed that for the RMS values calculated using the CII-Proposed, its FD value is smaller than that using the CII-NAMVOC. To be specific, the FD value for RMS: 0.0040<0.0206. This means that the RMS of the CII-Proposed are more insensitive to speed changes than that of the CII-NAMVOC. However, the FD value of the EHNR calculated using the CII-Proposed is a little bit greater than that using the CII-NAMVOC.

Based on the quantitative performance comparison using the OIR and FD values, it is observed that the RMS and EHNR results of the CII-Proposed have higher sensitivities to pinion tooth crack

severity progression, and the RMS result of the CII-proposed has higher insensitivity to speed changes. Therefore, it can be concluded that the proposed normalization method overall outperforms the NAMVOC method in terms of removing the AM induced by variable speed conditions and preserving the information on pinion tooth crack severity progression.

4.5 Conclusions

In this chapter, a new normalization method is proposed to remove the AM and FM of gearbox vibration signal induced by variable speed conditions. The focus of the proposed normalization method is placed on the CII rather than the entire vibration signal, for the purpose of avoiding attenuating the information on tooth crack severity progression. The CII is extracted using the modified AHD in the angle domain. The peak envelope of the CII is calculated and is regarded as the speed variation-induced AM of the CII and is further used to normalize the CII. The normalized CII is employed to calculate the RMS and EHNR values to track tooth crack severity progression.

The proposed normalization method is investigated using both simulated gearbox vibration signals and experimental gearbox vibration datasets. Analysis results show the benefits of using the proposed normalization to conduct gear tooth crack diagnosis under variable speed conditions. Quantitative comparisons of the performance on the removal of the speed variation-induced AM and preservation of the crack information between the proposed normalization method and the NAMVOC method are made using the OIR and FD metrics. Comparison results indicate that both RMS and EHNR of the CII-Proposed have higher sensitivities to gear tooth crack severity progression than those of the CII-NAMVOC, and RMS of the CII-proposed has higher insensitivity to speed variation. This means that the proposed normalization method is more robust to speed changes than the NAMVOC method. Besides, the proposed method preserves more information on tooth crack severity progression during the normalization process than the NAMVOC method.

In this chapter, only the scenario of the variable speed and constant load condition is involved. The effectiveness of the proposed normalization method in terms of removing the operating condition variation-induced AM and FM will be further investigated for other scenarios of time-varying operating conditions, such as constant speed and variable load conditions and variable speed and variable load conditions.

Chapter 5: Analysis of vibration signals and detection for multiple tooth cracks in spur gearboxes

Due to the harsh working environment, gearboxes may suffer from either one single tooth crack or multiple tooth cracks. However, for fixed-axis spur gearboxes with multiple tooth cracks, their vibration characteristics and detection methods have rarely been studied. To overcome this problem, as mentioned in Section 1.3, this chapter aims to get a good understanding of the vibration characteristics of a fixed-axis spur gearbox with multiple tooth cracks and propose an effective method for detecting the number and locations of multiple tooth cracks. The materials in this chapter are covered by the fourth research topic (Topic #4). The organization of this chapter is as follows. In Section 5.1, an introduction to the reported studies on tooth crack diagnosis of fixed-axis spur gearboxes is made. Section 5.2 presents the proposed overall methodology for procuring insights into the vibration characteristics of a fixed-axis spur gearbox with multiple tooth cracks and detecting the number and locations of multiple tooth cracks. Simulation analysis and experimental validation for the proposed methodology are presented in Section 5.3 and Section 5.4, respectively. Lastly, the conducted study is concluded in Section 5.5. The results of this chapter are documented in a journal paper [108] which is under review at present.

5.1 Introduction

During the last few decades, many studies for tooth crack diagnosis using various techniques have been reported. TSA is a useful tool to remove the vibration components that are asynchronous with the shaft on which the gear to be monitored is mounted [42,111]. Based on TSA signals, some tooth crack diagnosis methods were developed. Wang [77] developed a resonance demodulation method to extract crack features from cracked gear TSA signals for crack detection, but it failed to track early tooth crack growth. To overcome the deficiency of the study reported in Ref. [77], Yang et al. [104] conducted a thorough study on the cracked gear TSA signals and developed two powerful condition indicators for early tooth crack severity assessment. In industrial applications, there exists speed fluctuations in gearboxes, which makes it hard to diagnose tooth cracks. To tackle this problem, a normalization strategy was developed to remove the effects on gearbox

signals caused by speed variations, thus facilitating tooth crack diagnosis [107]. To assess tooth crack severity more accurately, many intelligent diagnosis methods were also developed. Weighted K nearest neighbor classification algorithms were adopted to process diagnostic features characterizing gear conditions to classify different tooth crack levels under constant operating conditions [123,135]. Aiming at the challenge of lacking sufficient samples of cracked gear vibration signals, He et al. [136] developed a deep transfer multiwavelet auto-encoder to assess tooth crack severity. To deal with strong environmental noise and imbalanced datasets, Li et al. [137] designed a fusion confidence weight support matrix-based framework to diagnose gear tooth cracks.

Although many reported methods have been developed for tooth crack diagnosis, most of them only considered the scenario of one tooth crack in a gearbox, which is not always the case since gearboxes may suffer from multiple tooth cracks in some situations owing to their harsh working environment [13–15]. The mechanism for multiple tooth cracks occurring in gearboxes is introduced in Subsection 1.1.2, which is not described herein for brevity. For the multiple tooth cracks occurred in fixed-axis spur gearboxes, they include two possible categories: (1) cracks on two or more adjacent or nonadjacent teeth of a single gear; (2) cracks on teeth of two or more gears, usually on two mating gears [13–15]. For two mating gears, the smaller gear is called the pinion, and the larger one is called the gear or wheel.

Because multiple tooth cracks may occur in industrial applications, it is worthy of studying their vibration characteristics and detection methods. To this end, dynamic model-based methods are preferred since they can eliminate interferences of environmental noise and get a good understanding of gearbox vibration behaviors. Recently, Mohamed et al. [138] generated vibration signals of a spur gearbox with multiple tooth cracks using dynamic modelling and vibration signals were studied in both time and frequency domains. In Ref. [138], four categories of multiple tooth cracks on the pinion were considered, and several CIs, such as RMS and kurtosis, were adopted to track crack severity progression. However, no method for detecting the number and locations of cracked teeth was presented. Herein, “locations of cracked teeth” refers to where the cracked teeth are in gearboxes. Later, Rezaei et al. [139] developed a method for detecting multi-crack locations and lengths using the transmission error ratio, which worked well when the cracks were located far enough. However, for adjacent tooth cracks, the method became incompetent [139]. Besides,

in Refs. [138,139], all the cracked teeth were only located on the pinion, failing to involve the scenario of multiple tooth cracks on both the pinion and the gear in a spur gearbox.

To overcome the deficiencies of the studies reported in Refs. [138,139], this chapter aims to first get a good understanding of the vibration characteristics of a spur gearbox with multiple tooth cracks using dynamic modelling. Firstly, a dynamic model of a spur gearbox including a pinion and a gear is built. To mimic multiple tooth cracks, three scenarios are considered, which includes: (1) Scenario 1: two nonadjacent tooth cracks on the pinion and a healthy gear; (2) Scenario 2: two adjacent tooth cracks on the pinion and a healthy gear; (3) Scenario 3: one tooth crack on the pinion and one tooth crack on the gear. Tooth mesh stiffness formulae for each scenario is analytically derived using the potential energy method [26,33,69] and is further substituted into the gearbox dynamic model, thus generating vibration responses for the three scenarios of multiple tooth cracks. Subsequently, mesh stiffness and vibration signals are analyzed in both time and frequency domains to gain insights into the vibration characteristics of a spur gearbox with multiple tooth cracks. Inspired by the obtained insights, a novel method is proposed to detect the number and locations of multiple tooth cracks, the focus of which is placed on the CII since they contain more information on tooth cracks [77,104,107]. A new strategy based on the SVD is developed to extract the CII from gearbox vibration signals. Afterwards, TSA is conducted on the CII to obtain the TSA signals for both the pinion and the gear, the squared envelopes of which are adopted to detect the number and locations of multiple tooth cracks. By analyzing simulated gearbox vibration signals and experimental gearbox vibration datasets, a good understanding of the vibration characteristics of spur gearboxes with multiple tooth cracks is obtained and the effectiveness of the proposed method for detecting the number and locations of multiple tooth cracks is demonstrated.

The novel contributions of this chapter include: (1) Gear tooth mesh stiffness for the three scenarios of multiple tooth cracks are analytically evaluated for the first time; (2) Insights into the vibration characteristics of a spur gearbox with multiple tooth cracks are obtained, such as two nonadjacent pinion tooth cracks induce two nonadjacent impulses in the vibration signal in one pinion revolution, two adjacent pinion tooth cracks induce two adjacent impulses in the vibration signal in one pinion revolution, and one pinion tooth crack and one gear tooth crack result in two groups of impulses in the vibration signal; (3) A novel method focusing on the CII is proposed to detect the number and locations of multiple tooth cracks in spur gearboxes.

The remainder of this chapter is organized as follows. Section 5.2 describes the proposed overall methodology. Simulated gearbox vibration signal analysis and experimental validation are presented in Section 5.3 and Section 5.4, respectively. Conclusions of the study conducted in this chapter are drawn in Section 5.5.

5.2 The overall methodology

The overall methodology consists of several parts, mainly including: (1) Dynamic modelling of a spur gearbox; (2) Derivation of gear tooth mesh stiffness formulae for the three scenarios of multiple tooth cracks; (3) Analysis of gear tooth mesh stiffness and gearbox vibration signals; (4) Development of a novel method for detecting the number and locations of multiple tooth cracks. Each part of the overall methodology is introduced in what follows.

5.2.1 Dynamic model of a spur gearbox

This chapter aims to model a one-stage fixed-axis spur gearbox, the dynamic model of which is shown in Fig. 2.2 in Section 2.4 of Chapter 2. The number of teeth of the pinion and the gear are N_p and N_g, respectively. The motion equations of the spur gearbox dynamic model are expressed with the Lagrange formulation, which is given by Eq. (3.1). Details of Eq. (3.1) are presented in Subsection 3.2.1.1 of Chapter 3. Gear tooth mesh stiffness is included in the stiffness matrix K. Analytical evaluation of the tooth mesh stiffness for the three considered scenarios of multiple tooth cracks is presented in Subsection 5.2.4 of this chapter, and the evaluated tooth mesh stiffness is inserted into Eq. (3.1) to generate gearbox vibration responses

5.2.2 Meshing process of a pair of engaged teeth

Before describing how to calculate gear tooth mesh stiffness, the meshing process of a pair of engaged teeth is first introduced. For a gear set with a contact ratio smaller than two and greater than one, which is the case considered in this thesis, contact usually takes places either between one single pair of teeth or two pairs of teeth [140]. Fig. 5.1 shows a gear set consisting of a pinion and a gear. ω_1 and ω_2 are the angular velocities of the pinion and the gear, respectively; θ_1 is the pinion angular displacement; θ_{LPSTC}, θ_{HPSTC}, and θ_{end} are the pinion angular displacements at the Lowest Point of Single Tooth Contact (LPSTC), at the Highest Point of Single Tooth Contact (HPSTC), and at the end of the engagement, respectively.

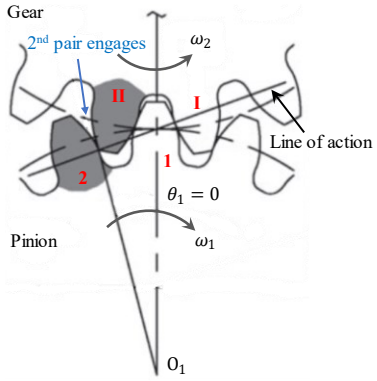

(a) Beginning of tooth engagement

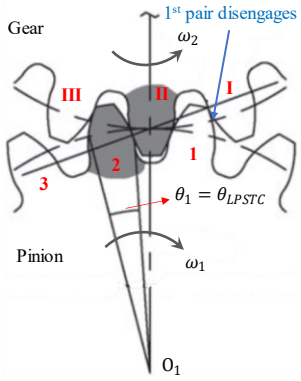

(b) Lowest point of single tooth contact

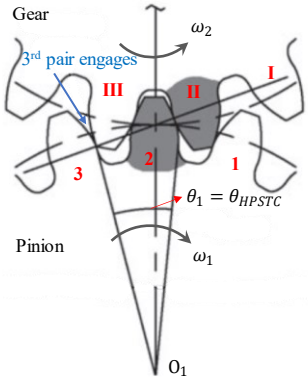

(c) Highest point of single tooth contact

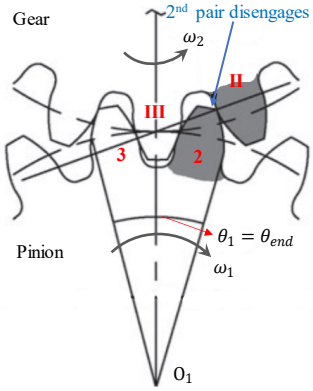

(d) End of tooth engagement

Fig. 5.1: Schematic for the meshing process of a pair of engaged teeth [140]

Referring to Fig. 5.1, the meshing process of a pair of engaged teeth is described. As shown in Fig. 5.1, the two shaded teeth "Pinion tooth 2 and Gear tooth II" forms a meshing pair, which is selected to introduce the gear meshing process herein. In Fig. 5.1(a), the target tooth pair "Pinion tooth 2 and Gear tooth II" starts to engage when the pinion tooth 2 contacts the tip of the gear tooth II [140]. This position is set as $\theta_1 = 0$ and is the reference point. Two pairs of teeth, namely the second pair "Pinion tooth 2 and Gear tooth II" and the first pair "Pinion tooth 1 and Gear tooth I", will be in mesh simultaneously after this position. Therefore, this position is the beginning of the first Double-tooth-pair mesh duration [26]. Fig. 5.1(b) shows the meshing situation at the position where $\theta_1 = \theta_{LPSTC}$, from which it is seen that the first pair will disengage after this position and only the second pair will be in mesh. This position is the end of the first Double-tooth-pair mesh duration and the commencement of the first Single-tooth-pair mesh duration [26]. Furthermore, it can be inferred that the lasting angle of one Double-tooth-pair mesh duration, which is termed θ_d, is equal to $\theta_{LPSTC} - 0$, so $\theta_d = \theta_{LPSTC}$. Afterwards, as shown in Fig. 5.1(c), when $\theta_1 = \theta_{HPSTC}$,

the third pair "Pinion tooth 3 and Gear tooth III" starts to engage, and both the second pair and the third pair will be in mesh after this position. Hence, this position is the end of the first Single-tooth-pair mesh duration and the beginning of the second Double-tooth-pair mesh duration, and it is concluded that the lasting angle of one Single-tooth-pair mesh duration, which is termed θ_s, is equal to $\theta_{HPSTC} - \theta_{LPSTC}$, so $\theta_s = \theta_{HPSTC} - \theta_{LPSTC}$. In Fig. 5.1(d), when $\theta_1 = \theta_{end}$, the second pair begins to disengage. After this position, only the third pair will be mesh. Therefore, this position is the end of the second Double-tooth-pair mesh duration and the beginning of the second Single-tooth-pair mesh duration. It can also be inferred that $\theta_{end} - \theta_{HPSTC} = \theta_d$.

In sum, for a certain pair of engaged teeth, such as the pair "Pinion tooth 2 and Gear tooth II" shown in Fig. 5.1, its meshing process lasts for an angular duration of $\theta_{end} - 0$, which is equal to $\theta_d + \theta_s + \theta_d$. Calculations of θ_d and θ_s were presented in Ref. [26]. Mesh stiffness of a pair of healthy teeth is a periodic function with regards to the pinion angular displacement and its period is $\theta_d + \theta_s = 2\pi/N_p\ (rad)$, which is termed "one mesh period" [26,141]. The meshing process of a pair of engaged teeth lasts for two mesh periods since $round[(\theta_d + \theta_s + \theta_d)/(\theta_d + \theta_s)] = 2$. Likewise, it can be found that the meshing process of N ($N \geq 2$) adjacent pairs of engaged teeth lasts for $N + 1$ mesh periods, and the meshing process of N ($N \geq 2$) nonadjacent pairs of engaged teeth lasts for $2N$ mesh periods. These conclusions will be used in the following sections.

5.2.3 Tooth mesh stiffness evaluation for a pair of engaged teeth

For a pair of engaged teeth of a gear set, such as the shaded tooth pair in Fig. 5.1, it consists of a pinion tooth and a gear tooth, the total mesh stiffness of which is calculated using Eq. (5.1) [26].

$$k_t = \frac{1}{1/k_h + 1/k_{b\_P} + 1/k_{a\_P} + 1/k_{s\_P} + 1/k_{b\_G} + 1/k_{a\_G} + 1/k_{s\_G}} \tag{5.1}$$

where k_t is the total mesh stiffness; k_h, k_b, k_a, and k_s represent the Hertzian contact stiffness, the bending stiffness, the axial compressive stiffness, and the shear stiffness, respectively; subscripts "P" and "G" denote the pinion tooth and the gear tooth, respectively.

For the Hertzian contact stiffness of a pair of engaged teeth, it is given in Eq. (5.2) [26].

$$k_h = \frac{\pi EL}{4(1-\nu^2)} \tag{5.2}$$

where E, v, and L denote the Young's modulus, the Poisson's ratio, and the width of tooth face, respectively.

For the calculations of k_b, k_a, and k_s of a healthy tooth, a healthy pinion tooth is used as an example for illustration. The schematic of a healthy pinion tooth is shown in Fig. 5.2, in which α_1 denotes the angle between the action force F and its vertical component F_b, α_2 denotes the half of the base tooth angle of the pinion tooth, R_{b1} is the base circle radius of the pinion.

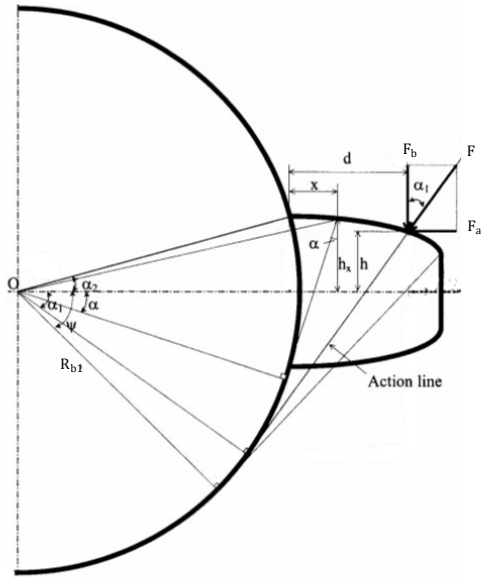

Fig. 5.2: Schematic of a healthy pinion tooth [26]

The reciprocals of k_b, k_a, and k_s of a healthy pinion tooth are given in Eq. (5.3) through Eq. (5.5) [26].

$$\frac{1}{k_{b\_H_P}} = \int_{-\alpha_1}^{\alpha_2} \frac{3\{1+\cos\alpha_1[(\alpha_2-\alpha)\sin\alpha-\cos\alpha]\}^2(\alpha_2-\alpha)\cos\alpha}{2EL[\sin\alpha+(\alpha_2-\alpha)\cos\alpha]^3}\,d\alpha \tag{5.3}$$

$$\frac{1}{k_{a\_H_P}} = \int_{-\alpha_1}^{\alpha_2} \frac{(\alpha_2-\alpha)\cos\alpha\sin^2\alpha_1}{2EL[\sin\alpha+(\alpha_2-\alpha)\cos\alpha]}\,d\alpha \tag{5.4}$$

$$\frac{1}{k_{s\_H_P}} = \int_{-\alpha_1}^{\alpha_2} \frac{1.2(1+v)(\alpha_2-\alpha)\cos\alpha\cos^2\alpha_1}{EL[\sin\alpha+(\alpha_2-\alpha)\cos\alpha]}\,d\alpha \tag{5.5}$$

where subscript "H_P" denotes a healthy pinion tooth.

By changing α_1 and α_2 to their counterparts for a gear tooth, namely α_1' and α_2', the reciprocals of k_b, k_a, and k_s of a healthy gear tooth are calculated using Eq. (5.6), Eq. (5.7), and Eq. (5.8), respectively.

$$\frac{1}{k_{b\_H_G}} = \int_{-\alpha_1'}^{\alpha_2'} \frac{3\{1+\cos\alpha_1'[(\alpha_2'-\alpha)\sin\alpha-\cos\alpha]\}^2(\alpha_2'-\alpha)\cos\alpha}{2EL[\sin\alpha+(\alpha_2'-\alpha)\cos\alpha]^3}d\alpha \tag{5.6}$$

$$\frac{1}{k_{a\_H_G}} = \int_{-\alpha_1'}^{\alpha_2'} \frac{(\alpha_2'-\alpha)\cos\alpha\sin^2\alpha_1'}{2EL[\sin\alpha+(\alpha_2'-\alpha)\cos\alpha]}d\alpha \tag{5.7}$$

$$\frac{1}{k_{s\_H_G}} = \int_{-\alpha_1'}^{\alpha_2'} \frac{1.2(1+\nu)(\alpha_2'-\alpha)\cos\alpha\cos^2\alpha_1'}{EL[\sin\alpha+(\alpha_2'-\alpha)\cos\alpha]}d\alpha \tag{5.8}$$

where subscript "H_G" denotes a healthy gear tooth.

For the calculations of k_b, k_a, and k_s of a cracked tooth, a pinion tooth with a root crack is used as an example for illustration, the schematic of which is shown in Fig. 2.3 in Chapter 2. Tooth crack propagation path is simplified as a straight line starting from the tooth root fillet, q_p is the pinion tooth crack depth and ϕ is the crack angle. In this chapter, the case where q_p is no greater than half of the base chordal tooth thickness of the pinion is considered, which corresponds to a shallow tooth crack [26]. Tooth cracks do not affect Hertzian contact stiffness k_h since the width of tooth face remains unchanged. Besides, for a tooth with a root crack, its axial compressive stiffness, namely $k_{a\_C_P}$ or $k_{a\_C_G}$, is the same as that of a healthy tooth since the crack part can still bear the axial compressive force as if there is no crack [26].

However, the bending stiffness k_b and the shear stiffness k_s are influenced by a pinion tooth crack [26], the reciprocals of which are calculated using Eq. (5.9) and Eq. (5.10), respectively.

$$\frac{1}{k_{b\_C_P}} = \int_{-\alpha_1}^{\alpha_2} \frac{12\{1+\cos\alpha_1[(\alpha_2-\alpha)\sin\alpha-\cos\alpha]\}^2(\alpha_2-\alpha)\cos\alpha}{EL\left[\sin\alpha_2-\frac{q_p}{R_{b1}}\sin\phi+\sin\alpha+(\alpha_2-\alpha)\cos\alpha\right]^3}d\alpha \tag{5.9}$$

$$\frac{1}{k_{s\_C_P}} = \int_{-\alpha_1}^{\alpha_2} \frac{2.4(1+\nu)(\alpha_2-\alpha)\cos\alpha\cos^2\alpha_1}{EL\left[\sin\alpha_2-\frac{q_p}{R_{b1}}\sin\phi+\sin\alpha+(\alpha_2-\alpha)\cos\alpha\right]}d\alpha \tag{5.10}$$

where subscript "C_P" denotes a cracked pinion tooth.

In Ref. [26], stiffness calculation for a cracked gear tooth was not involved. In this paper, k_b and k_s of a gear tooth with a root crack are derived, the reciprocals of which are shown in Eq. (5.11) and Eq. (5.12), respectively.

$$\frac{1}{k_{b\_C_G}} = \int_{-\alpha_1'}^{\alpha_2'} \frac{12\{1+\cos\alpha_1'[(\alpha_2'-\alpha)\sin\alpha-\cos\alpha]\}^2(\alpha_2'-\alpha)\cos\alpha}{EL\left[\sin\alpha_2'-\frac{q_g}{R_{b2}}\sin\phi+\sin\alpha+(\alpha_2'-\alpha)\cos\alpha\right]^3}d\alpha \tag{5.11}$$

$$\frac{1}{k_{s\_C_G}} = \int_{-\alpha_1'}^{\alpha_2'} \frac{2.4(1+v)(\alpha_2'-\alpha)\cos\alpha\cos^2\alpha_1'}{EL\left[\sin\alpha_2' - \frac{q_g}{R_{b2}}\sin\phi + \sin\alpha + (\alpha_2'-\alpha)\cos\alpha\right]} d\alpha \tag{5.12}$$

where subscript "C_G" denotes a cracked gear tooth; q_g is the depth of the gear tooth crack, R_{b2} is the base circle radius of the gear, α_2' is the half of the base tooth angle of the gear tooth, α_1' is the counterpart of α_1 for the gear tooth; ϕ is the gear tooth crack angle, which is set to be the same as the pinion tooth crack angle for simplicity.

In Eq. (5.3) through Eq. (5.12), α_1 and α_1' can be expressed as functions of the pinion angular displacement θ_1 [26], while α_2 and α_2' are two constants related to the pinion and gear geometry parameters. Therefore, $k_{b\_H_P}$, $k_{a\_H_P}$, $k_{s\_H_P}$, $k_{b\_H_G}$, $k_{a\_H_G}$, and $k_{s\_H_G}$ are functions of θ_1; $k_{b\_C_P}$ and $k_{s\_C_P}$ are functions of both θ_1 and q_p; $k_{b\_C_G}$ and $k_{s\_C_G}$ are functions of both θ_1 and q_g. The formulae shown in Eq. (5.3) through Eq. (5.12) are the bases of the derivations of the total mesh stiffness of a pair of engaged teeth presented in what follows.

For a pair of engaged teeth, it may result in four mesh cases according to the health conditions of the pinion tooth and the gear tooth, which are shown in Fig. 5.3. The four mesh cases are: (1) a healthy pinion tooth and a healthy gear tooth, which is the "H_P-H_G" shown in Fig. 5.3(a); (2) a pinion tooth with a root crack and a healthy gear tooth, which is the "C_P-H_G" shown in Fig. 5.3(b); (3) a healthy pinion tooth and a gear tooth with a root crack, which is the "H_P-C_G" shown in Fig. 5.3(c); (4) a pinion tooth with a root crack and a gear tooth with a root crack, which is the "C_P-C_G" illustrated in Fig. 5.3(d). Different combinations of these four mesh cases of a tooth pair result in different scenarios of multiple tooth cracks for a gear set. Therefore, before introducing how to evaluate the mesh stiffness for multiple tooth cracks, formulae of the mesh stiffness for these four cases are first derived. For the convenience of descriptions in Subsection 5.2.3.1 to Subsection 5.2.3.4, in Fig. 5.3, let the serial number of the pinion tooth H_P or C_P be p ($1 \leq p \leq N_p$) and that of the gear tooth H_G or C_G be g ($1 \leq g \leq N_g$).

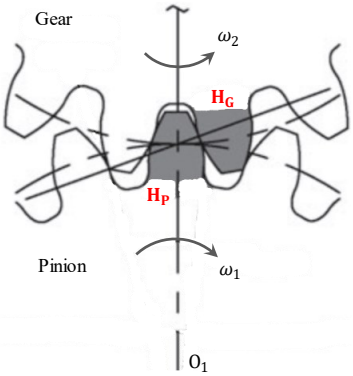

(a) First mesh case: H_P-H_G

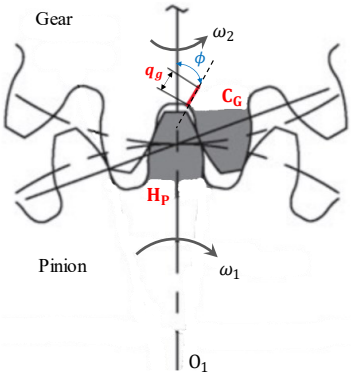

(c) Third mesh case: H_P-C_G

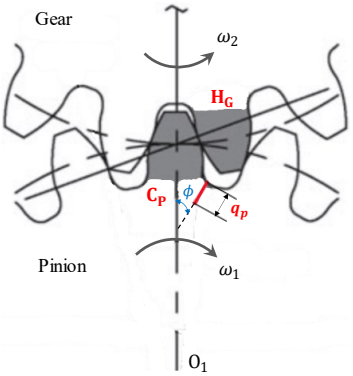

(b) Second mesh case: C_P-H_G

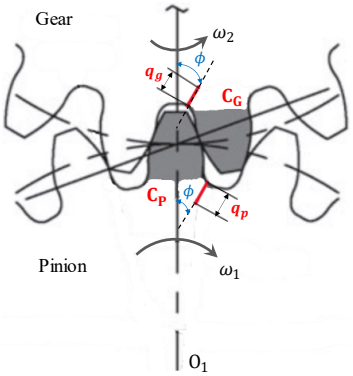

(d) Fourth mesh case: C_P-C_G

Fig. 5.3: Four mesh cases of a pair of engaged teeth of a gear set

5.2.3.1 A healthy pinion tooth and a healthy gear tooth

This case is shown in Fig. 5.3(a), its mesh stiffness is termed $k_{t\_H_P^p H_G^g}$ and is given in Eq. (5.13).

$$k_{t\_H_P^p H_G^g} = \frac{1}{{}^1\!/\!_{k_h} + {}^1\!/\!_{k_{b\_H_P^p}} + {}^1\!/\!_{k_{a\_H_P^p}} + {}^1\!/\!_{k_{s\_H_P^p}} + {}^1\!/\!_{k_{b\_H_G^g}} + {}^1\!/\!_{k_{a\_H_G^g}} + {}^1\!/\!_{k_{s\_H_G^g}}} \tag{5.13}$$

5.2.3.2 A pinion tooth with a root crack and a healthy gear tooth

This case is shown in Fig. 5.3(b), its mesh stiffness is termed $k_{t\_C_P^p H_G^g}$ and is given in Eq. (5.14).

$$k_{t\_C_P^p H_G^g} = \frac{1}{{}^1\!/\!_{k_h} + {}^1\!/\!_{k_{b\_C_P^p}} + {}^1\!/\!_{k_{a\_C_P^p}} + {}^1\!/\!_{k_{s\_C_P^p}} + {}^1\!/\!_{k_{b\_H_G^g}} + {}^1\!/\!_{k_{a\_H_G^g}} + {}^1\!/\!_{k_{s\_H_G^g}}} \tag{5.14}$$

5.2.3.3 A healthy pinion tooth and a gear tooth with a root crack

This case is shown in Fig. 5.3(c), its mesh stiffness is termed $k_{t\_H_P^p C_G^g}$ and is given in Eq. (5.15).

$$k_{t\_H_P^p C_G^g} = \frac{1}{1/k_h + 1/k_{b\_H_P^p} + 1/k_{a\_H_P^p} + 1/k_{s\_H_P^p} + 1/k_{b\_C_G^g} + 1/k_{a\_C_G^g} + 1/k_{s\_C_G^g}} \tag{5.15}$$

5.2.3.4 A pinion tooth with a root crack and a gear tooth with a root crack

This case is shown in Fig. 5.3(d), its mesh stiffness is termed $k_{t\_C_P^p C_G^g}$ and is given in Eq. (5.16).

$$k_{t\_C_P^p C_G^g} = \frac{1}{1/k_h + 1/k_{b\_C_P^p} + 1/k_{a\_C_P^p} + 1/k_{s\_C_P^p} + 1/k_{b\_C_G^g} + 1/k_{a\_C_G^g} + 1/k_{s\_C_G^g}} \tag{5.16}$$

In Eq. (5.13) through Eq. (5.16), subscript "H_P^p" denotes a healthy pinion tooth whose serial number is p, subscript "H_G^g" denotes a healthy gear tooth whose serial number is g, subscript "C_P^p" denotes a cracked pinion tooth whose serial number is p, and subscript "C_G^g" denotes a cracked gear tooth whose serial number is g. The derived mesh stiffness formulae shown in Eq. (5.13) through Eq. (5.16) are for a pair of engaged teeth, which will be used in Subsection 5.2.4.

5.2.4 Tooth mesh stiffness evaluation for a gear set with multiple tooth cracks

As mentioned in Section 5.1, three scenarios of multiple tooth cracks of a spur gearbox are studied in this paper. Based on the descriptions presented in Subsection 5.2.2 and Subsection 5.2.3, mesh stiffness formulae for the three scenarios of multiple tooth cracks are analytically derived, which are presented in what follows.

5.2.4.1 Scenario 1: two nonadjacent tooth cracks on the pinion and a healthy gear

Fig. 5.4 shows a gear set with two nonadjacent tooth cracks on the pinion and all the gear teeth are healthy. Let the serial numbers of the two cracked pinion teeth be "I" and "J" ($1 \le \mathrm{I} \le \mathrm{N_p}$, $1 \le \mathrm{J} \le \mathrm{N_p}$, $2 \le |I - J| \le \mathrm{N_p} - 2$), respectively. Depths of the two tooth cracks are q_{p1} and q_{p2}, respectively. Because all gear teeth are healthy, each gear tooth is assumed to be equivalent in terms of stiffness calculation. As the pinion and the gear rotate, the cracked pinion tooth "I" will first mesh with a healthy gear tooth, afterwards, the crack pinion tooth "J" will mesh with a healthy gear tooth. Let the position where the cracked pinion tooth "I" starts to mesh with a gear tooth be the reference point $\theta_1 = 0$, then after M revolutions of the pinion, namely when $\theta_1 = \mathrm{M} * 2\pi\ rad$ (M is a positive integer), the two cracked pinion teeth "I" and "J" will return to their original positions when $\theta_1 = 0$. Mesh stiffness of the gear set for "Scenario 1" is the same in each pinion revolution since it is a periodic function with regards to θ_1, and the period is $2\pi\ rad$.

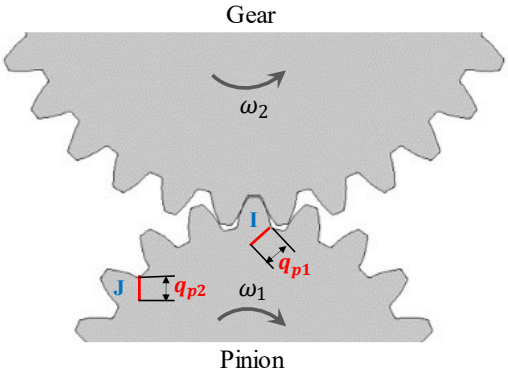

Fig. 5.4: Two nonadjacent tooth cracks on the pinion and a healthy gear

The cracked pinion tooth "I" and a healthy gear tooth forms the mesh case "C_P-H_G" shown in Fig. 5.3(b), which is also appliable to the cracked pinion tooth "J" and a healthy gear tooth. For other healthy pinion teeth, each of them and a healthy gear tooth forms the mesh case "H_P-H_G" shown in Fig. 5.3(a). The meshing process of "C_P-H_G" lasts for two mesh periods, namely $[0,2\frac{2\pi}{N_p}]$. Besides, in one Double-tooth-pair mesh duration, such as $[0,\theta_d]$, there are two meshing pairs, so the total mesh stiffness is the sum of the mesh stiffness of the two meshing pairs. While in one Single-tooth-pair mesh duration, such as $\left[\theta_d,\frac{2\pi}{N_p}\right]$, there is only one meshing pair, so the total mesh stiffness is the mesh stiffness of the meshing pair. Based on above analysis, the mesh stiffness for "Scenario 1" is calculated using Eq. (5.17).

$$K_I=\begin{cases}k_{t\_q_{p1}}, & \theta_1\in\left[0,2\frac{2\pi}{N_p}\right]+(\mathrm{I}-1)\frac{2\pi}{N_p}+(m-1)2\pi\\ k_{t\_q_{p2}}, & \theta_1\in\left[0,2\frac{2\pi}{N_p}\right]+(\mathrm{J}-1)\frac{2\pi}{N_p}+(m-1)2\pi\\ k_{t\_H}, & \theta_1\ equals\ other\ angles\end{cases} \tag{5.17}$$

where m is the number of pinion revolutions (m is a positive integer); $k_{t\_q_{p1}}$ is the mesh stiffness for the meshing pair consisting of the cracked pinion tooth "I" and a healthy gear tooth, $k_{t\_q_{p2}}$ is the mesh stiffness for the meshing pair consisting of the cracked pinion tooth "J" and a healthy gear tooth, and k_{t_H} is the mesh stiffness for the meshing pair consisting of a healthy pinion tooth and a healthy gear tooth, the values of which in one pinion revolution are given by Eq. (5.18), Eq. (5.19), and Eq. (5.20), respectively.

$$k_{t\_q_{p1}} = \begin{cases} k_{t\_H_P^{I-1}H_G^{g-1}} + k_{t\_C_P^I H_G^g}, & \theta_1 \in [0, \theta_d] + (\mathrm{I}-1)\frac{2\pi}{N_p} \\ k_{t\_C_P^I H_G^g}, & \theta_1 \in \left[\theta_d, \frac{2\pi}{N_p}\right] + (\mathrm{I}-1)\frac{2\pi}{N_p} \\ k_{t\_C_P^I H_G^g} + k_{t\_H_P^{I+1}H_G^{g+1}}, & \theta_1 \in \left[\frac{2\pi}{N_p}, \frac{2\pi}{N_p} + \theta_d\right] + (\mathrm{I}-1)\frac{2\pi}{N_p} \\ k_{t\_H_P^{I+1}H_G^{g+1}}, & \theta_1 \in \left[\frac{2\pi}{N_p} + \theta_d, 2\frac{2\pi}{N_p}\right] + (\mathrm{I}-1)\frac{2\pi}{N_p} \end{cases} \tag{5.18}$$

where $k_{t\_C_P^I H_G^g} = \frac{1}{1/k_h{}^{+1}/k_{b\_C_P^I}{}^{+1}/k_{a\_C_P^I}{}^{+1}/k_{s\_C_P^I}{}^{+1}/k_{b\_H_G^g}{}^{+1}/k_{a\_H_G^g}{}^{+1}/k_{s\_H_G^g}}$, in which $k_{b\_C_P^I}$, $k_{a\_C_P^I}$, and $k_{s\_C_P^I}$ are the bending stiffness, axial compressive stiffness, and shear stiffness for the cracked pinion tooth "I" whose crack depth is q_{p1}, respectively.

$$k_{t\_q_{p2}} = \begin{cases} k_{t\_H_P^{J-1}H_G^{g-1}} + k_{t\_C_P^J H_G^g}, & \theta_1 \in [0, \theta_d] + (\mathrm{J}-1)\frac{2\pi}{N_p} \\ k_{t\_C_P^J H_G^g}, & \theta_1 \in \left[\theta_d, \frac{2\pi}{N_p}\right] + (\mathrm{J}-1)\frac{2\pi}{N_p} \\ k_{t\_C_P^J H_G^g} + k_{t\_H_P^{J+1}H_G^{g+1}}, & \theta_1 \in \left[\frac{2\pi}{N_p}, \frac{2\pi}{N_p} + \theta_d\right] + (\mathrm{J}-1)\frac{2\pi}{N_p} \\ k_{t\_H_P^{J+1}H_G^{g+1}}, & \theta_1 \in \left[\frac{2\pi}{N_p} + \theta_d, 2\frac{2\pi}{N_p}\right] + (\mathrm{J}-1)\frac{2\pi}{N_p} \end{cases} \tag{5.19}$$

where $k_{t\_C_P^J H_G^g} = \frac{1}{1/k_h{}^{+1}/k_{b\_C_P^J}{}^{+1}/k_{a\_C_P^J}{}^{+1}/k_{s\_C_P^J}{}^{+1}/k_{b\_H_G^g}{}^{+1}/k_{a\_H_G^g}{}^{+1}/k_{s\_H_G^g}}$, in which $k_{b\_C_P^J}$, $k_{a\_C_P^J}$, and $k_{s\_C_P^J}$ are the bending stiffness, axial compressive stiffness, and the shear stiffness for the cracked pinion tooth "J" whose crack depth is q_{p2}, respectively.

$$k_{t\_H} = \begin{cases} k_{t\_H_P^{p-1}H_G^{g-1}} + k_{t\_H_P^p H_G^g}, & \theta_1 \in [0, \theta_d] + (p-1)\frac{2\pi}{N_p} \\ k_{t\_H_P^p H_G^g}, & \theta_1 \in \left[\theta_d, \frac{2\pi}{N_p}\right] + (p-1)\frac{2\pi}{N_p} \end{cases} \tag{5.20}$$

where $k_{t\_H_P^p H_G^g}$ is shown in Eq. (5.13).

5.2.4.2 Scenario 2: two adjacent tooth cracks on the pinion and a healthy gear

Fig. 5.5 shows a gear set with two adjacent tooth cracks on the pinion and all the gear teeth are healthy. Let the serial numbers of the two cracked teeth be "I" and "I+1" ($1 \le \mathrm{I} < N_p$). Depths of the two pinion tooth cracks are q_{p1} and q_{p2}, respectively. As the pinion and the gear rotate, the cracked pinion tooth "I" will first mesh with a healthy gear tooth, afterwards, the crack pinion

tooth "I+1" will mesh with a healthy gear tooth. Let the position where the pinion tooth "I" starts to mesh with a gear tooth be the reference point $\theta_1 = 0$, then after M pinion revolutions, namely when $\theta_1 = \mathrm{M} * 2\pi$ rad, the two cracked pinion teeth "I" and "I+1" will return to their original positions when $\theta_1 = 0$. Mesh stiffness of the gear set for "Scenario 2" is the same in each pinion revolution since it is a periodic function with regards to θ_1, and the period is 2π rad.

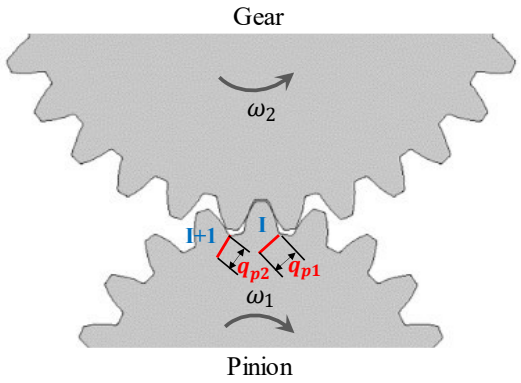

Fig. 5.5: Two adjacent tooth cracks on the pinion and a healthy gear

Either cracked pinion tooth "I" or "I+1"and a healthy gear tooth forms the mesh case "$\mathrm{C_P}$-$\mathrm{H_G}$". The meshing process of two adjacent pairs of "$\mathrm{C_P}$-$\mathrm{H_G}$" lasts for three mesh periods, namely $[0,3\frac{2\pi}{N_p}]$. Therefore, mesh stiffness for "Scenario 2" is calculated using Eq. (5.21).

$$K_{II} = \begin{cases} k_{t\_q_{p1}\_q_{p2}}, & \theta_1 \in \left[0,3\frac{2\pi}{N_p}\right] + (\mathrm{I}-1)\frac{2\pi}{N_p} + (m-1)2\pi \\ k_{t\_H}, & \theta_1 \; equals \; other \; angles \end{cases} \tag{5.21}$$

where k_{t_H} is the mesh stiffness for a healthy meshing pair shown in Eq. (5.20); $k_{t\_q_{p1}\_q_{p2}}$ is the mesh stiffness for two adjacent meshing pairs consisting of the cracked pinion teeth "I" and "I+1" and two healthy gear teeth, the value of which in one pinion revolution is given by Eq. (5.22).

$$k_{t\_q_{p1}\_q_{p2}} = \begin{cases} k_{t\_H_P^{I-1}H_G^{g-1}} + k_{t\_C_P^I H_G^g}, & \theta_1 \in [0, \theta_d] + (\mathrm{I}-1)\frac{2\pi}{N_p} \\ k_{t\_C_P^I H_G^g}, & \theta_1 \in \left[\theta_d, \frac{2\pi}{N_p}\right] + (\mathrm{I}-1)\frac{2\pi}{N_p} \\ k_{t\_C_P^I H_G^g} + k_{t\_C_P^{I+1} H_G^{g+1}}, & \theta_1 \in \left[\frac{2\pi}{N_p}, \frac{2\pi}{N_p} + \theta_d\right] + (\mathrm{I}-1)\frac{2\pi}{N_p} \\ k_{t\_C_P^{I+1} H_G^{g+1}}, & \theta_1 \in \left[\frac{2\pi}{N_p} + \theta_d, 2\frac{2\pi}{N_p}\right] + (\mathrm{I}-1)\frac{2\pi}{N_p} \\ k_{t\_C_P^{I+1} H_G^{g+1}} + k_{t\_H_P^{I+2} H_G^{g+2}}, & \theta_1 \in \left[2\frac{2\pi}{N_p}, 2\frac{2\pi}{N_p} + \theta_d\right] + (\mathrm{I}-1)\frac{2\pi}{N_p} \\ k_{t\_H_P^{I+2} H_G^{g+2}}, & \theta_1 \in \left[2\frac{2\pi}{N_p} + \theta_d, 3\frac{2\pi}{N_p}\right] + (\mathrm{I}-1)\frac{2\pi}{N_p} \end{cases} \tag{5.22}$$

where $k_{t\_C_P^I H_G^g} = \frac{1}{1/k_h + 1/k_{b\_C_P^I} + 1/k_{a\_C_P^I} + 1/k_{s\_C_P^I} + 1/k_{b\_H_G^g} + 1/k_{a\_H_G^g} + 1/k_{s\_H_G^g}}$, in which $k_{b\_C_P^I}$, $k_{a\_C_P^I}$, and $k_{s\_C_P^I}$ are the bending stiffness, axial compressive stiffness, and shear stiffness for the cracked pinion tooth "I" with crack depth q_{p1}, respectively;

$k_{t\_C_P^{I+1} H_G^g} = \frac{1}{1/k_h + 1/k_{b\_C_P^{I+1}} + 1/k_{a\_C_P^{I+1}} + 1/k_{s\_C_P^{I+1}} + 1/k_{b\_H_G^g} + 1/k_{a\_H_G^g} + 1/k_{s\_H_G^g}}$, in which $k_{b\_C_P^{I+1}}$, $k_{a\_C_P^{I+1}}$, and $k_{s\_C_P^{I+1}}$ are the bending stiffness, axial compressive stiffness, and shear stiffness for the cracked pinion tooth "I+1" with crack depth q_{p2}, respectively.

5.2.4.3 Scenario 3: one tooth crack on the pinion and one tooth crack on the gear

Fig. 5.6 shows a gear set with one tooth crack on the pinion and one tooth crack on the gear, depths of which are q_p and q_g, respectively. Let the serial numbers of the two cracked teeth be "I" and "J" ($1 \le \mathrm{I} \le N_p$, $1 \le \mathrm{J} \le N_g$), respectively. As the pinion and the gear rotate, the cracked pinion tooth "I" will first mesh with the cracked gear tooth "J". Afterwards, the cracked pinion tooth "I" will mesh with a healthy gear tooth, and a healthy pinion tooth will mesh with the cracked gear tooth "J". Let the position where the cracked pinion tooth "I" starts to mesh with the cracked gear tooth "J" be the reference point $\theta_1 = 0$, then after $S * N_g$ pinion revolutions, namely when $\theta_1 = S * N_g * 2\pi$ rad (S is a positive integer), the two cracked teeth "I" and "J" will return to their original positions when $\theta_1 = 0$. Mesh stiffness of the gear set for "Scenario 3" is the same in every N_g pinion revolutions since it is a periodic function with regards to θ_1, and the period is $N_g * 2\pi$ rad.

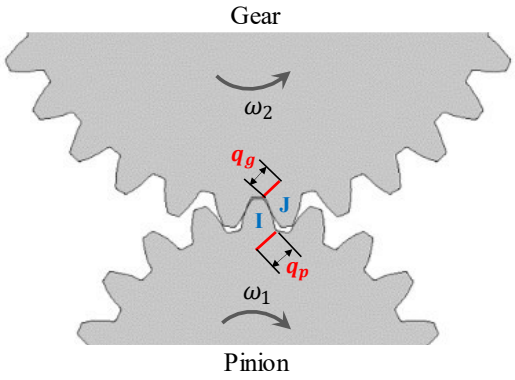

Fig. 5.6: One tooth crack on the pinion and one tooth crack on the gear

As shown in Fig. 5.3, a tooth pair may result in four mesh cases. For mesh cases "C_P-H_G" and "H_P-C_G", when the spacing between them is no greater than one tooth pair, they can form four variants: "Variant 1", "Variant 2", "Variant 3", and "Variant 4", which are shown in Fig. 5.7. These four variants represent the mesh cases of the "Scenario 3" of multiple tooth cracks at four different points in time and they have an equal possibility of occurrence.

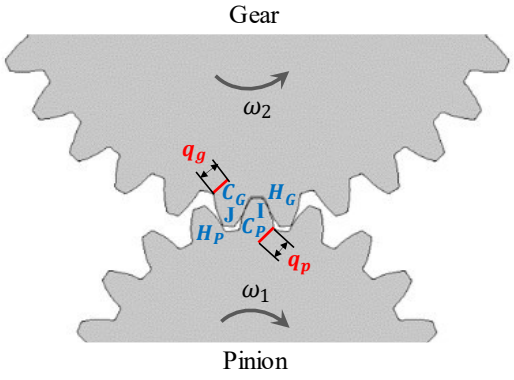

(a) Variant 1: "C_P-H_G" and "H_P-C_G"

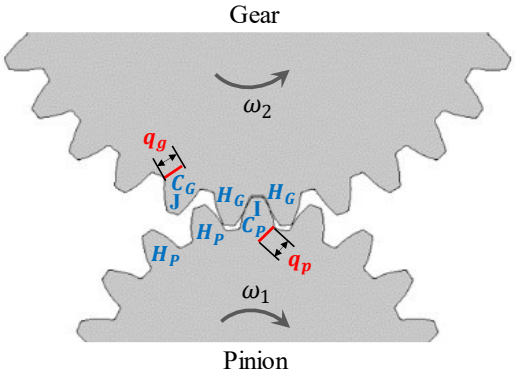

(b) Variant 2: "C_P-H_G", "H_P-H_G", and "H_P-C_G"

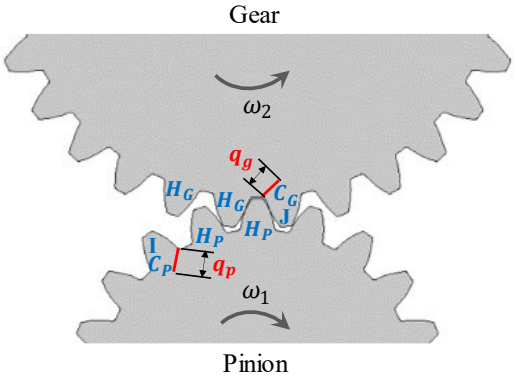

(c) Variant 3: "H_P-C_G", "H_P-H_G", and "C_P-H_G"

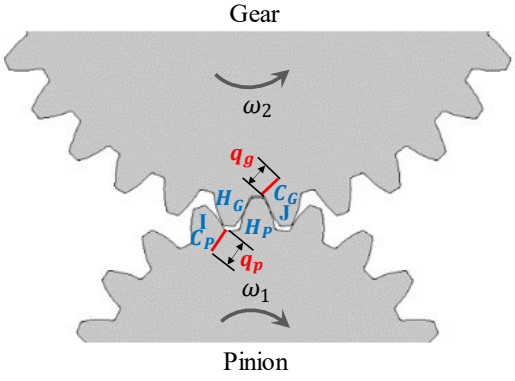

(d) Variant 4: "H_P-C_G" and "C_P-H_G"

Fig. 5.7: Four variants formed by the mesh cases "C_P-H_G" and "H_P-C_G"

Based on the analysis in Subsection 5.2.2, it is known that the meshing process of either "H_P-C_G" or "C_P-C_G" lasts for two mesh periods, namely $[0,2\frac{2\pi}{N_p}]$; the meshing process of either "Variant 1" or "Variant 4" lasts for three mesh periods, namely $[0,3\frac{2\pi}{N_p}]$; the meshing process of either "Variant 2" or "Variant 3" lasts for four mesh periods, namely $[0,4\frac{2\pi}{N_p}]$. Therefore, mesh stiffness for "Scenario 3" is calculated using Eq. (5.23).

$$K_{III} = \begin{cases} k_{t\_q_p\_q_g}, & \theta_1 \in \Omega_1 \\ k_{t\_q_p}, & \theta_1 \in \Omega_2 \\ k_{t\_q_g}, & \theta_1 \in \Omega_3 \\ k_{t\_H}, & \theta_1 \in \Omega_4 \\ k_{t\_V_1}, & \theta_1 \in \Omega_5 \\ k_{t\_V_2}, & \theta_1 \in \Omega_6 \\ k_{t\_V_3}, & \theta_1 \in \Omega_7 \\ k_{t\_V_4}, & \theta_1 \in \Omega_8 \end{cases} \tag{5.23}$$

where $k_{t\_q_p\_q_g}$ is the mesh stiffness for "C_P-C_G"; $k_{t\_q_p}$ is the mesh stiffness for "C_P-H_G"; $k_{t\_q_g}$ is the mesh stiffness for "H_P-C_G"; k_{t_H} is the mesh stiffness for "H_P-H_G"; $k_{t\_V_1}$ is the mesh stiffness for "Variant 1"; $k_{t\_V_2}$ is the mesh stiffness for "Variant 2"; $k_{t\_V_3}$ is the mesh stiffness for "Variant 3"; $k_{t\_V_4}$ is the mesh stiffness for "Variant 4". k_{t_H} is calculated using Eq. (5.20), the remaining 7 stiffness components in one period of K_{III} are calculated using Eq. (5.24) through Eq. (5.30). Ω_1, Ω_2, Ω_3, Ω_4, Ω_5, Ω_6, Ω_7, and Ω_8 are the corresponding value ranges of θ_1 for $k_{t\_q_p\_q_g}$, $k_{t\_q_p}$, $k_{t\_q_g}$, k_{t_H}, $k_{t\_V_1}$, $k_{t\_V_2}$, $k_{t\_V_3}$, and $k_{t\_V_4}$, respectively, which are shown in Eq. (5.31).

$$k_{t\_q_p\_q_g} = \begin{cases} k_{t\_H_P^{I-1}H_G^{J-1}} + k_{t\_C_P^I C_G^J}, & \theta_1 \in [0,\theta_d] + |\mathrm{I}-\mathrm{J}|\frac{2\pi}{N_p} \\ k_{t\_C_P^I C_G^J}, & \theta_1 \in \left[\theta_d, \frac{2\pi}{N_p}\right] + |\mathrm{I}-\mathrm{J}|\frac{2\pi}{N_p} \\ k_{t\_C_P^I C_G^J} + k_{t\_H_P^{I+1}H_G^{J+1}}, & \theta_1 \in \left[\frac{2\pi}{N_p}, \frac{2\pi}{N_p}+\theta_d\right] + |\mathrm{I}-\mathrm{J}|\frac{2\pi}{N_p} \\ k_{t\_H_P^{I+1}H_G^{J+1}}, & \theta_1 \in \left[\frac{2\pi}{N_p}+\theta_d, 2\frac{2\pi}{N_p}\right] + |\mathrm{I}-\mathrm{J}|\frac{2\pi}{N_p} \end{cases} \tag{5.24}$$

where $k_{t\_C_P^I C_G^J} = \frac{1}{1/k_h + 1/k_{b\_C_P^I} + 1/k_{a\_C_P^I} + 1/k_{s\_C_P^I} + 1/k_{b\_C_G^J} + 1/k_{a\_C_G^J} + 1/k_{s\_C_G^J}}$, in which $k_{b\_C_P^I}$, $k_{a\_C_P^I}$, and $k_{s\_C_P^I}$ are the bending stiffness, axial compressive stiffness, and shear stiffness of the cracked

pinion tooth "I" whose crack depth is q_p, respectively; $k_{b\_C_G^J}$, $k_{a\_C_G^J}$, and $k_{s\_C_G^J}$ are the bending stiffness, axial compressive stiffness, and shear stiffness of the cracked gear tooth "J" whose crack depth is q_g, respectively.

$$k_{t\_q_p} = \begin{cases} k_{t\_H_P^{I-1}H_G^{g-1}} + k_{t\_C_P^I H_G^g}, & \theta_1 \in [0, \theta_d] + (\mathrm{I}-1)\frac{2\pi}{N_p} \\ k_{t\_C_P^I H_G^g}, & \theta_1 \in \left[\theta_d, \frac{2\pi}{N_p}\right] + (\mathrm{I}-1)\frac{2\pi}{N_p} \\ k_{t\_C_P^I H_G^g} + k_{t\_H_P^{I+1}H_G^{g+1}}, & \theta_1 \in \left[\frac{2\pi}{N_p}, \frac{2\pi}{N_p} + \theta_d\right] + (\mathrm{I}-1)\frac{2\pi}{N_p} \\ k_{t\_H_P^{I+1}H_G^{g+1}}, & \theta_1 \in \left[\frac{2\pi}{N_p} + \theta_d, 2\frac{2\pi}{N_p}\right] + (\mathrm{I}-1)\frac{2\pi}{N_p} \end{cases} \tag{5.25}$$

where $k_{t\_C_P^I H_G^g} = \frac{1}{1/k_h{}^{+1}/k_{b\_C_P^I}{}^{+1}/k_{a\_C_P^I}{}^{+1}/k_{s\_C_P^I}{}^{+1}/k_{b\_H_G^g}{}^{+1}/k_{a\_H_G^g}{}^{+1}/k_{s\_H_G^g}}$, in which $k_{b\_C_P^I}$, $k_{a\_C_P^I}$, and $k_{s\_C_P^I}$ are the bending stiffness, axial compressive stiffness, and shear stiffness of the cracked pinion tooth "I" with crack depth q_p, respectively.

$$k_{t\_q_g} = \begin{cases} k_{t\_H_P^{p-1}H_G^{J-1}} + k_{t\_H_P^p C_G^J}, & \theta_1 \in [0, \theta_d] + (\mathrm{J}-1)\frac{2\pi}{N_p} \\ k_{t\_H_P^p C_G^J}, & \theta_1 \in \left[\theta_d, \frac{2\pi}{N_p}\right] + (\mathrm{J}-1)\frac{2\pi}{N_p} \\ k_{t\_H_P^p C_G^J} + k_{t\_H_P^{p+1}H_G^{J+1}}, & \theta_1 \in \left[\frac{2\pi}{N_p}, \frac{2\pi}{N_p} + \theta_d\right] + (\mathrm{J}-1)\frac{2\pi}{N_p} \\ k_{t\_H_P^{p+1}H_G^{J+1}} & \theta_1 \in \left[\frac{2\pi}{N_p} + \theta_d, 2\frac{2\pi}{N_p}\right] + (\mathrm{J}-1)\frac{2\pi}{N_p} \end{cases} \tag{5.26}$$

where $k_{t\_H_P^p C_G^J} = \frac{1}{1/k_h{}^{+1}/k_{b\_H_P^p}{}^{+1}/k_{a\_H_P^p}{}^{+1}/k_{s\_H_P^p}{}^{+1}/k_{b\_C_G^J}{}^{+1}/k_{a\_C_G^J}{}^{+1}/k_{s\_C_G^J}}$, in which $k_{b\_C_G^J}$, $k_{a\_C_G^J}$, and $k_{s\_C_G^J}$ are the bending stiffness, axial compressive stiffness, and shear stiffness of the cracked gear tooth "J" with crack depth q_g, respectively.

$$k_{t\_V_1}=\begin{cases} k_{t\_H_P^{I-1}H_G^{J-2}}+k_{t\_C_P^{I}H_G^{J-1}}, & \theta_1\in[0,\theta_d]+\left(\mathrm{I}-1+aN_p\right)\frac{2\pi}{N_p} \\ k_{t\_C_P^{I}H_G^{J-1}}, & \theta_1\in\left[\theta_d,\frac{2\pi}{N_p}\right]+\left(\mathrm{I}-1+aN_p\right)\frac{2\pi}{N_p} \\ k_{t\_C_P^{I}H_G^{J-1}}+k_{t\_H_P^{I+1}C_G^{J}}, & \theta_1\in\left[\frac{2\pi}{N_p},\frac{2\pi}{N_p}+\theta_d\right]+\left(\mathrm{I}-1+aN_p\right)\frac{2\pi}{N_p} \\ k_{t\_H_P^{I+1}C_G^{J}} & \theta_1\in\left[\frac{2\pi}{N_p}+\theta_d,2\frac{2\pi}{N_p}\right]+\left(\mathrm{I}-1+aN_p\right)\frac{2\pi}{N_p} \\ k_{t\_H_P^{I+1}C_G^{J}}+k_{t\_H_P^{I+2}H_G^{J+1}} & \theta_1\in\left[2\frac{2\pi}{N_p},2\frac{2\pi}{N_p}+\theta_d\right]+\left(\mathrm{I}-1+aN_p\right)\frac{2\pi}{N_p} \\ k_{t\_H_P^{I+2}H_G^{J+1}} & \theta_1\in\left[2\frac{2\pi}{N_p}+\theta_d,3\frac{2\pi}{N_p}\right]+\left(\mathrm{I}-1+aN_p\right)\frac{2\pi}{N_p} \end{cases} \tag{5.27}$$

$$k_{t\_V_2}=\begin{cases} k_{t\_H_P^{I-1}H_G^{J-3}}+k_{t\_C_P^{I}H_G^{J-2}}, & \theta_1\in[0,\theta_d]+\left(\mathrm{I}-1+aN_p\right)\frac{2\pi}{N_p} \\ k_{t\_C_P^{I}H_G^{J-2}}, & \theta_1\in\left[\theta_d,\frac{2\pi}{N_p}\right]+\left(\mathrm{I}-1+aN_p\right)\frac{2\pi}{N_p} \\ k_{t\_C_P^{I}H_G^{J-2}}+k_{t\_H_P^{I+1}H_G^{J-1}}, & \theta_1\in\left[\frac{2\pi}{N_p},\frac{2\pi}{N_p}+\theta_d\right]+\left(\mathrm{I}-1+aN_p\right)\frac{2\pi}{N_p} \\ k_{t\_H_P^{I+1}H_G^{J-1}} & \theta_1\in\left[\frac{2\pi}{N_p}+\theta_d,2\frac{2\pi}{N_p}\right]+\left(\mathrm{I}-1+aN_p\right)\frac{2\pi}{N_p} \\ k_{t\_H_P^{I+1}H_G^{J-1}}+k_{t\_H_P^{I+2}C_G^{J}} & \theta_1\in\left[2\frac{2\pi}{N_p},2\frac{2\pi}{N_p}+\theta_d\right]+\left(\mathrm{I}-1+aN_p\right)\frac{2\pi}{N_p} \\ k_{t\_H_P^{I+2}C_G^{J}} & \theta_1\in\left[2\frac{2\pi}{N_p}+\theta_d,3\frac{2\pi}{N_p}\right]+\left(\mathrm{I}-1+aN_p\right)\frac{2\pi}{N_p} \\ k_{t\_H_P^{I+2}C_G^{J}}+k_{t\_H_P^{I+3}H_G^{J+1}} & \theta_1\in\left[3\frac{2\pi}{N_p},3\frac{2\pi}{N_p}+\theta_d\right]+\left(\mathrm{I}-1+aN_p\right)\frac{2\pi}{N_p} \\ k_{t\_H_P^{I+3}H_G^{J+1}} & \theta_1\in\left[3\frac{2\pi}{N_p}+\theta_d,4\frac{2\pi}{N_p}\right]+\left(\mathrm{I}-1+aN_p\right)\frac{2\pi}{N_p} \end{cases} \tag{5.28}$$

$$k_{t\_V_3}=\begin{cases} k_{t\_H_P^{I-3}H_G^{J-1}}+k_{t\_H_P^{I-2}C_G^{J}}, & \theta_1\in[0,\theta_d]+\left(\mathrm{I}-1+aN_p\right)\frac{2\pi}{N_p} \\ k_{t\_H_P^{I-2}C_G^{J}}, & \theta_1\in\left[\theta_d,\frac{2\pi}{N_p}\right]+\left(\mathrm{I}-1+aN_p\right)\frac{2\pi}{N_p} \\ k_{t\_H_P^{I-2}C_G^{J}}+k_{t\_H_P^{I-1}H_G^{J+1}}, & \theta_1\in\left[\frac{2\pi}{N_p},\frac{2\pi}{N_p}+\theta_d\right]+\left(\mathrm{I}-1+aN_p\right)\frac{2\pi}{N_p} \\ k_{t\_H_P^{I-1}H_G^{J+1}} & \theta_1\in\left[\frac{2\pi}{N_p}+\theta_d,2\frac{2\pi}{N_p}\right]+\left(\mathrm{I}-1+aN_p\right)\frac{2\pi}{N_p} \\ k_{t\_H_P^{I-1}H_G^{J+1}}+k_{t\_C_P^{I}H_G^{J+2}} & \theta_1\in\left[2\frac{2\pi}{N_p},2\frac{2\pi}{N_p}+\theta_d\right]+\left(\mathrm{I}-1+aN_p\right)\frac{2\pi}{N_p} \\ k_{t\_C_P^{I}H_G^{J+2}} & \theta_1\in\left[2\frac{2\pi}{N_p}+\theta_d,3\frac{2\pi}{N_p}\right]+\left(\mathrm{I}-1+aN_p\right)\frac{2\pi}{N_p} \\ k_{t\_C_P^{I}H_G^{J+2}}+k_{t\_H_P^{I+1}H_G^{J+3}} & \theta_1\in\left[3\frac{2\pi}{N_p},3\frac{2\pi}{N_p}+\theta_d\right]+\left(\mathrm{I}-1+aN_p\right)\frac{2\pi}{N_p} \\ k_{t\_H_P^{I+1}H_G^{J+3}} & \theta_1\in\left[3\frac{2\pi}{N_p}+\theta_d,4\frac{2\pi}{N_p}\right]+\left(\mathrm{I}-1+aN_p\right)\frac{2\pi}{N_p} \end{cases} \tag{5.29}$$

$$k_{t\_V_4}=\begin{cases} k_{t\_H_P^{I-2}H_G^{J-1}}+k_{t\_H_P^{I-1}C_G^{J}}, & \theta_1\in[0,\theta_d]+\left(\mathrm{I}-1+aN_p\right)\frac{2\pi}{N_p} \\ k_{t\_H_P^{I-1}C_G^{J}}, & \theta_1\in\left[\theta_d,\frac{2\pi}{N_p}\right]+\left(\mathrm{I}-1+aN_p\right)\frac{2\pi}{N_p} \\ k_{t\_H_P^{I-1}C_G^{J}}+k_{t\_C_P^{I}H_G^{J+1}}, & \theta_1\in\left[\frac{2\pi}{N_p},\frac{2\pi}{N_p}+\theta_d\right]+\left(\mathrm{I}-1+aN_p\right)\frac{2\pi}{N_p} \\ k_{t\_C_P^{I}H_G^{J+1}} & \theta_1\in\left[\frac{2\pi}{N_p}+\theta_d,2\frac{2\pi}{N_p}\right]+\left(\mathrm{I}-1+aN_p\right)\frac{2\pi}{N_p} \\ k_{t\_C_P^{I}H_G^{J+1}}+k_{t\_H_P^{I+1}H_G^{J+2}} & \theta_1\in\left[2\frac{2\pi}{N_p},2\frac{2\pi}{N_p}+\theta_d\right]+\left(\mathrm{I}-1+aN_p\right)\frac{2\pi}{N_p} \\ k_{t\_H_P^{I+1}H_G^{J+2}} & \theta_1\in\left[2\frac{2\pi}{N_p}+\theta_d,3\frac{2\pi}{N_p}\right]+\left(\mathrm{I}-1+aN_p\right)\frac{2\pi}{N_p} \end{cases} \tag{5.30}$$

$$\Omega_1=\left[0,2\frac{2\pi}{N_p}\right]+|\mathrm{I}-\mathrm{J}|\frac{2\pi}{N_p}+(s-1)N_g*2\pi \tag{5.31.1}$$

$$\Omega_2=\left[0,2\frac{2\pi}{N_p}\right]+\left(\mathrm{I}-1+aN_p\right)\frac{2\pi}{N_p}+(s-1)N_g*2\pi,\ (a=1,2,\dots,N_g-1,\ \text{except the values that make } 1\le\left|\left(\mathrm{I}-1+aN_p\right)-\left(\mathrm{J}-1+bN_g\right)\right|\le 2) \tag{5.31.2}$$

$$\Omega_3=\left[0,2\frac{2\pi}{N_p}\right]+\left(\mathrm{J}-1+bN_g\right)\frac{2\pi}{N_p}+(s-1)N_g*2\pi,\ (b=1,2,\dots,N_p-1,\ \text{except the values that make } 1\le\left|\left(\mathrm{I}-1+aN_p\right)-\left(\mathrm{J}-1+bN_g\right)\right|\le 2) \tag{5.31.3}$$

$$\Omega_5=\left[0,3\frac{2\pi}{N_p}\right]+\left(\mathrm{I}-1+aN_p\right)\frac{2\pi}{N_p}+(s-1)N_g*2\pi,\ (a\ \text{equals the values that makes } \left(\mathrm{I}-1+aN_p\right)-\left(\mathrm{J}-1+bN_g\right)=-1) \tag{5.31.4}$$

$$\Omega_6=\left[0,4\frac{2\pi}{N_p}\right]+\left(\mathrm{I}-1+aN_p\right)\frac{2\pi}{N_p}+(s-1)N_g*2\pi,\ (a\ \text{equals the values that makes } \left(\mathrm{I}-1+aN_p\right)-\left(\mathrm{J}-1+bN_g\right)=-2) \tag{5.31.5}$$

$$\Omega_7=\left[0,4\frac{2\pi}{N_p}\right]+\left(\mathrm{I}-1+aN_p\right)\frac{2\pi}{N_p}+(s-1)N_g*2\pi,\ (a\ \text{equals the values that makes } \left(\mathrm{I}-1+aN_p\right)-\left(\mathrm{J}-1+bN_g\right)=2) \tag{5.31.6}$$

$$\Omega_8=\left[0,3\frac{2\pi}{N_p}\right]+\left(\mathrm{I}-1+aN_p\right)\frac{2\pi}{N_p}+(s-1)N_g*2\pi,\ (a\ \text{equals the values that makes } \left(\mathrm{I}-1+aN_p\right)-\left(\mathrm{J}-1+bN_g\right)=1) \tag{5.31.7}$$

$$\Omega_4=\left[0,S*N_g*2\pi\right]-\Omega_1-\Omega_2-\Omega_3-\Omega_5-\Omega_6-\Omega_7-\Omega_8 \tag{5.31.8}$$

where s is the number of periods of K_{III} (s is a positive integer); a is the number of "one pinion revolution ($N_p \frac{2\pi}{N_p}$)", and b is the number of "one gear revolution ($N_g \frac{2\pi}{N_p}$)". In Eq. (5.27) through Eq. (5.30), a takes the values that satisfy the conditions shown in Eq. (5.31.4) through Eq. (5.31.7).

5.2.5 Analysis of tooth mesh stiffness and gearbox vibration signals

To procure insights into vibration characteristics of spur gearboxes with the three scenarios of multiple tooth cracks considered in this chapter, tooth mesh stiffness for each scenario is first analyzed in both angle and frequency domains to reveal the effects of multiple tooth cracks on tooth mesh stiffness. The reason why mesh stiffness is analyzed in angle domain is to verify the descriptions presented in Subsection 5.2.4, namely mesh stiffness for multiple tooth cracks are periodic functions with regards to the pinion angular displacement θ_1. Because constant working condition is considered in this chapter, analyses of mesh stiffness in angle domain are equivalent to those in time domain. In the angle domain, mesh stiffness corresponding to each scenario of multiple tooth cracks will be illustrated to show how tooth cracks affect mesh stiffness. Besides, mesh stiffness will be analyzed in frequency domain to reveal its frequency composition. Differences of mesh stiffness for the three scenarios of multiple tooth cracks will also be described.

Besides, vibration signals of spur gearboxes with the three scenarios of multiple tooth cracks will be analyzed in both time and frequency domains. Firstly, time domain waveforms of gearbox vibration signals will be displayed to show how they are affected by multiple tooth cracks. In addition, frequency spectra of gearbox vibration signals will be examined to identify the frequency components corresponding to gear mesh and those related to multiple tooth cracks. Differences of gearbox vibration signals for the three scenarios of multiple tooth cracks will be discussed as well.

5.2.6 Detection of the number and locations of multiple tooth cracks

5.2.6.1 Procedure for the proposed method

Fig. 5.8 shows the procedure for the proposed method for detecting the number and locations of multiple tooth cracks in spur gearboxes. The proposed method consists of two parts: (1) extract the CII from gearbox vibration signals using an SVD-based strategy; (2) conduct TSA on CII for both the pinion and the gear to get their TSA signals, squared envelopes of which are obtained

using envelope analysis. According to the squared envelopes of the pinion and gear TSA signals, the number and locations of multiple tooth cracks are detected.

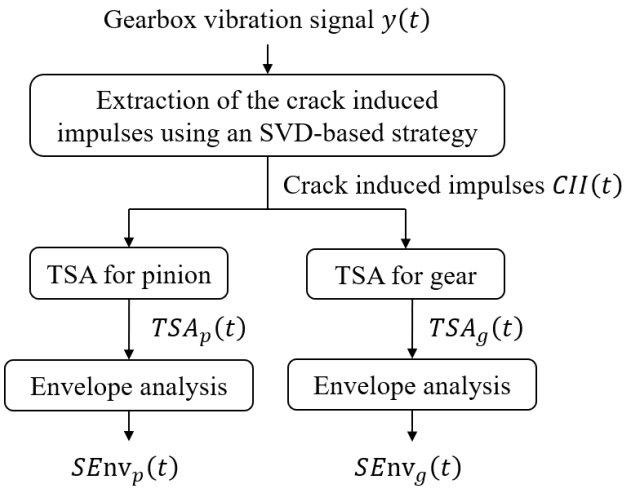

Fig. 5.8: Procedure for the proposed method

5.2.6.2 Extraction of crack induced impulses using an SVD-based strategy

Inspired by the obtained insights into vibration characteristics for multiple tooth cracks, it is known that the CII include information on multiple tooth cracks. Besides, the CII contain more information on tooth cracks than other signal components [77,104,107]. Therefore, for the proposed method, its focus is placed on the CII, and one key step of it is to extract the CII from gearbox vibration signals. To this end, SVD is a feasible approach since it has been widely employed to analyze gearbox vibration signals [96,97]. However, there are still some deficiencies of the studies reported in Refs. [96,97] when using SVD to extract CII from gearbox vibration signals, which are overcome in this chapter by proposing a new SVD-based strategy. To show the limitations of the studies reported in Refs. [96,97] and illustrate the new SVD-based strategy, fundamentals of SVD are first introduced. SVD is a method for conducting the orthonormal decomposition of an $m \times n$ real matrix $\boldsymbol{H}$, which is given by Eq. (5.32) [95–97].

$$\boldsymbol{H} = \boldsymbol{U}\boldsymbol{\Sigma}V^T \tag{5.32}$$

where $\boldsymbol{U} = [\boldsymbol{u}_1, \boldsymbol{u}_2, \boldsymbol{u}_3, \dots, \boldsymbol{u}_m] \in \boldsymbol{R}^{m\times m}$ and $\boldsymbol{V} = [\boldsymbol{v}_1, \boldsymbol{v}_2, \boldsymbol{v}_3, \dots, \boldsymbol{v}_n] \in \boldsymbol{R}^{n\times n}$ are orthonormal matrices; $\boldsymbol{\Sigma}$ is a diagonal matrix storing the singular values of the matrix $\boldsymbol{H}$ in the descending order, namely $\boldsymbol{\Sigma} = [diag(\sigma_1, \sigma_2, \sigma_3, \dots, \sigma_l), \boldsymbol{0}] \in R^{m\times n}$, in which $l = min(m, n)$ and $\boldsymbol{0}$ is a zero matrix, and $\sigma_1 \geq \sigma_2 \geq \sigma_3 \geq \cdots \geq \sigma_l$; superscript "$T$" denotes the operation of matrix transposition.

To apply SVD to a 1-D signal, such as $\boldsymbol{x} = [x(1), x(2), x(3), \dots, x(N)]$, the 1-D signal needs to be first converted into a matrix. The Hankel matrix is a good choice since it has the unique property of zero phase shift [142]. The construction of the Hankel matrix of signal $\boldsymbol{x}$ is shown in Eq. (5.33).

$$\boldsymbol{H} = \begin{bmatrix} x(1) & x(2) & \cdots & x(n) \\ x(2) & x(3) & \cdots & x(n+1) \\ \vdots & \vdots & \ddots & \vdots \\ x(m) & x(m+1) & \cdots & x(N) \end{bmatrix} \tag{5.33}$$

where $m = N - n + 1$; parameter m is used to determine the number of the singular values of the Hankel matrix $\boldsymbol{H}$, and usually m is set to be smaller than n.

According to Eq. (5.32), the SVD result of the Hankel matrix $\boldsymbol{H}$ can be expressed in the form of m sub-matrix $\boldsymbol{H}_i$ $(i = 1, 2, \dots, m)$, which is given by

$$\boldsymbol{H} = [\boldsymbol{u}_1, \boldsymbol{u}_2, \boldsymbol{u}_3, \dots, \boldsymbol{u}_m] \begin{bmatrix} \sigma_1 & 0 & \cdots & 0 & \boldsymbol{0} \\ 0 & \sigma_2 & \cdots & 0 & \boldsymbol{0} \\ \vdots & \vdots & \ddots & \vdots & \boldsymbol{0} \\ 0 & 0 & \cdots & \sigma_m & \boldsymbol{0} \end{bmatrix} \begin{bmatrix} \boldsymbol{v}_1^T \\ \boldsymbol{v}_2^T \\ \vdots \\ \boldsymbol{v}_n^T \end{bmatrix}$$

$$= \sigma_1 \boldsymbol{u}_1 \boldsymbol{v}_1^T + \sigma_2 \boldsymbol{u}_2 \boldsymbol{v}_2^T + \cdots + \sigma_m \boldsymbol{u}_m \boldsymbol{v}_m^T = \boldsymbol{H}_1 + \boldsymbol{H}_2 + \cdots + \boldsymbol{H}_m \tag{5.34}$$

where $\boldsymbol{u}_i \in \boldsymbol{R}^{m \times 1}$ is the i^{th} column vector of the left singular matrix $\boldsymbol{U}$, $\boldsymbol{v}_i \in \boldsymbol{R}^{n \times 1}$ is the i^{th} column vector of the right singular matrix $\boldsymbol{V}$.

Each sub-matrix $\boldsymbol{H}_i$ in Eq. (5.34) corresponds to a Singular Component (SC) of the input signal $\boldsymbol{x}$, namely $\boldsymbol{x}_i$, which can be procured from the sub-matrix $\boldsymbol{H}_i$ by averaging its anti-diagonals [97]. On this basis, all the components of the input signal $\boldsymbol{x}$, namely $\boldsymbol{x}_1$, $\boldsymbol{x}_2$, …, and $\boldsymbol{x}_m$, can be obtained. For different purposes, a signal with specific information can be reconstructed in different ways by choosing different SCs to sum. Therefore, the reconstructed signal $\boldsymbol{s}$ is expressed as follows:

$$\boldsymbol{s} = \sum \boldsymbol{x}_i \tag{5.35}$$

where $\boldsymbol{x}_i$ are the SCs selected to get a reconstructed signal for a particular purpose.

Singular values of the Hankel matrix $\boldsymbol{H}$ reflect the energy of their corresponding SCs [95], and an SC with a larger singular value has a higher energy. In conventional SVD-based methods, SCs with larger singular values were selected for signal reconstruction to remove noise. However, the energy-based criterion for selecting SCs is not suitable to extract weak tooth crack features

embedded in gearbox vibration signals since SCs with higher energy do not necessarily have more information on tooth cracks [95]. To overcome this deficiency, Zhao et al. [97] developed another criterion to select SCs for signal reconstruction, which was based on an indicator termed Periodic Modulation Intensity (PMI). PMI measures the strength of CII and represents the energy ratio between CII and other signal components. An SC with a larger PMI value has more significant signature for tooth cracks. PMI is calculated as follows [97].

$$PMI = \frac{R_{Env}(T_{crack})}{R_{Env}(0) - R_{Env}(T_{crack})} \tag{5.36}$$

where T_{crack} is the repetition period of the CII; $R_{Env}(T_{crack})$ is the autocorrelation of the envelope signal Env at T_{crack}, which represents the energy of the CII; $R_{Env}(0)$ is the autocorrelation of the Env at 0, which represents the energy of the envelope signal.

The envelope of a signal is calculated using Eq. (5.37).

$$Env(t) = abs\left[x(t) + jHT\left(x(t)\right)\right] \tag{5.37}$$

where j is the imaginary unit; HT represents the Hilbert Transform.

The advantages and disadvantages of the PMI-based SVD methods [96,97] have been discussed in Subsection 1.2.2.3. To overcome the disadvantages, this chapter utilizes the comb notch filtering to remove the gear meshing harmonics since it is easier to implement. The proposed SVD-based strategy for extracting the CII consists of the following steps.

Step 1: Pre-process the raw signal. Conduct comb notch filtering on the raw gearbox vibration signal $y(t)$ to remove the gear meshing harmonics and their associated sidebands, thus obtaining the residual signal $Res(t)$. Find out the frequency band in which the CII exist using the energy spectral density and conduct band-pass filtering on the residual signal using the identified frequency range to get the band-pass filtered residual signal $ResBpf(t)$.

Step 2: Implement SVD. Apply the SVD to decompose the band-pass filtered residual signal $ResBpf(t)$ into m SCs. The value of m is determined using the guidance presented in Ref. [97].

Step 3: Evaluate crack information. Calculate the PMI values of all the m SCs using Eq. (5.36).

Step 4: Extract the CII. The SCs with PMI values greater than the preset threshold p_{TH} are selected for signal reconstruction, and the reconstructed signal is regarded as the CII. The threshold p_{TH} is

determined as the average of the PMI values of the SCs obtained from healthy gearbox vibration signals. Therefore, the CII is expressed in Eq. (5.38).

$$CII = \sum SC_k * PMI_{SC_k} \tag{5.38}$$

where SC_k are the SCs with PMI values greater than the threshold p_{TH}, PMI_{SC_k} is the PMI value of SC_k; $k \in$ P, P is the set storing the indices of the PMI which are greater than p_{TH} (P is a subset of the set $\{1,2,\dots,m\}$).

5.2.6.3 Time synchronous average and envelope analysis

TSA has been widely used to extract periodic components related to a target shaft from gearbox vibration signals [42,111]. TSA can separate the target gear tooth crack signature under analysis from interfering vibration components which are asynchronous with the gear to be monitored [77,104]. Details of TSA have been introduced in Subsection 2.2.1, which are not described herein for brevity. TSA is conducted on the CII for both the pinion and the gear shafts, thus procuring TSA signals for both the pinion and the gear, namely the TSA_p and TSA_g shown in Fig. 5.8, which contain the information about if there are tooth cracks on the pinion and the gear or not. Squared envelopes of $TSA_p$and TSA_g are calculated using Eq. (5.39) and Eq. (5.40), respectively.

$$SEnv_p = \left\{abs\left[TSA_p + jHT\left(TSA_p\right)\right]\right\}^2 \tag{5.39}$$

$$SEnv_g = \left\{abs\left[TSA_g + jHT\left(TSA_g\right)\right]\right\}^2 \tag{5.40}$$

where j is the imaginary unit; HT represents the Hilbert Transform.

By examining the distinct impulses in $SEnv_p$ and calculating the time interval between them, the number and locations of tooth cracks on the pinion can be detected. Likewise, the number and locations of tooth cracks on the gear can also be detected by examining the impulses in $SEnv_g$. On this basis, the number and locations of multiple tooth cracks in spur gearboxes are detected.

5.3 Simulation analysis

5.3.1 Generation of simulated gearbox vibration signals

In this chapter, parameters of the spur gearbox system shown in Fig. 2.2 are set to be the same as those tabulated in Table 3.1. Besides, the driving motor torque is $M_1 = 19$ Nm, the driving motor speed is $SPD = 30$ Hz, and the torque exerted on the load machine is $M_2 = 48$ Nm. Parameters for the three scenarios of multiple tooth cracks are shown in Table 5.1, Table 5.2, and Table 5.3, respectively. Tooth mesh stiffness for the three scenarios of multiple tooth cracks can be evaluated using the mesh stiffness formulae derived in Subsection 5.2.3 and Subsection 5.2.4. The tooth mesh stiffness is substituted into the gearbox system motion equation shown in Eq. (3.1), and gearbox dynamic responses are calculated using the Newmark integration algorithm. The y-direction acceleration signal of the pinion is used as the simulated gearbox vibration signal.

Table 5.1: Parameters for the first scenario of multiple tooth cracks (Scenario 1 in Fig. 5.4)

Parameter	value
Serial number of the first cracked pinion tooth	$\mathrm{I} = 1$
Serial number of the second cracked pinion tooth	$\mathrm{J} = 7$
Crack depth of the first cracked pinion tooth	$q_{p1} = 3\ mm$
Crack depth of the second cracked pinion tooth	$q_{p2} = 2.4\ mm$
Crack angle	$\phi = 45^{\circ}$

Table 5.2: Parameters for the second scenario of multiple tooth cracks (Scenario 2 in Fig. 5.5)

Parameter	value
Serial number of the first cracked pinion tooth	$\mathrm{I} = 1$
Serial number of the second cracked pinion tooth	$\mathrm{I} + 1 = 2$
Crack depth of the first cracked pinion tooth	$q_{p1} = 3\ mm$
Crack depth of the second cracked pinion tooth	$q_{p2} = 2.4\ mm$
Crack angle	$\phi = 45^{\circ}$

Table 5.3: Parameters for the third scenario of multiple tooth cracks (Scenario 3 in Fig. 5.6)

Parameter	value
Serial number of the cracked pinion tooth	$\mathrm{I} = 1$
Serial number of the cracked gear tooth	$\mathrm{J} = 1$
Crack depth of the cracked pinion tooth	$q_p = 3\ mm$
Crack depth of the cracked gear tooth	$q_g = 2.4\ mm$
Crack angle	$\phi = 45^{\circ}$

5.3.2 Analysis of gear tooth mesh stiffness and simulated gearbox vibration signals

In this subsection, gear tooth mesh stiffness and simulated gearbox vibration signals for the three scenarios of multiple tooth cracks are analyzed using the scheme described in Subsection 5.2.5, thus procuring insights into the vibration characteristics of spur gearboxes with multiple tooth cracks.

5.3.2.1 Scenario 1: two nonadjacent tooth cracks on the pinion and a healthy gear

The angle domain waveform and frequency spectrum of the gear tooth mesh stiffness for "Scenario 1" (K_I) are illustrated in Fig. 5.9 and Fig. 5.10, respectively. As shown in Fig. 5.9(a), gear tooth mesh stiffness K_I has a period of $2\pi\ rad$ since its values in every $2\pi\ rad$ are the same. From Fig. 5.9(b), it is observed that either $k_{t\_q_p1}$ or $k_{t\_q_p2}$ lasts for two mesh periods, so two nonadjacent pinion tooth cracks affect four mesh periods. Either $k_{t\_q_p1}$ or $k_{t\_q_p2}$ appears once in one period of K_I. Besides, the decrease of the mesh stiffness of the first pinion tooth crack ($k_{t\_q_p1}$) is larger than that of the second pinion tooth crack ($k_{t\_q_p2}$). These observations demonstrate the correct implementation of gear tooth mesh stiffness evaluation presented in Subsection 5.2.4.1. From Fig. 5.10(a), it is seen that the frequency spectrum of K_I is mainly dominated by gear meshing frequency (570 Hz) and its multiples. Besides, there are many frequency spikes in the frequency range [0,400] Hz, which are shown in Fig. 5.10(b). It is seen that the spikes are the pinion rotational frequency 30Hz and its multiples, and their magnitudes are much smaller than those of the gear meshing harmonics.

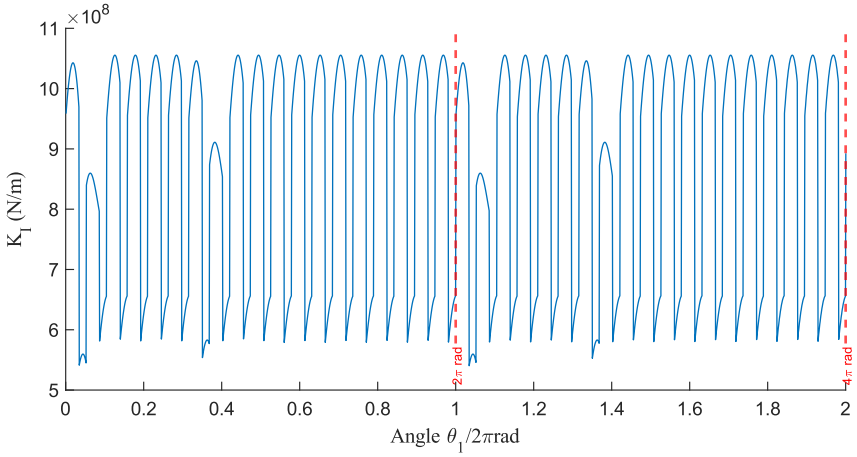

(a) Mesh stiffness for multiple tooth cracks "Scenario 1" (K_I in two periods $2 * 2\pi\ rad$)

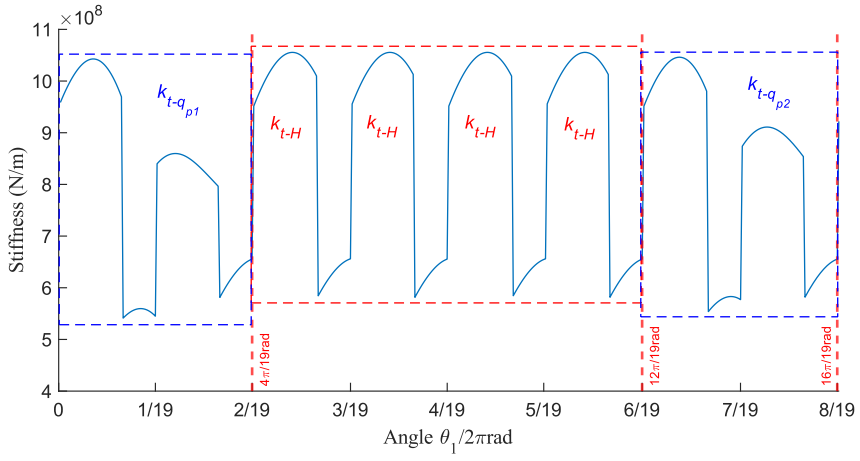

(b) $k_{t\_q_{p1}}$ (2 mesh periods $[0, 2\frac{2\pi}{19}]$), $k_{t\_q_{p2}}$ (2 mesh periods $[6\frac{2\pi}{19}, 8\frac{2\pi}{19}]$), and k_{t_H}

Fig. 5.9: Mesh stiffness for multiple tooth cracks "Scenario 1" (K_I)

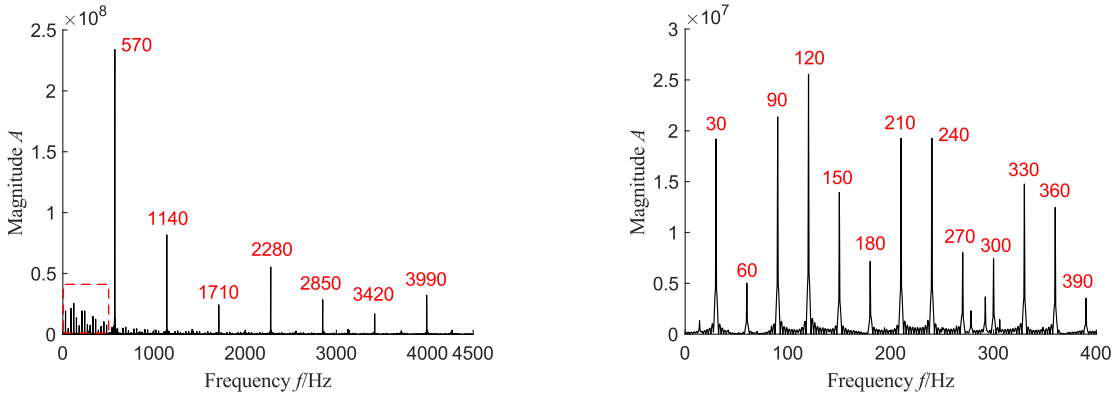

(a) Full-scale view (b) Zoomed-in view in [0, 400] Hz

Fig. 5.10: Frequency spectrum of mesh stiffness K_I

The time waveform and frequency spectrum of the gearbox dynamic response for "Scenario 1" are illustrated in Fig. 5.11. As shown in the top plot of Fig. 5.11(a), it is observed that there are two nonadjacent impulses (in each red dashed rectangle) in one pinion revolution. The frequency spectrum shown in the bottom plot of Fig. 5.11(a) is dominated by gear meshing harmonics (multiples of 570 Hz). Besides, there is a frequency cluster in the frequency range [2900, 3900] Hz, details of which are shown in Fig. 5.11(b). It is seen that the frequency cluster consists of a group of spikes with a uniform interval of 30 Hz, such as 3330-3300=30 Hz, which is the pinion rotational speed. Therefore, the frequency cluster consists of frequency components of the impulses induced by the two nonadjacent pinion tooth cracks.

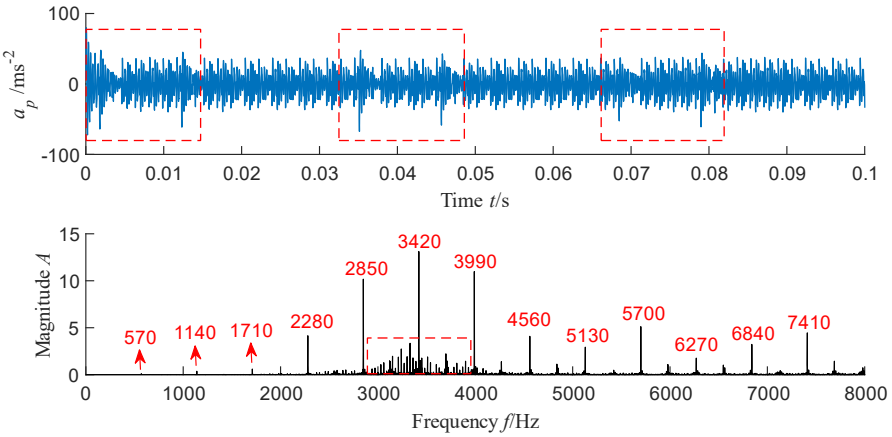

(a) Time waveform and frequency spectrum (full-scale view)

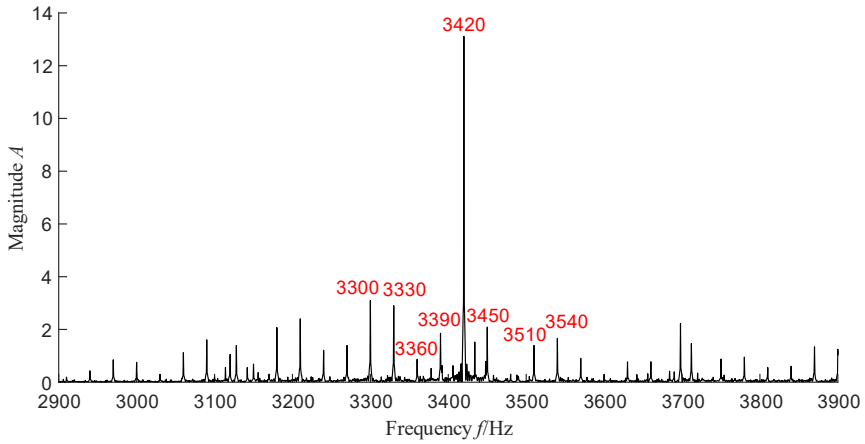

(b) Frequency spectrum (zoomed-in view in [2900, 3900] Hz)

Fig. 5.11: Time waveform and frequency spectrum of gearbox dynamic response (Scenario 1)

5.3.2.2 Scenario 2: two adjacent tooth cracks on the pinion and a healthy gear

The angle domain waveform and frequency spectrum of the gear tooth mesh stiffness for "Scenario 2" (K_{II}) are illustrated in Fig. 5.12 and Fig. 5.13, respectively. As shown in Fig. 5.12(a), gear tooth mesh stiffness K_{II} has a period of $2\pi\ rad$ since its values in every $2\pi\ rad$ are the same. From Fig. 5.12 (b), it is observed that $k_{t\_q_{p1}\_q_{p2}}$ lasts for three mesh periods $[0,3\frac{2\pi}{19}]$, so two adjacent pinion tooth cracks affect three mesh periods. $k_{t\_q_{p1}\_q_{p2}}$ appears once in one period of K_{II}. Besides, the decrease of the mesh stiffness of the first pinion tooth crack (3 mm) is larger than that of the second pinion tooth crack (2.4 mm). These observations demonstrate the correct implementation of mesh stiffness evaluation presented in Subsection 5.2.4.2. From Fig. 5.13(a), it is seen that the frequency spectrum of K_{II} is mainly dominated by the gear meshing harmonics (570 Hz and its multiples).

Besides, there are many frequency spikes in the frequency range [0,500] Hz, which are shown in Fig. 5.13(b). It is seen that the spikes are the pinion rotational frequency 30 Hz and its multiples, and their magnitudes are much smaller than those of the gear meshing harmonics. Besides, the magnitudes of the spikes in Fig. 5.13(b) change in a regular pattern, which is totally different from that shown in Fig. 5.10(b). This means that the effect of two adjacent pinion tooth cracks on the frequency spectrum of gear tooth mesh stiffness is different from that of two nonadjacent pinion tooth cracks.

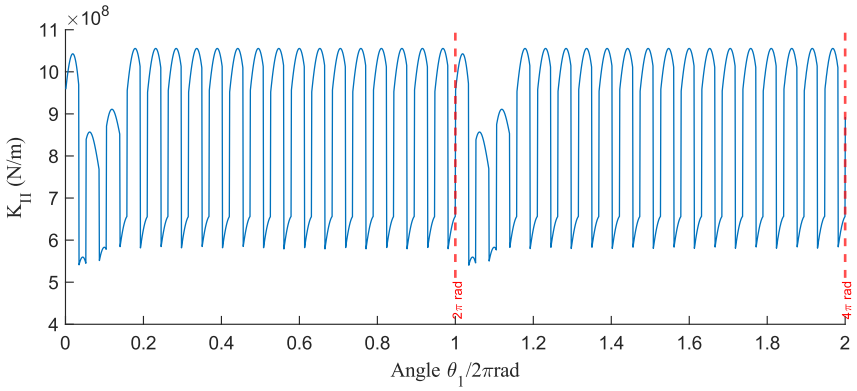

(a) Mesh stiffness for multiple tooth cracks "Scenario 2" (K_{II} in two periods $2 * 2\pi\ rad$)

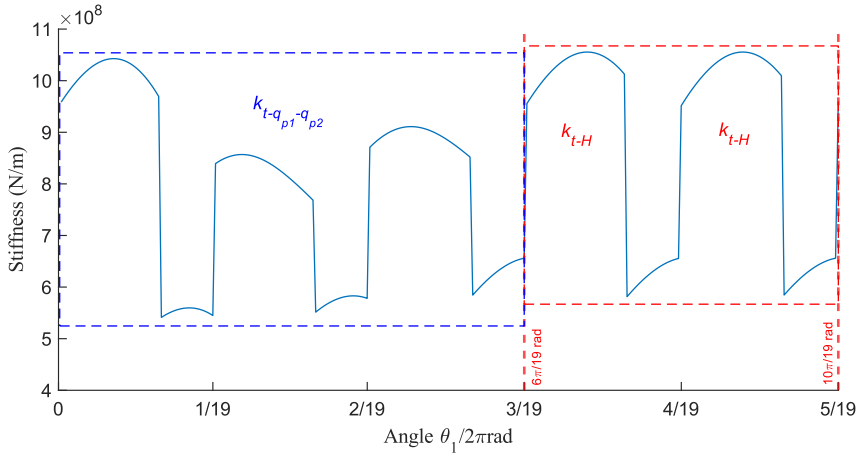

(b) $k_{t\_q_{p1}\_q_{p2}}$ (3 mesh periods $[0, 3\frac{2\pi}{19}]$), and k_{t_H}.

Fig. 5.12: Mesh stiffness for multiple tooth cracks "Scenario 2" (K_{II})

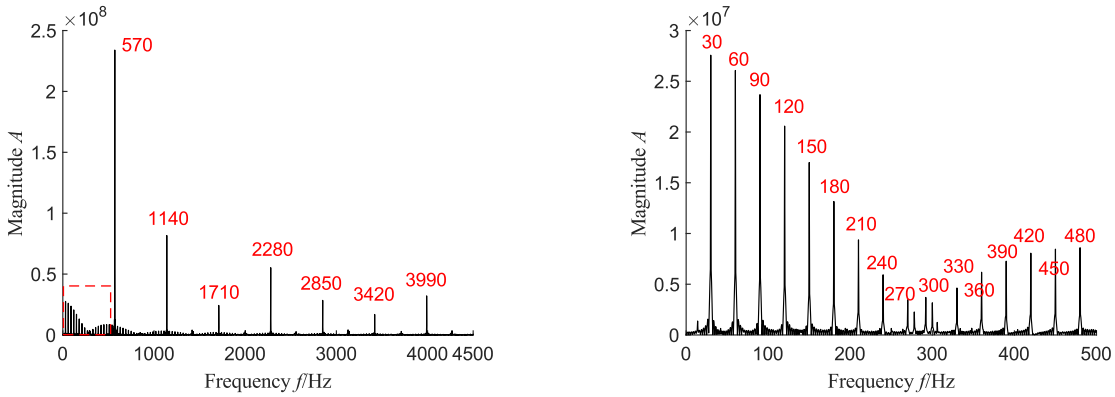

(a) Full-scale view (b) Zoomed-in view in [0, 500] Hz

Fig. 5.13: Frequency spectrum of mesh stiffness K_{II}

The time waveform and frequency spectrum of the gearbox dynamic response for "Scenario 2" are illustrated in Fig. 5.14. As shown in the top plot of Fig. 5.14(a), there are two adjacent impulses (in each red dashed rectangle) in one pinion revolution. The frequency spectrum shown in the bottom plot of Fig. 5.14(a) is dominated by gear meshing harmonics. Besides, there is a frequency cluster in the frequency range [2900, 3900] Hz, details of which are shown in Fig. 5.14(b). It is found that the frequency cluster consists of a group of spikes with a uniform interval of 30 Hz, such as 3390-3360=30 Hz, which is the pinion rotational speed. This indicates that the frequency cluster consists of frequency components of the impulses induced by the two adjacent pinion tooth cracks. Comparing Fig. 5.14(b) to Fig. 5.11(b), it is found that magnitudes of the frequency spikes in [2900, 3900] Hz for "Scenario 2" are different from those for "Scenario 1".

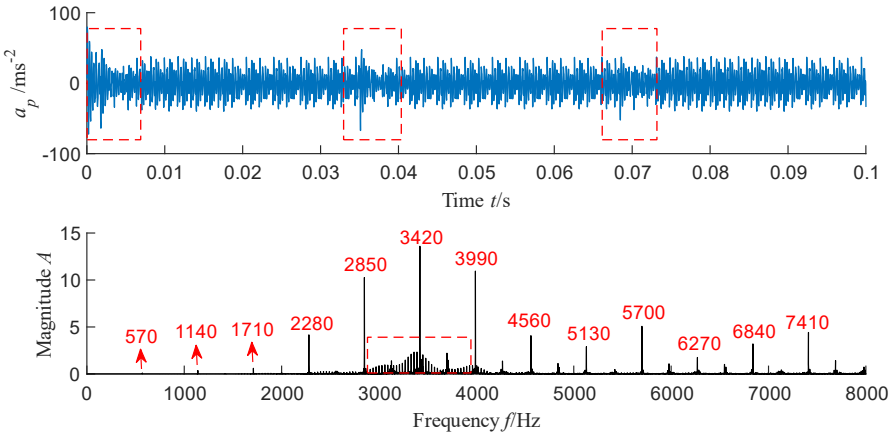

(a) Time waveform and frequency spectrum (full-scale view)

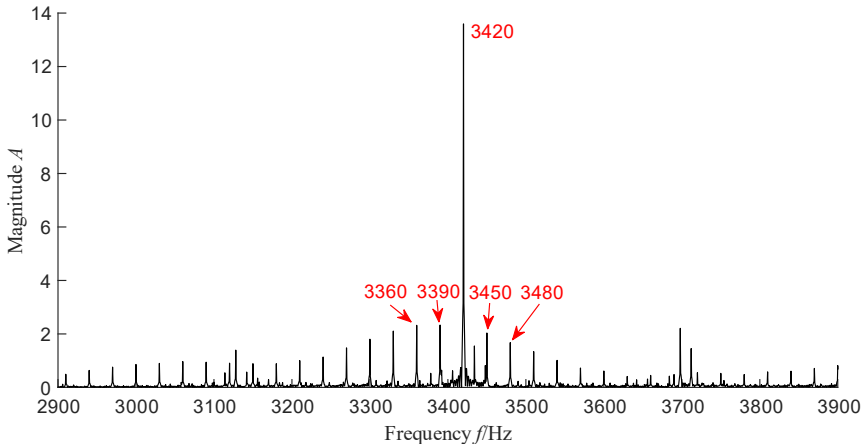

(b) Frequency spectrum (zoomed-in view in [2900, 3900] Hz)

Fig. 5.14: Time waveform and frequency spectrum of gearbox dynamic response (Scenario 2)

5.3.2.3 Scenario 3: one tooth crack on the pinion and one tooth crack on the gear

The angle domain waveforms of the gear tooth mesh stiffness for "Scenario 3" (K_{III}) are illustrated in Fig. 5.15. As shown in Fig. 5.15(a), gear tooth mesh stiffness K_{III} has a period of $48 * 2\pi$ rad since its values in every $48 * 2\pi$ rad are the same. In one period, such as $[0, 48 * 2\pi]$ rad, it is found that K_{III} has eight types of mesh stiffness components, which is consistent with Eq. (5.23). The eight types of components of K_{III} are marked in Fig. 5.15(b), which are the $k_{t\_q_p\_q_g}$, $k_{t\_q_p}$, $k_{t\_q_g}$, k_{t_H}, $k_{t\_V_1}$, $k_{t\_V_2}$, $k_{t\_V_3}$, and $k_{t\_V_4}$. These eight components are shown in Fig. 5.16, from which it is seen that either $k_{t\_q_p\_q_g}$, or $k_{t\_q_p}$, or $k_{t\_q_g}$ lasts for 2 mesh periods $[0, 2\frac{2\pi}{19}]$; either $k_{t\_V_1}$ or $k_{t\_V_4}$ lasts for 3 mesh periods $[0, 3\frac{2\pi}{19}]$; either $k_{t\_V_2}$ or $k_{t\_V_3}$ lasts for 4 mesh periods $[0, 4\frac{2\pi}{19}]$. Besides, in one period of K_{III}, either $k_{t\_q_p\_q_g}$, or $k_{t\_V_1}$, or $k_{t\_V_2}$, or $k_{t\_V_3}$, or $k_{t\_V_4}$ only appears once, $k_{t\_q_p}$ appears 43 times, $k_{t\_q_g}$ appears 14 times. All these observations demonstrate the correct implementation of mesh stiffness evaluation presented in Subsection 5.2.4.3. Besides, by comparing Fig. 5.16(b) and Fig. 5.16(c), it is seen that although the gear tooth crack depth ($q_g = 2.4\ mm$) is smaller than the pinion tooth crack depth ($q_p = 3\ mm$), the gear tooth crack results in a larger decrease of the mesh stiffness during the Single-tooth-pair mesh duration.

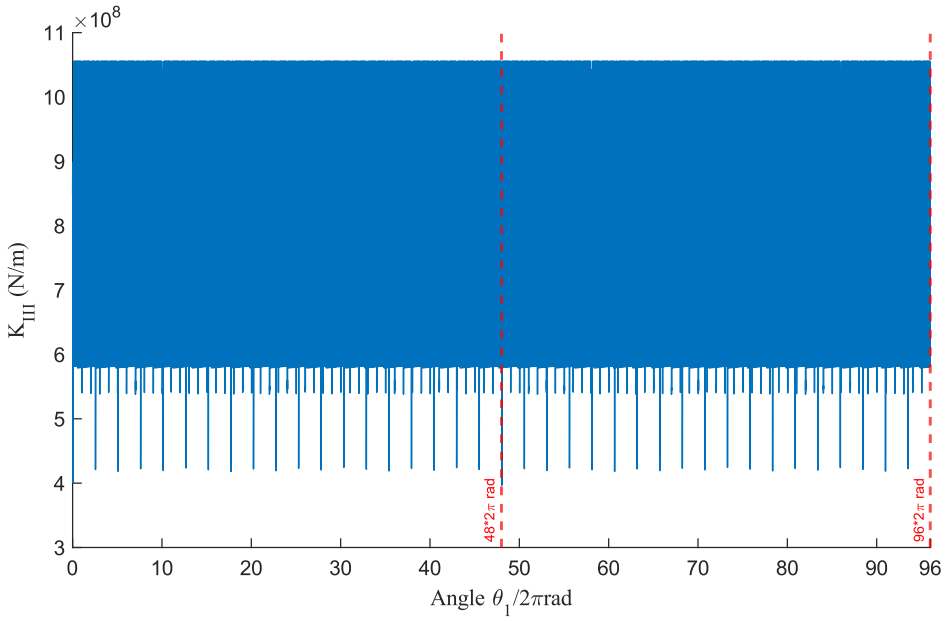

(a) Mesh stiffness for multiple tooth cracks "Scenario 3" (K_{III} in two periods $96 * 2\pi\ rad$)

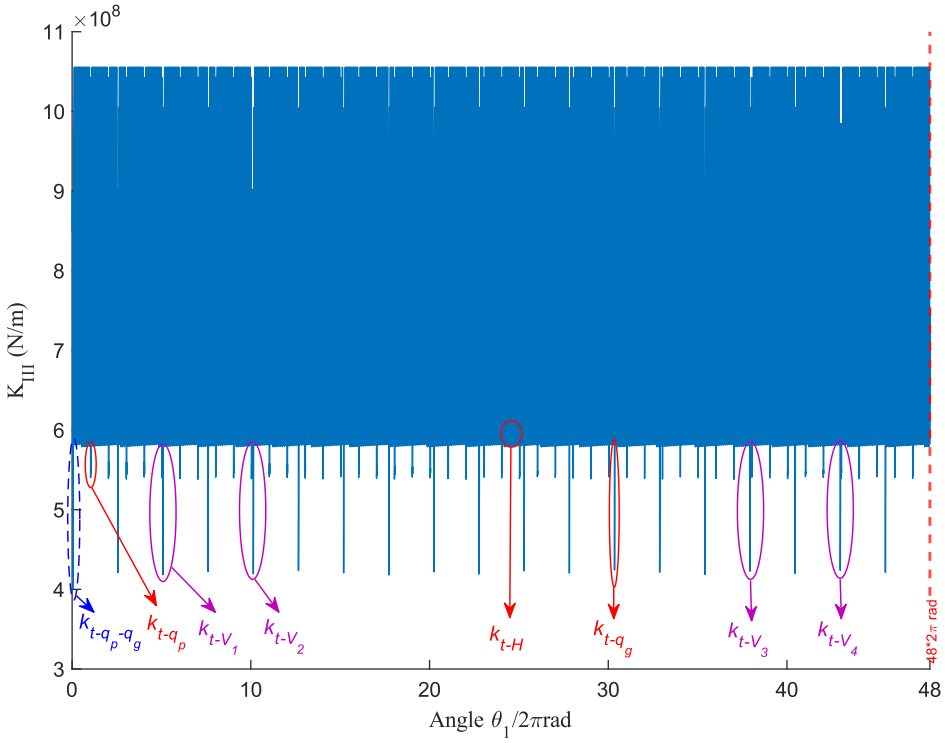

(b) Mesh stiffness for multiple tooth cracks "Scenario 3" (K_{III} in one period $48 * 2\pi\ rad$)

Fig. 5.15: Mesh stiffness for multiple tooth cracks "Scenario 3" (K_{III})

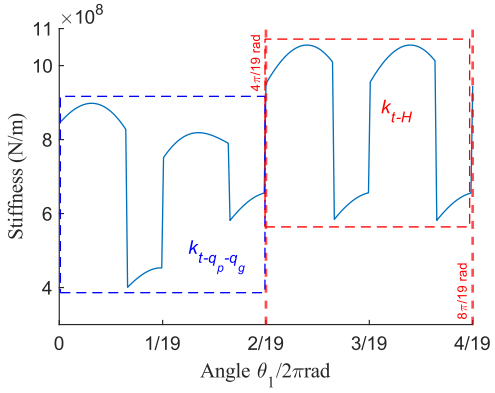

(a) $k_{t\_q_p\_q_g}$ (2 mesh periods [0, $2\frac{2\pi}{19}$]) and k_{t_H}

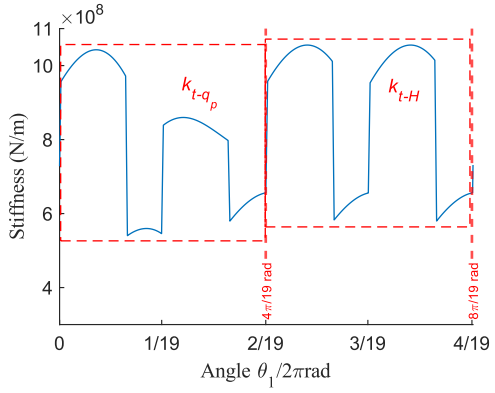

(b) $k_{t\_q_p}$ (2 mesh periods [0, $2\frac{2\pi}{19}$]) and k_{t_H}

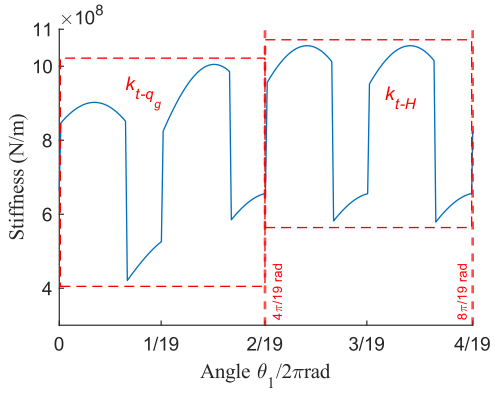

(c) $k_{t\_q_g}$ (2 mesh periods [0, $2\frac{2\pi}{19}$]) and k_{t_H}

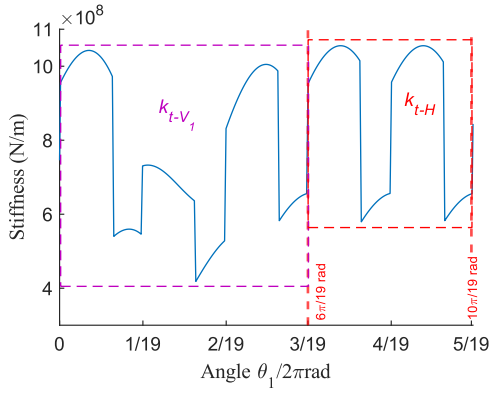

(d) $k_{t\_V_1}$ (3 mesh periods [0, $3\frac{2\pi}{19}$]) and k_{t_H}

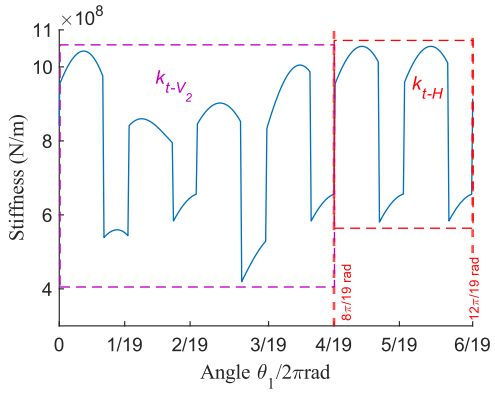

(e) $k_{t\_V_2}$ (4 mesh periods [0, $4\frac{2\pi}{19}$]) and k_{t_H}

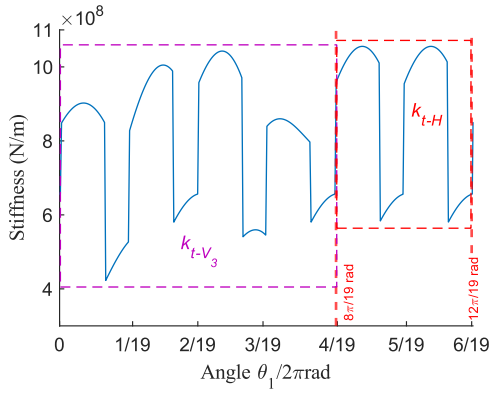

(f) $k_{t\_V_3}$ (4 mesh periods [0, $4\frac{2\pi}{19}$]) and k_{t_H}

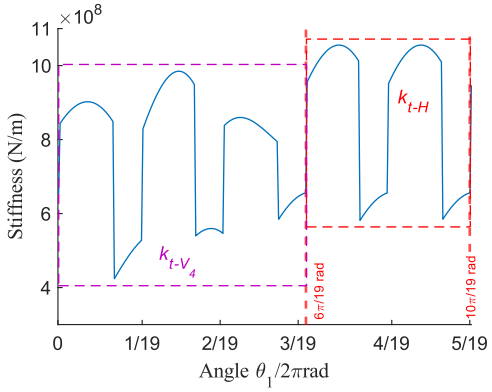

(g) $k_{t\_V_4}$ (3 mesh periods [0, $3\frac{2\pi}{19}$]) and k_{t_H}

Fig. 5.16: Eight components of mesh stiffness K_{III}

Frequency spectrum of K_{III} is illustrated in Fig. 5.17. As shown in Fig. 5.17(a), frequency spectrum of K_{III} is mainly dominated by gear meshing harmonics. There are frequency spikes in the frequency range [0,500] Hz, part of which are shown in Fig. 5.17(b). It is seen that there are two group of spikes: (1) the pinion rotational frequency 30 Hz and its multiples, (2) the gear rotational frequency 11.875 Hz (11.875=30*19/48) and its multiples. This phenomenon is different from those observed from the frequency spectra of K_I and K_{II} shown in Fig. 5.10(b) and Fig. 5.13(b). Therefore, it is concluded that if multiple tooth cracks are only on the pinion, there is only one group of spikes in the frequency spectrum of mesh stiffness and the spike interval is the pinion rotational frequency. However, if there are multiple tooth cracks on both the pinion and the gear, there exists two groups of spikes in the frequency spectrum of mesh stiffness, the interval between every two neighbouring spikes in each group is either the pinion or the gear rotational frequency.

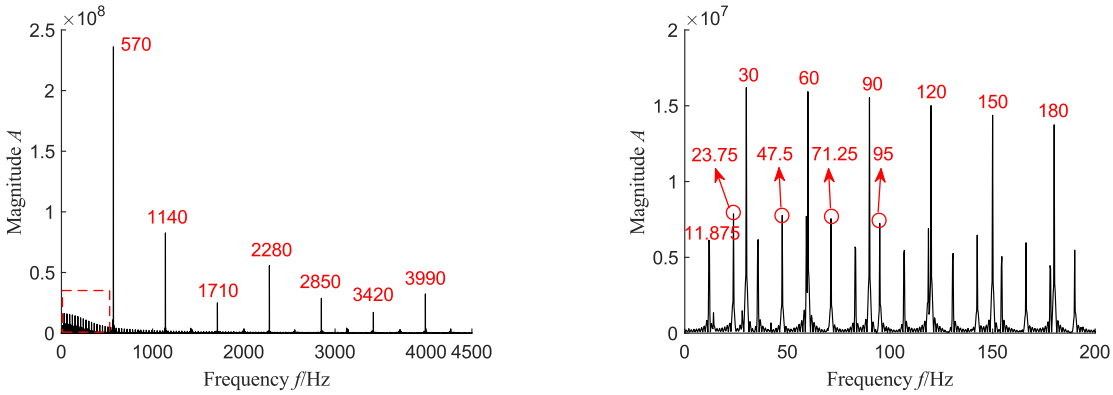

(a) Full-scale view (b) Zoomed-in view in [0, 200] Hz

Fig. 5.17: Frequency spectrum of mesh stiffness K_{III}

Time waveform and frequency spectrum of the gearbox dynamic response for "Scenario 3" are illustrated in Fig. 5.18. As shown in the top plot of Fig. 5.18(a), there are two groups of impulses in the signal, those with higher magnitudes are caused by the gear tooth crack, while others with lower magnitudes are caused by the pinion tooth crack. The frequency spectrum shown in the bottom plot of Fig. 5.18(a) is dominated by gear meshing harmonics. There is a frequency cluster in the frequency range [3000, 3600] Hz, details of which are shown in Fig. 5.18(b). It is found that the frequency cluster consists of two group of spikes, the first group of spikes have a uniform interval of 30 Hz, such as 3390-3360=30 Hz, which is the pinion rotational frequency; the second group of spikes have a uniform interval of 11.875 Hz, such as 3408.125-3396.25=11.875 Hz, which is the gear rotational frequency. Therefore, the frequency cluster consists of frequency components of the impulses induced by both the pinion tooth crack and the gear tooth crack.

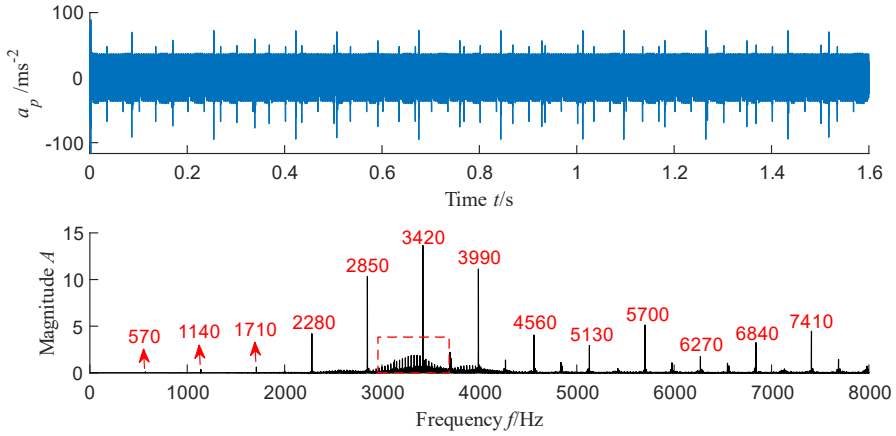

(a) Time waveform and frequency spectrum (full-scale view)

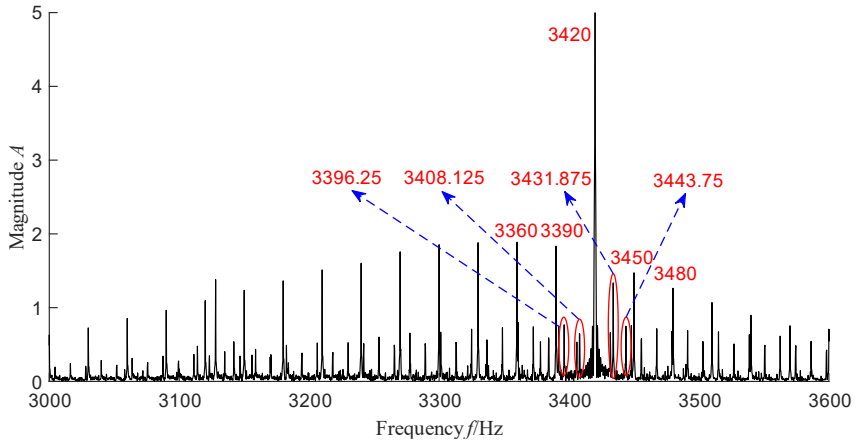

(b) Frequency spectrum (zoomed-in view in [2900, 3900] Hz)

Fig. 5.18: Time waveform and frequency spectrum of gearbox dynamic response (Scenario 3)

5.3.2.4 Summary of the obtained insights into gearbox vibration characteristics

In this subsection, the insights into the vibration characteristics of a spur gearbox with the three considered multiple tooth cracks obtained in Subsection 5.3.2.1 through Subsection 5.3.2.3 are summarized, which are as follows.

For “Scenario 1”, two nonadjacent pinion tooth cracks affect four mesh periods of mesh stiffness K_I in one pinion revolution. Frequency spectrum of mesh stiffness K_I is dominated by gear meshing harmonics and pinion rotational frequency and its multiples. For “Scenario 2”, two adjacent pinion tooth cracks affect three mesh periods of mesh stiffness K_{II} in one pinion revolution. Frequency spectrum of mesh stiffness K_{II} is dominated by gear meshing harmonics and pinion rotational frequency and its multiples. However, magnitudes of the pinion rotational frequency and its multiples for “Scenario 2” vary in a regular pattern, which is different from those for “Scenario 1”, indicating that the effects of two adjacent pinion tooth cracks on the mesh stiffness are different from those of two nonadjacent pinion tooth cracks. For “Scenario 3”, the mesh stiffness K_{III} has eight types of components. Frequency spectrum of mesh stiffness K_{III} is dominated by gear meshing harmonics and two groups of frequency spikes, which are (1) the pinion rotational frequency and its multiples; (2) the gear rotational frequency and its multiples. This phenomenon is different from those observed from the frequency spectra of the mesh stiffness of “Scenario 1” and “Scenario 2”. Besides, for either “Scenario 1” or “Scenario 2”, a cracked pinion tooth with a larger crack depth leads to a bigger decrease of mesh stiffness. However, for “Scenario 3”, although a cracked gear tooth has a relatively smaller crack depth than that of a cracked pinion tooth, it can result in a bigger decrease of mesh stiffness, thus causing impulses with higher magnitudes.

For “Scenario 1”, two nonadjacent pinion tooth cracks induce two nonadjacent impulses in one pinion revolution. For “Scenario 2”, two adjacent pinion tooth cracks induce two adjacent impulses in one pinion revolution. For “Scenario 3”, one pinion tooth crack and one gear tooth crack induce two groups of impulses in the vibration signal. Frequency spectrum of the simulated vibration signal for either “Scenario 1” or “Scenario 2” is dominated by gear meshing harmonics and one single group of frequency spikes, and the frequency spikes are caused by pinion tooth cracks since the interval between every two neighboring spikes is the pinion rotational frequency. However, for “Scenario 3”, except the gear meshing harmonics, there are two group of spikes in the

frequency spectrum of simulated vibration signal. The first group of spikes have a uniform interval of the pinion rotational frequency, which are caused by the pinion tooth crack, while the second group of spikes have a uniform interval of the gear rotational frequency, which are caused by the gear tooth crack.

The insights into the vibration characteristics of a spur gearbox with multiple tooth cracks summarized above fill the knowledge gaps in the field of gearbox tooth crack diagnosis since multiple tooth cracks have rarely been studied in the literature. Besides, the relationships between multiple tooth cracks and their associated impulses in the vibration signals are revealed, which inspires the idea that the focus of the proposed method for detecting the number and locations of multiple tooth cracks is placed on the CII.

5.3.3 Detection of the number and locations of multiple tooth cracks

To verify the effectiveness of the proposed method for detecting the number and locations of multiple tooth cracks in fixed-axis spur gearboxes, a white Gaussian noise with SNR=1 dB is added to simulated gearbox vibration signals to mimic environmental noise. The simulated gearbox vibration signals with white noise added for the three scenarios of multiple tooth cracks are shown in Fig. 5.19, from which it is difficult to obtain any information on the number and locations of multiple tooth cracks.

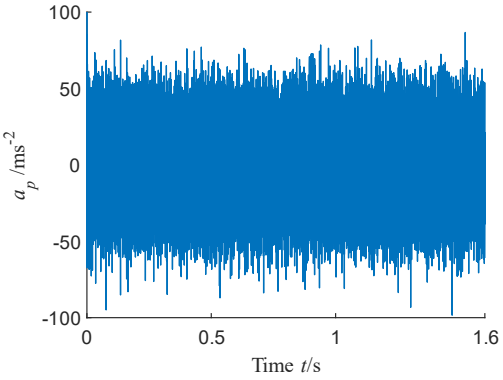

(a) Simulated signal for “Scenario 1”

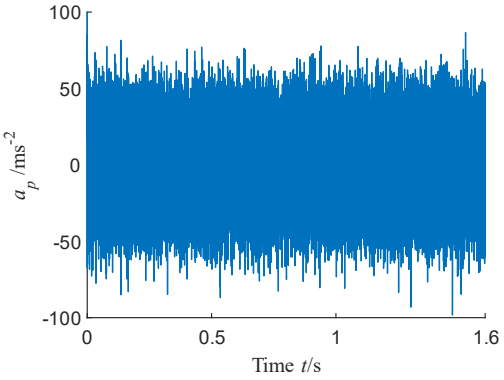

(b) Simulated signal for “Scenario 2”

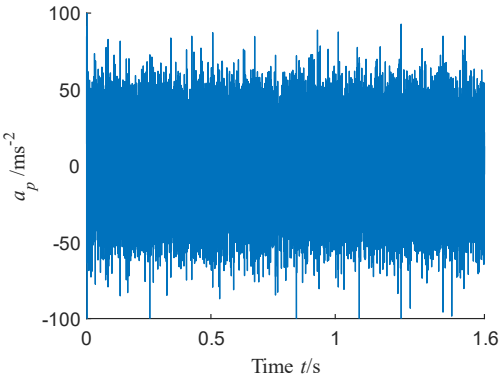

(c) Simulated signal for "Scenario 3"

Fig. 5.19: Simulated vibration signals (with noise) for the three scenarios of multiple tooth cracks

The proposed method described in Subsection 5.2.6 is adopted to analyze the simulated gearbox vibration signals for multiple tooth cracks. Herein, analysis results of the simulated vibration signal for "Scenario 1" (two nonadjacent tooth cracks on the pinion and a healthy gear) are used as an example to illustrate the procedure for the proposed method shown in Fig. 5.8. Firstly, comb notch filtering is conducted on the simulated signal for "Scenario 1" to remove the gear meshing harmonics and the associated first two pairs of sidebands, thus obtaining the residual signal $Res(t)$. Center frequencies of the comb notch filter are set as the gear meshing harmonics, namely 570 Hz and its multiples. The bandwidth of the notch filter is set as 2 sideband pairs. The residual signal and its energy spectral density are shown in Fig. 5.20, from which it is seen that the frequency range in which the CII exist is about [2000, 5000] Hz. Therefore, [2000, 5000] Hz is used as the pass band to band-pass filter the residual signal. The band-pass filtered residual signal $ResBpf(t)$ and its energy spectral density are illustrated in Fig. 5.21.

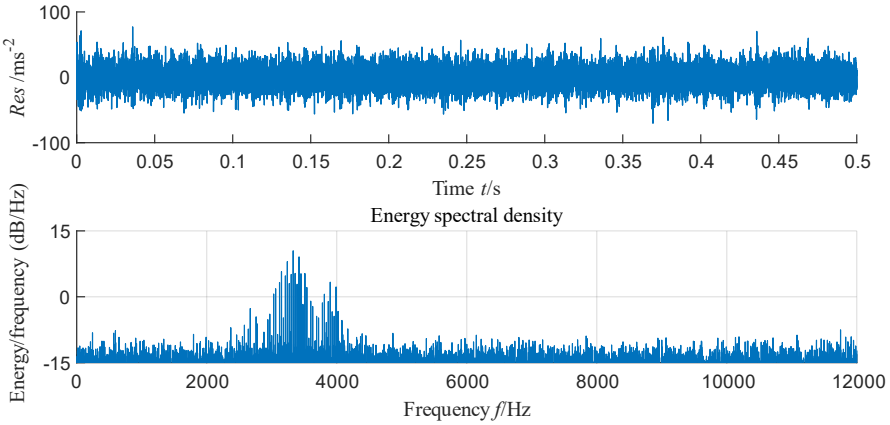

Fig. 5.20: Residual signal and its energy spectral density (Scenario 1)

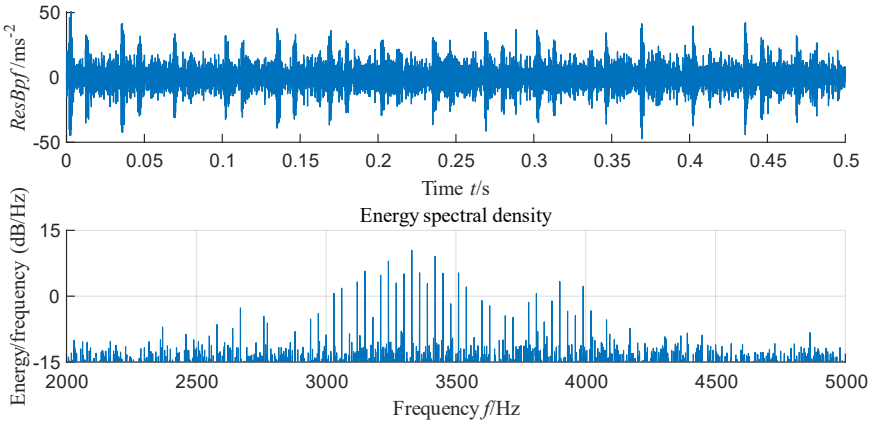

Fig. 5.21: Band-pass filtered residual signal and its energy spectral density (Scenario 1)

Afterwards, SVD is applied to decompose the band-pass filtered residual signal shown in Fig. 5.21. The value of m is empirically set to 60, therefore 60 SCs are obtained, the PMI values of which are calculated using Eq. (5.36). Besides, the threshold p_{TH} is set to 0.06, which is the average of the PMI values of the SCs obtained from healthy gearbox vibration signals. PMI values of the 60 SCs are shown in Fig. 5.22 together with p_{TH} (red dashed horizontal line), from which the PMI values that are greater than p_{TH} are identified, further being used to pick out their corresponding SCs. In this case, 34 SCs are picked out from the 60 obtained SCs. The index set of the selected 34 SCs is P={1, 2, 3, 4, 5, 6, 10, 11, 12, 14, 15, 16, 17, 18, 25, 26, 28, 29, 30, 31, 34, 35, 36, 37, 38, 39, 40, 45, 46, 54, 56, 58, 59, 60}. Based on the obtained index set P, the reconstructed signal, namely the extracted CII, is calculated using Eq. (5.38). The CII is illustrated in Fig. 5.23, from which it is seen that the impulses are more significant than those shown in Fig. 5.21.

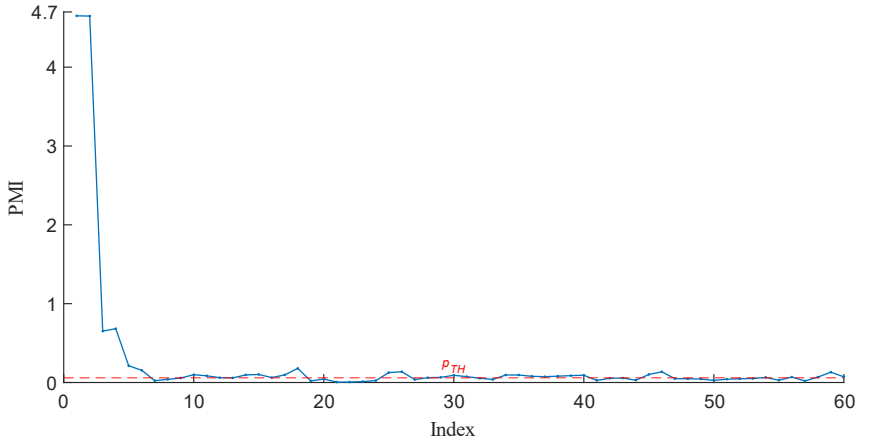

Fig. 5.22: PMI values of the SCs obtained using the SVD (Scenario 1)

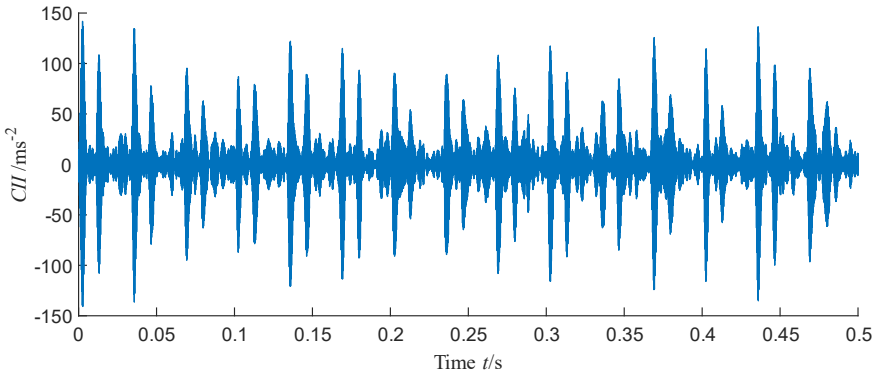

Fig. 5.23: The extracted CII (Scenario 1)

Finally, TSA is conducted on the CII shown in Fig. 5.23 using both the pinion and the gear shaft rotational information. The pinion TSA signal TSA_p and the gear TSA signal TSA_g are obtained, which are shown in Fig. 5.24. Squared envelopes of TSA_p and TSA_g, namely $SEnv_p$ and $SEnv_g$, are calculated using Eq. (5.39) and Eq. (5.40), respectively, which are illustrated in Fig. 5.25. As shown in Fig. 5.25, there are two distinct impulses in $SEnv_p$ and the time interval between them is 0.01045 s, which approximately equals six mesh periods since $round(0.01045/0.00174) = 6$ (when the pinion rotational speed is 30 Hz, time length of one pinion revolution is 0.033 s, so one mesh period lasts for 0.00174 s since $0.033/19 = 0.00174$). This indicates that there are two nonadjacent tooth cracks on the pinion and the difference between the serial numbers of the two cracked teeth is 6, which is consistent with the specifications of "Scenario 1" tabulated in Table 5.1 (I=1, J=7, J-I=6). However, there is no impulse in $SEnv_g$, which indicates that there are no cracked teeth on the gear.

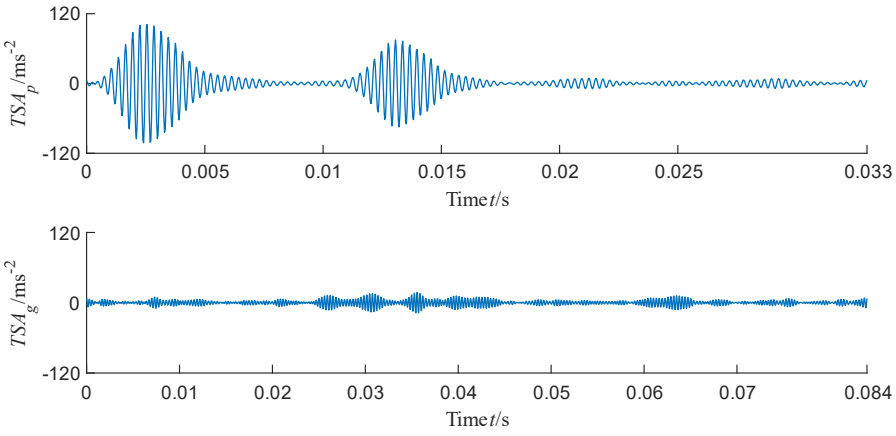

Fig. 5.24: Pinion TSA signal TSA_p and gear TSA signal TSA_g (Scenario 1)

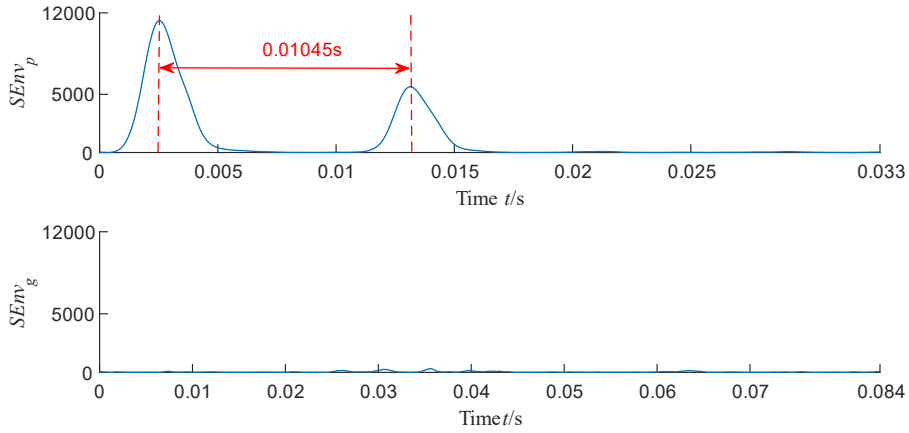

Fig. 5.25: Squared envelopes $SEnv_p$ and $SEnv_g$ for "Scenario 1"

Likewise, by applying the proposed method to the simulated vibration signals for "Scenario 2" and "Scenario 3", the corresponding squared envelopes of the pinion and gear TSA signals can be obtained as well. The $SEnv_p$ and $SEnv_g$ for "Scenario 2" are illustrated in Fig. 5.26, and those for "Scenario 3" are shown in Fig 5.27. For "Scenario 2", as shown in Fig. 5.26, there are two distinct impulses in $SEnv_p$ and the time interval between them is 0.00174 s, which is equal to one mesh period since $round(0.00174/0.00174) = 1$. This indicates that there are two adjacent tooth cracks on the pinion, namely the difference between the serial numbers of the two cracked teeth is 1, which is consistent with the specifications of "Scenario 2" presented in Table 5.2. However, there is no impulse in $SEnv_g$, which indicates that there are no cracked teeth on the gear. For "Scenario 3", as shown in Fig. 5.27, there is only one distinct impulse in $SEnv_p$, which means that there is only one tooth crack on the pinion. Besides, there is only one significant impulse in $SEnv_g$, indicating that the gear has one cracked tooth as well. This is consistent with the specifications of "Scenario 3" shown in Table 5.3. Therefore, all these simulation signal analysis results verify that the proposed method shown in Fig. 5.8 can accurately detect the number and locations of the cracked teeth for the three scenarios of multiple tooth cracks in spur gearboxes.

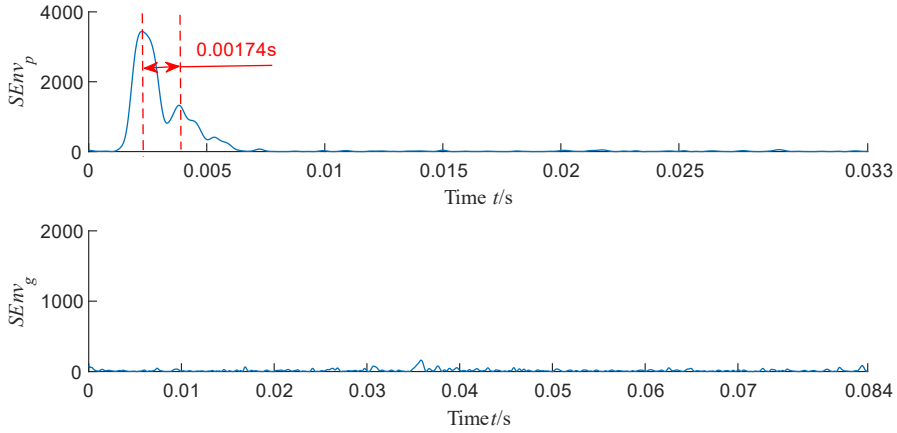

Fig. 5.26: Squared envelopes $SEnv_p$ and $SEnv_g$ for "Scenario 2"

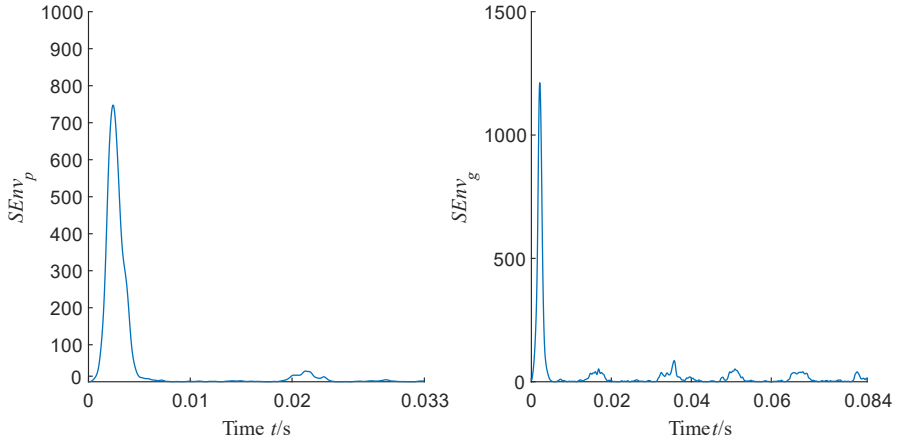

Fig. 5.27: Squared envelopes $SEnv_p$ and $SEnv_g$ for "Scenario 3"

5.4 Experimental validation

In this section, the insights into vibration characteristics of spur gearboxes with multiple tooth cracks obtained from simulation analysis and the effectiveness of the proposed method for detecting the number and locations of multiple tooth cracks are further validated using experimental gearbox vibration datasets. Experimental validations are performed for "Scenario 1" (two nonadjacent tooth cracks on the pinion and a healthy gear) and "Scenario 2" (two adjacent tooth cracks on the pinion and a healthy gear) due to the data availability.

5.4.1 Experiment setup

Details of the test rig and experimental fixed-axis spur gearbox have been described in Subsection 2.5.1 of Chapter 2. Specifications of the target pinion on which the multiple tooth cracks were

seeded have been introduced in Table 2.6. For "Scenario 1", cracks were seeded on the root fillets of two nonadjacent teeth of the target pinion, which is shown in the two red circles in Fig. 5.28(a), and the mating gear is healthy. For "Scenario 2", cracks were seeded on the root fillets of two adjacent teeth of the target pinion, which is illustrated in the two red circles in Fig. 5.28(b), and the mating gear is healthy as well. All tooth cracks were artificially created using an electric discharge machine (EDM). Each cracked tooth was assumed to have the same crack propagation path, which is shown in Fig. 5.29. In Fig. 5.29, w is crack length, L_b is half-length of tooth base chordal thickness, q is crack depth, α_c is crack angle, t is crack thickness. Tooth crack is assumed to extend through the whole tooth face with a uniform crack depth. Depth of each tooth crack is different by specifying different values of q, and t is determined by the diameter of the EDM wire electrode, which was 0.2 mm in the experiments. Specifications of the pinion tooth cracks for "Scenario 1" and "Scenario 2" are tabulated in Table 5.4.

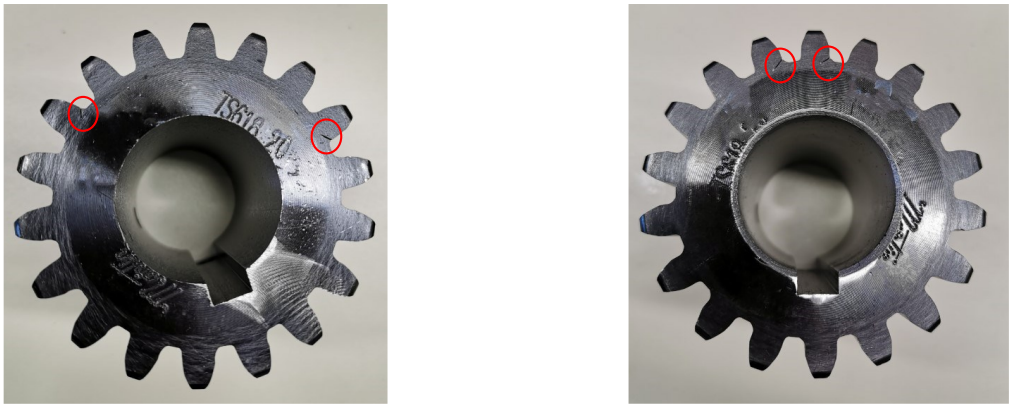

(a) Two nonadjacent tooth cracks (Scenario 1) (b) Two adjacent tooth cracks (Scenario 2)

Fig. 5.28: Target pinion with multiple tooth cracks "Scenario 1" and "Scenario 2"

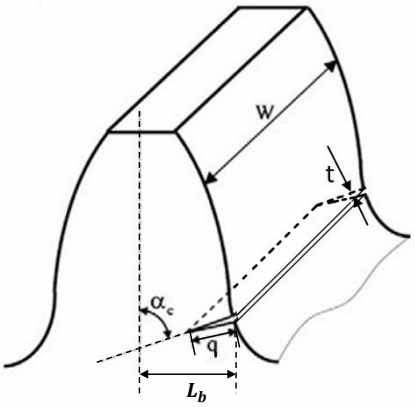

Fig. 5.29: Crack propagation schematic of the target pinion cracked tooth

Table 5.4: Specifications of the two scenarios of multiple tooth cracks on the target pinion

Scenario	Crack lengths of two cracked teeth (w/cm)	Crack angles of two cracked teeth (α_c/Deg)	Crack depths of two cracked teeth (q/mm)	Difference between serial numbers of two cracked teeth
Scenario 1	5.08 and 5.08	60 and 60	4 and 3.2	6
Scenario 2	5.08 and 5.08	60 and 60	4 and 3.2	1

In the experiments, vibration datasets of the target spur gearbox for the two scenarios of multiple tooth cracks were collected when the target pinion rotational frequency was 2.955 Hz and the applied torque on the load motor was 120 Nm. Therefore, GMF of the input mesh pair shown in Fig. 2.12(b) is $GMF_{in} = 53.2$ Hz, and that of the output mesh pair is $GMF_{out} = 189.2$ Hz. The sampling frequency was 25.6 kHz. Time length of each vibration signal was 3 seconds. A tachometer signal was collected using a speed sensor simultaneously with vibration signal collection. Without loss of generality, vibration signals collected using the accelerometer 3, which is shown in Fig. 2.12(c), are analyzed in this chapter.

5.4.2 Analysis of experimental gearbox vibration datasets

In the experiments, gearbox acceleration signals were collected, but gear tooth mesh stiffness was not experimentally acquired. Therefore, only gearbox acceleration signals are analyzed in both time and frequency domains to validate the insights into vibration characteristics of spur gearboxes with multiple tooth cracks obtained from simulation analysis. Time waveform and frequency spectrum of the acceleration signal for "Scenario 1" are illustrated in Fig. 5.30, and those for "Scenario 2" are shown in Fig. 5.31.

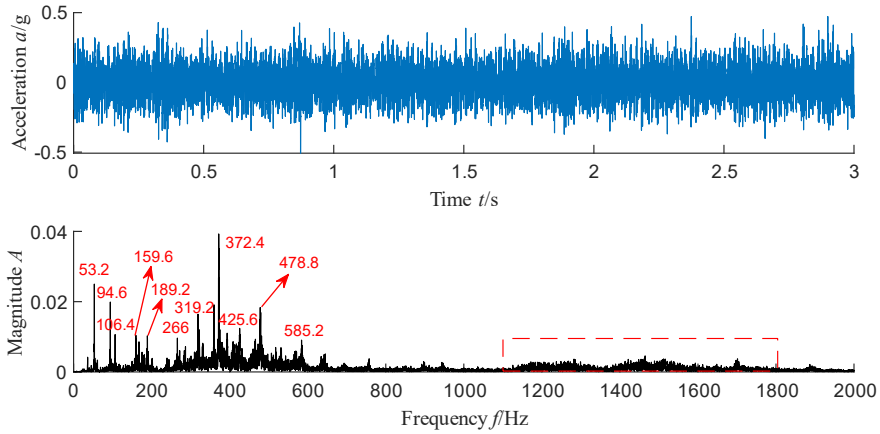

(a) Time waveform and frequency spectrum (full range)

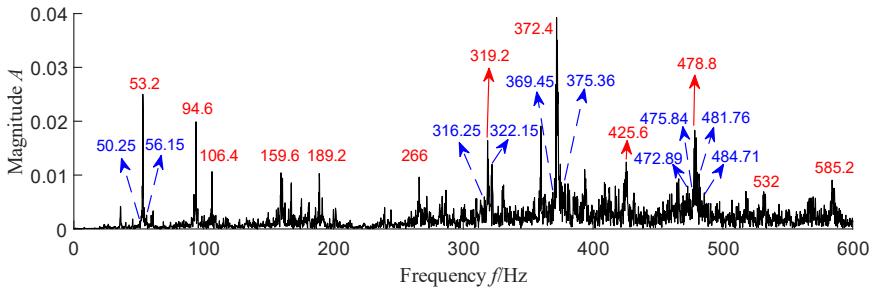

(b) Frequency spectrum in [0, 600] Hz

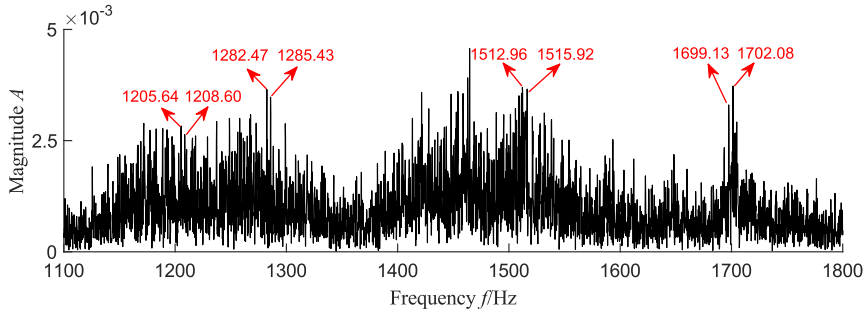

(c) Frequency spectrum in [1100, 1800] Hz

Fig. 5.30: Experimental gearbox vibration signal for “Scenario 1”

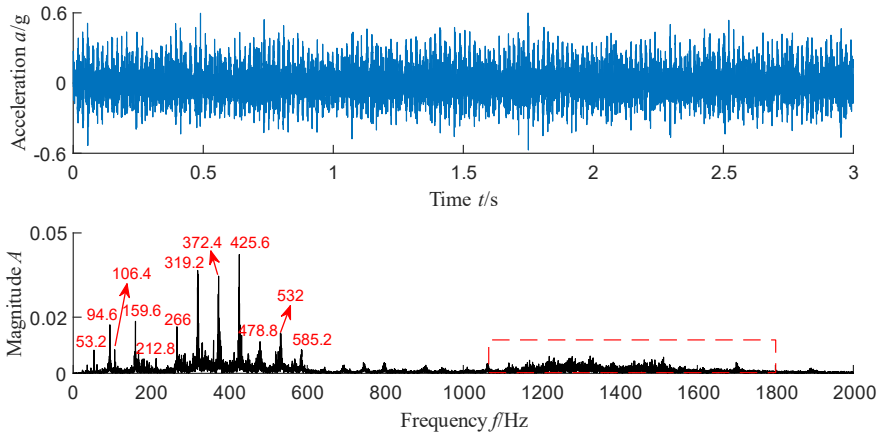

(a) Time waveform and frequency spectrum (full range)

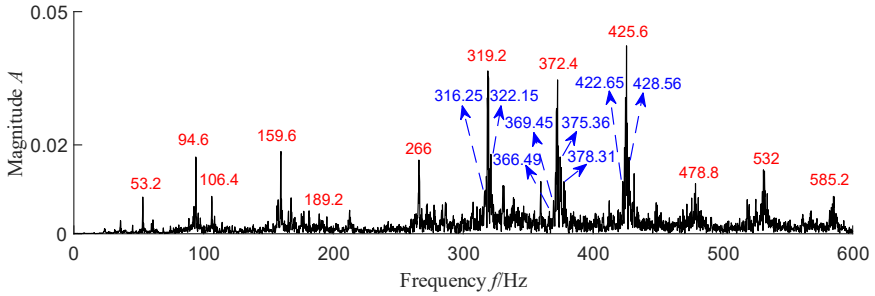

(b) Frequency spectrum in [0, 600] Hz

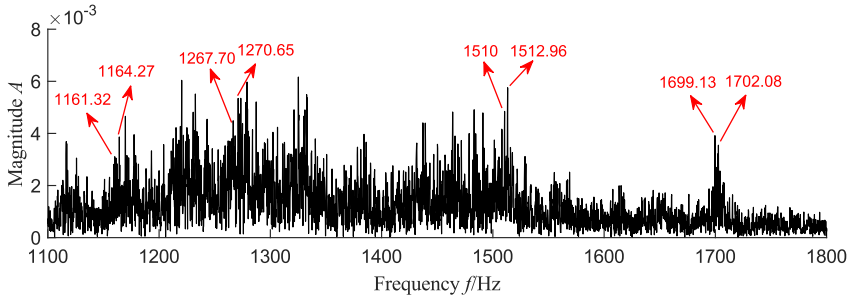

(c) Frequency spectrum in [1100, 1800] Hz

Fig. 5.31: Experimental gearbox vibration signal for "Scenario 2"

As shown in Fig. 5.30(a), there are many impulses in the time waveform, but it is difficult to get any information on the number and locations of tooth cracks due to strong background noise. Frequency spectrum of vibration signal is mainly dominated by gear meshing harmonics of the input mesh pair of the target spur gearbox, namely GMF_{in} (53.2 Hz) and its multiples. Although there are also gear meshing harmonics of the output mesh pair in the spectrum, namely GMF_{out} (189.2 Hz) and its multiples, their magnitudes are relatively smaller. Gear meshing harmonics of the two mesh pairs are mainly located in the frequency range [0, 600] Hz, details of which are shown in Fig. 5.30(b). There are either one or two pairs of sidebands around the gear meshing harmonics, which are caused by gear manufacturing errors and are not related to pinion tooth cracks. For brevity, only the significant sidebands around the dominant gear meshing harmonics are labelled and marked in blue. Besides, there are a group of frequency spikes in the range [1100, 1800] Hz (in the red dashed rectangle), details of which are shown in Fig. 5.30(c). It is seen that the frequency interval between every two neighbouring frequency spikes is about 2.955 Hz, such as 1702.08-1699.13=2.95 Hz and 1285.43-1282.47=2.96 Hz, which is the target pinion rotational frequency, indicating that the spikes in [1100, 1800] Hz are caused by the two nonadjacent tooth cracks on the target pinion. These observations are consistent with those obtained from the simulated signal analysis for "Scenario 1" shown in Subsection 5.3.2.1, which means that obtained insights for "Scenario 1" are correct, validating the correctness of the mesh stiffness formulae for "Scenario 1" derived in Subsection 5.2.4.1.

As shown in Fig. 5.31(a), frequency spectrum of acceleration signal for "Scenario 2" is mainly dominated by the gear meshing harmonics of the input mesh pair (53.2 Hz and its multiples), which are in the frequency range [0, 600] Hz. From Fig. 5.31(b), it is found that there are either one or

two pairs of sidebands around the gear meshing harmonics, which are caused by gear manufacturing errors as well and are not related to pinion tooth cracks. Likewise, only the significant sidebands around the dominant gear meshing harmonics are labelled and marked in blue. Besides, there is also a group of frequency spikes in the frequency range [1100, 1800] Hz, details of which are illustrated in Fig. 5.31(c). It is found that the frequency interval between every two neighbouring frequency spikes is about 2.955 Hz, such as 1702.08-1699.13=2.95 Hz and 1512.96-1510=2.96 Hz, which is the target pinion rotational frequency. This indicates that these frequency spikes are caused by the two adjacent tooth cracks on the target pinion. However, magnitudes of the frequency spikes in [1100, 1800] Hz for "Scenario 2" are different from those for "Scenario 1", which means that the effects on gearbox vibration signals caused by "Scenario 1" and "Scenario 2" are different. All these observations are consistent with those obtained from simulation signal analyses presented in Subsection 5.3.2.2, which demonstrates the correctness of the obtained insights into gearbox vibration characteristics, further indicating that the mesh stiffness formulae for "Scenario 2" derived in Subsection 5.2.4.2 are correct.

5.4.3 Detection of the number and locations of multiple tooth cracks in a spur gearbox

To further validate the effectiveness of the proposed method for detecting the number and locations of multiple tooth cracks, the proposed method is adopted to process experimental gearbox vibration signals for the two scenarios of multiple tooth cracks described in Table 5.4. Analysis results of experimental vibration signal for "Scenario 1" are used as examples to illustrate the procedure for the proposed method. Because there are two meshing pairs in the target spur gearbox, the corresponding gear meshing harmonics, namely GMF_{in} (53.2 Hz) and its multiples, and GMF_{out} (189.2 Hz) and its multiples, and the first two pairs of sidebands around them are removed using comb notch filtering. The obtained residual signal $Res(t)$ is shown in Fig. 5.32 together with its energy spectral density, from which it is seen that the frequency range in which the CII exist is about [1100, 1800] Hz, which is consistent with the observations obtained from Fig. 5.30(c). Therefore, [1100, 1800] Hz is used as the pass band to band-pass filter the residual signal, and the obtained band-pass filtered residual signal $ResBpf(t)$ and its energy spectral density are illustrated in Fig. 5.33.

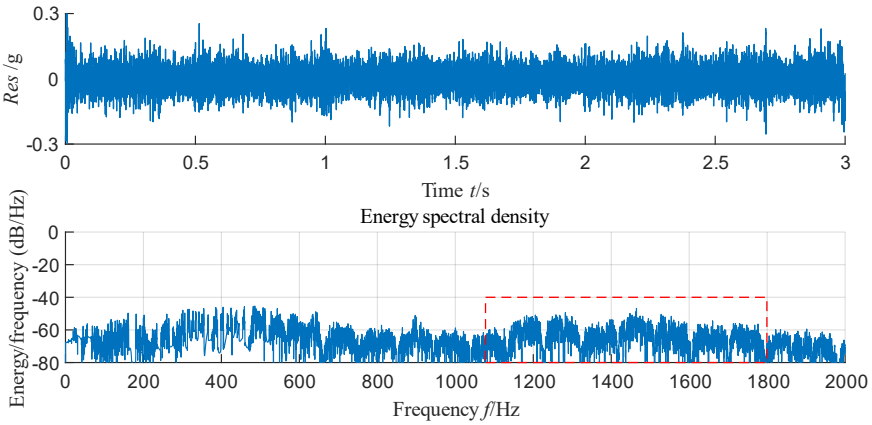

Fig. 5.32: Residual signal and its energy spectral density for “Scenario 1”

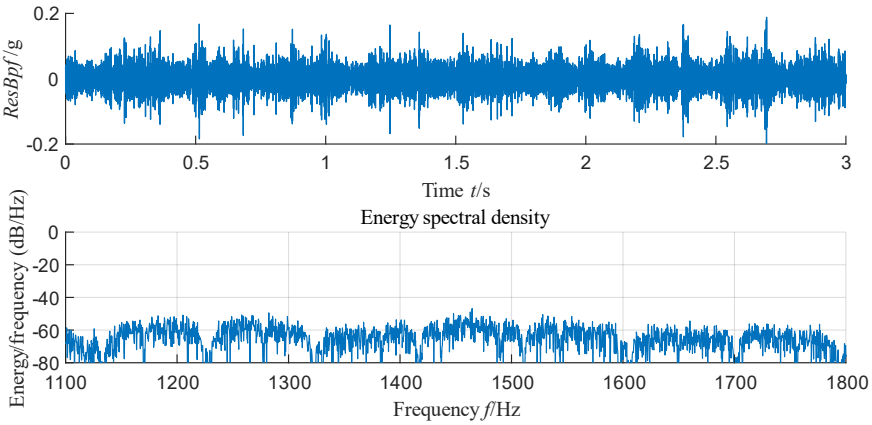

Fig. 5.33: Band-pass filtered residual signal and its energy spectral density for “Scenario 1”

Afterwards, SVD is applied to decompose the band-pass filtered residual signal shown in Fig. 5.33. The value of m is set to 60, therefore 60 SCs are obtained, the PMI values of which are calculated using Eq. (5.36). The threshold p_{TH} is set to 0.1261, which is the average of the PMI values of the SCs obtained from healthy gearbox vibration signals. PMI values of the 60 SCs are shown in Fig. 5.34 together with p_{TH}, from which the PMI values that are greater than p_{TH} are identified, further being used to pick out their corresponding SCs. In this case, 18 SCs are picked out from the 60 obtained SCs. The index set of the 18 selected SCs is P={1, 2, 3, 4, 5, 6, 7, 8, 10, 16, 17, 18, 19, 20, 21, 22, 23, 24}. Based on the obtained index set P, the CII is calculated using Eq. (5.38). The obtained CII is illustrated in Fig. 5.35, from which it is seen that the impulses are more significant than those shown in Fig. 5.33.

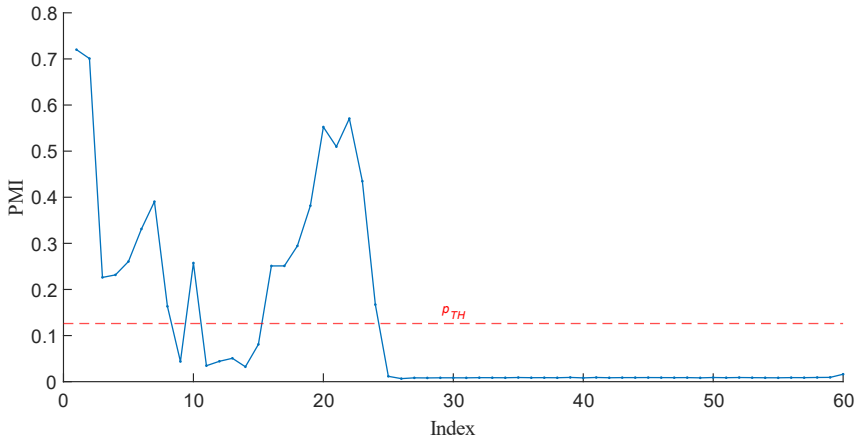

Fig. 5.34: PMI values of the SCs obtained using the SVD (experimental signal, Scenario 1)

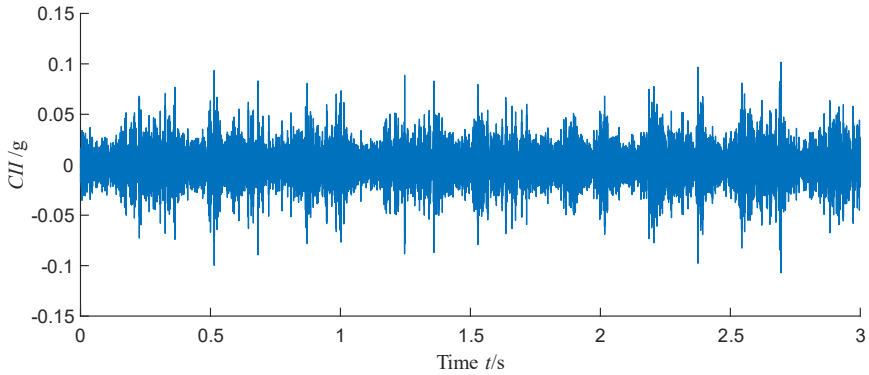

Fig. 5.35: The extracted CII (experimental signal, Scenario 1)

Finally, TSA is conducted on the CII shown in Fig. 5.35 using both the pinion and the gear shaft rotational information. The pinion TSA signal TSA_p and the gear TSA signal TSA_g are obtained and are shown in Fig. 5.36. Squared envelopes of TSA_p and TSA_g, namely $SEnv_p$ and $SEnv_g$, are calculated using Eq. (5.39) and Eq. (5.40), respectively, which are illustrated in Fig. 5.37. As shown in Fig. 5.37, there are two distinct impulses in $SEnv_p$ and the time interval between them is 0.11282 s, which is about six mesh periods since $round(0.11282/0.0188) = 6$ (when the target pinion speed is 2.955 Hz, time length of one pinion revolution is 0.338 s, so one mesh period lasts for 0.0188 s since $0.338/18 = 0.0188$). This indicates that there are two nonadjacent tooth cracks on the target pinion and the difference between the serial numbers of the two cracked pinion teeth is 6, which is consistent with the specifications of "Scenario 1" shown in Table 5.4. There is no distinct impulse in $SEnv_g$, indicating that there are no cracked teeth on the mating gear of the target pinion, which is true since all teeth of the mating gear were healthy in the experiments.

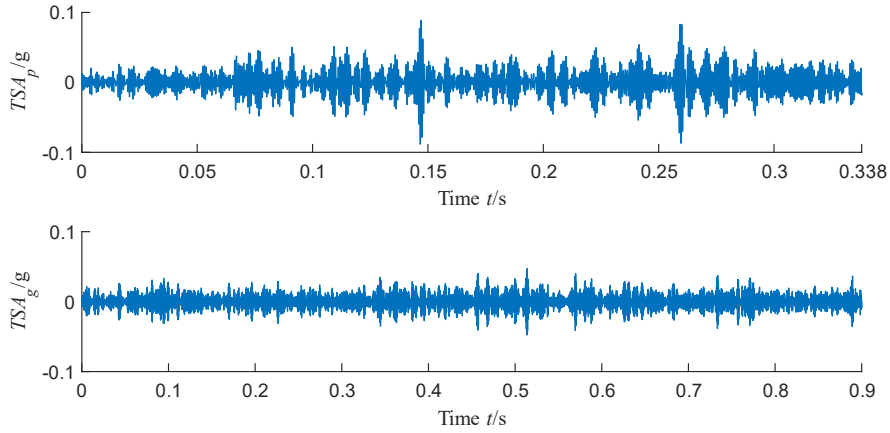

Fig. 5.36: Pinion TSA signal TSA_p and gear TSA signal TSA_g (experimental signal, Scenario 1)

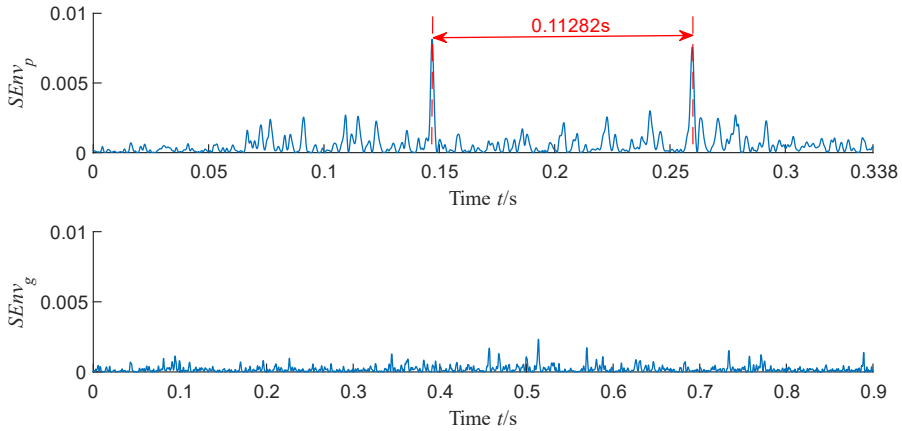

Fig. 5.37: Squared envelopes $SEnv_p$ and $SEnv_g$ (experimental signal, Scenario 1)

Likewise, by applying the proposed method to the experimental vibration signal for "Scenario 2", the corresponding squared envelopes of the pinion and gear TSA signals are obtained as well, which are illustrated in Fig. 5.38. It is seen that there are two distinct impulses in $SEnv_p$ and the interval between them is 0.0199 s, which is approximately equal to one mesh period since $round(0.0199/0.0188) = 1$. This indicates that there are two adjacent tooth cracks on the target pinion, namely the difference between the serial numbers of the two cracked pinion teeth is 1, which is consistent with the specifications of "Scenario 2" in Table 5.4. There is also no distinct impulse in $SEnv_g$, indicating that there are no cracked teeth on the mating gear, which is true since no cracks were seeded on the gear in the experiments.

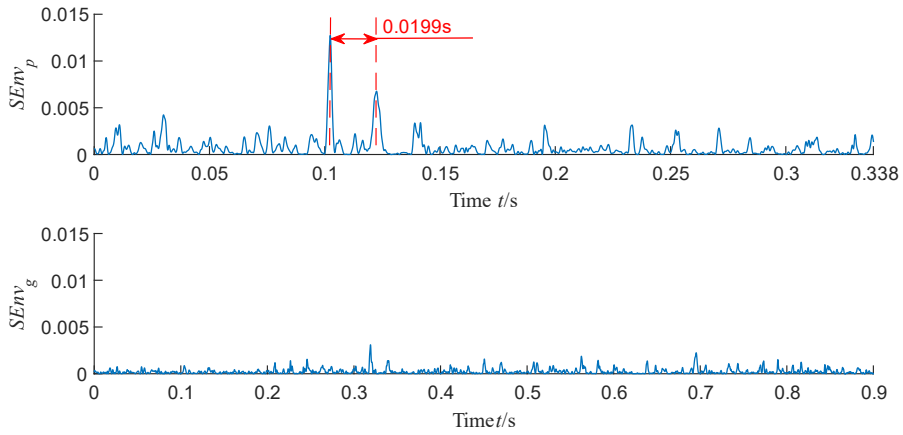

Fig. 5.38: Squared envelopes $SEnv_p$ and $SEnv_g$ (experimental signal, Scenario 2)

Therefore, based on the analysis results of experimental gearbox vibration signals for both "Scenario 1" and "Scenario 2" presented above, the number and locations of the two scenarios of multiple cracked teeth on the target pinion can be accurately detected using the proposed method, which validates the effectiveness of the proposed method for detecting the number and locations of multiple tooth cracks in spur gearboxes.

5.5 Conclusions

This chapter brings some insights into the vibration characteristics of spur gearboxes with multiple tooth cracks and proposes a novel method for detecting the number and locations of multiple tooth cracks. In this chapter, three scenarios of multiple tooth cracks in spur gearboxes are studied. Firstly, gear tooth mesh stiffness formulae for each scenario of multiple tooth cracks are analytically derived, and how multiple tooth cracks affect gear tooth mesh stiffness is studied in both angle and frequency domains. Afterwards, gear tooth mesh stiffness is exerted into the spur gearbox dynamic model to generate simulated vibration signals, which are further analyzed in both time and frequency domains to reveal the effects of multiple tooth cracks on gearbox vibration signals. The insights into gearbox vibration characteristics obtained from simulation analysis is validated using experimental vibration datasets of a spur gearbox with multiple tooth cracks on the pinion. The obtained insights into vibration characteristics of spur gearboxes with multiple tooth cracks fill the knowledge gaps in the field of gearbox tooth crack diagnosis.

In addition, a novel method focusing on the CII is proposed to detect the number and locations of multiple tooth cracks in spur gearboxes. The CII are first extracted from gearbox vibration signals using a new SVD-based strategy. TSA is conducted on the CII to get the TSA signals for both the pinion and the gear, the squared envelopes of which are calculated. By identifying the distinct impulses in the squared envelopes of the pinion and gear TSA signals and calculating the time interval between the identified impulses, the number and locations of multiple tooth cracks can be accurately detected. The effectiveness of the proposed method is demonstrated using both simulated gearbox vibration signals and experimental gearbox vibration datasets.

In this chapter, the two scenarios of multiple tooth cracks on the pinion in spur gearboxes are studied for experimental validation, and only constant working conditions are considered. In the future, the scenario of multiple tooth cracks on both the pinion and the gear will be studied experimentally and the time-varying working conditions will be involved.

Chapter 6: Summary and future work

In this chapter, the novel contributions of the research work conducted in this thesis are summarized in Section 6.1. In addition, several research problems that are worth to be explored in the future are presented in Section 6.2.

6.1 Summary

Vibration analysis has been widely utilized for fault detection and severity assessment of fixed-axis spur gearboxes since vibration signals are easy to acquire and contain abundant information on gearbox health conditions. To develop effective vibration analysis methods for fixed-axis gearbox fault diagnosis, a good understanding of the vibration characteristics of a fixed-axis gearbox in both healthy and faulty conditions is of necessity. The overarching objective of this thesis is to procure some insights into vibration properties of a fixed-axis spur gearbox with tooth cracks under either constant and time-varying operating conditions through dynamic simulation, and the obtained insights are further employed to guide the development of effective vibration signal analysis methods for gear tooth crack detection and severity assessment. The contributions of this thesis are summarized in four aspects, which are presented in the following four subsections.

6.1.1 Development of new condition indicators for early tooth crack severity assessment

Diagnosis of gear tooth cracks at an early stage is important to prevent catastrophic failures of gearboxes, which helps improve gearbox reliability and decrease gearbox system operation and maintenance costs. Many studies have been reported to assess tooth crack severity, but they failed to work well when a tooth crack was in the early stage. To overcome this problem, this thesis proposes a new method to extract the CII from gearbox vibration signals, conduct a thorough analysis on the CII, and develop two new CIs based on the CII for early tooth crack severity assessment. The idea that the proposed method focuses on the CII is inspired by the observation that the CII can well reflect tooth crack severity progression, which is obtained via gearbox dynamic simulation. Details of the proposed method have been presented in Chapter 2. To be specific, the TSA technique is first applied to gearbox vibration signals to get the gear TSA signal.

Afterwards, gear meshing harmonics and their associated sidebands are removed from the gear TSA signal using comb notch filters. The matrix pencil method is further utilized to identify SDOF IRs (dominant resonances) from the comb notch filtered signal, and the identified SDOF IRs are used to reconstruct the CII. Lastly, the energy of the reconstructed CII and the sum of the energy of the SDOF IRs with their carrier frequencies in a specific frequency band are proposed as two new CIs for early tooth crack severity assessment. The effectiveness of the proposed method and the two new CIs for early tooth crack severity assessment have been demonstrated using both simulated gearbox vibration signals and experimental gearbox vibration datasets.

6.1.2 Investigation of the effects of time-varying operating conditions on gearbox vibration signals

It has been reported that time-varying operating conditions induce AM and FM into gearbox vibration signals. However, the relationship between time-varying operating conditions and gearbox vibration signals are not known yet. In Chapter 3 of this thesis, a comprehensive study is conducted to investigate how time-varying operating conditions affect vibration characteristics of a fixed-axis spur gearbox with a tooth crack. The involved time-varying operating conditions include two scenarios, namely the variable load and constant speed condition, and the constant load and variable speed condition. Firstly, gear tooth mesh stiffness of a gear pair involving tooth crack severity progression is evaluated under time-varying operating conditions, through which gearbox vibration responses are generated. Gear tooth mesh stiffness and gearbox vibration signals are analyzed to reveal the effects caused by time-varying operating conditions. Besides, the relationship between the CII and the variable load or variable speed is studied as well, and a linear dependence of the AM of the CII on the variable load or variable speed is identified. The identified linear dependence is further used to develop a novel condition indicator for tracking tooth crack severity progression under time-varying operating conditions. The linear dependence of the AM of the CII on time-varying operating conditions and the effectiveness of the proposed condition indicator for tracking tooth crack severity progression have been demonstrated using both simulated gearbox vibration signals and experimental gearbox vibration datasets.

6.1.3 Removal of the speed variation-induced AM and FM for tracking tooth crack severity progression

As revealed in Chapter 3 of this thesis that variable speeds induce both AM and FM into gearbox vibration signals, which can mask the existence of a tooth crack and make it difficult to distinguish between changes of tooth crack severity and speed variations. To tackle this problem, in Chapter 4 of this thesis, a novel normalization method has been proposed to remove the speed variation-induced AM and FM for effectively tracking tooth crack severity progression under variable speed conditions. The focus of the proposed normalization method is placed on the CII since the CII contain abundant information on tooth crack growth, which has been demonstrated in Chapter 2 and Chapter 3 of this thesis. For the proposed normalization method, firstly, the raw gearbox vibration signal is processed using the computed order tracking technique to remove the speed variation-induced FM. Afterwards, the CII and the speed variation-induced AM of the CII are obtained using the modified AHD method and the envelope analysis method, respectively. Based on the speed variation-induced AM of the CII, the CII is normalized, thus removing the interfering AM caused by variable speed conditions. The normalized CII not only eliminate the effect of speed variation-induced AM and FM but also preserve information on tooth crack growth. Condition indicators such as RMS and EHNR calculated using the normalized CII work well in tracking tooth crack severity progression under variable speed conditions. The effectiveness of the proposed normalization method for removing the speed variation-induced AM and FM in terms of tracking tooth crack severity progression under variable speed conditions has been demonstrated using both simulated gearbox vibration signals and experimental gearbox vibration datasets.

6.1.4 Study of vibration characteristics and detection of multiple toot cracks

In industrial applications, gearboxes may suffer from multiple tooth cracks due to their harsh working environment. However, analysis of vibration properties of gearboxes with multiple tooth cracks and detection of multiple tooth cracks have rarely been conducted in the literature. To overcome this problem, in Chapter 5 of this thesis, vibration characteristics of a fixed-axis spur gearbox with multiple tooth cracks have been studied via dynamic simulation, and the obtained insights into gearbox vibration characteristics have been adopted to guide the development of a new method for detecting the number and locations of multiple tooth cracks. To be specific, three scenarios of multiple tooth cracks are considered, including two nonadjacent tooth cracks on the

pinion and a healthy gear, two adjacent tooth cracks on the pinion and a healthy gear, and one tooth crack on the pinion and one tooth crack on the gear. Gear tooth mesh stiffness for the three scenarios of multiple tooth cracks have been evaluated analytically using the potential energy method and have been inserted into gearbox dynamic model to generate dynamic responses. Analyses of gear tooth mesh stiffness and gearbox dynamic responses have been conducted, which reveal that the CII contain useful information on multiple tooth cracks. Inspired by this finding, a new method with its focus on the CII has been proposed to detect the number and locations of multiple tooth cracks in fixed-axis spur gearboxes. Firstly, an SVD-based method is developed to extract the CII from gearbox vibration signals. TSA is further conducted on the CII using both pinion and gear rotational information to get the pinion and gear TSA signals, squared envelopes of which are calculated. Lastly, by identifying the distinct impulses in the squared envelopes of the pinion and gear TSA signals and calculating the time interval between the identified impulses, the number and locations of multiple tooth cracks can be detected. The insights into gearbox vibration properties and the effectiveness of the proposed method have been demonstrated using both simulated gearbox vibration signals and experimental gearbox vibration datasets.

6.2 Future work

Although the studies conducted in this thesis have overcome the limitations and drawbacks of the relevant reported research work on dynamic simulation and vibration-based tooth crack detection and severity assessment of fixed-axis spur gearboxes, there still exists some challenges and problems that need further considerations and explorations, which are described in the following subsections.

6.2.1 Assessment of early tooth crack severity under time-varying operating conditions

In this thesis, two new CIs have been developed for early tooth crack severity assessment under constant load and constant speed conditions. However, in real industrial applications, gearboxes oftentimes work under time-varying operating conditions. The CIs proposed in Chapter 2 of this thesis will become incompetent to assess early tooth crack severity under time-varying operating conditions since changes in CIs may indicate the changes of gearbox vibration signals caused by either the deterioration of gear health conditions, or the operating condition variations, or both.

Therefore, early tooth crack severity assessment under time-varying operating conditions deserves a further study.

6.2.2 Investigation of the effects of variable load and variable speed conditions on gearbox vibration characteristics

In this thesis, only two scenarios of time-varying operating conditions have been considered when studying their effects on gearbox vibration properties, namely the variable load and constant speed condition, and the constant load and variable speed condition. However, industrial gearboxes may also experience variable load and variable speed conditions when their driving motors are controlled by open-loop control strategies. In this situation, the load and speed are correlated since they need to follow the driving motor torque-speed characteristic curve [20,66], which is totally different from the two scenarios considered in Chapter 3 of this thesis. The effects of the variable load and variable speed conditions on gearbox vibration characteristics and tooth crack diagnosis under variable load and variable speed conditions need to be further investigated.

6.2.3 Investigation of the effect of tooth lubrication on gearbox vibration characteristics

In this thesis, tooth lubrication is not considered when conducting dynamic simulations for fixed-axis spur gearboxes with tooth cracks. However, in industrial applications, gear teeth are always lubricated. To make gearbox dynamic simulation more practical, it is of necessity to take tooth lubrication into account when modelling the mesh interactions between engaged gear teeth. To be specific, the oil film stiffness and oil film damping produced by the lubrication oil film between engaged gear teeth should also be considered when evaluating the total stiffness and total damping of the gear tooth mesh interactions apart from the conventional tooth mesh stiffness and tooth mesh damping [54,143–145]. For the calculations of the oil film stiffness and oil film damping of tooth lubrication oil film, the elastohydrodynamic lubrication theory can be adopted to model the gear tooth lubrication [146–148]. On this basis, the obtained total stiffness and total damping include the effects of tooth lubrication, tooth mesh, and tooth crack severity progression. After inserting the total stiffness and total damping into gearbox motion equations, gearbox dynamic responses can be generated. Afterwards, the effect of tooth lubrication on the vibration characteristics of gearboxes with tooth cracks can be revealed by analyzing the gearbox dynamic responses.

6.2.4 Dynamic simulation and diagnosis of gearboxes with both gear and bearing faults

In this thesis, only diagnosis of gear faults (gear tooth cracks) is studied using dynamic simulation and signal processing, which means that all the bearings in a gearbox are assumed to be healthy. However, for practical gearboxes used in the industry, they may suffer from both gear faults and bearing faults simultaneously [15]. Therefore, it is worthy of conducting dynamic simulation and diagnosis of gearboxes involving both gear and bearing faults. To consider both bearing and gear faults simultaneously in gearbox dynamic simulation, the gearbox dynamic model presented in the thesis needs to be modified. The required modifications include: (1) bearing faults need to be simulated using a bearing dynamic model; (2) the coupling effect of bearings and gears need to be considered. To be specific, the inner race of a bearing is connected to a pinion by a rigid rotating shaft, therefore the motion of the bearing inner race of the pinon needs to be considered by taking both the gear tooth mesh force and the contact force between the bearing rollers and races into consideration. After conducting dynamic simulation, vibration characteristics of gearboxes with both bearing and gear faults will be known well. It is expected that when bearing faults occur in a gearbox, the bearing stiffness and damping will change accordingly, thus affecting the loading conditions and vibrations of the gears. Besides, for the diagnosis of gearboxes with both bearing and gear faults, advanced signal processing methods such as blind source separation and signal decomposition approaches are first needed to separate signal components related to bearing faults and those related to gear faults. Afterwards, the signal analysis developed in this thesis can be used for gear fault diagnosis and bearing fault diagnosis can be achieved using the signal demodulation and envelope analysis methods. More endeavour is needed for the study on dynamic simulation and diagnosis of gearboxes with both gear and bearing faults.

6.2.5 Evaluation of gear tooth mesh damping

In this thesis, the gear tooth mesh damping is assumed to be linearly proportional to the gear tooth mesh stiffness [26,149]. This assumption may work well for some situations but may not for other ones. Given that the damping effect of gear tooth mesh interactions is related to the energy dissipation of a gearbox system [150], which may be affected by gearbox geometry parameters and working condition properties, how to evaluate the gear tooth mesh damping of a gearbox working under specific conditions needs to be further investigated. In addition, the effect of gear tooth mesh damping on gearbox vibration characteristics needs further explorations as well.

6.2.6 Development of advanced methods for fault diagnosis under variable load conditions

Variable load conditions include two possible scenarios, namely constant speed and variable load condition, and variable speed and variable load condition. Gearboxes oftentimes experience variable load conditions in the industry, so it is important to conduct gearbox fault diagnosis when load fluctuations exist. Variable load conditions induce additional AM and FM into gearbox vibration signals, which lead to difficulties of fault diagnosis. Therefore, the load variation-induced AM and FM needs to be removed. In Chapter 4 of this thesis, the proposed normalization method has demonstrated its effectiveness in terms of removing the speed variation-induced AM and FM. The effectiveness of the normalization method proposed in Chapter 4 in terms of removing the load variation-induced AM and FM needs to be further checked. If it cannot work well, new advanced methods need to be developed to eliminate the load variation-induced AM and FM for gearbox fault diagnosis under variable load conditions.

References

[1] How Does a Wind Turbine Work?, Energy.Gov. (n.d.). https://www.energy.gov/maps/how-does-wind-turbine-work (accessed February 2, 2022).

[2] C.-H. Pan, J.J. Moskwa, Dynamic Modeling and Simulation of the Ford AOD Automobile Transmission, SAE Transactions. 104 (1995) 1689–1697.

[3] Auto parts for transmission, (n.d.). http://www.excel-bg.com/en/auto-parts-for-transmission (accessed February 2, 2022).

[4] G. Michalec, F. Buchsbaum, H. Tanaka, Elements of metric gear technology, Stock Drive Products & Sterling Instrument, n.d. https://gearkade.com/wp-content/uploads/2019/08/Elements-of-Metric-Gear-Technology.pdf (accessed February 11, 2022).

[5] Y. Fang, Dynamics of a Spur Gear Pair under Stochastic Internal and External Excitations, University of Alberta, 2019. https://era.library.ualberta.ca/items/72ed763e-db30-4e2b-b8b9-607505006edd (accessed February 2, 2022).

[6] B. Youngblood, Gear Train : Gear Ratio, Torque and Speed Calculations, SMLease Design. (2018). https://www.smlease.com/entries/mechanism/gear-train-gear-ratio-torque-and-speed-calculation/ (accessed February 3, 2022).

[7] Functionally Matching Gears (teeth count) in Planetary Gearbox, Engineering Stack Exchange. (n.d.). https://engineering.stackexchange.com/questions/24004/functionally-matching-gears-teeth-count-in-planetary-gearbox (accessed February 3, 2022).

[8] How Gears Work - Different Types of Gears, their Functions, Mechanisms and Applications, (n.d.). https://www.thomasnet.com/articles/machinery-tools-supplies/understanding-gears (accessed February 2, 2022).

[9] QTC Metric Gears - Product Listing, (n.d.). https://qtcgears.com/products/ (accessed February 4, 2022).

[10] S. Sheng, Gearbox Typical Failure Modes, Detection and Mitigation Methods, (2011) 24.

[11] R. Errichello, S. Sheng, M. McDade, Wind turbine gearbox failure modes – a brief, (2011) 26.

[12] R. Errichello, How to analyze gear failures, Practical Failure Analysis. 2 (2002) 8–16. https://doi.org/10.1007/BF02715492.

[13] P.J.L. Fernandes, Tooth bending fatigue failures in gears, Engineering Failure Analysis. 3 (1996) 219–225. https://doi.org/10.1016/1350-6307(96)00008-8.

[14] L.E. Alban, Systematic analysis of gear failures, American Society for Metals, Metals Park, Ohio, 1985.

[15] W. Teng, X. Ding, X. Zhang, Y. Liu, Z. Ma, Multi-fault detection and failure analysis of wind turbine gearbox using complex wavelet transform, Renewable Energy. 93 (2016) 591–598. https://doi.org/10.1016/j.renene.2016.03.025.

[16] J. Wattenphul, How Does Closed Loop Control Work in a VFD?, KEB. (2019). https://www.kebamerica.com/blog/how-does-closed-loop-control-work-in-a-vfd/ (accessed February 7, 2022).

[17] I. Antoniadou, G. Manson, W.J. Staszewski, T. Barszcz, K. Worden, A time–frequency analysis approach for condition monitoring of a wind turbine gearbox under varying load conditions, Mechanical Systems and Signal Processing. 64–65 (2015) 188–216. https://doi.org/10.1016/j.ymssp.2015.03.003.

[18] C.M. Vicuña, F. Chaari, Analysis of a Planetary Gearbox Under Non-stationary Operating Conditions: Numerical and Experimental Results, in: F. Chaari, R. Zimroz, W. Bartelmus, M. Haddar (Eds.), Advances in Condition Monitoring of Machinery in Non-Stationary Operations, Springer International Publishing, Cham, 2016: pp. 351–362. https://doi.org/10.1007/978-3-319-20463-5_26.

[19] F. Chaari, W. Bartelmus, R. Zimroz, T. Fakhfakh, M. Haddar, Gearbox vibration signal amplitude and frequency modulation, Shock and Vibration. (2012). https://doi.org/10.3233/SAV-2011-0656.

[20] D. Wright, DANotes: Design and Analysis of Machine Elements, (n.d.). http://www-mdp.eng.cam.ac.uk/web/library/enginfo/textbooks_dvd_only/DAN/intro/contents.html (accessed February 6, 2022).

[21] R. Shu, J. Wei, R. Tan, X. Wu, B. Fu, Investigation of dynamic and synchronization properties of a multi-motor driving system: Theoretical analysis and experiment, Mechanical Systems and Signal Processing. 153 (2021) 107496. https://doi.org/10.1016/j.ymssp.2020.107496.

[22] J.M. Ha, H. Oh, J. Park, B.D. Youn, Classification of operating conditions of wind turbines for a class-wise condition monitoring strategy, Renewable Energy. 103 (2017) 594–605. https://doi.org/10.1016/j.renene.2016.10.071.

[23] X. Liang, M.J. Zuo, Z. Feng, Dynamic modeling of gearbox faults: A review, Mechanical Systems and Signal Processing. 98 (2018) 852–876. https://doi.org/10.1016/j.ymssp.2017.05.024.

[24] L. Bachar, I. Dadon, R. Klein, J. Bortman, The effects of the operating conditions and tooth fault on gear vibration signature, Mechanical Systems and Signal Processing. 154 (2021) 107508. https://doi.org/10.1016/j.ymssp.2020.107508.

[25] C.W. de Silva, Modeling and Control of Engineering Systems, CRC Press, Boca Raton, 2009. https://doi.org/10.1201/9781420076875.

[26] X.H. Tian, Dynamic simulation for system response of gearbox including localized gear faults, Master Thesis, University of Alberta, 2004.

[27] X. Liang, Dynamics Based Vibration Signal Modeling and Fault Detection of Planetary Gearboxes, University of Alberta, 2016. https://doi.org/10.7939/R3S46HB7Q.

[28] J. Wu, Y. Yang, X. Yang, J. Cheng, Fault feature analysis of cracked gear based on LOD and analytical-FE method, Mechanical Systems and Signal Processing. 98 (2018) 951–967. https://doi.org/10.1016/j.ymssp.2017.05.041.

[29] N.K. Raghuwanshi, A. Parey, Mesh stiffness measurement of cracked spur gear by photoelasticity technique, Measurement. 73 (2015) 439–452. https://doi.org/10.1016/j.measurement.2015.05.035.

[30] N.K. Raghuwanshi, A. Parey, Experimental measurement of gear mesh stiffness of cracked spur gear by strain gauge technique, Measurement. 86 (2016) 266–275. https://doi.org/10.1016/j.measurement.2016.03.001.

[31] D.G. Lewicki, Gear Crack Propagation Path Studies-Guidelines for Ultra-Safe Design, Journal of the American Helicopter Society. 47 (2002) 64–72. https://doi.org/10.4050/JAHS.47.64.

[32] A. Belsak, J. Flasker, Detecting cracks in the tooth root of gears, Engineering Failure Analysis. 14 (2007) 1466–1475. https://doi.org/10.1016/j.engfailanal.2007.01.013.

[33] S. Wu, M.J. Zuo, A. Parey, Simulation of spur gear dynamics and estimation of fault growth, Journal of Sound and Vibration. 317 (2008) 608–624. https://doi.org/10.1016/j.jsv.2008.03.038.

[34] Y. Pandya, A. Parey, Failure path based modified gear mesh stiffness for spur gear pair with tooth root crack, Engineering Failure Analysis. 27 (2013) 286–296. https://doi.org/10.1016/j.engfailanal.2012.08.015.

[35] O.D. Mohammed, M. Rantatalo, J.-O. Aidanpää, U. Kumar, Vibration signal analysis for gear fault diagnosis with various crack progression scenarios, Mechanical Systems and Signal Processing. 41 (2013) 176–195. https://doi.org/10.1016/j.ymssp.2013.06.040.

[36] J. Urbanek, T. Barszcz, M. Strączkiewicz, A. Jablonski, Normalization of vibration signals generated under highly varying speed and load with application to signal separation, Mechanical Systems and Signal Processing. 82 (2017) 13–31. https://doi.org/10.1016/j.ymssp.2016.04.017.

[37] A. Aherwar, An investigation on gearbox fault detection using vibration analysis techniques: A review, Australian Journal of Mechanical Engineering. 10 (2012) 169–183. https://doi.org/10.7158/M11-830.2012.10.2.

[38] J. Gribble, Acoustic Analysis for the Rest of Us, (n.d.). https://www.machinerylubrication.com/Read/839/acoustic-analysis-lubrication (accessed February 10, 2022).

[39] A. Almasi, Oil analysis methods and lubrication monitoring, Plant Services. (n.d.). https://www.plantservices.com/articles/2014/oil-analysis-methods-lubrication-monitoring/ (accessed February 10, 2022).

[40] M. Lebold, K. McClintic, R. Campbell, C. Byington, K. Maynard, Review of vibration analysis methods for gearbox diagnostics and prognostics, Proceedings of the 54th Meeting of the Society for Machinery Failure Prevention Technology. (2000) 623–634.

[41] A.S. Sait, Y.I. Sharaf-Eldeen, A Review of Gearbox Condition Monitoring Based on vibration Analysis Techniques Diagnostics and Prognostics, in: T. Proulx (Ed.), Rotating Machinery, Structural Health Monitoring, Shock and Vibration, Volume 5, Springer, New York, NY, 2011: pp. 307–324. https://doi.org/10.1007/978-1-4419-9428-8_25.

[42] E. Bechhoefer, M. Kingsley, A review of time synchronous average algorithms, Annual Conference of the Prognostics and Health Management Society. 1 (2009) 1–10.

[43] Z. Feng, M. Liang, F. Chu, Recent advances in time–frequency analysis methods for machinery fault diagnosis: A review with application examples, Mechanical Systems and Signal Processing. 38 (2013) 165–205. https://doi.org/10.1016/j.ymssp.2013.01.017.

[44] F. Hlawatsch, G.F. Boudreaux-Bartels, Linear and quadratic time-frequency signal representations, IEEE Signal Processing Magazine. 9 (1992) 21–67. https://doi.org/10.1109/79.127284.

[45] N. Hess-Nielsen, M.V. Wickerhauser, Wavelets and time-frequency analysis, Proceedings of the IEEE. 84 (1996) 523–540. https://doi.org/10.1109/5.488698.

[46] L. Cohen, Time-frequency distributions-a review, Proceedings of the IEEE. 77 (1989) 941–981. https://doi.org/10.1109/5.30749.

[47] N. Huang, Z. Shen, S. Long, M.L.C. Wu, H. Shih, Q. Zheng, N.-C. Yen, C.-C. Tung, H. Liu, The empirical mode decomposition and the Hilbert spectrum for nonlinear and non-stationary time series analysis, Proceedings of the Royal Society of London. Series A: Mathematical, Physical and Engineering Sciences. 454 (1998) 903–995. https://doi.org/10.1098/rspa.1998.0193.

[48] P. Avitabile, Modal Testing: A Practitioner's Guide, John Wiley & Sons Ltd, Chichester, UK, 2017. https://doi.org/10.1002/9781119222989.

[49] W. Bartelmus, Mathematical modelling and computer simulations as an aid to gearbox diagnostics, Mechanical Systems and Signal Processing. 15 (2001) 855–871. https://doi.org/10.1006/mssp.2001.1411.

[50] H. Nevzat Özgüven, D.R. Houser, Mathematical models used in gear dynamics—A review, Journal of Sound and Vibration. 121 (1988) 383–411. https://doi.org/10.1016/S0022-460X(88)80365-1.

[51] W.A. Tuplin, Gear-Tooth Stresses at High Speed, Proceedings of the Institution of Mechanical Engineers. 163 (1950) 162–175. https://doi.org/10.1243/PIME_PROC_1950_163_020_02.

[52] M. Utagawa, Dynamic Loads on Spur Gear Teeth, Bulletin of JSME. 1 (1958) 397–403. https://doi.org/10.1299/jsme1958.1.397.

[53] K. Nakamura, Tooth Separations and Abnormal Noise on Power-Transmission Gears, Bulletin of JSME. 10 (1967) 846–854. https://doi.org/10.1299/jsme1958.10.846.

[54] Y. Luo, Dynamic Modelling and Fault Feature Analysis of Gear Tooth Pitting and Spalling, Thesis, Université d'Ottawa / University of Ottawa, 2019. https://doi.org/10.20381/ruor-23086.

[55] J. Wang, R. Li and, X. Peng, Survey of nonlinear vibration of gear transmission systems, Applied Mechanics Reviews. 56 (2003) 309–329. https://doi.org/10.1115/1.1555660.

[56] H.N. Özgüven, D.R. Houser, Dynamic analysis of high speed gears by using loaded static transmission error, Journal of Sound and Vibration. 125 (1988) 71–83. https://doi.org/10.1016/0022-460X(88)90416-6.

[57] A. Kahraman, R. Singh, Non-linear dynamics of a spur gear pair, Journal of Sound and Vibration. 142 (1990) 49–75. https://doi.org/10.1016/0022-460X(90)90582-K.

[58] A. Kahraman, R. Singh, Non-linear dynamics of a geared rotor-bearing system with multiple clearances, Journal of Sound and Vibration. 144 (1991) 469–506. https://doi.org/10.1016/0022-460X(91)90564-Z.

[59] Z.-I. Korka, I.-C. Mituletu, A Review of Dynamic Models Used in Simulation of Gear Transmissions, Analele Universitatii "Eftimie Murgu." 21 (2014) 165–174.

[60] H. Iida, A. Tamura, K. Kikuchi, H. Agata, Coupled Torsional-flexural Vibration of a Shaft in a Geared System of Rotors (1st Report), Bulletin of JSME. 23 (1980) 2111–2117. https://doi.org/10.1299/jsme1958.23.2111.

[61] J. Shi, X. Gou, L. Zhu, C. Qi, Nonlinear Dynamic Modeling of 3-DOF Gear System with Tooth Contact Temperature, in: J. Tan, F. Gao, C. Xiang (Eds.), Advances in Mechanical Design, Springer, Singapore, 2018: pp. 213–226. https://doi.org/10.1007/978-981-10-6553-8_14.

[62] A. Kahraman, H.N. Ozguven, D.R. Houser, J.J. Zakrajsek, Dynamic Analysis of Geared Rotors by Finite Elements, Journal of Mechanical Design. 114 (1992) 507–514. https://doi.org/10.1115/1.2926579.

[63] O.D. Mohammed, M. Rantatalo, J.-O. Aidanpää, Dynamic modelling of a one-stage spur gear system and vibration-based tooth crack detection analysis, Mechanical Systems and Signal Processing. 54–55 (2015) 293–305. https://doi.org/10.1016/j.ymssp.2014.09.001.

[64] Z. Tian, M.J. Zuo, S. Wu, Crack propagation assessment for spur gears using model-based analysis and simulation, Journal of Intelligent Manufacturing. 23 (2012) 239–253. https://doi.org/10.1007/s10845-009-0357-8.

[65] M.T. Khabou, N. Bouchaala, F. Chaari, T. Fakhfakh, M. Haddar, Study of a spur gear dynamic behavior in transient regime, Mechanical Systems and Signal Processing. 25 (2011) 3089–3101. https://doi.org/10.1016/j.ymssp.2011.04.018.

[66] F. Chaari, W. Bartelmus, R. Zimroz, T. Fakhfakh, M. Haddar, Gearbox vibration signal amplitude and frequency modulation, Shock and Vibration. 19 (2012) 635–652. https://doi.org/10.3233/SAV-2011-0656.

[67] Y. Luo, N. Baddour, M. Liang, Dynamical modeling and experimental validation for tooth pitting and spalling in spur gears, Mechanical Systems and Signal Processing. 119 (2019) 155–181. https://doi.org/10.1016/j.ymssp.2018.09.027.

[68] S. Jia, I. Howard, Comparison of localised spalling and crack damage from dynamic modelling of spur gear vibrations, Mechanical Systems and Signal Processing. 20 (2006) 332–349. https://doi.org/10.1016/j.ymssp.2005.02.009.

[69] D.C.H. Yang, J.Y. Lin, Hertzian Damping, Tooth Friction and Bending Elasticity in Gear Impact Dynamics, Journal of Mechanisms, Transmissions, and Automation in Design. 109 (1987) 189–196. https://doi.org/10.1115/1.3267437.

[70] P. Sainsot and, P. Velex, O. Duverger, Contribution of Gear Body to Tooth Deflections—A New Bidimensional Analytical Formula, Journal of Mechanical Design. 126 (2004) 748–752. https://doi.org/10.1115/1.1758252.

[71] X. Zhou, Y. Shao, Y. Lei, M. Zuo, Time-Varying Meshing Stiffness Calculation and Vibration Analysis for a 16DOF Dynamic Model With Linear Crack Growth in a Pinion, Journal of Vibration and Acoustics. 134 (2011). https://doi.org/10.1115/1.4004683.

[72] F. Chaari, T. Fakhfakh, M. Haddar, Analytical modelling of spur gear tooth crack and influence on gearmesh stiffness, European Journal of Mechanics - A/Solids. 28 (2009) 461–468. https://doi.org/10.1016/j.euromechsol.2008.07.007.

[73] Y. Pandya, A. Parey, Failure path based modified gear mesh stiffness for spur gear pair with tooth root crack, Engineering Failure Analysis. 27 (2013) 286–296. https://doi.org/10.1016/j.engfailanal.2012.08.015.

[74] O.D. Mohammed, M. Rantatalo, U. Kumar, Analytical Crack Propagation Scenario for Gear Teeth and Time-Varying Gear Mesh Stiffness, International Journal of Aerospace and Mechanical Engineering. 6 (2012) 1544–1549.

[75] Z. Chen, Y. Shao, Dynamic simulation of spur gear with tooth root crack propagating along tooth width and crack depth, Engineering Failure Analysis. 18 (2011) 2149–2164. https://doi.org/10.1016/j.engfailanal.2011.07.006.

[76] P.D. McFadden, Examination of a technique for the early detection of failure in gears by signal processing of the time domain average of the meshing vibration, Mechanical Systems and Signal Processing. 1 (1987) 173–183. https://doi.org/10.1016/0888-3270(87)90069-0.

[77] W. Wang, Early detection of gear tooth cracking using the resonance demodulation technique, Mechanical Systems and Signal Processing. 15 (2001) 887–903. https://doi.org/10.1006/mssp.2001.1416.

[78] R.B. Randall, A New Method of Modeling Gear Faults, Journal of Mechanical Design. 104 (1982) 259–267. https://doi.org/10.1115/1.3256334.

[79] B. Forrester, Advanced vibration analysis techniques for fault detection and diagnosis in geared transmission systems, PhD Thesis, Swinburne University of Technology, 1996. https://www.semanticscholar.org/paper/Advanced-vibration-analysis-techniques-for-fault-in-Forrester/655056c8bd66febdb43ddbc01cf05ddd5fc78b47 (accessed February 21, 2022).

[80] S. Schmidt, P.S. Heyns, Normalisation of the amplitude modulation caused by time-varying operating conditions for condition monitoring, Measurement. 149 (2020) 106964. https://doi.org/10.1016/j.measurement.2019.106964.

[81] C.J. Stander, P.S. Heyns, W. Schoombie, Using vibration monitoring for local fault detection on gears operating under fluctuating load conditions, Mechanical Systems and Signal Processing. 16 (2002) 1005–1024. https://doi.org/10.1006/mssp.2002.1479.

[82] R.M. Stewart, Some Useful Data Analysis Techniques for Gearbox Diagnostics, Applications of Time Series Analysis. (1977) 19.

[83] H.J. Decker, D.G. Lewicki, Spiral Bevel Pinion Crack Detection in a Helicopter Gearbox, in: Phoenix, AZ, 2003. https://ntrs.nasa.gov/citations/20030064140 (accessed February 24, 2022).

[84] H.J. Decker, Crack Detection for Aerospace Quality Spur Gears, U.S. Army Research Laboratory Glenn Research Center, Cleveland, Ohio, 2002.

[85] J.J. Zakrajsek, R.F. Handschuh, H.J. Decker, Application of Fault Detection Techniques to Spiral Bevel Gear Fatigue Data., National Aeronautics and Space Administration Cleveland OH Lewis Research Center, 1994. https://apps.dtic.mil/sti/citations/ADA289970 (accessed January 24, 2021).

[86] V. Sharma, A. Parey, Gear crack detection using modified TSA and proposed fault indicators for fluctuating speed conditions, Measurement. 90 (2016) 560–575. https://doi.org/10.1016/j.measurement.2016.04.076.

[87] Z. Man, W. Wang, S. Khoo, J. Yin, Optimal sinusoidal modelling of gear mesh vibration signals for gear diagnosis and prognosis, Mechanical Systems and Signal Processing. 33 (2012) 256–274. https://doi.org/10.1016/j.ymssp.2012.07.004.

[88] P. Zhou, Y. Yang, H. Wang, M. Du, Z. Peng, W. Zhang, The relationship between fault-induced impulses and harmonic-cluster with applications to rotating machinery fault diagnosis, Mechanical Systems and Signal Processing. 144 (2020) 106896. https://doi.org/10.1016/j.ymssp.2020.106896.

[89] R. Yan, R.X. Gao, X. Chen, Wavelets for fault diagnosis of rotary machines: A review with applications, Signal Processing. 96 (2014) 1–15. https://doi.org/10.1016/j.sigpro.2013.04.015.

[90] Z.K. Peng, F.L. Chu, Application of the wavelet transform in machine condition monitoring and fault diagnostics: a review with bibliography, Mechanical Systems and Signal Processing. 18 (2004) 199–221. https://doi.org/10.1016/S0888-3270(03)00075-X.

[91] C. Junsheng, Y. Dejie, Y. Yu, Research on the intrinsic mode function (IMF) criterion in EMD method, Mechanical Systems and Signal Processing. 20 (2006) 817–824. https://doi.org/10.1016/j.ymssp.2005.09.011.

[92] Z. Wu, N. Huang, Ensemble Empirical Mode Decomposition: a Noise-Assisted Data Analysis Method, Adv. Data Sci. Adapt. Anal. (2009). https://doi.org/10.1142/S1793536909000047.

[93] J.S. Smith, The local mean decomposition and its application to EEG perception data, Journal of The Royal Society Interface. 2 (2005) 443–454. https://doi.org/10.1098/rsif.2005.0058.

[94] K. Baker, Singular Value Decomposition Tutorial, (n.d.) 24.

[95] Y. Miao, B. Zhang, Y. Yi, J. Lin, Application of improved reweighted singular value decomposition for gearbox fault diagnosis based on built-in encoder information, Measurement. 168 (2021) 108295. https://doi.org/10.1016/j.measurement.2020.108295.

[96] Y. Chen, X. Liang, M.J. Zuo, An improved singular value decomposition-based method for gear tooth crack detection and severity assessment, Journal of Sound and Vibration. 468 (2020) 115068. https://doi.org/10.1016/j.jsv.2019.115068.

[97] M. Zhao, X. Jia, A novel strategy for signal denoising using reweighted SVD and its applications to weak fault feature enhancement of rotating machinery, Mechanical Systems and Signal Processing. 94 (2017) 129–147. https://doi.org/10.1016/j.ymssp.2017.02.036.

[98] W.-X. Yang, P.W. Tse, Development of an advanced noise reduction method for vibration analysis based on singular value decomposition, NDT & E International. 36 (2003) 419–432. https://doi.org/10.1016/S0963-8695(03)00044-6.

[99] X. Zhao, B. Ye, Selection of effective singular values using difference spectrum and its application to fault diagnosis of headstock, Mechanical Systems and Signal Processing. 25 (2011) 1617–1631. https://doi.org/10.1016/j.ymssp.2011.01.003.

[100] K.R. Fyfe, E.D.S. Munck, Analysis of computed order tracking, Mechanical Systems and Signal Processing. 11 (1997) 187–205. https://doi.org/10.1006/mssp.1996.0056.

[101] D. Abboud, J. Antoni, M. Eltabach, S. Sieg-Zieba, Speed-spectral whitening for enhancing envelope analysis in speed varying conditions, in: VISHNO 2014, France, 2014. https://hal.archives-ouvertes.fr/hal-00994090 (accessed November 27, 2019).

[102] D. Abboud, J. Antoni, S. Sieg-Zieba, M. Eltabach, Deterministic-random separation in nonstationary regime, Journal of Sound and Vibration. 362 (2016) 305–326. https://doi.org/10.1016/j.jsv.2015.09.029.

[103] X. Yang, M.J. Zuo, Z. (Will) Tian, Tooth Crack Severity Assessment in the Early Stage of Crack Propagation Using Gearbox Dynamic Model, PHM_CONF. 11 (2019). https://doi.org/10.36001/phmconf.2019.v11i1.801.

[104] X. Yang, M.J. Zuo, Z. Tian, Development of crack induced impulse-based condition indicators for early tooth crack severity assessment, Mechanical Systems and Signal Processing. 165 (2022) 108327. https://doi.org/10.1016/j.ymssp.2021.108327.

[105] X. Yang, P. Zhou, M.J. Zuo, Z. Tian, Z. Peng, The effect of time-varying operating condition on the crack induced impulses and its application to gearbox tooth crack diagnosis, Mechanical Systems and Signal Processing. (2021) 1–40.

[106] X. Yang, M.J. Zuo, Z. Tian, Normalization of gearbox vibration signal for tracking tooth crack severity progression under time-varying operating conditions, in: 2020 Asia-Pacific International Symposium on Advanced Reliability and Maintenance Modeling (APARM), 2020: pp. 1–6. https://doi.org/10.1109/APARM49247.2020.9209396.

[107] X. Yang, P. Zhou, M.J. Zuo, Z. Tian, Normalization of gearbox vibration signal for tooth crack diagnosis under variable speed conditions, Quality and Reliability Engineering International. (2021) 1–27. https://doi.org/10.1002/qre.3029.

[108] X. Yang, D. Wei, M.J. Zuo, Z. Tian, Analysis of vibration signals and detection for multiple tooth cracks in spur gearboxes, Mechanical Systems and Signal Processing. (2022) 1–46.

[109] S. Sheng, W. Yang, Wind turbine drivetrain condition monitoring - an overview (presentation), National Renewable Energy Lab. (NREL), Golden, CO (United States), 2013. https://www.osti.gov/biblio/1087787 (accessed December 27, 2019).

[110] A.K.S. Jardine, D. Lin, D. Banjevic, A review on machinery diagnostics and prognostics implementing condition-based maintenance, Mechanical Systems and Signal Processing. 20 (2006) 1483–1510. https://doi.org/10.1016/j.ymssp.2005.09.012.

[111] W.D. Mark, Time-synchronous-averaging of gear-meshing-vibration transducer responses for elimination of harmonic contributions from the mating gear and the gear pair, Mechanical Systems and Signal Processing. 62–63 (2015) 21–29. https://doi.org/10.1016/j.ymssp.2015.03.006.

[112] T.K. Sarkar, O. Pereira, Using the matrix pencil method to estimate the parameters of a sum of complex exponentials, IEEE Antennas and Propagation Magazine. 37 (1995) 48–55. https://doi.org/10.1109/74.370583.

[113] Y. Hua, T.K. Sarkar, Matrix pencil method for estimating parameters of exponentially damped/undamped sinusoids in noise, IEEE Transactions on Acoustics, Speech, and Signal Processing. 38 (1990) 814–824. https://doi.org/10.1109/29.56027.

[114] P. Kundu, A. Darpe, M. S. Kulkarni, A correlation coefficient based vibration indicator for detecting natural pitting progression in spur gears, Mechanical Systems and Signal Processing. 129 (2019). https://doi.org/10.1016/j.ymssp.2019.04.058.

[115] J.M. Ha, B.D. Youn, H. Oh, B. Han, Y. Jung, J. Park, Autocorrelation-based time synchronous averaging for condition monitoring of planetary gearboxes in wind turbines, Mechanical Systems and Signal Processing. 70–71 (2016) 161–175. https://doi.org/10.1016/j.ymssp.2015.09.040.

[116] J. Antoni, R.B. Randall, The spectral kurtosis: application to the vibratory surveillance and diagnostics of rotating machines, Mechanical Systems and Signal Processing. 20 (2006) 308–331. https://doi.org/10.1016/j.ymssp.2004.09.002.

[117] Y. Li, K. Ding, G. He, H. Lin, Vibration mechanisms of spur gear pair in healthy and fault states, Mechanical Systems and Signal Processing. 81 (2016) 183–201. https://doi.org/10.1016/j.ymssp.2016.03.014.

[118] X. Yang, K. Ding, G. He, Phenomenon-model-based AM-FM vibration mechanism of faulty spur gear, Mechanical Systems and Signal Processing. 134 (2019) 106366. https://doi.org/10.1016/j.ymssp.2019.106366.

[119] P. Lemmerling, S. Van Huffel, Analysis of the structured total least squares problem for Hankel/Toeplitz matrices, Numerical Algorithms. 27 (2001) 89–114. https://doi.org/10.1023/A:1016775707686.

[120] D. Potts, M. Tasche, Parameter estimation for exponential sums by approximate Prony method, Signal Processing. 90 (2010) 1631–1642. https://doi.org/10.1016/j.sigpro.2009.11.012.

[121] G. Liu, J. Quintero, V.M. Venkatasubramanian, Oscillation monitoring system based on wide area synchrophasors in power systems, in: 2007 IREP Symposium - Bulk Power System

Dynamics and Control - VII. Revitalizing Operational Reliability, 2007: pp. 1–13. https://doi.org/10.1109/IREP.2007.4410548.

[122] T. Hastie, R. Tibshirani, J. Friedman, The elements of statistical learning: data mining, inference, and prediction, second, Springer Science & Business Media, 2009.

[123] Y. Lei, M.J. Zuo, Gear crack level identification based on weighted K nearest neighbor classification algorithm, Mechanical Systems and Signal Processing. 23 (2009) 1535–1547. https://doi.org/10.1016/j.ymssp.2009.01.009.

[124] Z. Cheng, N. Hu, X. Zhang, Crack level estimation approach for planetary gearbox based on simulation signal and GRA, Journal of Sound and Vibration. 331 (2012) 5853–5863. https://doi.org/10.1016/j.jsv.2012.07.035.

[125] W. Bartelmus, F. Chaari, R. Zimroz, M. Haddar, Modelling of gearbox dynamics under time-varying nonstationary load for distributed fault detection and diagnosis, European Journal of Mechanics - A/Solids. 29 (2010) 637–646. https://doi.org/10.1016/j.euromechsol.2010.03.002.

[126] P. Zhou, Z. Peng, S. Chen, Z. Tian, M.J. Zuo, Sinusoidal FM patterns of fault-related vibration signals for planetary gearbox fault detection under non-stationary conditions, Mechanical Systems and Signal Processing. 155 (2021) 107623. https://doi.org/10.1016/j.ymssp.2021.107623.

[127] W. Bartelmus, Gearbox dynamic multi-body modelling for condition monitoring under the case of varying operating condition, Journal of Coupled Systems and Multiscale Dynamics. 2 (2014) 224–237. https://doi.org/10.1166/jcsmd.2014.1057.

[128] F. Chaari, R. Zimroz, W. Bartelmus, T. Fakhfakh, M. Haddar, Model based investigation on a two stages gearbox dynamics under non-stationary operations, in: T. Fakhfakh, W. Bartelmus, F. Chaari, R. Zimroz, M. Haddar (Eds.), Condition Monitoring of Machinery in Non-Stationary Operations, Springer, Berlin, Heidelberg, 2012: pp. 133–142. https://doi.org/10.1007/978-3-642-28768-8_14.

[129] W. Bartelmus, R. Zimroz, Vibration condition monitoring of planetary gearbox under varying external load, Mechanical Systems and Signal Processing. 23 (2009) 246–257. https://doi.org/10.1016/j.ymssp.2008.03.016.

[130] W. Bartelmus, R. Zimroz, A new feature for monitoring the condition of gearboxes in non-stationary operating conditions, Mechanical Systems and Signal Processing. 23 (2009) 1528–1534. https://doi.org/10.1016/j.ymssp.2009.01.014.

[131] K. Buchin, M. Buchin, C. Wenk, Computing the Fréchet distance between simple polygons, Computational Geometry. 41 (2008) 2–20. https://doi.org/10.1016/j.comgeo.2007.08.003.

[132] H. Alt, M. Godau, Computing the fréchet distance between two polygonal curves, Int. J. Comput. Geom. Appl. 05 (1995) 75–91. https://doi.org/10.1142/S0218195995000064.

[133] Z. Feng, M.J. Zuo, Vibration signal models for fault diagnosis of planetary gearboxes, Journal of Sound and Vibration. 331 (2012) 4919–4939. https://doi.org/10.1016/j.jsv.2012.05.039.

[134] X. Xu, M. Zhao, J. Lin, Y. Lei, Envelope harmonic-to-noise ratio for periodic impulses detection and its application to bearing diagnosis, Measurement. 91 (2016) 385–397. https://doi.org/10.1016/j.measurement.2016.05.073.

[135] D. Wang, K-nearest neighbors based methods for identification of different gear crack levels under different motor speeds and loads: Revisited, Mechanical Systems and Signal Processing. 70–71 (2016) 201–208. https://doi.org/10.1016/j.ymssp.2015.10.007.

[136] Z. He, H. Shao, P. Wang, J. (Jing) Lin, J. Cheng, Y. Yang, Deep transfer multi-wavelet auto-encoder for intelligent fault diagnosis of gearbox with few target training samples, Knowledge-Based Systems. 191 (2020) 105313. https://doi.org/10.1016/j.knosys.2019.105313.

[137] X. Li, J. Cheng, H. Shao, K. Liu, B. Cai, A Fusion CWSMM-based Framework for Rotating Machinery Fault Diagnosis under Strong Interference and Imbalanced Case, IEEE Transactions on Industrial Informatics. (2021) 1–1. https://doi.org/10.1109/TII.2021.3125385.

[138] A.S. Mohamed, S. Sassi, M. Roshun Paurobally, Model-Based Analysis of Spur Gears' Dynamic Behavior in the Presence of Multiple Cracks, Shock and Vibration. 2018 (2018) e1913289. https://doi.org/10.1155/2018/1913289.

[139] M. Rezaei, M. Poursina, S.H. Jazi, F.H. Aboutalebi, Multi crack detection in helical gear teeth using transmission error ratio, J Mech Sci Technol. 33 (2019) 1115–1121. https://doi.org/10.1007/s12206-019-0111-x.

[140] V. Spitas, G.A. Papadopoulos, C. Spitas, T. Costopoulos, Experimental Investigation of Load Sharing in Multiple Gear Tooth Contact Using the Stress-Optical Method of Caustics, Strain. 47 (2011) e227–e233. https://doi.org/10.1111/j.1475-1305.2008.00558.x.

[141] X.-H. Liang, Z.-L. Liu, J. Pan, M.J. Zuo, Spur Gear Tooth Pitting Propagation Assessment Using Model-based Analysis, Chin. J. Mech. Eng. 30 (2017) 1369–1382. https://doi.org/10.1007/s10033-017-0196-z.

[142] X. Zhao, B. Ye, Singular value decomposition packet and its application to extraction of weak fault feature, Mechanical Systems and Signal Processing. 70–71 (2016) 73–86. https://doi.org/10.1016/j.ymssp.2015.08.033.

[143] Z. Xiao, C. Zhou, S. Chen, Z. Li, Effects of oil film stiffness and damping on spur gear dynamics, Nonlinear Dyn. 96 (2019) 145–159. https://doi.org/10.1007/s11071-019-04780-6.

[144] C. Zhou, Z. Xiao, Stiffness and damping models for the oil film in line contact elastohydrodynamic lubrication and applications in the gear drive, Applied Mathematical Modelling. 61 (2018) 634–649. https://doi.org/10.1016/j.apm.2018.05.012.

[145] Y. Luo, N. Baddour, M. Liang, Dynamical modeling and experimental validation for tooth pitting and spalling in spur gears, Mechanical Systems and Signal Processing. 119 (2019) 155–181. https://doi.org/10.1016/j.ymssp.2018.09.027.

[146] S. Li, A. Kahraman, A tribo-dynamic model of a spur gear pair, Journal of Sound and Vibration. 332 (2013) 4963–4978. https://doi.org/10.1016/j.jsv.2013.04.022.

[147] S. Li, A. Kahraman, A Transient Mixed Elastohydrodynamic Lubrication Model for Spur Gear Pairs, Journal of Tribology. 132 (2009). https://doi.org/10.1115/1.4000270.

[148] C. Zhou, Z. Xiao, S. Chen, X. Han, Normal and tangential oil film stiffness of modified spur gear with non-Newtonian elastohydrodynamic lubrication, Tribology International. 109 (2017) 319–327. https://doi.org/10.1016/j.triboint.2016.12.045.

[149] M. Amabili, A. Rivola, Dynamic analysis of spur gear pairs: steady-state response and stability of the SDOF model with time-varying meshing damping, Mechanical Systems and Signal Processing. 11 (1997) 375–390. https://doi.org/10.1006/mssp.1996.0072.

[150] D.C.H. Yang, Z.S. Sun, A rotary model for spur gear dynamics, Journal of Mechanisms, Transmissions, and Automation in Design. 107 (1985) 529–535.